231654

UCRL-MA-109338 Pt. II

# Numerical Electromagnetics Code – NEC–4

## Method of Moments

## Part II: Program Description – Theory

Gerald J. Burke

January 1992

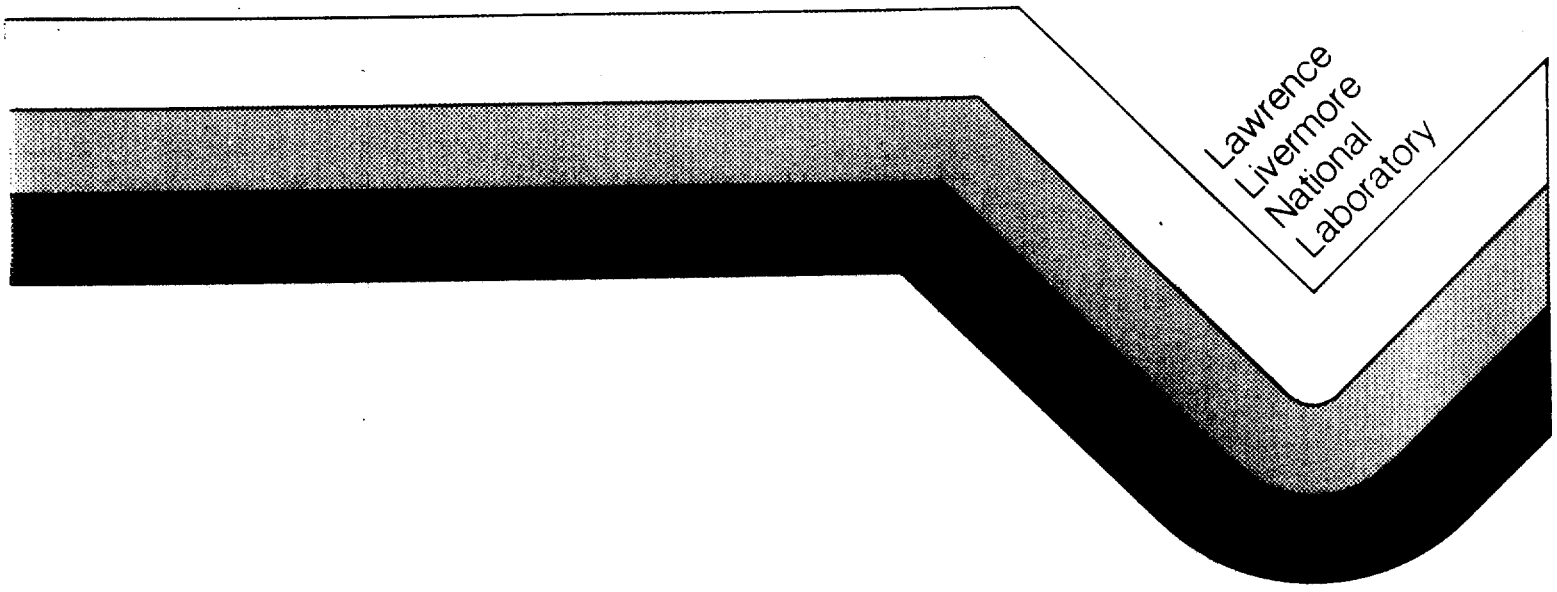

Work performed under the auspices of the U.S. Department of Energy by Lawrence Livermore National Laboratory under Contract W-7405-ENG-48.

# Preface

NEC–4 is the latest version of The Numerical Electromagnetics Code — Method of Moments that has been developed at the Lawrence Livermore National Laboratory, Livermore, California, under the sponsorship of the U.S. Army, ISEC and CECOM, the Naval Ocean Systems Center and the Air Force Weapons Laboratory. The development of the version NEC–4 was sponsored by the U.S. Army ISEC at Ft. Huachuca, AZ. The NEC Method of Moments code started as an advanced version of the Antenna Modeling Program (AMP) developed in the early 1970's by MBAssociates for the Naval Research Laboratory, Naval Ship Engineering Center, U.S. Army ECOM/Communications Systems, U.S. Army Strategic Communications Command and Rome Air Development Center, under Office of Naval Research Contract N00014-71-C-0187.

The documentation for NEC–4 consists of three volumes:

Part I: NEC Program Description — Theory
Part II: NEC Program Description — Code
Part III: NEC User's Guide

The documentation for successive versions of NEC has been prepared by updating manuals for previous versions of the code, starting from AMP. In some cases this led to minor changes in the original documents, while in many cases major modifications were required.

Over the years many individuals have been contributors to AMP and NEC, and are acknowledged here as follows:

R. W. Adams
M. J. Barth
H. Bosserman
J. K. Breakall
J. N. Brittingham
G. J. Burke
F. J. Deadrick
K. K. Hazard
W. A. Johnson
D. L. Knepp
D. L. Lager
A. P. Ludwigsen
R. J. Lytle
E. K. Miller
J. B. Morton
G. M. Pjerrou
A. J. Poggio
E. S. Selden
R. W. Ziolkowski

Special mention is due to E. K. Miller who has provided the main driving force behind the development of the code and modeling techniques since the development of the code BRACT which preceded AMP. A. J. Poggio has also made major contributions to the code development and documentation throughout the development of NEC. Dr. W. A. Johnson provided valuable assistance in validating the model for wires penetrating the ground and the basic Sommerfeld integral evaluation, and Dr. R. W. Ziolkowski provided assistance and guidance in developing the asymptotic approximations for the field near ground.

The development of NEC has also benefitted greatly from suggestions and guidance from individuals at the sponsoring agencies. Particular mention is due to J. Logan, J. W. Rockway and S. T. Li at the Naval Ocean Systems Center and J. McDonald and R. Franklin at ISEC, Ft. Huachuca AZ.

# Contents

APPENDICES

# 1. Introduction

The *Numerical Electromagnetics Code (NEC) — Method of Moments* is a computer program for analyzing the electromagnetic response of antennas and scatterers. The code is based on the numerical solution of integral equations by the method of moments, and combines an electric-field integral equation for modeling thin wires with a magnetic-field integral equation for closed perfectly conducting surfaces. This manual specifically describes the NEC–4 program which is the latest in a series of NEC-MoM programs, and includes a number of changes to improve modeling accuracy. Other versions of NEC currently in use include NEC–2, which can model wire structures in free space or over finitely conducting ground, and NEC–3 which is the same as NEC–2 but can also model wires buried in the ground or penetrating from air into ground.

These codes offer a number of features for modeling antennas or scatterers and their environments, including excitation by voltage sources or plane waves, lumped or distributed loading, and networks and transmission lines. The code output includes current distributions, impedances, power input, dissipation and efficiency, and radiation patterns and gains or scattering cross section. The model description and instructions for running the code are generally entered as commands read from an input file, although independent pre- and post-processors have been developed to streamline this process [1].

The modeling algorithms in NEC–4 have been revised to avoid loss of precision when modeling electrically small structures. The single-precision (32-bit) code will now give accurate results for many electrically small models that would have required double precision with NEC–3 or earlier codes. Also, a new treatment is used for wire radius and junctions for accurate modeling of stepped-radius wires and junctions of tightly coupled wires. Some other minor features have been added for convenience in modeling, and the insulated-wire model, that was available in a special version of NEC–3, is now included in the standard NEC–4 code. Also, the code structure has been extensively revised, with more use of Fortran 77 constructs, to make it more modular and easier to understand and maintain.

NEC–4 and earlier versions of NEC have been used to model a wide variety of antennas and scatterers including antennas in complex environments such as ships and aircraft. However, since the computer time and resources required by the moment-method solution increase with increasing size of the model relative to the wavelength, the solution may become difficult or impractical for large structures at high frequencies. The approach used in NEC is most applicable to the types of problems encountered at HF, VHF and lower frequencies. Problems such as a UHF antenna on a surface, or even a VHF antenna on a large aircraft may be handled better with other techniques such as the GTD approach used in the NEC Basic Scattering Code [2]. Also, finite difference codes [3] may be better suited to problems involving volumes of many cubic wavelengths or for interior coupling problems.

This manual describes in detail the mathematical and numerical techniques used in the NEC–4 program for modeling antennas and scatterers. A brief review of the integral equations and the method of moments technique for solving them is included in sections 2 and 3, but these topics are not considered in general terms. The reader is referred to [4] for

details on the derivation of the integral equations and to [5] for a comprehensive discussion of the method of moments. There are also a number of other sources that cover these topics. Persons wanting to learn to use NEC should start with the NEC–4 User's Guide, Part III of the NEC documentation. Part II, the Code Manual, contains detailed descriptions of the coding of subroutines in NEC–4 and information on the overall code structure, and will be of interest to persons wanting to modify or extend the code.

The code NEC–4 is the latest in a series of antenna modeling programs, each of which has built on the previous one. The first in the series was the code BRACT which was developed at MBAssociates in San Ramon, California, with funding from the Air Force Space and Missiles Systems Organization [ 6, 7]. The development of BRACT was based on the early work of J. Richmond [8, 9] in modeling wires by the solution of a Pocklington's integral equation. The three-term sinusoidal current expansion then being employed by Yeh and Mei [10] in solving Hallèn's type integral equations was used in BRACT along with point matching of the boundary condition. BRACT was capable of modeling wire antennas and scatterers and could include the effect of interaction with a finitely conducting ground through the Fresnel reflection-coefficient approximation [11]. However, BRACT was used mainly by its developers.

AMP [12, 13, 14] was the first code released as a tool for use by the general electromagnetics community. It was developed under Office of Naval Research Contract N00014-71-C-0187 with funding from the Naval Research Laboratory, Naval Ship Engineering Center, U.S. Army ECOM/Communications Systems, U.S. Army Strategic Communications Command and the U.S. Air Force Rome Air Development Center. Like BRACT, AMP solved Pocklington's integral equation for thin wires with a three-term sinusoidal current expansion and point matching. The current expansion was chosen so that the current on a segment, with the form $A_i + B_i \sin ks + C_i \cos ks$, when extrapolated to the centers of the adjacent segments would coincide with the values of current on those segments. At a junction of several wires the current was extrapolated to the center of a "phantom segment" whose length was the average of the connected segments. This extrapolation procedure smoothed the current distribution along wires, but still left discontinuities in current and charge density.

AMP included options to model lumped or distributed loading on wires, transmission lines and networks, and was capable of using disk storage for solving problems too large for the primary computer memory. AMP also had an option so a partially completed solution could be stopped and saved on a file, and latter restarted. This restart capability has been dropped from NEC, but is a valuable feature for running large problems. A flexible input language was developed in AMP for defining the model, selecting calculation options and requesting specific computations and output data. Perhaps most important, detailed documentation was written for AMP, consisting of a User's Manual, Engineering Manual and Code Manual.

AMP was restricted to modeling thin wires and surfaces represented as wire grids. However, a later version of the code, AMP–2 [15], included a magnetic-field integral equation model for surfaces and allowed connection of wires to surfaces using a technique demonstrated in [16].

The code NEC–1 was developed from AMP–2 with support from the Naval Ocean Systems Center and the Air Force Weapons Laboratory. NEC–1 included a new way of implementing the three-term sinusoidal current expansion so that current and charge density exactly satisfied continuity conditions imposed at the junctions. The current was forced to satisfy Kirchhoff's current law at the junction, and the charge densities on wires were related to a function of the log of wire radius to provide approximate continuity of potential. NEC–1 also included a bicone model for voltage sources and several other developments for increased accuracy and efficiency.

NEC–2 [17], developed with support of the Naval Ocean Systems Center, added two significant new modeling features to the capabilities of NEC–1. The Numerical Green's Function option implemented a partitioned-matrix solution so that a solution for a basic model could be saved on a file. New antennas or other modifications could then be added to the basic model and the solution obtained without repeating calculations for the part of the model coming from the file. Also, a solution for wires over a lossy ground was implemented using the rigorous Sommerfeld-integral approach and a table-lookup algorithm to reduce computation time.

In NEC–3, which was developed with support of the Naval Ocean Systems Center, the Sommerfeld-integral ground model was extended to wires buried in the ground or penetrating from air into ground [18]. Table-lookup, least-squares parameter estimation and asymptotic approximations were used to reduce computation time. NEC–3 will also model wires or surfaces in an infinite dielectric or lossy medium.

NEC–4 retains all of the capabilities of NEC–3, with changes and additions to improve the accuracy and add new features. Techniques to avoid loss of precision with electrically small models were developed with support of the Naval Ocean Systems Center [65, 66]. The treatment for electrically small loops has not been included in the current NEC–4 but may be added in the future. The new treatment for stepped-radius wires and junctions was developed with support of the U. S. Army, ISEC, and the development of the code and documentation has been sponsored by ISEC.

# 2. The Electric and Magnetic Field Integral Equations

The NEC program uses both an electric-field integral equation (EFIE) and a magnetic-field integral equation (MFIE) to model the electromagnetic response of general structures. Each equation has advantages for particular structure types. The EFIE is well suited for thin-wire structures of small or vanishing conductor volume while the MFIE, which fails for the thin-wire case, is more attractive for voluminous structures, especially those having large smooth surfaces. The EFIE can also be used to model surfaces and is preferred for thin structures where there is little separation between a front and back surface. Although the EFIE is specialized to thin wires in this program, it has been used to represent surfaces by wire grids with reasonable success for far-field quantities but with variable accuracy for surface fields. For a structure including both wires and surfaces the EFIE and MFIE are coupled. This combination of the EFIE and MFIE was demonstrated by Albertsen, Hansen and Jensen at the Technical University of Denmark [16] although the details of their numerical solution differ from those in NEC. A rigorous derivation of the EFIE and MFIE is given by Poggio and Miller [4]. The equations and their derivation are outlined in the following sections.

## 2.1 The Electric Field Integral Equation

The form of the EFIE used in NEC follows from an integral representation for the electric field of a volume current distribution $\mathbf{J}$,

$$\mathbf{E}(\mathbf{r}) = \frac{-j\eta}{4\pi k} \int_V \mathbf{J}(\mathbf{r}') \cdot \bar{\bar{\mathbf{G}}}(\mathbf{r}, \mathbf{r}')\, dV' \tag{2-1}$$

where

$$\bar{\bar{\mathbf{G}}}(\mathbf{r}, \mathbf{r}') = \left(k^2 \bar{\bar{\mathbf{I}}} + \nabla\nabla\right) g(\mathbf{r}, \mathbf{r}')$$
$$g(\mathbf{r}, \mathbf{r}') = \exp(-jk|\mathbf{r} - \mathbf{r}'|)/|\mathbf{r} - \mathbf{r}'|$$
$$k = \omega\sqrt{\mu_0\epsilon_0}\,, \qquad \eta = \sqrt{\mu_0/\epsilon_0}$$

and the time convention is $e^{j\omega t}$. $\bar{\bar{\mathbf{I}}}$ is the identity dyadic $\hat{\mathbf{e}}_x\hat{\mathbf{e}}_x + \hat{\mathbf{e}}_y\hat{\mathbf{e}}_y + \hat{\mathbf{e}}_z\hat{\mathbf{e}}_z$. When the current distribution is limited to the surface of a perfectly conducting body (2-1) becomes

$$\mathbf{E}(\mathbf{r}) = \frac{-j\eta}{4\pi k} \int_S \mathbf{J}_s(\mathbf{r}') \cdot \bar{\bar{\mathbf{G}}}(\mathbf{r}, \mathbf{r}')\, dA' \tag{2-2}$$

with $\mathbf{J}_s$ the surface current density. The observation point $\mathbf{r}$ is restricted to be off the surface $S$ so that $\mathbf{r} \neq \mathbf{r}'$.

If $\mathbf{r}$ approaches $S$ as a limit, (2-2) can be written

$$\mathbf{E}(\mathbf{r}) = \frac{-j\eta}{4\pi k} \fint_S \mathbf{J}_s(\mathbf{r}') \cdot \bar{\bar{\mathbf{G}}}(\mathbf{r}, \mathbf{r}')\, dA' \tag{2-3}$$

where the principal value integral, $\fint$, is indicated since $g(\mathbf{r}, \mathbf{r}')$ is now unbounded. The integral in (2-3) may not exist even in a principal value sense, due to the degree of singularity. In practice the approximations are generally made to avoid $\mathbf{r}$ coinciding with $\mathbf{r}'$.

An integral equation for the current induced on $S$ by an incident field $\mathbf{E}^I$ can be obtained from (2-3) and the boundary condition for $\mathbf{r} \in S$,

$$\hat{\mathbf{n}}(\mathbf{r}) \times \Big[\mathbf{E}^s(\mathbf{r}) + \mathbf{E}^I(\mathbf{r})\Big] = 0 \tag{2-4}$$

where $\hat{\mathbf{n}}(\mathbf{r})$ is the unit normal vector of the surface at $\mathbf{r}$ and $\mathbf{E}^s$ is the field due to the induced current $\mathbf{J}_s$. Substituting (2-3) for $\mathbf{E}_s$ yields the integral equation

$$-\hat{\mathbf{n}}(\mathbf{r}) \times \mathbf{E}^I(\mathbf{r}) = \frac{-j\eta}{4\pi k}\hat{\mathbf{n}}(\mathbf{r}) \times \int\!\!\!\!\!\!\diagup_S \mathbf{J}_s(\mathbf{r}') \cdot \Big(k^2\overline{\overline{\mathbf{I}}} + \nabla\nabla\Big)\, g(\mathbf{r},\mathbf{r}')\, dA'. \tag{2-5}$$

The vector integral in (2-5) can be reduced to a scalar integral equation when the conducting surface is that of a cylindrical thin wire, thereby making the solution much easier. This reduction is accomplished by neglecting circumferential current on the wire and also neglecting variation of the longitudinal current around the wire circumference. The boundary condition is then enforced on only the axial component of electric field.

In addition, approximations are usually applied in evaluating the integral equation kernel to avoid difficulties resulting from the singularity when $\mathbf{r}'$ coincides with $\mathbf{r}$ in (2-5). In a commonly used form of the thin-wire kernel, the current is located on the wire surface, while the boundary condition is enforced on the wire axis. This modification has a physical justification in the extended boundary condition proposed by Waterman [19]. Waterman noted that due to the analytic continuability of the solution of the integral equation, forcing the field to vanish over any region within a closed surface is sufficient to make it vanish everywhere within the surface, and thus on the surface for electric field. Evaluating the field on the axis removes the singularity and also simplifies the integration, since integration around the wire becomes trivial when the evaluation point is on its axis. For evaluation points outside of the wire, the field is commonly approximated by treating the total current as a filament on the wire surface at a position 90° from the direction of observation.

In an alternative form sometimes used for the thin-wire kernel, the total current is treated as a filament on the wire axis and the boundary condition is enforced on the wire surface. This procedure has the apparent advantage that the current filament remains continuous at a bend in the wire or a step in radius, so that point or ring charges are avoided. However, this approximation of the thin-wire kernel does not produce the correct behavior of charge at a step in wire radius when used with a continuous current distribution and point matching. With the current treated as a filament on the axis, the solution tends to converge with continuous linear charge density across a step in radius, while it is known that more charge should concentrate on the wire with the larger radius. The point charges that may occur at a step in radius are generally not a problem in the MM solution. They can be eliminated by smoothing the current over the annular surface at a step in radius or, with more difficulty, at a bend. However, as long as current continuity (Kirchhoff's current law) is enforced in the current expansion, the field due to inadvertent point charges can simply be dropped from the evaluation. Also, continuous testing functions or finite-difference evaluation of charge will smooth the effect of point charges. The current was located on the wire axis in NEC–3 and earlier codes, but NEC–4 puts the current on the surface and matches the boundary condition on the axis.

Other forms of the thin-wire kernel use approximations of the exact kernel, with current and field evaluation on the wire surface. A two-term series approximation of the exact kernel is used as the "extended thin-wire kernel" in NEC-3 and earlier versions. An advantage of approximating the exact kernel is that the wire can have either open or closed ends, while ends should be closed when the extended boundary condition is used. The extended thin-wire kernel is not included in NEC–4, since the thin-wire kernel with closed wire ends was found to give as good accuracy for thick wires.

With the approximation of an axial current with uniform distribution around the wire, the surface current $\mathbf{J}_s(\mathbf{r})$ on a wire of radius $a$ can be replaced by a filamentary current $I$ where

$$I(s)\hat{\mathbf{s}} = 2\pi a \mathbf{J}_s(\mathbf{r})$$

with $s$ the distance along the wire axis at $\mathbf{r}$, and $\hat{\mathbf{s}}$ the unit vector tangent to the wire axis at $\mathbf{r}$. Equation (2-5) then becomes

$$-\hat{\mathbf{n}}(\mathbf{r}) \times \mathbf{E}^I(\mathbf{r}) = \frac{-j\eta}{4\pi k}\hat{\mathbf{n}}(\mathbf{r}) \times \int_L I(s') \left( k^2 \hat{\mathbf{s}}' - \nabla \frac{\partial}{\partial s'} \right) g(\mathbf{r}, \mathbf{r}')\, ds' \tag{2-6}$$

where the integration is over the length of the wire. Enforcing the boundary condition in the axial direction reduces (2-6) to the scalar equation

$$-\hat{\mathbf{s}} \cdot \mathbf{E}^I(\mathbf{r}) = \frac{-j\eta}{4\pi k} \int_L I(s') \left( k^2 \hat{\mathbf{s}} \cdot \hat{\mathbf{s}}' - \frac{\partial^2}{\partial s \partial s'} \right) g(\mathbf{r}, \mathbf{r}')\, ds' \tag{2-7}$$

Since $\mathbf{r}'$ is now the point at $s'$ on the wire axis while $\mathbf{r}$ is a point at $s$ on the wire surface $|\mathbf{r} - \mathbf{r}'| \geq a$ and the integrand is bounded.

### 2.2 The Magnetic Field Integral Equation

The MFIE is derived from the integral representation for the magnetic field of a surface current distribution $\mathbf{J}_s$,

$$\mathbf{H}^S(\mathbf{r}) = \frac{1}{4\pi} \int_S \mathbf{J}_s(\mathbf{r}') \times \nabla' g(\mathbf{r}, \mathbf{r}')\, dA' \tag{2-8}$$

where the differentiation is with respect to the integration variable $\mathbf{r}'$. If the current $\mathbf{J}_s$ is induced by an external incident field $\mathbf{H}^I$, then the total magnetic field inside the perfectly conducting surface must be zero. Hence, for $\mathbf{r}$ just inside the surface $S$,

$$\mathbf{H}^I(\mathbf{r}) + \mathbf{H}^S(\mathbf{r}) = 0 \tag{2-9}$$

where $\mathbf{H}^I$ is the incident field with the structure removed, and $\mathbf{H}^S$ is the scattered field given by (2-8). The integral equation for $\mathbf{J}_s$ may be obtained by letting $\mathbf{r}$ approach the surface point $\mathbf{r}_0$ from inside the surface along the normal $\hat{\mathbf{n}}(\mathbf{r}_0)$. The surface component of equation (2-9) with (2-8) substituted for $\mathbf{H}^S$ is then

$$-\hat{\mathbf{n}}(\mathbf{r}_0) \times \mathbf{H}^I(\mathbf{r}_0) = \hat{\mathbf{n}}(\mathbf{r}) \times \frac{1}{4\pi} \lim_{\mathbf{r} \to \mathbf{r}_o} \int_S \mathbf{J}_s(\mathbf{r}') \times \nabla' g(\mathbf{r}, \mathbf{r}')\, dA'$$

where $\hat{\mathbf{n}}(\mathbf{r}_0)$ is the outward directed normal vector at $\mathbf{r}_0$. The limit can be evaluated by using a result of potential theory [20] to yield the integral equation

$$-\hat{\mathbf{n}}(\mathbf{r}) \times \mathbf{H}^I(\mathbf{r}_0) = -\frac{1}{2}\mathbf{J}_s(\mathbf{r}_0) + \frac{1}{4\pi}\int\!\!\!\!\!\!\diagup_S \hat{\mathbf{n}}(\mathbf{r}_0) \times \left[\mathbf{J}_s(\mathbf{r}') \times \nabla' g(\mathbf{r}_0, \mathbf{r}')\right] \, dA'. \tag{2-10}$$

For solution in NEC, this vector integral equation is resolved into two scalar equations along the orthogonal surface vectors $\hat{\mathbf{t}}_1$ and $\hat{\mathbf{t}}_2$ where

$$\hat{\mathbf{t}}_1(\mathbf{r}_0) \times \hat{\mathbf{t}}_2(\mathbf{r}_0) = \hat{\mathbf{n}}(\mathbf{r}_0).$$

By using the identity $\mathbf{u} \cdot (\mathbf{v} \times \mathbf{w}) = (\mathbf{u} \times \mathbf{v}) \cdot \mathbf{w}$ and noting that $\hat{\mathbf{t}}_1 \times \hat{\mathbf{n}} = -\mathbf{t}_2$ and $\hat{\mathbf{t}}_2 \times \hat{\mathbf{n}} = \hat{\mathbf{t}}_1$, the scalar equations can be written

$$\hat{\mathbf{t}}_2(\mathbf{r}_0) \cdot \mathbf{H}^I(\mathbf{r}_0) = -\frac{1}{2}\hat{\mathbf{t}}_1(\mathbf{r}_0) \cdot \mathbf{J}_s(\mathbf{r}_0) - \frac{1}{4\pi}\int\!\!\!\!\!\!\diagup_S \hat{\mathbf{t}}_2(\mathbf{r}_0) \cdot \left[\mathbf{J}_s(\mathbf{r}') \times \nabla' g(\mathbf{r}_0, \mathbf{r}')\right] \, dA' \tag{2-11}$$

$$-\hat{\mathbf{t}}_1(\mathbf{r}_0) \cdot \mathbf{H}^I(\mathbf{r}_0) = -\frac{1}{2}\hat{\mathbf{t}}_2(\mathbf{r}_0) \cdot \mathbf{J}_s(\mathbf{r}_0) + \frac{1}{4\pi}\int\!\!\!\!\!\!\diagup_S \hat{\mathbf{t}}_1(\mathbf{r}_0) \cdot \left[\mathbf{J}_s(\mathbf{r}') \times \nabla' g(\mathbf{r}_0, \mathbf{r}')\right] \, dA'. \tag{2-12}$$

These two components suffice since there is no normal component of (2-10).

### 2.3 The EFIE-MFIE Hybrid Equation

Program NEC uses the EFIE for thin wires and the MFIE for surfaces. For a structure with both wires and surfaces, $\mathbf{r}$ in (2-7) is restricted to wires, with the integral for $\mathbf{E}^S(\mathbf{r})$ extending over the complete structure. The thin-wire form of the integral in (2-7) is used over wires while the more general form of (2-5) must be used on surfaces. Likewise, $\mathbf{r}_0$ is restricted to surfaces in (2-11) and (2-12), with the integrals for $\mathbf{H}^S(\mathbf{r})$ extending over the complete structure. On wires the integral is simplified by the thin-wire approximation. The resulting coupled integral equations are, for $\mathbf{r}$ on wire surfaces,

$$\begin{aligned} -\hat{\mathbf{s}} \cdot \mathbf{E}^I(\mathbf{r}) =& \frac{-j\eta}{4\pi k}\int_L I(s') \left(k^2 \hat{\mathbf{s}} \cdot \hat{\mathbf{s}}' - \frac{\partial^2}{\partial s \partial s'}\right) g(\mathbf{r}, \mathbf{r}') \, ds' \\ & - \frac{j\eta}{4\pi k}\int_{S_1} \mathbf{J}_s(\mathbf{r}') \cdot \left[k^2 \hat{\mathbf{s}} - \nabla' \frac{\partial}{\partial s}\right] g(\mathbf{r}, \mathbf{r}') \, dA' \end{aligned} \tag{2-13}$$

and for $\mathbf{r}$ on surfaces excluding wires

$$\begin{aligned} \hat{\mathbf{t}}_2(\mathbf{r}) \cdot \mathbf{H}^I(\mathbf{r}) =& \frac{-1}{4\pi}\hat{\mathbf{t}}_2(\mathbf{r}) \cdot \int_L I(s') \left[\hat{\mathbf{s}}' \times \nabla' g(\mathbf{r}, \mathbf{r}')\right] \, ds' - \frac{1}{2}\hat{\mathbf{t}}_1(\mathbf{r}) \cdot \mathbf{J}_s(\mathbf{r}) \\ & - \frac{1}{4\pi}\int\!\!\!\!\!\!\diagup_{S_1} \hat{\mathbf{t}}_2(\mathbf{r}) \cdot \left[\mathbf{J}_s(\mathbf{r}') \times \nabla' g(\mathbf{r}, \mathbf{r}')\right] \, dA' \end{aligned} \tag{2-14}$$

and

$$\begin{aligned} -\hat{\mathbf{t}}_1(\mathbf{r}) \cdot \mathbf{H}^I(\mathbf{r}) =& \frac{1}{4\pi}\hat{\mathbf{t}}_1(\mathbf{r}) \cdot \int_L I(s') \left[\hat{\mathbf{s}}' \times \nabla' g(\mathbf{r}, \mathbf{r}')\right] \, ds' - \frac{1}{2}\hat{\mathbf{t}}_2(\mathbf{r}) \cdot \mathbf{J}_s(\mathbf{r}) \\ & + \frac{1}{4\pi}\int\!\!\!\!\!\!\diagup_{S_1} \hat{\mathbf{t}}_1(\mathbf{r}) \cdot \left[\mathbf{J}_s(\mathbf{r}') \times \nabla' g(\mathbf{r}, \mathbf{r}')\right] \, dA'. \end{aligned} \tag{2-15}$$

The symbol $\int_L$ represents integration over wires while $\int\!\!\!\!\!\!\diagup_{S_1}$ represents integration over surfaces excluding wires. The numerical method used to solve equations (2-13), (2-14) and (2-15) is described in section 3.

# 3. The Moment-Method Solution

The integral equations (2-13), (2-14) and (2-15) are solved numerically in NEC by the method of moments. The basic procedure for this solution is described in this section, starting with a brief review of the moment method. The NEC solution combines point matching of the fields with a three-term current expansion on wires and a pulse expansion on surfaces. The point-matching approach is particularly convenient for combining different modeling techniques that lead to a Green's-function representation. Hence, the EFIE for wires, MFIE for surfaces and the solution for a point source near the ground are combined in NEC. The evaluation of the fields due to the distributed sources for these cases forms the computational core of the code, together with the solution of the matrix equation, and is discussed in succeeding sections.

## 3.1 Outline of the Moment Method

An excellent introduction to the moment method was given by R. F. Harrington in the book *Field Computation by Moment Methods* [5]. A brief outline of the method follows.

The method of moments applies to a general linear-operator equation,

$$Lf = e \tag{3-1}$$

where $e$ is a known excitation, $f$ is an unknown response and $L$ is a linear operator (an integral operator in the present case.) The unknown function $f$ is expanded in a sum of basis functions $f_j$ as

$$f = \sum_{j=1}^{N} \alpha_j f_j \tag{3-2}$$

and a set of linear equations for the coefficients $\alpha_j$ is then obtained by taking the inner product of (3-1) with a set of weighting functions $\{w_i\}$ as

$$\langle w_i,\ Lf \rangle = \langle w_i,\ e \rangle \qquad i = 1, \ldots, N.$$

The inner product is typically defined as

$$\langle f,\ g \rangle = \int_S f(\mathbf{r}) g(\mathbf{r})\, dA$$

where the integration is over the structure surface. The number of weighting functions is taken here to be equal to the number of basis functions, so that the number of equations is equal to the number of unknown coefficients in (3-2). Due to the linearity of $L$, equation (3-2) substituted for $f$ yields

$$\sum_{j=1}^{N} \alpha_j \langle w_i,\ Lf_j \rangle = \langle w_i,\ e \rangle, \qquad i = 1, \ldots, N.$$

This set of linear equations can be written in matrix notation as

$$[G][A] = [E]$$

where $G_{ij} = \langle w_i,\ Lf_j \rangle$, $A_j = \alpha_j$ and $E_i = \langle w_i,\ e \rangle$. The solution can then be written in terms of the inverse matrix as

$$[A] = [G]^{-1}[E].$$

The choice of basis and weighting functions has an important role in determining the efficiency and accuracy of the moment-method solution. Each basis function can either extend over the entire domain of the current, or a subdomain. Common choices for the basis functions are rectangular pulses, piecewise-linear or piecewise-sinusoidal functions, or polynomials. When $w_i = f_i$, the procedure is known as Galerkin's method. In NEC the basis and weighting functions are different, $w_i$ being chosen as a set of delta functions

$$w_i(\mathbf{r}) = \delta(\mathbf{r} - \mathbf{r}_i)$$

with $\{\mathbf{r}_i\}$ a set of points on the conducting surface. The result is a point sampling of the integral equation, known as point matching. Wires are divided into short straight segments with a sample point at the center of each segment, while surfaces are approximated by a set of flat patches with a sample point at the center of each patch.

With point sampling, the derivatives on the Green's function for the EFIE place particular importance on a smooth representation of the current with continuous derivatives. Hence a three-term sinusoidal expansion is used for the current on wires in NEC. The MFIE for surfaces can be solved with a simpler current expansion. Good results are obtained with a delta-function representation of the current on surfaces. Subdomain basis functions are used on both wires and surfaces, with support of $f_i$ restricted to a region near $\mathbf{r}_i$. This choice simplifies the evaluation of the integrals and ensures that the matrix $G$ will be well conditioned. Details of the current basis functions are given in the following sections.

### 3.2 Current Expansion on Wires

Wires in NEC are modeled by short straight segments, with the current on each segment represented in the form

$$I_j(s) = A_j + B_j \sin k_s(s - s_j) + C_j[\cos k_s(s - s_j) - 1], \qquad |s - s_j| < \Delta_j/2 \tag{3-3}$$

where $s_j$ is the value of $s$ at the center of segment $j$, and $\Delta_j$ is the length of the segment. This expansion was first used by Yeh and Mei [10] and has been shown to provide rapid solution convergence [21, 22] , particularly on longer wires. It has the added advantage that the electric fields of the sinusoidal currents are easily evaluated in closed form when $k_s$ is equal to the wave number in the medium. In most circumstances $k_s$ is chosen equal to the wave number in the medium containing the wire, since (3-3) then represents the natural form for current on a long wire. However, in some cases, such as insulated wires in dielectric or lossy media, a different choice of $k_s$ is more suitable.

In NEC–3 and earlier codes the current expansion on each segment had the form

$$I_j(s) = A'_j + B_j \sin k_s(s - s_j) + C_j \cos k_s(s - s_j), \qquad |s - s_j| < \Delta_j/2. \tag{3-4}$$

This form is equivalent to (3-3) except that precision may be lost in evaluating (3-4) on short segments, with $k_s\Delta_j \ll 1$, due to cancellation of the constant and cosine terms. The form of

(3-3) can be used on very short segments without loss of precision, as long as the constants are evaluated carefully.

While (3-3) involves three arbitrary constants per segment, two of these are eliminated by imposing continuity conditions on the current and charge at the segment ends. The remaining constant for each segment is determined by solving the moment-method equations. Continuity conditions at the segment ends are enforced on the current and the linear charge density $q$, which is related to the derivative of current through the continuity equation

$$\frac{dI(s)}{ds} = -j\omega q(s).$$

At a junction of two segments with equal radius the obvious conditions are that the current and charge are continuous across the junction. At a junction of more than two wires, the continuity of current is generalized to Kirchhoff's law that the sum of currents into the junction is zero.

The appropriate condition on charge is not as obvious at a junction of three or more wires, or a step in wire radius. The actual distribution of charge in the vicinity of such a junction, or even on a single wire at a bend, will be complex, with higher-order variations along the wire and around its circumference. Variations around the wire must be neglected in the thin-wire approximation, and the basis functions cannot support the rapid variation or singularity that occurs at an edge. Hence, what is needed is a condition that results in the best match of the boundary condition that is possible with the particular basis functions. One approach, used in [23], is to allow an unknown discontinuity in charge density at a junction, and determine the value in the moment-method solution by including new equations involving additional weighting functions. However, the increased matrix order with this approach can significantly increase computation time for large models. In NEC, the approximate distribution of charge at a junction is determined from conditions in the vicinity of the junction through quasistatic approximations. These conditions are derived in section 3.4. For now the proportionality factor for charge on each wire at a junction, relative to other wires at that junction, will be represented as $a_i^-$ or $a_i^+$, respectively, for end 1 or end 2 of segment $i$ relative to the reference direction. Thus for all segments $i$ connected to a junction, the condition on the derivative of current is $dI(s)/ds|_{s=s_{\text{junction}}} = a_i^{\pm} Q$, where $Q$ is an unknown constant related to the total charge associated with the junction, and the $+$ or $-$ is chosen for the end of the segment that connects to the junction.

At a free wire end the current must go to zero. However, if the current can flow onto an end cap it goes to zero at the center of the cap rather than at the edge of the wire cylinder. An approximate treatment of wire end caps is included in the NEC–4 wire model, as described in section 3.5. In the development of the general basis functions, the current at the end of the wire cylinder will be related to the derivative of current through a proportionality factor $X_i$ for segment $i$, so that

$$I(s_{\text{end}}) = \pm X_i \frac{d}{ds} I(s) \bigg|_{s=s_{\text{end}}}$$

where $s_{\text{end}}$ is the value of $s$ at the edge of the cylinder on segment $i$, and the $+$ or $-$ signs apply for the free end at end 1 or end 2 of the segment, respectively. The value of $X_i$ will

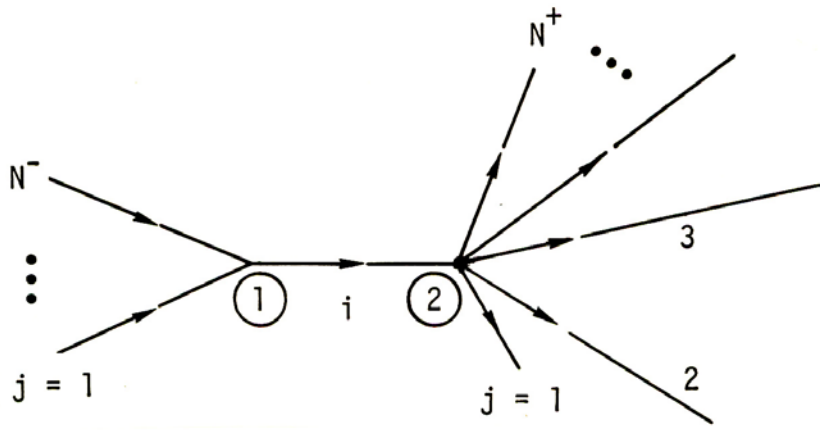


**Fig. 3-1** Segments covered by the $i$th basis function.

be determined from a quasistatic treatment of the end cap. If there is no end cap $X_i$ can be set to zero.

The above conditions on current and charge are enforced on the three-term current expansion of equation (3-3) in defining the basis functions. The conditions are then satisfied by the total current for any combination of these basis functions. The general form of the basis function will be developed for the configuration of segments shown in Fig. 3-1. The basis function for segment $i$ extends onto all segments connected to segment $i$, going to zero with zero derivative at the outer ends of the connected segments. Thus it forms what could be considered a generalized B-spline function. The current on each segment has the form of (3-3), so that the current on segment $i$ is

$$f_i^0(s) = A_i^0 + B_i^0 \sin k_s(s - s_i) + C_i^0[\cos k_s(s - s_i) - 1], \qquad |s - s_i| < \Delta_i/2 \tag{3-5}$$

while on segments connected to end 1 of segment $i$,

$$f_j^-(s) = A_j^- + B_j^- \sin k_s(s - s_j) + C_j^-[\cos k_s(s - s_j) - 1], \qquad |s - s_j| < \Delta_j/2 \tag{3-6}$$

with $j = 1, \ldots, N^-$, and on segments connected to end 2 of segment $i$,

$$f_\ell^+(s) = A_\ell^+ + B_\ell^+ \sin k_s(s - s_\ell) + C_\ell^+[\cos k_s(s - s_\ell) - 1], \qquad |s - s_\ell| < \Delta_\ell/2. \tag{3-7}$$

with $\ell = 1, \ldots, N^+$. The total current expansion for a wire model with $N$ segments is then

$$I(s) = \sum_{i=0}^{N} \alpha_i f_i(s) \tag{3-8}$$

where the basis function centered on segment $i$ is

$$f_i(s) = f_i^0(s) + \sum_{j=1}^{N^-} f_j^-(s) + \sum_{\ell=1}^{N^+} f_\ell^+(s) \tag{3-9}$$

with the components of the basis function for segment $i$ given by equations (3-5) through (3-7).

Equations (3-5), (3-6) and (3-7), forming the complete basis function associated with segment $i$, involve $3(N^- + N^+ + 1)$ constants. All but one of these constants are eliminated by enforcing the conditions on current and its derivative at the segment ends. At the ends of segment $i$ the conditions are

$$\frac{d}{ds} f_i^0(s)\Big|_{s=s_i-\Delta_i/2} = k_s a_i^- Q_i^- \tag{3-10}$$

$$\frac{d}{ds} f_i^0(s)\Big|_{s=s_i+\Delta_i/2} = k_s a_i^+ Q_i^+ \tag{3-11}$$

where $Q_i^-$ and $Q_i^+$ are related to the charge associated with the junctions at end 1 and end 2 of segment $i$, respectively. If end 1 of segment $i$ is a free end ($N^- = 0$) equation (3-10) is replaced by

$$f_i^0(s_i - \Delta_i/2) = \frac{X_i}{k_s} \frac{d}{ds} f_i^0(s)\Big|_{s=s_i-\Delta_i/2} \tag{3-12}$$

while if end 2 of segment $i$ is a free end ($N^+ = 0$) equation (3-11) is replaced by

$$f_i^0(s_i + \Delta_i/2) = -\frac{X_i}{k_s} \frac{d}{ds} f_i^0(s)\Big|_{s=s_i+\Delta_i/2}. \tag{3-13}$$

On segments connected to end 1 of segment $i$ the end conditions are

$$f_j^-(s_j - \Delta_j/2) = 0 \tag{3-14}$$

$$\frac{d}{ds} f_j^-(s)\Big|_{s=s_j-\Delta_j/2} = 0 \tag{3-15}$$

$$\frac{d}{ds} f_j^-(s)\Big|_{s=s_j+\Delta_j/2} = k_s a_j^+ Q_i^- \tag{3-16}$$

while on segments connected to end 2 of segment $i$ the conditions are

$$f_\ell^+(s_\ell + \Delta_\ell/2) = 0 \tag{3-17}$$

$$\frac{d}{ds} f_\ell^+(s)\Big|_{s=s_\ell+\Delta_\ell/2} = 0 \tag{3-18}$$

$$\frac{d}{ds} f_\ell^+(s)\Big|_{s=s_\ell-\Delta_\ell/2} = k_s a_\ell^- Q_i^+. \tag{3-19}$$

Generalizing for connected segments with reference directions opposed to segment $i$, equations (3-14), (3-15) and (3-16) are solved for the constants in (3-6) to yield

$$A_j^- = \mp \left[ \frac{1}{2 \sin k_s \Delta_j/2} - \frac{1}{\sin k_s \Delta_j} \right] a_j^\pm Q_i^- \tag{3-20}$$

$$B_j^- = \frac{a_j^\pm Q_i^-}{2 \cos k_s \Delta_j/2} \tag{3-21}$$

$$C_j^- = \frac{\mp a_j^\pm Q_i^-}{2 \sin k_s \Delta_j/2}. \tag{3-22}$$

and equations (3-17), (3-18) and (3-19) are solved for the constants in (3-7) to yield

$$A_\ell^+ = \pm \left[ \frac{1}{2\sin k_s\Delta_\ell/2} - \frac{1}{\sin k_s\Delta_\ell} \right] a_\ell^\mp Q_i^+ \tag{3-23}$$

$$B_\ell^+ = \frac{a_\ell^\mp Q_i^+}{2\cos k_s\Delta_\ell/2} \tag{3-24}$$

$$C_\ell^+ = \frac{\pm a_\ell^\mp Q_i^+}{2\sin k_s\Delta_\ell/2}. \tag{3-25}$$

The upper sign in these equations applies when the reference direction of the segment is as shown in Fig. 3-1, and the lower sign for the opposite reference direction.

Since there is one less equation than unknowns for all parts of the basis function, we arbitrarily set $A_i^0 - C_i^0 = -1$, since this results in a basis function with positive amplitude. The basis function could be normalized to unit magnitude, but this is not done to save computation time. The normalization is absorbed into the constants $\alpha_j$ in (3-2). When $N^- \neq 0$ and $N^+ \neq 0$ equations (3-10) and (3-11) can be solved for the constants in (3-5) to yield

$$A_i^0 = C_i^0 - 1 \tag{3-26}$$

$$B_i^0 = \left( a_i^- Q_i^- + a_i^+ Q_i^+ \right) \frac{\sin k_s\Delta_i/2}{\sin k_s\Delta_i} \tag{3-27}$$

$$C_i^0 = \left( a_i^- Q_i^- - a_i^+ Q_i^+ \right) \frac{\cos k_s\Delta_i/2}{\sin k_s\Delta_i}. \tag{3-28}$$

The constants $Q_i^\pm$ can then be eliminated by enforcing Kirchhoff's law on the current at the junctions

$$\sum_{j=1}^{N^-} f_j^-(s_j + \Delta_j/2) = f_i^0(s_i - \Delta_i/2)$$

$$\sum_{\ell=1}^{N^+} f_\ell^+(s_\ell - \Delta_\ell/2) = f_i^0(s_i + \Delta_i/2)$$

to obtain

$$Q_i^\pm = \frac{\pm a_i^\mp(\cos k_s\Delta_i - 1) - P_i^\mp \sin k_s\Delta_i}{\left( P_i^- P_i^+ + a_i^- a_i^+ \right)\sin k_s\Delta_i + \left( P_i^- a_i^+ - P_i^+ a_i^- \right)\cos k_s\Delta_i} \tag{3-29}$$

where

$$P_i^- = -\sum_{j=1}^{N^-} \left( \frac{\cos k_s\Delta_j - 1}{\sin k_s\Delta_j} \right) a_j^\pm$$

$$P_i^+ = \sum_{\ell=1}^{N^+} \left( \frac{\cos k_s\Delta_\ell - 1}{\sin k_s\Delta_\ell} \right) a_\ell^\mp.$$

The upper sign applies when the reference direction of the connected segment is the same as that of segment $i$ and the lower sign is for opposed reference directions. The sum for

$P_i^-$ is over segments connected to end 1 of segment $i$, and the sum for $P_i^+$ is over segments connected to end 2.

For $N^- = 0$ and $N^+ \neq 0$ the constants in (3-5) are

$$A_i^0 = C_i^0 - 1 \tag{3-30}$$

$$B_i^0 = \frac{\sin k_s\Delta_i/2}{\cos k_s\Delta_i - X_i \sin k_s\Delta_i} + a_i^+ Q_i^+ \frac{\cos k_s\Delta_i/2 - X_i \sin k_s\Delta_i/2}{\cos k_s\Delta_i - X_i \sin k_s\Delta_i} \tag{3-31}$$

$$C_i^0 = \frac{\cos k_s\Delta_i/2}{\cos k_s\Delta_i - X_i \sin k_s\Delta_i} + a_i^+ Q_i^+ \frac{\sin k_s\Delta_i/2 + X_i \cos k_s\Delta_i/2}{\cos k_s\Delta_i - X_i \sin k_s\Delta_i} \tag{3-32}$$

with

$$Q_i^+ = \frac{\cos k_s\Delta_i - 1 - X_i \sin k_s\Delta_i}{\left(a_i^+ + X_i P_i^+\right)\sin k_s\Delta_i + \left(a_i^+ X_i - P_i^+\right)\cos k_s\Delta_i} \tag{3-33}$$

For $N^- \neq 0$ and $N^+ = 0$ the constants are

$$A_i^0 = C_i^0 - 1 \tag{3-34}$$

$$B_i^0 = \frac{-\sin k_s\Delta_i/2}{\cos k_s\Delta_i - X_i \sin k_s\Delta_i} + a_i^- Q_i^- \frac{\cos k_s\Delta_i/2 - X_i \sin k_s\Delta_i/2}{\cos k_s\Delta_i - X_i \sin k_s\Delta_i} \tag{3-35}$$

$$C_i^0 = \frac{\cos k_s\Delta_i/2}{\cos k_s\Delta_i - X_i \sin k_s\Delta_i} - a_i^- Q_i^- \frac{\sin k_s\Delta_i/2 + X_i \cos k_s\Delta_i/2}{\cos k_s\Delta_i - X_i \sin k_s\Delta_i} \tag{3-36}$$

with

$$Q_i^- = \frac{1 - \cos k_s\Delta_i + X_i \sin k_s\Delta_i}{\left(a_i^- - X_i P_i^-\right)\sin k_s\Delta_i + \left(a_i^- X_i + P_i^-\right)\cos k_s\Delta_i}. \tag{3-37}$$

If $N^- = N^+ = 0$, the complete basis function is

$$f_i^0 = \frac{\cos k_s(s - s_i)}{\cos k_s\Delta_i/2 - X_i \sin k_s\Delta_i/2} - 1. \tag{3-38}$$

This function satisfies the conditions that have been defined for the current at free ends. The use of a single isolated segment cannot be expected to yield an accurate solution for current on the segment, but the segment may be useful as a source for fields illuminating another part of the model, where the accuracy of the current on the source segment is not important.

When a segment end is connected to a ground plane or to a surface modeled with the MFIE, the end condition on both the total current and the last basis function is

$$\frac{d}{ds} I_j(s)\bigg|_{s=s_{\text{end}}} = 0$$

replacing the condition of zero current at a free end. This condition does not require a separate treatment, but is obtained by computing the last basis function as if the last segment connected to its image segment on the other side of the surface.

In the program AMP, a predecessor of NEC, the current expansion also had the form of (3-3). However, continuity of current was approximated by requiring that when the current function on a segment was extrapolated to adjacent segments it coincided with the current at the centers of those segments. The resulting basis function for segment $i$ had unit magnitude at the center of segment $i$ and went to zero at the centers of the adjacent segments. Hence, the amplitude of basis function $i$, $\alpha_i$ in (3-2), was the value of the total current at the center of segment $i$. This is not true in NEC, so the current at the center of segment $i$ must be computed by summing the contributions of all basis functions extending onto segment $i$.

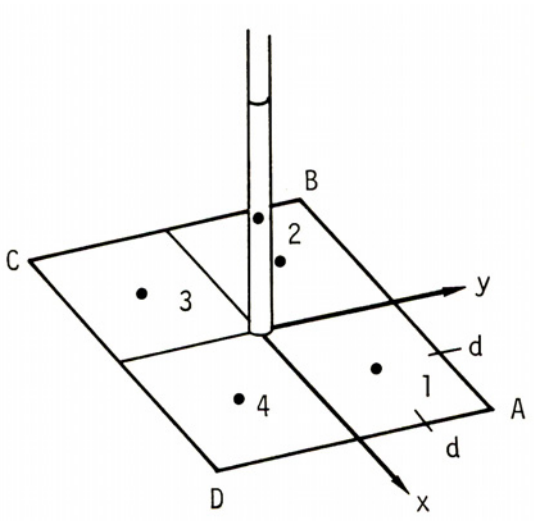


**Fig. 3-2** Detail of the connection of a wire to a surface.

### 3.3 Current Expansion on Surfaces

Surfaces on which the MFIE is used are modeled by small flat patches. The surface current on each patch is expanded in a set of pulse functions with two orthogonal components per patch. A special treatment is used in the region of wire connections. The pulse function expansion for $N_p$ patches is

$$\mathbf{J}_s(\mathbf{r}) = \sum_{j=1}^{N_p} (J_{1j}\hat{\mathbf{t}}_{1j} + J_{2j}\hat{\mathbf{t}}_{2j}) V_j(\mathbf{r}) \tag{3-39}$$

where $\mathbf{r}_j$ is the position of the center of patch $j$, $\hat{\mathbf{t}}_{1j}$ and $\hat{\mathbf{t}}_{2j}$ are the orthogonal unit vectors on the surface at $\mathbf{r}_j$ and $V_j(\mathbf{r}) = 1$ for $\mathbf{r}$ on patch $j$ and 0 otherwise.

The constants $J_{1j}$ and $J_{2j}$ are the average surface-current densities over the patch, representing the $\alpha_j$ in (3-2), and are determined by the solution of the matrix equation. The integrals for fields due to the pulse basis functions are evaluated numerically at a single point, so that for integration the pulses could be reduced to delta functions at the patch centers. That this simple approximation of the current yields good accuracy is one of the advantages of the MFIE for surfaces.

A more realistic representation of the surface current is needed in the region where a wire connects to the surface. The treatment used in NEC involves the four coplanar patches about the connection point, and is very similar to that used by Albertsen et al. [16]. In the region of the wire connection, the surface current contains a singular component due to the current flowing from the wire onto the surface. With the coordinates as shown in Fig. 3-2, the total surface current should satisfy the condition

$$\nabla_s \cdot \mathbf{J}_s(x, y) = J_0(x, y) + I_0 \delta(x, y)$$

where $\delta(x, y)$ is a two-dimensional Dirac delta function, $\nabla_s$ denotes the surface divergence, $J_0(x, y)$ is a continuous function in the region ABCD and $I_0$ is the current at the base of the

wire flowing onto the surface. The form used in NEC is

$$\mathbf{J}_s(x,y) = I_0\mathbf{f}(x,y) + \sum_{j=1}^{4} g_j(x,y)\,(\mathbf{J}_j - I_0\mathbf{f}_j) \tag{3-40}$$

where $\mathbf{J}_j = \mathbf{J}_s(x_j, y_j)$, $\mathbf{f}_j = \mathbf{f}(x_j, y_j)$ with

$$\mathbf{f}(x,y) = \frac{x\hat{\mathbf{x}} + y\hat{\mathbf{y}}}{2\pi(x^2+y^2)}$$

and $x_j$ and $y_j$ are the values of $x$ and $y$ at the center of patch $j$. The interpolation functions $g_j(x,y)$ are chosen such that $g_j(x,y)$ is differentiable on ABCD, $g_j(x_i,y_i) = \delta_{ij}$ and $\sum_{j=1}^{4} g_j(x,y) = 1$. The functions used in NEC are as follows:

$$g_1(x,y) = (d+x)(d+y)/4d^2 \qquad g_2(x,y) = (d-x)(d+y)/4d^2$$

$$g_3(x,y) = (d-x)(d-y)/4d^2 \qquad g_4(x,y) = (d+x)(d-y)/4d^2.$$

Equation (3-40) is used when computing the electric field at the center of the connected wire segment due to the surface current on the four surrounding patches. In computing the field on any other segments or on any patches, the pulse-function form is used for all patches, including those at the connection point. This saves integration time and is sufficiently accurate for the greater source to observation-point separations involved.

### 3.4 The Condition on Charge at a Junction

Kirchhoff's current law is implicit in the general NEC basis function for wires. However, the conditions on charge were left as unspecified proportionality constants. Determining a correct condition on charge is not as easy as for current, since the charge must distribute so that the tangential electric field is minimized over the junction or, in the quasistatic form, the electric scalar potential is continuous across the junction. Various conditions may affect the distribution of charge at a junction, including changing wire radius, the proximity of wires at the junction, different media permittivities when a wire crosses an interface, or the transition from insulated to bare wire.

Approximations have been developed in an attempt to account for wire radius in the basis functions without the need to solve an integral equation. Early junction treatments assumed constant linear charge density [24] or constant surface charge density [25] at a junction of wires with differing radius. By analysis of a wire with tapered radius, Wu and King [26] derived a condition that charge distributes so that

$$q_i \propto \left[\ln\left(\frac{2}{ka_i}\right) - 0.5772\right]^{-1} \tag{3-41}$$

where $q_i$ is the linear charge density at the junction on wire $i$ and $a_i$ is the wire radius. A similar condition was derived by Shulkunoff and Friss [27] by equating potentials while

treating each wire as infinite and isolated from adjacent wires. This condition was applied at junctions in NEC–3 and prior versions of NEC.

By obtaining a highly resolved solution at a step in radius, using a surface moment-method code, Glisson and Wilton [28] have shown that charge is singular at the outer edge of the step, and goes to zero at the inner edge, as occurs on linear wedges. Outside of the region of edge effects, the charge on opposite sides of the step differs approximately by the ratio predicted by (3-41). This result suggests that (3-41) is not an appropriate condition to apply precisely at the junction of wires with different radii. The charge will generally have higher-order variations at a step, bend or multiple wire junction, but these usually do not need to be included in a thin-wire model. What is needed is a condition on charge that comes as close to the correct charge behavior as is possible with the given current expansion.

Popović et al. [23] obtained suitable conditions on charge by requiring that an approximate integral of electric field along wires crossing the junction is zero. This treatment takes account of wire radius as well as the configuration of wires at the junction. At a junction of $M$ wires the resulting $M-1$ equations are appended to the moment-method equations, along with the equation expressing Kirchhoff's law. However, increasing the size of the matrix is undesirable due to the $M^3$ dependence of solution time.

In NEC–4, charge distributions for the basis functions are determined with minimal computational overhead by executing a small moment-method solution for each junction. Any junction on which the charge cannot be determined as uniform due to symmetry is considered isolated from the rest of the structure with the wires extended to infinity away from the junction. An integral equation based on continuity of scalar potential can then be written for the junction of $M$ wires as

$$\sum_{\ell=1}^{M} \int_0^{\infty} q_\ell(s') \frac{e^{-jkR_{i\ell}(s,s')}}{R_{i\ell}(s,s')}\, ds' = C \qquad \begin{cases} i = 1, \ldots, M \\ 0 < s < s_{\max} \end{cases} \tag{3-42}$$

where $q_\ell(s')$ is the charge density at $s'$ on wire $\ell$ and $R_{i\ell}(s,s')$ is the distance between the points at $s$ on wire $i$ and $s'$ on wire $\ell$, and $C$ is an arbitrary constant. The distance $s_{\max}$ should approach zero for continuity of potential, but a finite but electrically small value is used for the numerical solution.

Since the the current expansion of (3-3) results in an approximately piecewise linear representation of charge, a similar treatment is used in solving (3-42). As shown in Fig. 3-3, the charge is expanded in triangular basis functions terminated with a constant function extending to infinity to avoid introducing effects of truncation lengths for the wires. The charge on wire $\ell$ is then

$$q_\ell(s) = \sum_{j=1}^{n} q_{\ell j} f_{\ell j}(s)$$

where the first basis function is

$$\begin{aligned} f_{\ell 1}(s) &= \Delta_\ell - s \qquad && \text{for} \quad 0 \le s \le \Delta_\ell \\ &= 0 && \text{otherwise.} \end{aligned}$$

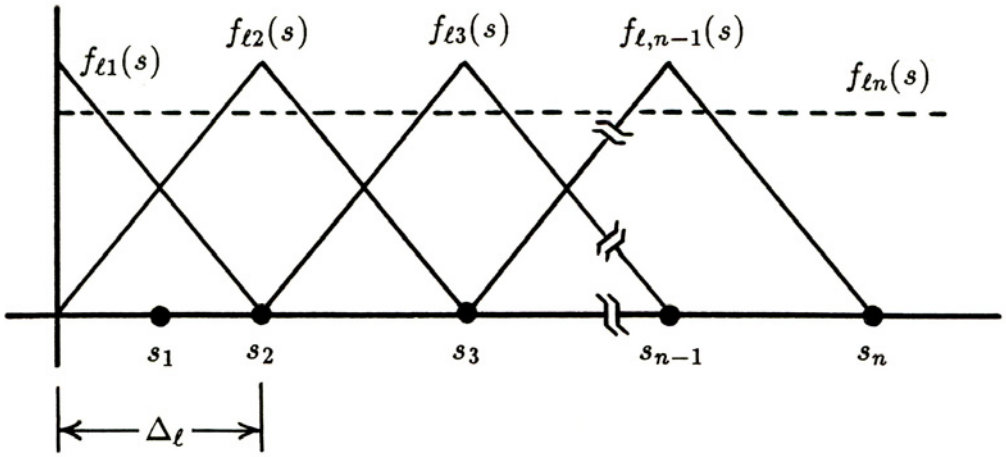


**Fig. 3-3** Basis functions and match points for the solution for charge on wire $\ell$.

For $j = 2, \ldots, n-1$,

$$\begin{aligned} f_{\ell j}(s) &= s - (j-2)\Delta_\ell \qquad \text{for} \quad (j-2)\Delta_\ell \le s \le (j-1)\Delta_\ell \\ &= j\Delta_\ell - s \qquad\quad \text{for} \quad (j-1)\Delta_\ell \le s \le j\Delta_\ell \\ &= 0 \qquad\qquad\quad \text{otherwise} \end{aligned}$$

while the last basis function is

$$f_{\ell n}(s) = \Delta_\ell \qquad\qquad \text{for} \quad s > 0.$$

Substitution of this current expansion into (3-42) with the match points on wire $i$ of

$$s_k = \begin{cases} \Delta_i/2 & \text{for } k = 1 \\ (k-1)\Delta_i & \text{for } k = 2, \ldots, n \end{cases}$$

leads to the set of equations

$$\sum_{\ell=1}^{m} \sum_{j=1}^{n} q_{\ell j} \Phi_{ik,\ell j} = C \qquad \begin{cases} i = 1, \ldots, m \\ k = 1, \ldots, n \end{cases} \tag{3-43}$$

where

$$\Phi_{ik,\ell j} = \int_0^\infty f_{\ell j}(s') \frac{e^{-jkR_{i\ell}(s_k, s')}}{R_{i\ell}(s_k, s')}\, ds'. \tag{3-44}$$

The evaluation of the integral in (3-44) is discussed in Appendix A. The length $\Delta_\ell$ is the segment length at the junction on wire $\ell$. Hence $s_1$ coincides with the match point in the moment-method solution for current.

Equation (3-43) is solved for the basis function amplitudes, from which the charge density on wire $\ell$ at the junction is obtained as

$$Q_\ell = (q_{\ell 1} + q_{\ell n})\Delta_\ell.$$

$Q_\ell$ is then used for the $a_i^\pm$ in the basis functions. Since only the ratios of charge densities are needed, the number of equations in (3-43) could be reduced by one by subtracting one equation from the others and dividing by one of the unknowns. Little is gained by this however since the solution time for the small matrix is negligible compared to the time to evaluate the matrix elements.

Tests for stepped-radius wires and multiple wire junctions have shown excellent convergence for the charge density at the junction with $n = 2$ in (3-43), using only the half-triangle and semi-infinite basis functions. Hence, while the code to solve (3-43) has been written for arbitrary $n$, $n$ has been set to 2. The time to solve (3-43) for a junction of two wires with differing radii, including the evaluation of the four elements of the $\Phi$ matrix, is then about five times the time to evaluate a single matrix element in the full impedance matrix. Since this solution for charge must be done only once for each junction the increase in time is generally small. For a structure with ten segments and one step in radius the time to fill the impedance matrix is increased by about five percent.

Several other conditions may occur at a wire end that call for alternate junction treatments. When a wire is connected to a perfectly conducting surface the charge, or derivative of current, is set to zero at the wire end. If the wire meets the surface at an angle from normal the charge will vary around the wire circumference. However, since the current and its image must form an even function about the plane, zero charge is the appropriate condition in the thin-wire approximation.

When a wire crosses an interface between two different media the current remains continuous and charge density is discontinuous as $q_+/q_- = \epsilon_+/\epsilon_-$, where $\epsilon_+$ and $\epsilon_-$ are the permittivities of the upper and lower media, respectively [18]. This condition results from the requirement of continuity of radial electric field across the interface when the penetrating wire is normal to the interface. However, the condition has been used for wires tilted by more than 60 degrees from the normal with apparently good results, based on small values of tangential electric field computed along the wire at the interface. For a lossy medium the condition on derivative of current is

$$I'_+/I'_- = \tilde{\epsilon}_+/\tilde{\epsilon}_- \tag{3-45}$$

where $\tilde{\epsilon}_+$ and $\tilde{\epsilon}_-$ are the complex permittivities. In the basis functions, the $a_i^\pm$ at a junction of wires on opposite sides of the interface are set equal to $\tilde{\epsilon}_+$ or $\tilde{\epsilon}_-$ for the medium containing the wire.

Well converged results have been obtained using (3-45) on a monopole on a buried radial-wire ground screen. While (3-45) does not include the interaction of horizontal screen wires with the interface, it represents the dominant effect on charge when crossing the interface. However poor convergence is obtained when using (3-41) at a junction of a monopole and a radial-wire screen just above the interface. In the latter case, segment lengths at the junction must be on the order of the distance of the screen from the interface to obtain a converged result.

No simple condition has been derived for charge at a junction of a wire with a dielectric or conducting sheath and a bare wire. In such a case, the best approach may be to leave

the charge condition as undetermined and include an equation minimizing tangential electric field at the junction as part of the moment-method equations. The same appears true when interaction with an interface has a substantial effect on charge distribution at a junction. The charge discontinuity can be introduced as an unknown in the moment-method solution by including an additional basis function ending at the junction with zero value but nonzero derivative. A suitable basis function can be obtained from the derivation in section 3.2 by evaluating the basis function as if the end of the segment at the junction was a free end with $X_i = 0$. To apply this method at a junction of $n$ wires the new basis functions would be added on $n - 1$ of the wires at the junction. This does not introduce an asymmetry at the junction, since the other basis functions will adjust accordingly.

# 4. Evaluation of the Field in Free Space

The moment-method solution of equations (2-13), (2-14) and (2-15) requires the evaluation of near electric and magnetic fields due to source currents on wire segments and surface patches. The evaluation is considered first in this section for the case of sources in free space or in an infinite dielectric or lossy medium. The evaluation of the electric field near an interface between free space and earth is covered in section 5. The evaluation of the electric field due to a wire segment is the most involved, due to the three components of current, constant, $\sin k_s s$ and $\cos k_s s$, and also because considerable care is needed to avoid loss of precision at low frequencies. An approximate treatment of end caps on wires is also included in this section.

## 4.1 The Electric Fields due to Wire Segments

In evaluating the field due to the basis functions on wires, the fields due to the component functions in (3-5), constant, $\sin k_s s$ and $\cos k_s s$, are evaluated and then combined using the constants derived for the basis functions. Care is needed in the evaluation of the field to avoid loss of precision at low frequencies and in particular limits of the coordinates. One cause of precision loss is the cancellation of the fields due to the point or ring charges at the segment ends. These point charges are an artificial result of treating continuous wires as made up of discrete segments, and the resulting fields must cancel exactly. Since the continuity of current, as required by Kirchhoff's law, is enforced in the basis functions, the fields due to the point charges can simply be dropped from the evaluation, thus eliminating this source of precision loss. These terms are dropped in NEC–4, but not in NEC–3 and earlier codes.

NEC–3 also differs from NEC–4 in the evaluation of the thin-wire kernel. In NEC–3 the current is treated as a filament on the wire axis and the boundary condition is matched on the wire surface. Also, NEC–3 includes an extended thin-wire kernel, which is an approximate evaluation of the field on the surface of the wire due to current on the surface. The extended thin-wire kernel is not used in NEC–4, since the extended boundary condition model, with end caps on the wires, gives at least as good results for thick wires.

As discussed in section 2, the NEC–4 wire model employes the extended boundary condition in the thin wire approximation, so that the current is treated as a tubular distribution on the wire surface, while the boundary condition is enforced on the wire axis. In evaluating the field of the current on the wire surface the segment is considered on the $z$ axis of a cylindrical coordinate system, as shown in Fig. 4-1. The integral over $z$ is evaluated first and then the integral over $\phi$. Hence the field due to a current filament on the $z$ axis will be considered first.

Although in general the integral for the near fields of a current distribution cannot be evaluated in closed form, such an evaluation is possible for a straight filament of current with $\sin k_s(z - z_0)$ distribution when $k_s$ is equal to the wave number in the medium. This result was derived by Brillouin [29] and is included in [30]. For a current filament extending from $z_1$ to $z_2$ on the $z$ axis of a cylindrical coordinate system, as shown in Fig. 4-1a, with

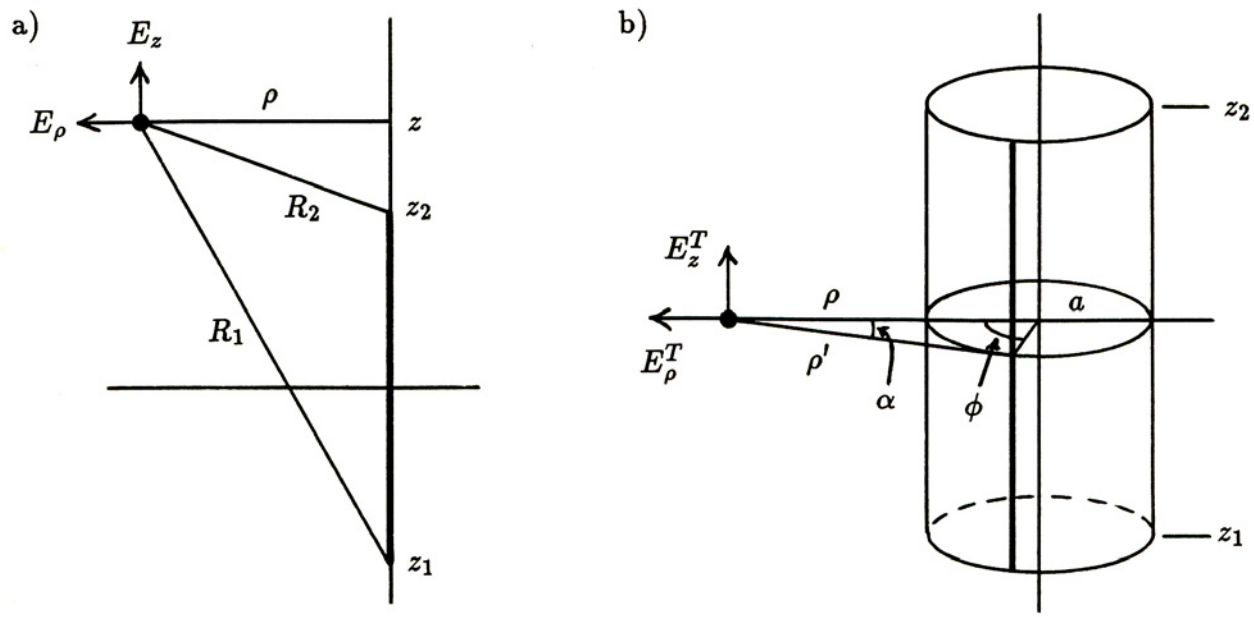


Fig. 4-1 Coordinates for evaluation of the field; a) current filament on the $z$ axis, b) current on a round wire segment.

current distribution

$$I(z') = I_0 \begin{pmatrix} \sin kz' \\ \cos kz' \end{pmatrix}$$

where $k$ is the wave number in the medium, the field components at the point $(\rho, z)$ are

$$E_\rho^{\substack{S\\C}}(\rho,z) = \frac{-j\eta I_0}{4\pi k\rho}\frac{e^{-jkR}}{R}\left\{k(z-z')\begin{pmatrix}\cos kz' \\ -\sin kz'\end{pmatrix} + \left[1-\frac{(z-z')^2}{R^2}(1+jkR)\right]\begin{pmatrix}\sin kz' \\ \cos kz'\end{pmatrix}\right\}\Bigg|_{z'=z_1}^{z'=z_2} \tag{4-1}$$

$$E_z^{\substack{S\\C}}(\rho,z) = \frac{j\eta I_0}{4\pi k}\frac{e^{-jkR}}{R}\left\{k\begin{pmatrix}\cos kz' \\ -\sin kz'\end{pmatrix} - (1+jkR)\frac{(z-z')}{R^2}\begin{pmatrix}\sin kz' \\ \cos kz'\end{pmatrix}\right\}\Bigg|_{z'=z_1}^{z'=z_2}. \tag{4-2}$$

For a constant current of strength $I_0$ the field components are

$$E_\rho^K(\rho,z) = \frac{-j\eta\rho I_0}{4\pi k}\left[(1+jkR)\frac{e^{-jkR}}{R^3}\right]_{z'=z_1}^{z'=z_2} \tag{4-3}$$

$$E_z^K(\rho,z) = \frac{-j\eta I_0}{4\pi k}\left\{\left[(1+jkR)(z-z')\frac{e^{-jkR}}{R^3}\right]_{z'=z_1}^{z'=z_2} + k^2\int_{z_1}^{z_2}\frac{e^{-jkR}}{R}\,dz'\right\} \tag{4-4}$$

where $R = [\rho^2 + (z-z')^2]^{1/2}$.

Although the fields due to the $\sin(kz')$ or $\cos(kz')$ currents are expressed as terms evaluated at the segment ends, the fields are due to current and charge distributed along the segment as well as point charges at the ends where the current is discontinuous. For

the constant current there is only the current on the segment and point charges at the ends. Since continuity of current is enforced in the NEC basis functions, the field components due to point charges at the segment ends can be dropped. The point-charge field for the segment on the z axis is

$$\mathbf{E}_q(\rho,z) = \frac{-j\eta I(z')}{4\pi k}(1+jkR)\frac{e^{-jkR}}{R^3}\mathbf{R}\Big|_{z'=z_1}^{z'=z_2} \tag{4-5}$$

where $\mathbf{R} = \rho\hat{\rho} + (z-z')\hat{\mathbf{z}}$. Subtracting the components of $\mathbf{E}_q$ from equations (4-1) through (4-4) leaves

$$\overset{S}{E}{}_\rho^C(\rho,z) = \frac{-j\eta I_0}{4\pi\rho}e^{-jkR}\left[\frac{(z-z')}{R}\begin{pmatrix}\cos kz'\\ -\sin kz'\end{pmatrix} - j\begin{pmatrix}\sin kz'\\ \cos kz'\end{pmatrix}\right]_{z'=z_1}^{z'=z_2} \tag{4-6}$$

$$\overset{S}{E}{}_z^C(\rho,z) = \frac{j\eta I_0}{4\pi}\frac{e^{-jkR}}{R}\begin{pmatrix}\cos kz'\\ -\sin kz'\end{pmatrix}\Big|_{z'=z_1}^{z'=z_2} \tag{4-7}$$

$$E_\rho^K(\rho,z) = 0 \tag{4-8}$$

$$E_z^K(\rho,z) = \frac{-j\eta I_0 k}{4\pi}\int_{z_1}^{z_2}\frac{e^{-jkR}}{R}\,dz'. \tag{4-9}$$

The above equations for fields due to $\sin ks$ and $\cos ks$ currents are restricted to $k$ in the current expansion equal to the wave number in the medium. This is usually the desirable choice since it results in a current expansion approximating the natural form of current on a long wire. However, in some cases, such as on an insulated wire embedded in a dielectric or lossy medium, it is better to use a factor $k_s$ in the current expansion that is different from $k$. In this case additional terms must be included in (4-1) and (4-2). The field components for current distributions of

$$I(z') = I_0\begin{pmatrix}\sin k_s z'\\ \cos k_s z'\end{pmatrix}$$

are

$$\begin{aligned}\overset{S}{E}{}_\rho^C(\rho,z) = \frac{-j\eta I_0}{4\pi k\rho}\Bigg\{&\frac{e^{-jkR}}{R}\Bigg[k_s(z-z')\begin{pmatrix}\cos k_s z'\\ -\sin k_s z'\end{pmatrix}\\ &+\left(1-\frac{(z-z')^2}{R^2}(1+jkR)\right)\begin{pmatrix}\sin k_s z'\\ \cos k_s z'\end{pmatrix}\Bigg]\Bigg|_{z'=z_1}^{z'=z_2}\\ &-(k^2-k_s^2)\int_{z_1}^{z_2}\begin{pmatrix}\sin k_s z'\\ \cos k_s z'\end{pmatrix}(z-z')\frac{e^{-jkR}}{R}\,dz'\Bigg\}\end{aligned} \tag{4-10}$$

$$\begin{aligned}\overset{S}{E}{}_z^C(\rho,z) = \frac{j\eta I_0}{4\pi k}\Bigg\{&\frac{e^{-jkR}}{R}\left[k_s\begin{pmatrix}\cos k_s z'\\ -\sin k_s z'\end{pmatrix} - (1+jkR)\frac{(z-z')}{R^2}\begin{pmatrix}\sin k_s z'\\ \cos k_s z'\end{pmatrix}\right]\Bigg|_{z'=z_1}^{z'=z_2}\\ &-(k^2-k_s^2)\int_{z_1}^{z_2}\begin{pmatrix}\sin k_s z'\\ \cos k_s z'\end{pmatrix}\frac{e^{-jkR}}{R}\,dz'\Bigg\}.\end{aligned} \tag{4-11}$$

Eliminating the components due to point charges at the segment ends, these fields are

$$E_\rho^{S_C}(\rho,z) = \frac{-j\eta I_0}{4\pi k\rho}\Bigg\{e^{-jkR}\left[\frac{k_s(z-z')}{R}\begin{pmatrix}\cos k_s z'\\ -\sin k_s z'\end{pmatrix} - jk\begin{pmatrix}\sin k_s z'\\ \cos k_s z'\end{pmatrix}\right]_{z'=z_1}^{z'=z_2}$$
$$- (k^2-k_s^2)\int_{z_1}^{z_2}\begin{pmatrix}\sin k_s z'\\ \cos k_s z'\end{pmatrix}(z-z')\frac{e^{-jkR}}{R}\,dz'\Bigg\} \tag{4-12}$$

$$E_z^{S_C}(\rho,z) = \frac{j\eta I_0}{4\pi k}\Bigg\{k_s\begin{pmatrix}\cos k_s z'\\ -\sin k_s z'\end{pmatrix}\frac{e^{-jkR}}{R}\Bigg|_{z'=z_1}^{z'=z_2}$$
$$- (k^2-k_s^2)\int_{z_1}^{z_2}\begin{pmatrix}\sin k_s z'\\ \cos k_s z'\end{pmatrix}\frac{e^{-jkR}}{R}\,dz'\Bigg\}. \tag{4-13}$$

The equations (4-6) through (4-9) are an improvement over those including the point charges, but still present problems for numerical evaluation in some cases. They are exact, however, with the restriction that the current is continuous, goes to zero at free ends and the sum of currents into any junction is zero. Since the current expansion in NEC satisfies these conditions, equations (4-6) through (4-10) are used as the basic forms for evaluating the method of moments matrix and near fields. When a segment connects to a surface modeled with the MFIE the field of the point charge at the connected end must be included, to cancel the corresponding point charge on the surface. Also, at a junction of wires on opposite sides of the air-ground interface the point-charge fields must be included in the field for each connected end since the charges are located in different media. These point-charge fields are obtained by evaluating (4-5) for the particular segment end.

For a segment with length $\Delta = 2\delta$ extending from $z_1 = -\delta$ to $z_2 = \delta$ the field components given by (4-6) through (4-9) become

$$E_\rho^S(\rho,z) = \frac{-j\eta I_0}{4\pi\rho}\Bigg\{\Big[(z-\delta)\frac{e^{-jkR_2}}{R_2} - (z+\delta)\frac{e^{-jkR_1}}{R_1}\Big]\cos(k\delta)$$
$$- j(e^{-jkR_2}+e^{-jkR_1})\sin(k\delta)\Bigg\} \tag{4-14}$$

$$E_\rho^C(\rho,z) = \frac{j\eta I_0}{4\pi\rho}\Bigg\{\Big[(z-\delta)\frac{e^{-jkR_2}}{R_2} + (z+\delta)\frac{e^{-jkR_1}}{R_1}\Big]\sin(k\delta)$$
$$+ j(e^{-jkR_2}-e^{-jkR_1})\cos(k\delta)\Bigg\} \tag{4-15}$$

$$E_z^S(\rho,z) = \frac{j\eta I_0}{4\pi}\Big(\frac{e^{-jkR_2}}{R_2} - \frac{e^{-jkR_1}}{R_1}\Big)\cos(k\delta) \tag{4-16}$$

$$E_z^C(\rho,z) = \frac{-j\eta I_0}{4\pi}\Big(\frac{e^{-jkR_2}}{R_2} + \frac{e^{-jkR_1}}{R_1}\Big)\sin(k\delta) \tag{4-17}$$

$$E_z^K(\rho,z) = \frac{-j\eta I_0 k}{4\pi}\int_{-\delta}^{\delta}\frac{e^{-jkR}}{R}\,dz' \tag{4-18}$$

where $R_1 = [\rho^2+(z+\delta)^2]^{1/2}$ and $R_2 = [\rho^2+(z-\delta)^2]^{1/2}$. Numerical precision may be lost in evaluating equations (4-14) through (4-18) in the limit of small $kR$ or when $R$ is much larger

than $\Delta$ or for small $\rho$ when $|z| > \delta$. Also, the subtraction of $E_z^C - E_z^K$ in evaluating the field due to the $\cos k_s(s - s_j) - 1$ term in (3-5) requires careful treatment. Approximations valid for these cases are given in Appendix B.

To evaluate the field of a tubular current distribution the field of a current filament is integrated around the circumference of the cylinder, using the geometry of Fig. 4-1b. Taking account of the change in direction of the $\hat{\rho}$ vector from the filament to the evaluation point, the fields of the current on the cylinder, in terms of the field components $E_z$ and $E_\rho$ for the filament with unit current, are

$$E_z^T(\rho, z) = \frac{I_0}{2\pi} \int_0^{2\pi} E_z(\rho', z)\, d\phi$$

and

$$E_\rho^T(\rho, z) = \frac{I_0}{2\pi} \int_0^{2\pi} \cos\alpha\, E_\rho(\rho', z)\, d\phi$$

where

$$\rho' = (\rho^2 + a^2 - 2\rho a \cos\phi)^{1/2}$$

and

$$\cos\alpha = \frac{\rho - a\cos\phi}{\rho'}.$$

Using (4-6) through (4-9) for the field of the filament, the field of the tubular current distribution can be written

$$E_\rho^{S_C^C}(\rho, z) = \frac{-j\eta I_0}{4\pi} \left[ G_2(z - z') \begin{pmatrix} \cos kz' \\ -\sin kz' \end{pmatrix} - jG_3 \begin{pmatrix} \sin kz' \\ \cos kz' \end{pmatrix} \right]_{z'=z_1}^{z'=z_2} \tag{4-19}$$

$$E_z^{S_C^C}(\rho, z) = \frac{j\eta I_0}{4\pi} G_1 \begin{pmatrix} \cos kz' \\ -\sin kz' \end{pmatrix} \Bigg|_{z'=z_1}^{z'=z_2} \tag{4-20}$$

$$E_z^K(\rho, z) = \frac{-j\eta I_0 k}{4\pi} G_4 \tag{4-21}$$

where $I_0$ is the magnitude of the total current on the cylinder and

$$G_1 = \frac{1}{2\pi} \int_0^{2\pi} \frac{e^{-jkR}}{R}\, d\phi \tag{4-22}$$

$$G_2 = \frac{1}{2\pi} \int_0^{2\pi} \frac{\cos\alpha}{\rho'} \frac{e^{-jkR}}{R}\, d\phi \tag{4-23}$$

$$G_3 = \frac{1}{2\pi} \int_0^{2\pi} \frac{\cos\alpha}{\rho'} e^{-jkR}\, d\phi \tag{4-24}$$

$$G_4 = \frac{1}{2\pi} \int_0^{2\pi} \int_{z_1}^{z_2} \frac{e^{-jkR}}{R}\, dz'\, d\phi. \tag{4-25}$$

with

$$R = (\rho^2 + a^2 + z^2 - 2a\rho\cos\phi)^{1/2}.$$

When the evaluation point is on the axis of the segment, so that $\rho = 0$, the evaluation of the integrals over $\phi$ becomes trivial. The result can be obtained by simply lumping the current in a filament at any position around surface of the cylinder. When $\rho$ is not zero the integrals cannot be evaluated in terms of simple functions. Approximations based on the assumption of a thin wire are commonly used in this case. An approximation that is sometimes used for evaluation points outside of the segment is to treat the total current as a filament located at the $\phi = 90°$ position. However, it is well known that the radial electric field outside of a wire is well approximated by treating the charge as a filament on the wire axis. The difference between the radial field with the filament on the surface at $\phi = 90°$ and on the axis can be significant when $\rho$ is on the order of the wire radius.

Approximations for the integrals in (4-22) through (4-25) are derived in Appendix D. Series approximations are considered that involve either $R$ to a point on the segment axis or to a point at $\phi = 90°$ on the surface. The approximations involving $R$ to the segment surface are used in NEC–4, so that

$$G_1 \approx G_1^b = \frac{e^{-jkR_t}}{R_t} \tag{4-26}$$

$$G_2 \approx G_2^b = \frac{e^{-jkR_t}}{\rho R_t} \tag{4-27}$$

$$G_3 \approx G_3^b = \frac{e^{-jkR_t}}{\rho} \tag{4-28}$$

$$G_4 \approx G_4^b = \int_{z_1}^{z_2} \frac{e^{-jkR_t}}{R_t}\, dz' \tag{4-29}$$

and $R_t = [\rho^2 + a^2 + (z - z')^2]^{1/2}$. Since $G_2$ and $G_3$ involve factors of $\rho^{-1}$ rather than $\rho'^{-1}$ the result is not the field of a current filament on the surface.

For $\rho < a$, the approximations for $G_2$ and $G_3$ in Appendix D do not have leading terms resembling the integrand evaluated at a point. Hence, it might seem reasonable, for the level of approximation in (4-26) through (4-29), to set $G_2$ and $G_3$ to zero for evaluation points inside the wire surface. This question is important in the case of a bend in a thick wire, where the segment lengths are short enough that the match point on one segment is buried inside the other segment. This is a pathological case that violates the thin-wire approximation. However it has been found that better results are obtained from the moment-method solution by continuing to use (4-26) through (4-29) when $\rho < a$ rather than setting the radial electric field to zero.

### 4.2 The Magnetic Field due to Wire Segments

The magnetic field of a wire segment is zero on the segment axis and $\phi$ directed outside of the wire. For a segment on the $z$ axis with length $\Delta = 2\delta$ and sinusoidal current distributions

$$I(z') = I_0 \begin{pmatrix} \sin kz' \\ \cos kz' \end{pmatrix}$$

the field components are

$$H_{\phi}^{\substack{S\\C}}(\rho,z) = \frac{-jI_0}{4\pi\rho}\left[e^{-jkR_2}\begin{pmatrix}\cos k\delta\\ -\sin k\delta\end{pmatrix} - e^{-jkR_1}\begin{pmatrix}\cos k\delta\\ \sin k\delta\end{pmatrix}\right.$$
$$\left. - j(z-\delta)\frac{e^{-jkR_2}}{R_2}\begin{pmatrix}\sin k\delta\\ \cos k\delta\end{pmatrix} + j(z+\delta)\frac{e^{-jkR_1}}{R_1}\begin{pmatrix}-\sin k\delta\\ \cos k\delta\end{pmatrix}\right] \quad (4\text{-}30)$$

where $R_1 = [\rho^2 + (z+\delta)^2]^{1/2}$ and $R_2 = [\rho^2 + (z-\delta)^2]^{1/2}$. For a constant current $I_0$ the field is

$$H_{\phi}^{K}(\rho,z) = \frac{\rho I_0}{4\pi}\int_{-\delta}^{\delta}(1+jkR)\frac{e^{-jkR}}{R^3}\,dz. \quad (4\text{-}31)$$

The integral in (4-31) is evaluated numerically using adaptive Romberg quadrature.

When $\rho \ll |z|$ and $|z| > \delta$ the evaluation of (4-30) may lead to numerical errors due to the cancellation of large terms. Hence, for $z > \delta$ and $\rho/(z-\delta) < 10^{-3}$ the field is evaluated using the approximation

$$H_{\phi}^{\substack{S\\C}}(\rho,z) \approx \frac{\rho I_0}{8\pi}e^{-jkz}\left\{\left[\frac{k}{z+\delta} - \frac{k}{z-\delta}\right]\begin{pmatrix}1\\ -j\end{pmatrix}\right.$$
$$\left. + \left[\frac{e^{jk\delta}}{(z-\delta)^2}\begin{pmatrix}\sin k\delta\\ \cos k\delta\end{pmatrix} - \frac{e^{-jk\delta}}{(z+\delta)^2}\begin{pmatrix}-\sin k\delta\\ \cos k\delta\end{pmatrix}\right]\right\}. \quad (4\text{-}32)$$

For $z < -\delta$ and $\rho/(|z|-\delta) < 10^{-3}$ equation (4-32) is evaluated for $-z$ and the relation $H_{\phi}^{\substack{S\\C}}(\rho,z) = \mp H_{\phi}^{\substack{S\\C}}(\rho,-z)$ is used.

### 4.3 The Electric and Magnetic Fields due to Surface Currents

The electric and magnetic fields due to each patch making up a surface are evaluated by treating the surface current over the patch as a point source located at the center of the patch. This approximation restricts the minimum separation of source and evaluation points, but is compatible with the moment-method solution. The terms $\hat{\mathbf{t}}\cdot\mathbf{J}\times\nabla' g(r,r')$ in equations (2-14) and (2-15) vanish when $\hat{\mathbf{t}}$, $\mathbf{J}$ and $\mathbf{r}-\mathbf{r}'$ lie in the same plane. Hence the surface integrals for magnetic field in these equations do not contribute to the self-interaction terms for flat patches, where the contribution of the singularity has been taken out as a separate term. With the point-source approximation, the magnetic field due to patches is evaluated as

$$\mathbf{H}(\mathbf{r}) = \frac{-1}{4\pi}\sum_{i=1}^{M}\frac{e^{-jkR}}{R^2}(1+jkR)(\hat{\mathbf{R}}\times\mathbf{J}_i)S_i \quad (4\text{-}33)$$

where $R = |\mathbf{r}-\mathbf{r}_i|$, $\hat{\mathbf{R}} = (\mathbf{r}-\mathbf{r}_i)/R$, $\mathbf{J}_i$ is the surface current on patch $i$ and $S_i$ is the area of the patch.

The electric field due to patches is evaluated as

$$\mathbf{E}(\mathbf{r}) = \frac{-j\eta}{4\pi k}\sum_{i=1}^{M}\frac{e^{-jkR}}{R^3}\left[\left(k^2R^2 - jkR - 1\right)\mathbf{J}_i - \left(k^2R^2 - 3jkr - 3\right)\left(\mathbf{J}_i\cdot\hat{\mathbf{R}}\right)\hat{\mathbf{R}}\right]S_i. \quad (4\text{-}34)$$

### 4.4 A Model for End Caps on Wires

In order for the extended boundary condition used in NEC–4 to be strictly valid the wire must be modeled as a closed surface. Hence the free ends of wires must be closed with caps. Popović et al. [23] described a careful treatment of end caps of flat or hemispherical shape. The cap was included in the moment-method solution with several match points located on the cap surface. This approach appears too cumbersome for large, complex structures, so a simpler treatment of end caps was used in NEC–4. The wire is assumed to have a flat end cap, as in Fig. 4-2, with a constant surface charge density that maintains continuity of current and charge density with the wire. For continuity of current from the wire surface onto the end cap, a surface current density of

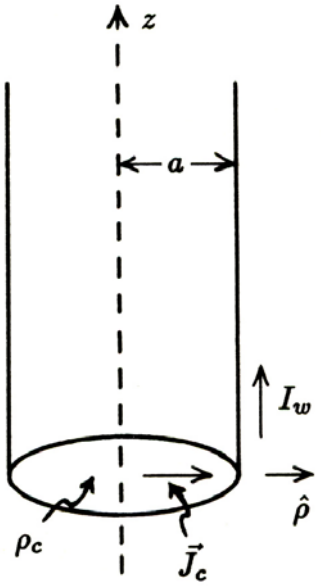


**Fig. 4-2** A wire end with a flat end cap.

$$\mathbf{J}_c(\rho) = \frac{\rho S}{2\pi a^2} I_w(0)\hat{\rho}$$

is assumed on the end cap, where $I_w$ is the total wire current and

$$S = \begin{cases} 1 & \text{if the reference direction for} \\ & I_w \text{ is away from the end cap} \\ -1 & \text{if the reference direction for} \\ & I_w \text{ is toward the end cap.} \end{cases}$$

From the continuity equation, the surface charge density is then

$$\rho_c = \frac{j}{\omega}\nabla \cdot \mathbf{J}_c(\rho) = \frac{jS}{\omega\pi a^2} I_w(0). \tag{4-35}$$

For continuity of charge density from the wire onto the end cap, it is required that

$$\rho_c = \frac{j}{2\pi a\omega}\frac{d}{dz} I_w(z)\bigg|_{z=0}$$

which, with (4-35), yields the condition

$$\frac{I_w'(z)}{I_w(z)}\bigg|_{z=0} = \frac{2S}{a}. \tag{4-36}$$

This value of $I_w'/I_w$ supplies the value for $X_i$ in equations (3-12) or (3-13) defining the basis function. A similar condition is imposed at wire ends in NEC–3 where

$$\frac{I_w'(z)}{I_w(z)}\bigg|_{z=0} = kS\frac{J_0(ka)}{J_1(ka)}.$$

With small argument approximations for the Bessel functions $J_0$ and $J_1$, this equation reduces to (4-36). However, in NEC–3 the field due to the charge on the end cap was neglected so the end condition did little good.

The field at a point $\mathbf{r}$ due to the constant charge density $\rho_c$ on the end cap with area $A_c$ is

$$\mathbf{E}_c(\mathbf{r}) = \frac{-\rho_c}{4\pi\epsilon} \nabla \int_{A_c} \frac{e^{-jkR}}{R}\, dA' \tag{4-37}$$

where $R = |\mathbf{r} - \mathbf{r}'|$ and $\mathbf{r}'$ is the integration point on $A_c$. Due to symmetry of the current $\mathbf{J}_c$, the vector potential is zero on the axis and is greatly reduced by cancellation at typical evaluation points off of the axis. Hence the vector potential is neglected in evaluating the field. The evaluation of the integral in (4-37) is discussed in Appendix E. The field $\mathbf{E}_c$ is included in the method of moments impedance matrix where it is added to the field due to the basis function at the wire end.

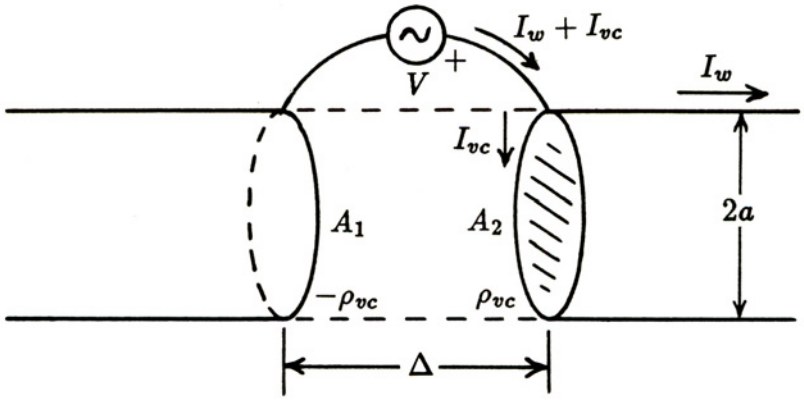


Fig. 4-3 Voltage source with end caps on the excitation gap.

End caps must also be added to segments with voltage sources to prevent these sources from exciting the inside of the wire. A schematic view of a segment with a voltage source is shown in Fig. 4-3. The source drives a current $I_w$ along the wire and also supplies a current $I_{vc}$ to charge the capacitor formed by the ends of the source gap. Using a simple approximation for the capacitance of the source gap of $C = \pi a^2 \epsilon/\Delta$ the current onto the end caps is

$$I_{vc} = \frac{j\pi\omega\epsilon a^2}{\Delta} V. \tag{4-38}$$

The total charge on the caps is $CV$, so the surface charge density, assuming a constant distribution, is

$$\rho_{vc} = \frac{\epsilon V}{\Delta} \tag{4-39}$$

on the cap at the "plus" end of the source and $-\rho_{vc}$ at the opposite end.

Neglecting the vector potential of the current, the field due to the charged caps on a segment $j$ with source voltage $V_j$ and cap $A_1$ on the negative end and $A_2$ on the positive

end is

$$\mathbf{E}_j^{vc}(\mathbf{r}) = \frac{\rho_{vc}}{4\pi\epsilon}\nabla\left(\int_{A_1}\frac{e^{-jkR}}{R}\,dA' - \int_{A_2}\frac{e^{-jkR}}{R}\,dA'\right). \tag{4-40}$$

Since the charge is proportional to the known source voltage, the field that it produces is added to the excitation term $\mathbf{E}^I$ in (2-13) or to the right-hand side of the matrix equation (3-4). Thus the field on segment $i$ located at $\mathbf{r}_i$ due to the source on segment $j$ is

$$\hat{\mathbf{s}}_i \cdot \mathbf{E}^I(\mathbf{r}_i) = \delta_{ij}\frac{V_j}{\Delta_j} + \hat{\mathbf{s}}_i \cdot \mathbf{E}_j^{vc}(\mathbf{r}_i)$$

where $\delta_{ij}$ is the Kronecker delta function. Without the end caps, only the first term is present, with zero field on all segments except the source segment.

A similar treatment is needed on segments with impedance loads, since a load is really a current-dependent voltage source. If segment $j$ is loaded with impedance $Z_j$, the gap voltage determining $\rho_{vc}$ in (4-40) is $V_L = I_j Z_j$, where $I_j$ is the current at the center of the segment. Thus $\rho_{vc} = I_j Z_j \epsilon/\Delta_j$. The charges on the end caps produce a field component $\hat{\mathbf{s}}_i \cdot \mathbf{E}_j^{vc}(\mathbf{r}_i)$ on segment $i$ that must be added to the matrix element for each basis function that extends onto segment $j$. Since only the coefficient of $A_j$ in (3-5) is not zero at the center of the segment only the component of field due to the constant current is affected.

The effect of including end caps on wire ends and voltage sources is shown in Fig. 4-4 and 4-5 for a quarter wave monopole with a wire radius of $0.01\lambda$. The monopole was divided into 80 segments so that the ratio of segment length to radius was 0.3125. Since the radius is constant, the thin-wire kernel (TWK) in NEC–3 is equivalent to putting the current on the surface and the match points on the axis. The invalid condition of zero field on the axis of an open cylinder results in non-physical oscillations of the current. These oscillations become apparent for segment lengths shorter than about two times the radius. The extended thin-wire kernel (ETWK) in NEC–3 represents a physically valid condition, with the current and match points on the surface of the cylinder. However, the field is evaluated with only the first two terms of a series expansion in radius. Hence oscillations in the current are greatly reduced but are still present. The end-cap treatment in NEC–4 reduces the oscillations at the wire ends and essentially eliminates them at the voltage source. That the oscillations are not completely eliminated at the end is probably the result of the approximation of a constant charge density on the end cap, neglecting the actual singular behavior of charge at the edge.

To completely close the wire surface, the field due to charge on the annular surface at a change in radius should also be included in the solution. This has been tested in a code limited to straight wires. The surface charge density on the annular surface was linearly interpolated between values on the wires. Also, Kirchhoff's law was modified to allow for charge accumulation on the annular surface. Initial tests showed that these changes reduced the invalid oscillations of current when segments with small length-to-radius ratio were used at a step in wire radius. However, this treatment has not been included in the present NEC–4 due to the difficulty of extending it to handle junctions of several wires with differing radii and directions. Also, there are other problems in applying the thin-wire approximation at such junctions.

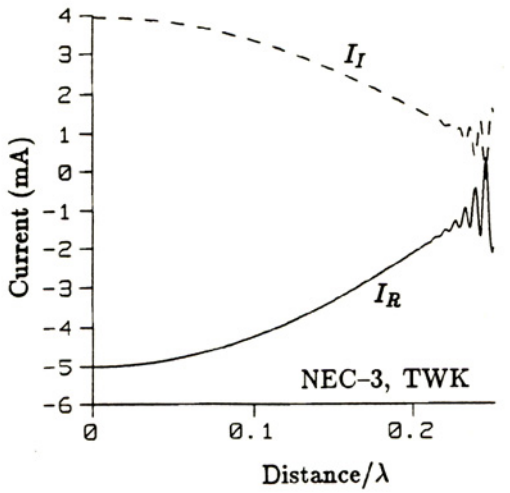


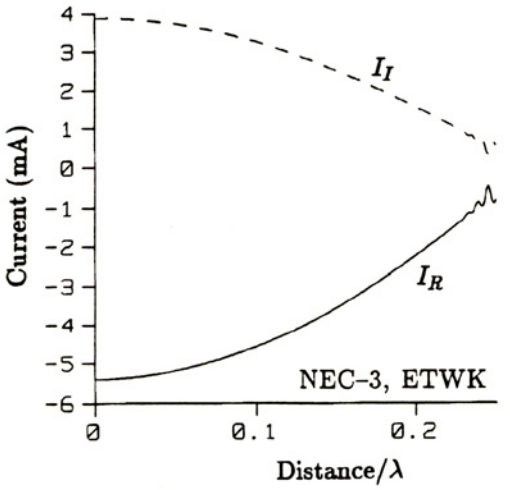


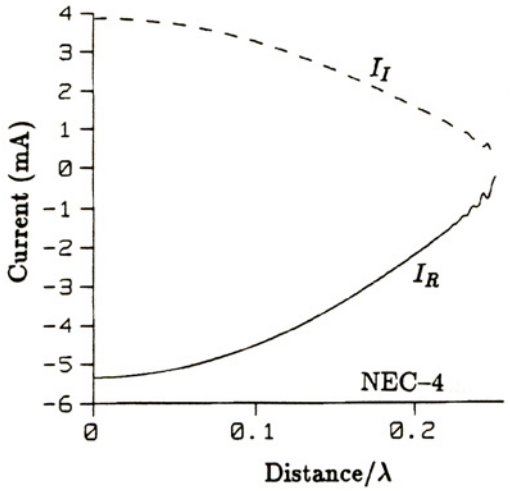


**Fig. 4-4** Current on a $\lambda/4$ monopole excited by an incident plane wave with 2 V/m. The monopole had a radius of $0.01\lambda$ and was modeled with 80 segments.

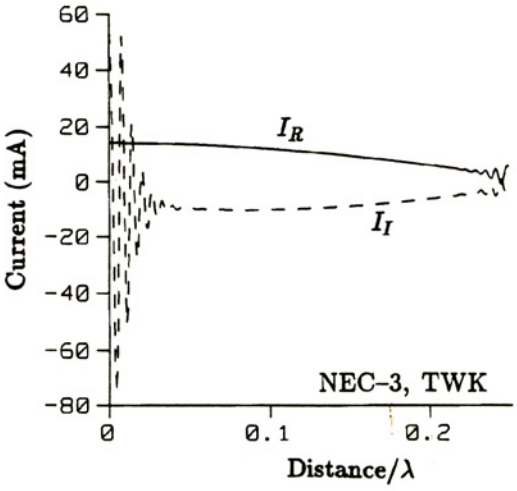


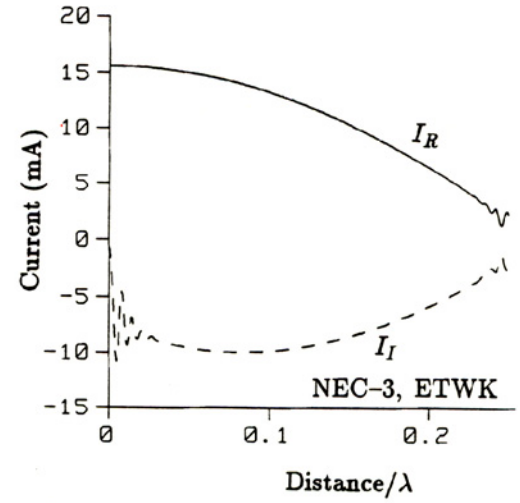


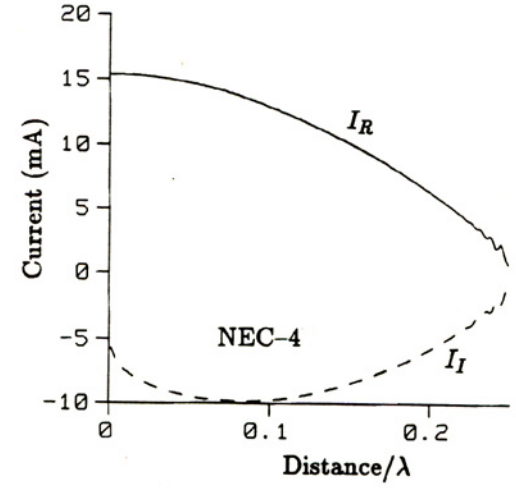


**Fig. 4-5** Current on a $\lambda/4$ monopole excited by a 1 V source at its base. The monopole had a radius of $0.01\lambda$ and was modeled with 80 segments.

# 5. Evaluation of the Field Near Ground

The previous discussion of field evaluation has dealt with currents in an infinite medium. The medium may be free space, dielectric or conducting with the proper choice of wave number $k$. NEC can also model antennas above or in a conducting half space with air as the upper medium and an arbitrary material such as earth or water below. The ground plane changes the solution in three ways: (1) by modifying the current distribution through near-field interaction; (2) by changing the field illuminating the structure; and (3) by changing the reradiated field. Effects (2) and (3) are easily analyzed in terms of plane-wave reflection, as a direct ray and a ray reflected from the ground. The reradiated field is not a plane wave when it reflects from the ground, but the strength of the field can be found from the reciprocal problem with a plane wave arriving at the ground from the distant evaluation point. Analysis of the near-field interaction is more difficult, however. The free-space Green's function in the kernel of the integral equation must be replaced by the Green's function for a source near an interface.

NEC offers three options for modeling grounds. For a perfectly conducting ground, the code simply includes the image of a source when evaluating the fields. The image field is evaluated with the formulas in Section 4 for an infinite medium. The most accurate model for a lossy ground is based on the solution for a point source near an interface, in terms of the Sommerfeld integrals [31]. Table-lookup and asymptotic approximations are used to reduce computation time. This model will be called the Sommerfeld/Asymptotic method. The third option treats a lossy ground with a modified image model using the Fresnel plane-wave reflection coefficients. While specular reflection is not accurate for spherical-wave near fields, this Reflection Coefficient Approximation (RCA) has been found to provide useful results for structures in air at least $0.1\lambda_0$ or more above the interface [11, 32, 33]. The advantage of this method is its simplicity and speed of computation, which are the same as for the image method for perfectly conducting ground. The Sommerfeld/Asymptotic model is presently implemented only for wires, but the same technique could be extended to the MFIE patch model.

The remainder of this section describes the field evaluations for the Sommerfeld/Asymptotic and RCA solutions. Other considerations in modeling a structure near a ground plane, including the effects on incident and radiated fields and the current expansion on a wire penetrating the interface, are discussed elsewhere in this manual.

## 5.1 The Sommerfeld/Asymptotic Solution

The development of the Sommerfeld/Asymptotic model in NEC can be traced back to the code WFLLL2A [34] which implemented a numerical evaluation of the Sommerfeld integrals in evaluating the elements of the moment-method matrix. The double integration in this approach, when the fields involving Sommerfeld integrals are integrated over the current distribution, can increase the computation time relative to that for a model in free space by as much as two orders of magnitude. A code SOMINT was then developed [35] that used bivariate interpolation in a table of pre-computed Sommerfeld integral values to obtain the field values needed for integration over current distributions. This method greatly reduces

the required computation time. NEC–2 used a similar approach, with the interpolation algorithm optimized. The singularity at the source and the free-space phase factor were removed analytically to reduce the solution time and allow modeling wires very close to the interface. For interaction distances beyond the range of the interpolation table, the Norton approximations [36] were used in NEC–2.

When the ground model was extended in NEC–3 for wires above, below or crossing the interface, the interpolation procedure became considerably more complicated. When source and evaluation points are on the same side of the interface, the field values depend only on the sum of the distances of the points from the interface and their radial separation. Hence only these two parameters were needed in a bivariate interpolation. When source and evaluation points are on opposite sides of the interface, the fields depend on the individual distances from the interface, so the interpolation space involves three parameters. Also, for some coordinate ranges, the field transmitted across the interface is not as well behaved as the reflected field.

For small separations of source and evaluation points, the algorithms developed for NEC–3, which are also used in NEC–4, employ a three-parameter interpolation with the singularity and phase variation suppressed. For somewhat larger separations, the field values are obtained by interpolation with a model in which terms suggested by the asymptotic form of the field equations are fit to computed field values with a least-squares algorithm. This approach, which can be termed model-based parameter estimation, allows a larger sampling interval in the computed values than would be possible with polynomial interpolation. At still larger distances, standard asymptotic approximations are used. The equations and numerical methods used in representing the field near ground are described in the remainder of this section.

### 5.1.1 The Field Equations

The Sommerfeld solution for a point source near an interface is usually derived by matching boundary conditions at the interface in a cylindrical-wave expansion of the Hertz potential. The form used here is taken from Baños [37] and involves $U$ and $V$ integrals. The geometry of the half-space problem is shown in Fig. 5-1. The relative permittivity and conductivity of the lower medium will be denoted $\epsilon_1$ and $\sigma_1$ respectively, while in the upper medium these parameters are $\epsilon_2$ and $\sigma_2$, and both media have free-space permeability $\mu_0$. Thus the wave numbers in the lower medium $k_1$ and upper medium $k_2$ are

$$k_1^2 = \omega^2 \mu_0 \epsilon_0 (\epsilon_1 - j\sigma_1/\omega\epsilon_0)$$

$$k_2^2 = \omega^2 \mu_0 \epsilon_0 (\epsilon_2 - j\sigma_2/\omega\epsilon_0).$$

In most of the development to follow $\epsilon_2$ and $\sigma_2$ will be arbitrary, although NEC is currently restricted to $\epsilon_2 = 1$, $\sigma_2 = 0$.

The notation for electric field will use a subscript to indicate the field component in cylindrical coordinates ($\rho$, $\phi$, $z$) and a superscript to indicate the source orientation, $V$ for a vertical electric dipole and $H$ for horizontal. If the horizontal source is located along the $x$ axis, the components $E_\rho^H$ and $E_z^H$ must be multiplied by $\cos\phi$ to obtain the $\rho$ and $z$

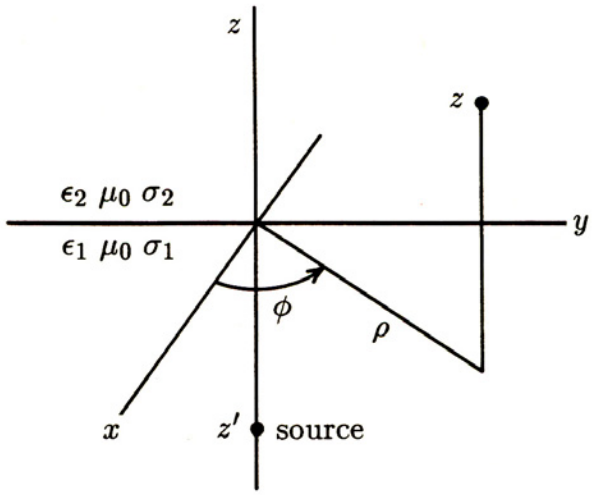


**Fig. 5-1** Coordinates for evaluation of the field due to a buried source at an elevated receiver.

components of field at an angle $\phi$ from the $x$ axis, while $E_\phi^H$ is multiplied by $\sin\phi$. These $\phi$ dependent terms will be omitted for now, since we want to use the field components in table lookup schemes with a minimum number of parameters. Also, a dipole with unit current moment $I\ell = 1$ will be assumed for now. The rectangular components of field due to an arbitrarily oriented electric dipole source with current moment $I\ell$ and direction $\hat{\mathbf{d}} = d_x\hat{\mathbf{x}} + d_y\hat{\mathbf{y}} + d_z\hat{\mathbf{z}}$ will eventually be obtained from these terms as

$$\begin{pmatrix} E_x \\ E_y \\ E_z \end{pmatrix} = \begin{pmatrix} \cos^2\phi E_\rho^H - \sin^2\phi E_\phi^H & \sin\phi\cos\phi(E_\rho^H + E_\phi^H) & \cos\phi E_\rho^V \\ \sin\phi\cos\phi(E_\rho^H + E_\phi^H) & \sin^2\phi E_\rho^H - \cos^2\phi E_\phi^H) & \sin\phi E_\rho^V \\ \cos\phi E_z^H & \sin\phi E_z^H & E_z^V \end{pmatrix} \begin{pmatrix} d_x \\ d_y \\ d_z \end{pmatrix} I\ell \quad (5\text{-}1)$$

The form of the field equations depends on the location of the source and evaluation points relative to the interface. When source and evaluation points are on opposite sides of the interface the fields involve only the Sommerfeld integral terms. When source and evaluation points are on the same side of the interface the equations include terms representing the direct field from source to observer and the field of an image of the source, in addition to the Sommerfeld integrals. The form of these equations is not unique. In fact, NEC uses only the equations for a source below the interface and observer above, with the other cases obtained from transformations given in Appendix G. The full set of electric field equations from Baños is included in Appendix F for reference.

For a source with $I\ell = 1$ at height $z'$ in medium 1 and evaluation point at height $z$ in medium 2 ($z' < 0$, $z \geq 0$) the electric field components are [37]

$$E_{\rho 12}^V = \frac{-j\omega\mu_0}{4\pi}\frac{\partial^2 V_{12}}{\partial\rho\partial z} \quad (5\text{-}2a)$$

$$E_{z12}^V = \frac{-j\omega\mu_0}{4\pi}\left(\frac{\partial^2}{\partial z^2} + k_2^2\right)V_{12} \quad (5\text{-}2b)$$

$$E_{\rho 12}^H = \frac{-j\omega\mu_0}{4\pi}\left(\frac{\partial^2 V_{12}}{\partial\rho^2} + U_{12}\right) \quad (5\text{-}2c)$$

$$E^H_{\phi 12} = \frac{j\omega\mu_0}{4\pi}\left(\frac{1}{\rho}\frac{\partial V_{12}}{\partial \rho} + U_{12}\right) \tag{5-2d}$$

$$E^H_{z12} = \frac{j\omega\mu_0}{4\pi}\frac{\partial^2 V_{12}}{\partial \rho \partial z'} \tag{5-2e}$$

where $V_{12}$ and $U_{12}$ are the Sommerfeld integrals

$$V_{12} = 2\int_0^\infty \frac{e^{\gamma_1 z' - \gamma_2 z}}{k_1^2\gamma_2 + k_2^2\gamma_1} J_0(\lambda\rho)\lambda\, d\lambda \tag{5-3}$$

$$U_{12} = 2\int_0^\infty \frac{e^{\gamma_1 z' - \gamma_2 z}}{\gamma_1 + \gamma_2} J_0(\lambda\rho)\lambda\, d\lambda \tag{5-4}$$

with $\gamma_1 = (\lambda^2 - k_1^2)^{1/2}$ and $\gamma_2 = (\lambda^2 - k_2^2)^{1/2}$. A subscript of 12 has been added to indicate that the source is in medium 1 and the evaluation point in medium 2. Using the symmetry properties of the Hankel function, (5-3) and (5-4) can also be written

$$V_{12} = \int_{-\infty}^\infty \frac{e^{\gamma_1 z' - \gamma_2 z}}{k_1^2\gamma_2 + k_2^2\gamma_1} H_0^{(2)}(\lambda\rho)\lambda\, d\lambda \tag{5-5}$$

$$U_{12} = \int_{-\infty}^\infty \frac{e^{\gamma_1 z' - \gamma_2 z}}{\gamma_1 + \gamma_2} H_0^{(2)}(\lambda\rho)\lambda\, d\lambda \tag{5-6}$$

Using the integrals from (5-3) and (5-4) and evaluating the derivatives in (5-2) results in the equations for the field components

$$E^V_{\rho 12} = \frac{j\omega\mu_0}{4\pi}\, 2\int_0^\infty \frac{\gamma_2 e^{\gamma_1 z' - \gamma_2 z}}{k_1^2\gamma_2 + k_2^2\gamma_1} J_0'(\lambda\rho)\lambda^2\, d\lambda \tag{5-7a}$$

$$E^V_{z12} = \frac{-j\omega\mu_0}{4\pi}\, 2\int_0^\infty \frac{e^{\gamma_1 z' - \gamma_2 z}}{k_1^2\gamma_2 + k_2^2\gamma_1} J_0(\lambda\rho)\lambda^3\, d\lambda \tag{5-7b}$$

$$E^H_{\rho 12} = \frac{-j\omega\mu_0}{4\pi}\left(2\int_0^\infty \frac{e^{\gamma_1 z' - \gamma_2 z}}{k_1^2\gamma_2 + k_2^2\gamma_1} J_0''(\lambda\rho)\lambda^3\, d\lambda + U_{12}\right) \tag{5-7c}$$

$$E^H_{\phi 12} = \frac{j\omega\mu_0}{4\pi}\left(\frac{2}{\rho}\int_0^\infty \frac{e^{\gamma_1 z' - \gamma_2 z}}{k_1^2\gamma_2 + k_2^2\gamma_1} J_0'(\lambda\rho)\lambda^2\, d\lambda + U_{12}\right) \tag{5-7d}$$

$$E^H_{z12} = \frac{j\omega\mu_0}{4\pi}\, 2\int_0^\infty \frac{\gamma_1 e^{\gamma_1 z' - \gamma_2 z}}{k_1^2\gamma_2 + k_2^2\gamma_1} J_0'(\lambda\rho)\lambda^2\, d\lambda \tag{5-7e}$$

which are evaluated by numerical integration. Similar equations result with the integrals (5-5) and (5-6).

### 5.1.2 Numerical evaluation of the Sommerfeld Integrals

The Sommerfeld Integrals in (5-7) cannot be evaluated in closed form. Various techniques have been used to obtain numerical or analytic approximations of these integrals,

including numerical integration, asymptotic techniques and quasistatic approximations. Of these, only numerical evaluation has been able to provide values with high accuracy for separations of source and evaluation points on the order of a wavelength and for a wide range of ground parameters.

A number of approaches have been tried for numerically evaluating the integrals. Siegel and King [38] integrated along the real $\lambda$ axis and Bubenik [39] applied Shanks algorithm to accelerate the convergence of the oscillating integrand. Johnson and Dudley [40] used a transformation of the integration variable to make the real-axis integration easier. Johnson's work was done as part of the development of NEC–3, and has been used to validate the NEC algorithms.

While integration on the real $\lambda$ axis offers the advantages of a real argument and easily determined zeros of the Bessel function, many of the troublesome features of the integrand can be avoided by deforming the integration contour into the complex $\lambda$ plane. Lytle and Lager [41] integrated along contours suggested by the form of the steepest-descent contours for the integrands. Parhami *et al.* [42] integrated on the actual steepest-descent contours with source and evaluation points on the same side of the interface. Numerical integration on the steepest-descent contour is a very efficient way of evaluating the integrals when the separation of source and evaluation points is large, since the integrand converges rapidly with minimum oscillation. However, when the separation is on the order of a wavelength, little is gained by following the steepest-descent contour in the vicinity of the origin, and more benefit may be gained by staying away from the pole near $k_2$. Also, when source and evaluation points are on opposite sides of the interface it is much more difficult to determine the saddle points and steepest descent paths.

An alternate integral form, known as the exact image method, has been obtained by Lindell [43] which is more easily evaluated numerically than (5-3) in some cases. In addition, linear filtering techniques have been applied in evaluating the integrals [44].

In NEC, the Sommerfeld integrals are evaluated by numerical integration along contours chosen to obtain rapid exponential convergence of the integrand. The basic technique is that used by Lytle and Lager [41], with some refinements to the contours. Since the integrands of $V_{12}$ and $U_{12}$ and the derivatives of $V_{12}$ in (5-7) have similar properties over the complex $\lambda$ plane, the integral (5-3) will be considered as typical. The integrands have branch points at $\pm k_1$ and $\pm k_2$ due to the square roots in $\gamma_1$ and $\gamma_2$. The branch cuts will be chosen to be vertical, as shown in Fig. 5-2. The implications of this choice of branch cuts and the choice of Riemann sheets are discussed in [41].

The key to rapid convergence in the numerical integration is to exploit the exponential decay of the exponential and Bessel functions for large $\lambda$. The integration contour is deformed from the real axis into the complex plane, without crossing branch cuts or the pole, to optimize convergence. The contour used with the integrals in the form of (5-3) is shown in Fig. 5-2. The dominant factor for convergence in this case is the exponential function as $\lambda_R$ increases. The Bessel function oscillates with slow convergence for increasing $\lambda_R$ and grows exponentially as $|\lambda_I|$ increases. Hence it is of little help in convergence but restricts

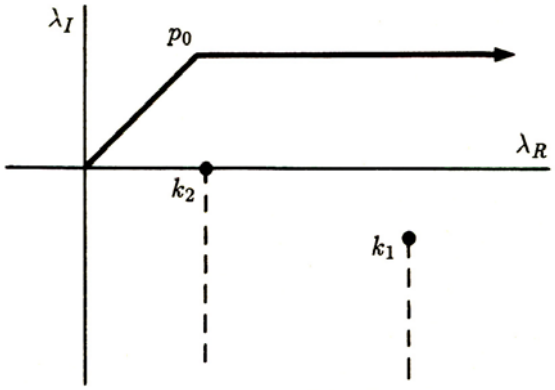


**Fig. 5-2** Contour for evaluation of the Bessel function form of the Sommerfeld integrals.

the contour to small $\rho|\lambda_I|$. The contour off of the real axis avoids the rapid oscillation and possible spike in the integrand in the region of $k_2$. The break in the contour was chosen at $p_0 = (1+j)\min[1/\rho,\ 1/(|z|+|z'|)]$.

When $(|z|+|z'|)/\rho$ is small, excessive oscillation can be encountered before convergence on the contour of Fig. 5-2. It is then easier to evaluate the integrals in the form of (5-5). This integral can be written as

$$V_{12} = \int_{-\infty}^{\infty} G(\lambda) e^{-F(\lambda)}\, d\lambda \tag{5-8}$$

where

$$G(\lambda) = \frac{\lambda H_0^{(2)}(\lambda\rho) e^{j\lambda\rho}}{k_1^2\gamma_2 + k_2^2\gamma_1}$$

and

$$F(\lambda) = \gamma_2 z - \gamma_1 z' + j\lambda\rho.$$

The function $G(\lambda)$ is relatively slowly varying, and the rapid oscillation is introduced by the exponential term. This behavior of the integrand is used in deriving asymptotic approximations for large $\rho$ and $z$ by the method of steepest descent. It also suggests an optimum contour for numerical integration. The steepest descent path passes through a saddle point, which is the solution of the equation

$$\frac{d}{d\lambda} F(\lambda) = 0$$

and follows a path on which the imaginary part of $F(\lambda)$ is constant. The exponential term in (5-8) provides rapid convergence without oscillation on the steepest descent path. A difficulty in using the steepest descent contour for numerical integration is that the saddle points and each point on the steepest descent contour must be found by iteration when source and evaluation points are on opposite sides of the interface. However, for small to moderate values of $\rho$, $z$ and $z'$, much of the contribution to the integral comes from regions where $|\lambda| \gg \max(|k_1|, |k_2|)$. In this case $F(\lambda)$ can be approximated as

$$F(\lambda) \approx \lambda[S_{\pm}(|z'|+|z|) + j\rho]$$

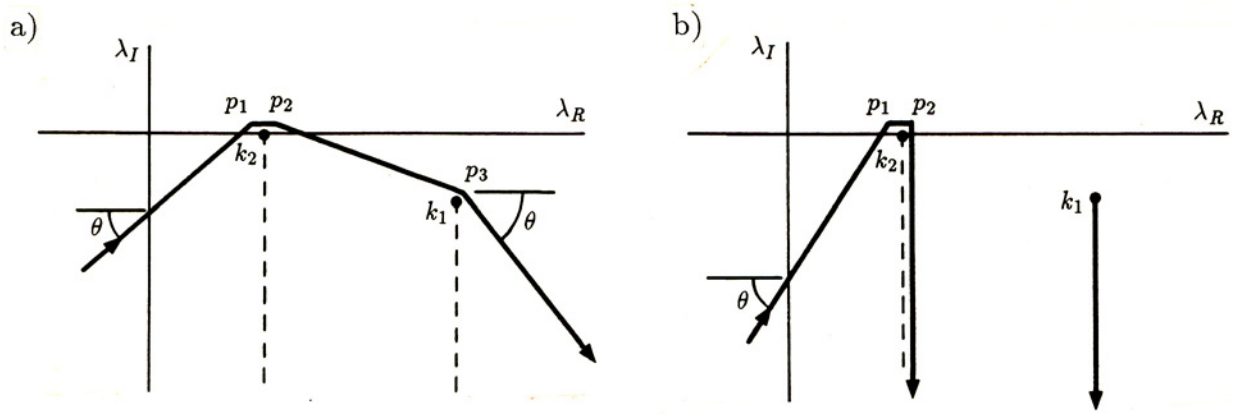


**Fig. 5-3** Contours for evaluation of the Hankel function form of the Sommerfeld integrals.

where, for $\mathrm{Im}(\lambda) < 0$

$$S_{\pm} = \begin{cases} 1 & \text{for } \mathrm{Re}(\lambda) > \max[\mathrm{Re}(k_1), \mathrm{Re}(k_2)] \\ -1 & \text{for } \mathrm{Re}(\lambda) < \min[\mathrm{Re}(k_1), \mathrm{Re}(k_2)]. \end{cases}$$

The asymptotic form of the steepest-descent contour, on which $\mathrm{Im}[F(\lambda)]$ is constant, is then approximated by the condition

$$\frac{\mathrm{Im}(\lambda)}{\mathrm{Re}(\lambda)} = -S_{\pm}\frac{\rho}{|z| + |z'|}.$$

The basic contour used with the Hankel function form of the integrals is shown in Fig. 5-3a, where

$$\theta = \tan^{-1}\left(\frac{\rho}{|z| + |z'|}\right).$$

The break points were determined by trial to reduce computation time. The points $p_1$ and $p_2$ are chosen to avoid the rapid variations of the integrand in the region of $k_2$ without excessively increasing the contour length. The values depend on the separation of source and evaluation points $R = [\rho^2 + (|z| + |z'|)^2]^{1/2}$, since this parameter influences the cost of increasing the contour length. The values used are

$$\begin{aligned} p_1 &= k_2 + (-1 + j)D_{\min} \\ p_2 &= k_2 + (1 + j)D_{\min} \end{aligned}$$

where

$$D_{\min} = k_2 \min\left[\left(\frac{0.06}{k_2 R} + 0.04\right),\ \frac{0.8}{1 + (z - z')/\rho}\right]$$

However, $\mathrm{Re}(p_2)$ is not allowed to be greater than $\mathrm{Re}(k_1 + k_2)/2$. The point $p_3$ is chosen as

$$p_3 = \max[1.01\mathrm{Re}(k_1),\ 1.2\mathrm{Re}(k_2)] + j0.95\mathrm{Im}(k_1)$$

to just miss $k_1$ but maintain a minimum distance from $k_2$. When $R$ is large, $|z| + |z'|$ is small and $\mathrm{Im}(k_1)/\mathrm{Re}(k_1)$ is small the contour in Fig. 5-3b is used to avoid oscillations on the

path from $p_2$ to $p_3$. In the numerical evaluation of the branch cut integral, the integration variable is changed to $s$ where $\lambda = k_1 + js^2$ to remove the infinite derivative with respect to $\lambda$ at $\lambda = k_1$.

The integration along these contours is accomplished with an adaptive interval-width Romberg integration routine [45] which evaluates three- and five-point Romberg quadrature formulas, and cuts or expands the interval size according to an estimate of the error. The contour in Fig. 5-2 is used for $(|z| + |z'|) > 0.5\rho$ and the contours in Fig. 5-3 are used with the Hankel-function form of the integrals for smaller $|z| + |z'|$. The algorithm in NEC can be used with $\rho = 0$ or $|z| + |z'| = 0$ and for $R$ approximately in the range $10^{-5} < k_2 R < 200$. The limitation for small $R$ is due to the changes in the integrand near the origin, relative to the large convergence distance, and the limitation for large $R$ is due to oscillations in the integrand as a result of not following the exact steepest-descent contour. The accuracy has been checked by comparing with independent numerical results from [40] and with series approximations for small $R$.

### 5.1.3 Table-Lookup and Interpolation Techniques

When the Sommerfeld solution for a point source near ground is used in a moment-method code the double integration, over the current distributions and over $\lambda$, can lead to excessive computation time that severely limits the size of structures that can be modeled. To reduce the computation time in NEC, the field near ground is evaluated by interpolation in tables generated in advance by an auxiliary program that evaluates the Sommerfeld integrals. This table-lookup approach must cover the range of separations of source and evaluation points from essentially zero to the range at which asymptotic approximations become accurate. Two different techniques were used to cover this range in NEC-3 and 4. For small separations of source and evaluation points the singular component of the field is subtracted in an analytic form, and linear interpolation is used on the remainder. At larger separations, the most rapid spatial variation in the field is due to the phase change. The phase functions can have a complex form, represented asymptotically by propagation along two separate ray paths. For these larger distances, NEC uses an interpolation algorithm in which functions suggested by the asymptotic approximations to the field are fit to numerically computed field values. This approach, which can be considered a form of model-based parameter estimation, requires substantially fewer field evaluations than would polynomial interpolation.

The linear interpolation technique in NEC–3 and 4 is similar to that in NEC–2. However, since NEC–2 was limited to source and evaluation points above ground, the field depended on only two parameters: the sum of the distances of the points from the interface and their radial separation. The field transmitted across the interface depends on the individual distances of the points from the interface, so a three-parameter interpolation is needed. As in NEC–2, the singular terms are subtracted from the field in analytic form. This step offers two advantages. The remainder functions to be interpolated remain smooth as the separation $R$ goes to zero, so that the point $\rho = z = z' = 0$ can be included in a table with uniform increments. Also, the integrals of the $R^{-2}$ and $R^{-3}$ terms, which have the same form as in the free-space field, can be evaluated with high accuracy using the equations from

section 4. The accurate evaluation of these singular terms makes it possible to model wires very close to the interface. The remainders from the field components after subtracting the singularities are

$$E''^V_{\rho 12} = E^V_{\rho 12} - S^V_{\rho 12} - S'^V_{\rho 12} \tag{5-9a}$$
$$E''^V_{z 12} = E^V_{z 12} - S^V_{z 12} - S'^V_{z 12} \tag{5-9b}$$
$$E''^H_{\rho 12} = E^H_{\rho 12} - S^H_{\rho 12} - S'^H_{\rho 12} \tag{5-9c}$$
$$E''^H_{\phi 12} = E^H_{\phi 12} - S^H_{\phi 12} - S'^H_{\phi 12} \tag{5-9d}$$
$$E''^H_{z 12} = E^H_{z 12} - S^H_{z 12} - S'^H_{z 12} \tag{5-9e}$$

where the $R^{-2}$ and $R^{-3}$ singularities in the fields are canceled by the terms

$$S^V_{\rho 12} = \frac{-j\omega\mu_0}{4\pi}\frac{2}{k_1^2+k_2^2}\left[\rho(z-z')\left(\frac{3}{R^2}+j\frac{3k_2}{R}-k_2^2\right)\right]\frac{e^{-jk_2R}}{R^3}$$
$$S^V_{z 12} = \frac{-j\omega\mu_0}{4\pi}\frac{2}{k_1^2+k_2^2}\left[(z-z')^2\left(\frac{3}{R^2}+j\frac{3k_2}{R}-k_2^2\right)-1-jk_2R+k_2^2R^2\right]\frac{e^{-jk_2R}}{R^3}$$
$$S^H_{\rho 12} = \frac{-j\omega\mu_0}{4\pi}\frac{2}{k_1^2+k_2^2}\left[\rho^2\left(\frac{3}{R^2}+j\frac{3k_2}{R}-k_2^2\right)-1-jk_2R\right]\frac{e^{-jk_2R}}{R^3}$$
$$S^H_{z 12} = \frac{-j\omega\mu_0}{4\pi}\frac{2}{k_1^2+k_2^2}(1+jk_2R)\frac{e^{-jk_2R}}{R^3}$$
$$S^H_{\phi 12} = \frac{-j\omega\mu_0}{4\pi}\frac{2}{k_1^2+k_2^2}\left[\rho(z-z')\left(\frac{3}{R^2}+j\frac{3k_2}{R}-k_2^2\right)\right]\frac{e^{-jk_2R}}{R^3}$$

which have the form of the free-space fields. The remaining $R^{-1}$ singularities are canceled by subtracting the terms

$$S'^V_{\rho 12} = \frac{-j\omega\mu_0}{4\pi}\left[C_2\frac{1-\sin\theta}{\cos\theta}-C_1\frac{z'\cos\theta}{R}\right]\frac{e^{-jk_2R}}{R}$$
$$S'^V_{z 12} = \frac{-j\omega\mu_0}{4\pi}\left[C_2-C_1\frac{z'\sin\theta}{R}\right]\frac{e^{-jk_2R}}{R}$$
$$S'^H_{\rho 12} = \frac{-j\omega\mu_0}{4\pi}\left[C_2\left(\frac{\sin^2\theta-\sin\theta}{\cos^2\theta}\right)+C_1\frac{z'}{R}\left(\sin\theta-\frac{1-\sin\theta}{\cos^2\theta}\right)+1\right]\frac{e^{-jk_2R}}{R}$$
$$S'^H_{\phi 12} = \frac{j\omega\mu_0}{4\pi}\left[-C_2\frac{1-\sin\theta}{\cos^2\theta}+C_1\frac{z'(1-\sin\theta)}{R\cos^2\theta}+1\right]\frac{e^{-jk_2R}}{R}$$
$$S'^H_{z 12} = \frac{j\omega\mu_0}{4\pi}\left[\frac{k_1^2C_2}{k_2^2}\frac{(1-\sin\theta)}{\cos\theta}+C_1\frac{z'\cos\theta}{R}\right]\frac{e^{-jk_2R}}{R}$$

with $R=[\rho^2+(z-z')^2]^{1/2}$, $\sin\theta=(z-z')/R$ and

$$C_1=\frac{k_1^2-k_2^2}{k_1^2+k_2^2},\qquad C_2=k_2^2\frac{k_1^2-k_2^2}{(k_1^2+k_2^2)^2}.$$

When $k_2R$ is sufficiently small, the subtraction is done in the integrands of the Sommerfeld integrals, as shown in Appendix H, to avoid loss of precision. When $|k_1R|$ is not small the subtraction should not be done, since the subtracted terms do not include the attenuation through the earth, and precision may be lost by subtracting and adding the much larger terms.

In NEC–2 only the $R^{-2}$ and $R^{-3}$ components of the field were subtracted and the remainder was multiplied by $R$ to get a finite value at $R = 0$. When this is done, the limit as $R$ goes to zero depends on the ratio of $(z + z')$ to $\rho$. In NEC–2, the interpolation was done in $R$ and $\theta$ coordinates so that a limit could be defined at $R = 0$. For the field crossing the interface it is difficult to choose a set of three parameters such that the limit for $R \to 0$ can be defined, the parameters range between constant limits and the tables with different interval sizes can be fitted together. Hence the added complexity of subtracting the $R^{-1}$ terms was necessary. The remainder is multiplied by $R$ so that the value is zero at $R = 0$.

The interpolation space in $\rho$, $z$ and $z'$ is divided into three regions for increasing depth of the source. The ranges of $z'$ for these tables are $0 < |z'| \le 0.4L_g$ in table 1, $0.4L_g \le |z'| \le L_g$ in table 2 and $L_g \le |z'| \le L_{\max}$ in table 3, where $L_g = \min(|k_2/k_1|, 0.3)\lambda_0$ and $L_{\max} = \min(15|k_2/k_1|, 1.)\lambda_0$. The limits of $\rho$ and $z$ in each table are $0 \le \rho \le L_G$ and $0 \le z \le L_G$. Before being stored in the tables, the field values are divided by functions to reduce the variations and make interpolation easier. For table 1 the singular components are subtracted during evaluation, leaving a remainder that is finite as $R$ approaches zero, but subtraction is not done in the other tables. The values are then multiplied by

$$\begin{aligned} F_1 =& Re^{jk_2R} \\ F_2 =& R^2 e^{j[k_2(\rho^2+z^2)^{1/2}+k_1|z'|]} \\ F_3 =& R^2 e^{j[k_2 z+k_1(\rho^2+z'^2)^{1/2}]} \end{aligned}$$

for tables 1, 2 and 3, respectively, to reduce the phase variation and improve the accuracy of the interpolation. These transformations are reversed after the values have been obtained from the tables by interpolation.

The transformed field values are then stored in tables, and the values needed are obtained by linear interpolation, using the formula

$$\begin{aligned} \tilde{f}(\rho, z, z') =& \frac{1}{(\rho_i - \rho_j)(z_k - z_\ell)(z'_m - z'_n)} \Big[ (\rho - \rho_j)(z - z_\ell)(z' - z'_n) f_{ikm} \\ &+ (\rho - \rho_j)(z - z_\ell)(z'_m - z') f_{ikn} + (\rho - \rho_j)(z_k - z)(z' - z'_n) f_{i\ell m} \\ &+ (\rho - \rho_j)(z_k - z)(z'_m - z') f_{i\ell n} + (\rho_i - \rho)(z - z_\ell)(z' - z'_n) f_{jkm} \\ &+ (\rho_i - \rho)(z - z_\ell)(z'_m - z') f_{jkn} + (\rho_i - \rho)(z_k - z)(z' - z'_n) f_{j\ell m} \\ &+ (\rho_i - \rho)(z_k - z)(z'_m - z') f_{j\ell n} \Big] \end{aligned}$$

where $\rho_i \le \rho \le \rho_j$, $z_k \le z \le z_\ell$ and $z'_m \le z' \le z'_n$ and $f_{ikm} = f(\rho_i, z_k, z'_m)$. If the singular terms have been subtracted, the $S'$ components are added to the interpolated values, and the

result is integrated over the current distribution using adaptive Romberg quadrature [45]. The integrals of the singular $S$ terms are evaluated using the free-space field algorithms, since these terms have the form of the free space field.

In NEC–2, cubic interpolation is used in the two-parameter tables. This could give better accuracy than the linear interpolation in NEC–3, or alternately allow larger parameter increments. However, a three-dimensional cubic interpolation was not used to minimize complexity and evaluation time.

*Interpolation Using Model-Based Parameter Estimation*

For larger separations of source and evaluation points than are used in the linear interpolation tables, particularly larger values of $\rho$, the phase variation cannot effectively be suppressed by dividing by a simple factor, since the phase has a more complex form. In asymptotic approximations the field is represented by two rays, one reaching the interface at an angle less than the totally reflecting angle and diffracting into the upper half-space, and the other reaching the interface at an angle greater than the totally reflecting angle and producing an evanescent field above the interface and a reflected wave in the ground. This asymptotic solution suggests the forms for functions that can be used in a model-based interpolation procedure, in which functions chosen on physical or mathematical grounds to be close to the expected field behavior are fit to computed field samples. If suitable model-based interpolation functions can be found, the number of stored data values can be greatly reduced from that needed with simple polynomial interpolation.

In the asymptotic model, the rays have phase factors of the form

$$\begin{aligned} P_1(\rho, z, z') =& e^{-F(\lambda_1)} \\ P_2(\rho, z, z') =& e^{-F(\lambda_2)} \end{aligned}$$

where

$$F(\lambda) = (\lambda^2 - k_2^2)^{1/2} z - (\lambda^2 - k_1^2)^{1/2} z' + j\lambda\rho$$

and $\lambda_1$ and $\lambda_2$ are saddle points of the integrand, which are solutions of the equation $F'(\lambda) = 0$ for the particular values of $\rho$, $z$ and $z'$. The solutions are chosen so that $\mathrm{Re}(\lambda_1) \leq \mathrm{Re}(k_2)$ and $\mathrm{Re}(k_2) < \mathrm{Re}(\lambda_2) \leq \mathrm{Re}(k_1)$. In addition, the field will involve spreading factors, such as $R_1^{-n}$ with $P_1$ and $R_2^{-n}$ with $P_2$, which can be approximated as

$$\begin{aligned} R_1 =& [\rho^2 + (z - |k_2/k_1| z')^2]^{1/2} \\ R_2 =& [\rho^2 + z'^2]^{1/2} \end{aligned}$$

and angle factors such as $z/R$, $z'/R$, $\rho/R$, etc. The field may then be approximated by a sum of functions

$$\tilde{E}(\rho, z, z') = \sum_{n=1}^{N_f} A_n f_n(\rho, z, z')$$

where each $f_n$ is a product of a phase factor, a spreading factor and an angle factor. The coefficients $A_n$ are determined by fitting $\tilde{E}$ to values of the field determined by numerical

evaluation of the Sommerfeld integrals at $N_f$ or more points over $\rho$, $z$ and $z'$. In NEC, the number of samples exceeds $N_f$. The over-determined system of equations is then solved by the method of Q-R decomposition [46]. The resulting $\tilde{E}$ represents a least-squares fit to the computed field values. With the constants $A_n$ determined in this way, $\tilde{E}$ can be used to interpolate or extrapolate from the computed points that were fit. If the $f_n$ are good approximations to the field behavior, then considerably fewer computed values should be needed for a given accuracy than with polynomial interpolation.

In NEC–3 and 4, this least-squares approximation technique is used with the sum of functions

$$\begin{aligned}\tilde{E}(\rho,z,z') = &\sum_{\ell=1}^{3}\sum_{m=0}^{3}\sum_{n=0}^{2} A_{\ell mn} R_1^{-\ell}\left(\frac{z}{R_1}\right)^m\left(\frac{z'}{R_1}\right)^n e^{-j(\beta_2 z-\beta_1 z'+\lambda_1\rho)} \\ &+\sum_{\ell=1}^{8} B_\ell F_\ell(\rho,z,z') \end{aligned} \tag{5-10}$$

where

$$\begin{aligned}F_1(\rho,z,z') =& R_1^{-1}\left(\frac{\rho}{R_1}\right)\left(\frac{z'}{R_1}\right)e^{-j(\beta_3 z+k_1 R_2)^{1/2}} \\ F_2(\rho,z,z') =& R_1^{-1}\left(\frac{\rho}{R_1}\right)\left(\frac{z'}{R_1}\right)^2 e^{-j(\beta_3 z+k_1 R_2)^{1/2}} \\ F_3(\rho,z,z') =& R_1^{-1}R_2^{-1}\left(\frac{\rho}{R_1}\right)e^{-j(\beta_3 z+k_1 R_2)^{1/2}} \\ F_4(\rho,z,z') =& R_1^{-1}R_2^{-1}\left(\frac{\rho}{R_1}\right)\left(\frac{z'}{R_1}\right)e^{-j(\beta_3 z+k_1 R_2)^{1/2}} \\ F_5(\rho,z,z') =& F_1(\rho,z,z')\left(\frac{z}{R_1}\right) \\ F_6(\rho,z,z') =& F_2(\rho,z,z')\left(\frac{z}{R_1}\right) \\ F_7(\rho,z,z') =& F_3(\rho,z,z')\left(\frac{z}{R_1}\right) \\ F_8(\rho,z,z') =& F_4(\rho,z,z')\left(\frac{z}{R_1}\right)\end{aligned}$$

with $\beta_1 = (k_1^2-\lambda_1)^{1/2}$, $\beta_2 = (k_2^2-\lambda_1)^{1/2}$ and $\beta_3 = (k_2^2-\lambda_2^2)^{1/2}$. The saddle point $\lambda_1$ is found by solving the equation $F'(\lambda_1) = 0$ for the solution between 0 and $k_2$, while for $\lambda_2$ the approximate solution $\lambda_2 = k_1\rho/(\rho^2+z'^2)^{1/2}$ is used. An additional factor of $\rho/R_1$ is included in all terms of (5-10) for fitting the field components $E_\rho^V$ and $E_z^H$. Also, a factor of $\rho/R_1$ is included in the coefficients of $A_{1,m,n}$ for fitting $E_z^V$. These forms were determined by studying the interpolation errors in using (5-10) while varying the spacing of the field samples.

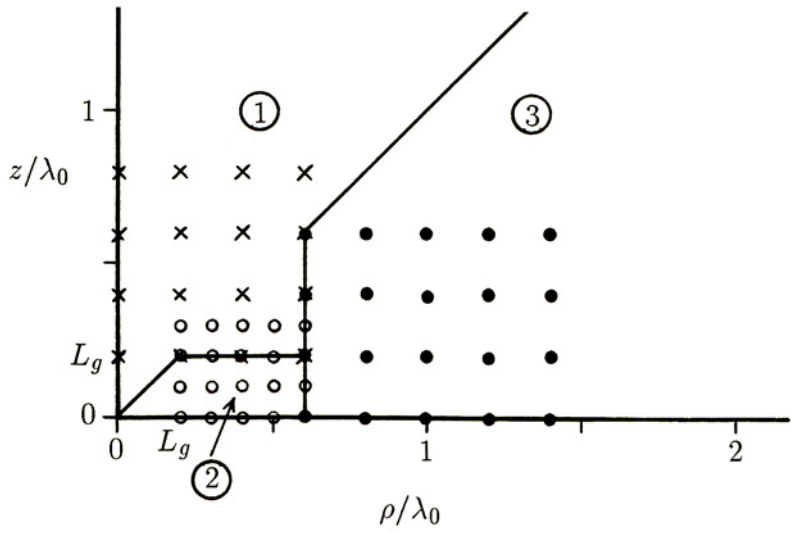


**Fig. 5-4** The three subregions used in the least-squares approximation. The sample points in $\rho$ and $z$ are shown for each subregion.

In the present code, this least squares approximation is used from the outer boundary of the interpolation region out to $3\lambda_0$ in $\rho$, $2\lambda_0$ in $z$ and to a source depth of $|z'| = 0.8L_g$, where $L_g = \min(|k_2/k_1|, 0.3)\lambda_0$. This region is divided into three subregions as shown in Fig. 5-4. The field sample points used in determining the constants in (5-10) in each subregion are given in the following table, and some of these points are indicated in Fig. 5-4. An additional set of samples near the interface, with small spacing in $\rho$, is included for subregions 2 and 3 to sample the wave traveling mainly through the ground. This wave is not significant in region 1, and the functions $F_\ell$ in (5-10) are dropped for this region.

The functional approximation using (5-10) over subregion 3 for a dielectric ground is shown in Fig. 5-5. Both the low frequency ($P_1$) and high frequency ($P_2$) components are present and are matched by the approximation. As can be seen, this method is effective for extrapolation as well as interpolation.

**Table 1.** Ranges of sample points used in determining the coefficients in equation (5-10) to approximate the field over each of three subregions in the $\rho$, $z$, $z'$ space.

| | | General Samples | | | Surface Samples | | |
|---|---|---|---|---|---|---|---|
| | Coord. | Start | $\Delta$ | $N$ | Start | $\Delta$ | $N$ |
| Region 1: | $\rho$ | 0. | 0.2 | 4 | | | 0 |
| | $z$ | $L_g$ | 0.2 | 4 | | | 0 |
| | $z'$ | 0. | $0.4L_g$ | 2 | | | 0 |
| Region 2: | $\rho$ | $L_g$ | to $\rho = 0.6$ | 5 | $L_g$ | $0.2L_g$ | 6 |
| | $z$ | 0. | $0.5L_g$ | 4 | 0. | $0.4L_g$ | 2 |
| | $z'$ | 0. | $0.4L_g$ | 2 | 0. | $0.5L_g$ | 3 |
| Region 3: | $\rho$ | 0.6 | 0.2 | 5 | 0.6 | $0.2L_g$ | 8 |
| | $z$ | 0. | 0.2 | 4 | 0. | $0.4L_g$ | 2 |
| | $z'$ | 0. | $0.4L_g$ | 2 | 0. | $0.5L_g$ | 3 |

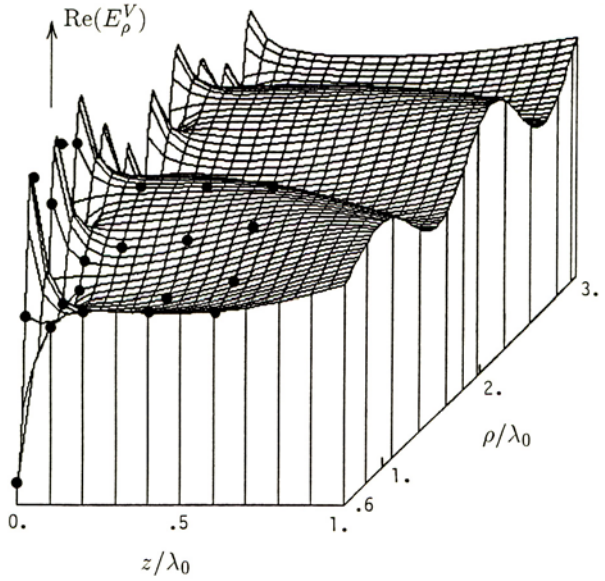


**Fig. 5-5** Field transmitted across the interface, $E_\rho^V$, with $\epsilon_1 = 16$, $\sigma_1 = 0$ S/m and source depth of $z' = 0.1\lambda_0$. A total of 88 points are fit (36 in the plane of this figure with visible ones shown) to cover the three-dimensional region $0.6 \leq \rho/\lambda_0 \leq 3.0$, $0 \leq z/\lambda_0 \leq 2.0$ and $0 \leq |z'|/\lambda_0 \leq 0.25$ with less than 4 percent error.

## 5.2 Asymptotic Approximations for the Field over Ground

When the separation of source and evaluation points is greater than about a wavelength, asymptotic approximations for the Sommerfeld integrals become practical. With higher-order terms these approximations can yield good accuracy for separations as small as half a wavelength for some parameter ranges. The resulting formulas for arbitrary location of source and evaluation points are not simple. The evaluation times for general asymptotic approximations are substantially less than for numerical evaluation of the integrals, but greater than the time for evaluation by table-lookup and interpolation. The asymptotic approximations become more accurate with larger separations of source and evaluation points, and hence can be used over the large region of space, out to infinity, that could not be covered with lookup tables.

Asymptotic approximations for the Sommerfeld integrals are obtained by the method of saddle-point integration on the steepest descent path. Uniformly valid approximations for all locations of source and receiver have not been attempted here, due to the difficulties introduced by branch points and poles in the integrand. A uniform approximation for source and evaluation points approaching the interface is developed, using the modified saddle-point method to account for the pole. For small radial separations of source and receiver the higher order approximations fail, but the first-order forms remain valid. Correction terms to improve the accuracy of the first-order approximations for small $\rho$ are obtained by interpolation when possible.

### 5.2.1 The Steepest-Descent Method

For asymptotic evaluation of the field we will consider the case of a buried source at $z'$ ($z' < 0$) and an elevated receiver at $z$ as shown in Fig. 5-1, and it will be assumed that $\mathrm{Re}(k_1) > \mathrm{Re}(k_2)$. Fields for other positions of source and receiver can be obtained through the formulas in Appendix G. The Sommerfeld integrals have the general form

$$S(\rho, z, z') = \int_{-\infty}^{\infty} T(\lambda) H_0^{(2)}(\lambda\rho) e^{\gamma_1 z' - \gamma_2 z}\, d\lambda \tag{5-11}$$

where $\gamma_1 = (\lambda^2 - k_1^2)^{1/2}$, $\gamma_2 = (\lambda^2 - k_2^2)^{1/2}$ and the contour of integration is along the real axis; just below the axis for $\lambda \leq 0$ and just above the axis for $\lambda > 0$. Assuming that $\rho$ is sufficiently large that $|\lambda\rho| \gg 1$ for values of $\lambda$ making a significant contribution to the integral, the Hankel function in (5-11) can be replaced by its large-argument asymptotic form

$$H_0^{(2)}(\lambda\rho) \sim \left(\frac{2j}{\pi\lambda\rho}\right)^{1/2} e^{-j\lambda\rho} \tag{5-12}$$

which yields

$$S(\rho, z, z') \approx \left(\frac{2j}{\pi\rho}\right)^{1/2} \int_{-\infty}^{\infty} \lambda^{-1/2} T(\lambda) e^{\gamma_1 z' - \gamma_2 z - j\lambda\rho}\, d\lambda.$$

This integral has the form

$$I = \int_{-\infty}^{\infty} G(\lambda) e^{-F(\lambda)}\, d\lambda \tag{5-13}$$

which is a standard form for evaluation by the steepest descent technique.

The procedure of steepest-descent evaluation of an integral is described in many textbooks. The discussions in [47] and [48] address the problem of evaluating the field near an interface. The basic procedure is to find a solution for $\lambda_s$ such that $F'(\lambda_s) = 0$. The point $\lambda_s$ is then a saddle point or minimax point of $F$. For example, there will be a path through $\lambda_s$ along which the real part of $F$ is a minimum and increases most rapidly away from $\lambda_s$. Normal to this direction of maximum increase $\mathrm{Re}(F)$ will decrease most rapidly away from $\lambda_s$. Due to the properties of analytic functions, $\mathrm{Im}(F)$ is constant along the paths on which $\mathrm{Re}(F)$ increases or decreases most rapidly. Hence the direction of most rapid increase in $\mathrm{Re}(F)$, with $\mathrm{Im}(F)$ constant, is an optimum path for evaluating the integral in (5-13), since the exponential will decrease rapidly away from $\lambda_s$, without oscillation. The objective is then to deform the original integration path to pass through $\lambda_s$ along the steepest descent path (SDP) of the exponential, taking proper account of any singular points encountered during the deformation.

When $F'(\lambda_s) = 0$ and $F''(\lambda_s) \neq 0$, an asymptotic expansion for the integral can be developed by making a transformation for the integration variable such that

$$F(\lambda) = F(\lambda_s) + s^2. \tag{5-14}$$

The integral (5-13) then becomes

$$I = e^{-F(\lambda_s)} \int_{-\infty}^{\infty} g(s) e^{-s^2}\, ds \tag{5-15}$$

where

$$g(s) = G(\lambda)\frac{d\lambda}{ds}.$$

The SDP in the $s$-plane is the real axis, with the saddle point at $s = 0$. For a sufficiently large parameter in $F$, the exponential in (5-15) will decay to a small value over a region about $s = 0$ in which $g(s)$ is slowly varying.

An asymptotic expansion of the integral (5-15) is obtained by expanding $g(s)$, within a radius limited by possible singularities, as

$$g(s) = g(0) + g'(0)s + \frac{g''(0)}{2}s^2 + \cdots + \frac{g^{(n)}(0)}{n!}s^n + \cdots \tag{5-16}$$

and integrating term by term. The first-order approximation is

$$I \sim g(0)e^{-F(\lambda_s)}\int_{-\infty}^{\infty} e^{-s^2}\,ds = \sqrt{\pi}q(0)e^{-F(\lambda_s)}.$$

From (5-14), the quantity $d\lambda/ds$ occurring in $g(s)$ is

$$\frac{d\lambda}{ds} = \frac{2s}{F'(\lambda)}.$$

Applying L'Hôpital's rule to evaluate the limit as $s$ goes to zero yields

$$\left.\frac{d\lambda}{ds}\right|_{s=0} = \sqrt{\frac{2}{F''(\lambda_s)}}$$

with $\arg(\sqrt{\ })$ equal to the argument of $d\lambda$ on the SDP. Hence

$$g(0) = G(\lambda_s)\sqrt{\frac{2}{F''(\lambda_s)}}$$

and the first order approximation for $I$ is

$$I \sim \left(\frac{2\pi}{F_2}\right)^{1/2} e^{-F_0}G_0 \tag{5-17}$$

where

$$F_n = \left.\frac{d^n}{d\lambda^n}F(\lambda)\right|_{\lambda=\lambda_s} \qquad \text{and} \qquad G_n = \left.\frac{d^n}{d\lambda^n}G(\lambda)\right|_{\lambda=\lambda_s}.$$

### 5.2.2 Steepest-Descent Evaluation of the Sommerfeld Integrals

Evaluation of the Sommerfeld integrals in the form of (5-13) by the method of steepest descent is complicated by the presence of branch points, which occur in both $F(\lambda)$ and $G(\lambda)$, and poles in $G(\lambda)$ in the integral for $V_{12}$. For all field components, the function $F(\lambda)$ is

$$F(\lambda) = (\lambda^2 - k_2^2)^{1/2}z - (\lambda^2 - k_1^2)^{1/2}z' + j\lambda\rho.$$

Branch points are located at $\pm k_1$ and $\pm k_2$, so that $F(\lambda)$ is represented by a four-sheeted Riemann surface.

The saddle points are solutions of the equation

$$F'(\lambda_s) = \lambda_s(\lambda_s^2 - k_2^2)^{-1/2} z - \lambda_s(\lambda_s^2 - k_1^2)^{-1/2} z' + j\rho = 0. \tag{5-18}$$

The contribution to the field integral from the saddle point at $\lambda_s$ can be interpreted as a ray traveling at an angle from the normal of $\theta_1$ in the lower medium and $\theta_2$ in the upper medium, where $k_1 \sin\theta_1 = k_2 \sin\theta_2 = \lambda_s$. Solutions of (5-18) can easily be obtained in the special cases of $z' = 0$, for which

$$\lambda_s = k_2 \frac{\rho}{\sqrt{z^2 + \rho^2}} = k_2 \sin\theta_2$$

and $z = 0$, for which

$$\lambda_s = k_1 \frac{\rho}{\sqrt{z'^2 + \rho^2}} = k_1 \sin\theta_1.$$

In general, (5-18) may have two solutions on the principal Riemann sheet that may be found by solving a quartic algebraic equation in $\lambda_s^2$. It is usually more practical to find the solutions by numerical means, however. The procedure used in NEC is described in Appendix I.

Loci of the saddle points are plotted in Fig. 5-6 for a typical case, where the upper medium is free space and the lower medium has a complex relative permittivity of $16 - j16$. Some steepest descent paths through these saddle points are shown in Fig. 5-7. The SDP always passes through a saddle point in the region between 0 and $k_2$. It may then go to $+\infty$ on the principal sheet or cross onto a lower sheet at a branch cut. In the latter case, a SDP through the second saddle point is needed to get to $+\infty$ on the principal sheet. The saddle point between 0 and $k_2$ represents a ray leaving the ground at an angle less than the angle $\theta_c = \sin^{-1}(k_2/k_1)$ for total reflection at the interface, and traveling mostly through air. As $z$ goes to zero this saddle point approaches $k_2$, and the SDP closes into a branch-cut integral in the direction of steepest descent from $k_2$. The ray then represents a lateral wave when the source and receiver are in the lower medium. The saddle point beyond $k_2$ represents a ray that reaches the interface at an angle greater than $\theta_c$, and the field produced in the upper medium is exponentially attenuated for increasing $z$. As $z'$ goes to zero this saddle point approaches $k_1$ and the integration path closes to a branch cut. This is the lateral wave when the source and receiver are in the upper medium.

The branch points at $\pm k_1$ and $\pm k_2$ also occur in $G(\lambda)$. However, they are not a limitation in the series expansion of $g(s)$, since they are removed by the transformation in (5-14). A transformation $\lambda = k_2 \sin w$ or $\lambda = k_1 \sin w$ is sometimes made to explicitly remove a branch point. These transformations do not change the result of the steepest descent evaluation, but put the result in a form more readily interpreted in terms of rays.

For the Sommerfeld integrals involving $V_{12}$ the function $G(\lambda)$ has a pole in the region between $\lambda = 0$ and $k_2$ that approaches $k_2$ as $k_1/k_2$ becomes large. This pole is not crossed in deforming the integration contour to the SDP. However, the pole does affect the steepest

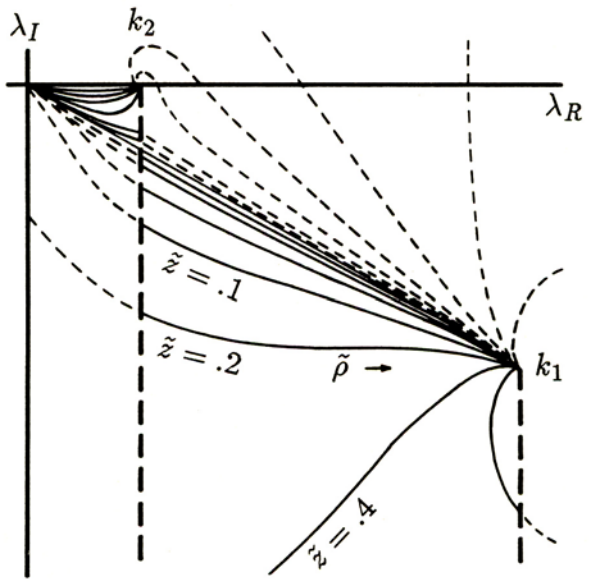


**Fig. 5-6** Saddle point loci for transmission across an interface, where $\tilde{z} = z/(z - z')$.

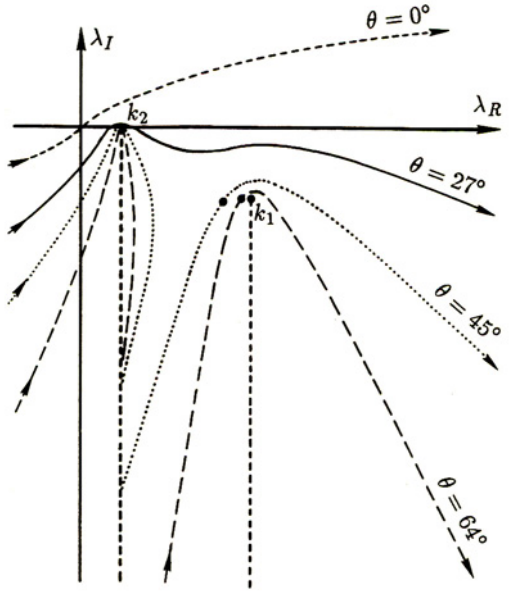


**Fig. 5-7** Steepest-descent paths for a source at height $z'$ in the ground and evaluation point at height $z$ in air with radial separation $\rho$, where $\tilde{z} = z/(z - z') = 0.33$ and $\theta = \tan^{-1}[\rho/(z - z')]$.

descent evaluation when $z$ and $z'$ are small, so that the saddle point is near to $k_2$. The contribution due to the pole is known as the surface wave.

The asymptotic evaluation used in NEC does not treat the general case of a function with two branch points and a pole. The contribution of the saddle point between 0 and $k_2$ is evaluated with second order terms, and including the effect of the pole. This wave is usually the dominant contribution to the field, and the evaluation yields accurate values down to the interface for $\rho$ as small as $\lambda/2$.

The saddle point associated with $k_1$ is assumed to be located at $\lambda_s = k_1\rho/\sqrt{\rho^2 + z'^2}$, so that the wave is assumed to propagate to a point on the interface directly below the receiver and then up to height $z$. This approximation for the saddle point is justified since the field attenuates exponentially with increasing $z$, and hence the contribution is negligible unless $z$ is small. The contribution from this saddle point is only evaluated to first order. Hence, the term vanishes as $z$ and $z'$ go to zero. In fact the field traveling in the lower medium does get smaller at grazing incidence than when $z'$ is nonzero, but it does not vanish. An asymptotic approximation including the waves above and below the interface and the pole contribution has been developed by King [49] for $z = 0$ and $|z'| \ll \rho$. King demonstrates the interference between the two waves when the loss tangent of the ground is small. A general extension of this approximation for nonzero $z$ and $z'$ would be difficult, however.

In summary, when the source and receiver are in the lower medium the asymptotic approximations in NEC will include direct, reflected and lateral waves, while for source and receiver on the interface or in the upper medium only the direct and reflected field with surface wave are included. This should be sufficient for most antenna applications, since the wave in the lower medium is usually strongly attenuated in a lossy ground. However, the approximation cannot be used when the lateral wave in the ground is needed, as for diagnostic purposes. Of course, all terms are included over short ranges where the Sommerfeld integrals are evaluated numerically.

The asymptotic evaluation also becomes difficult as the rays approach normal incidence. When $z = 0$ and $k_1$ and $k_2$ are real, the saddle point $\lambda_s = k_1\rho/\sqrt{\rho^2 + z'^2}$ approaches the branch point $k_2$, and coincides with it when $\rho/\sqrt{\rho^2 + z'^2} = \sin\theta_c = k_2/k_1$. The rays then merge in a caustic near $\theta_c$. Asymptotic approximations in this region are discussed in [48]. It is shown that the function $G(\lambda)$ in (5-13) cannot be treated as slowly varying at the saddle point, since the transmission or reflection coefficients have an infinite derivative at $\theta_c$. The asymptotic evaluation in [48], taking into account the rapid variation of the reflection coefficient near $\theta_c$, results in a modified saddle point, so that the reflected wave in the lower medium develops a lateral shift as it merges with the lateral wave. When the saddle points do not merge, the effectiveness of the steepest descent evaluation may still be reduced, since when $z$ and $\rho$ are small relative to $|z'|$ the function $F(\lambda)$ in (5-13) does not change significantly until $|\lambda|$ becomes greater than $|k_1|$. As a result, higher order terms in the asymptotic expansion may diverge until $|z'|$ becomes very large.

Another problem as $\rho$ becomes small is that the large argument approximation for the Hankel function can no longer be used. However, the first-order asymptotic approximation is valid to $\rho = 0$. This first-order result may be obtained from geometric optics, without restriction on $\rho$, as the product of a transmission coefficient and a divergence factor for the ray tube crossing the interface. Hence the first order approximation is used in NEC from angles somewhat greater than $\theta_c$ to $\theta = 0$. To improve the accuracy of this result, second order asymptotic terms are interpolated from an angle greater than $\theta_c$ to second order terms for $\rho = 0$ and added to the first order approximation. The interpolated second order terms improve accuracy for small $R$ when $z$ is not too small relative to $|z'|$, but cannot be used when $|z'|$ is large compared to $z$. Hence, only the first-order approximations are used when $z \ll |z - z'|$ and $\rho/\sqrt{\rho^2 + z'^2}$ is approaching or less than $\sin\theta_c$. The asymptotic

approximations used in NEC are derived below.

### 5.2.3 First-Order Asymptotic Evaluation of the Field

The derivation of first-order asymptotic approximations for the Sommerfeld integrals will be demonstrated for the function $V_{12}$ given by the integral

$$V_{12}(\rho, z, z') = \int_{-\infty}^{\infty} \frac{\lambda H_0^{(2)}(\lambda\rho)}{k_1^2\gamma_2 + k_2^2\gamma_1} e^{\gamma_1 z' - \gamma_2 z}\, d\lambda.$$

Substituting the large-argument form of the Hankel function from (5-12), this becomes

$$V_{12}(\rho, z, z') \approx \left(\frac{2j}{\pi\rho}\right)^{1/2} \int_{-\infty}^{\infty} \frac{\lambda^{1/2}}{k_1^2\gamma_2 + k_2^2\gamma_1} e^{\gamma_1 z' - \gamma_2 z - j\lambda\rho}\, d\lambda. \tag{5-19}$$

Equation (5-19) is then in the form of (5-13) with

$$G(\lambda) = \left(\frac{2j}{\pi\rho}\right)^{1/2} \frac{\lambda^{1/2}}{k_1^2\gamma_2 + k_2^2\gamma_1}$$

and

$$\begin{aligned} F(\lambda) &= (\lambda^2 - k_2^2)^{1/2} z - (\lambda^2 - k_1^2)^{1/2} z' + j\lambda\rho \\ F'(\lambda) &= \lambda(\lambda^2 - k_2^2)^{-1/2} z - \lambda(\lambda^2 - k_1^2)^{-1/2} z' + j\rho \\ F''(\lambda) &= -k_2^2(\lambda^2 - k_2^2)^{-3/2} z + k_1^2(\lambda^2 - k_1^2)^{-3/2} z'. \end{aligned}$$

From (5-17), the first-order approximation for $V_{12}$ is then

$$V_{12} \sim \frac{2e^{j\pi/4}\sqrt{\lambda_s/\rho}}{k_1^2\Gamma_2 + k_2^2\Gamma_1} \frac{e^{\Gamma_1 z' - \Gamma_2 z - j\lambda_s\rho}}{\left(k_1^2\Gamma_1^{-3} z' - k_2^2\Gamma_2^{-3} z\right)^{1/2}} \tag{5-20}$$

where $\Gamma_1 = (\lambda_s^2 - k_1^2)^{1/2}$ and $\Gamma_2 = (\lambda_s^2 - k_2^2)^{1/2}$ with $\lambda_s$ a saddle point obtained by solving (5-18). A term in (5-20) becomes indeterminate when $\rho$ goes to zero. However, the result does not blow up, since $\lambda_s$ also goes to zero in this case. Likewise, $\Gamma_1$ may go to zero with $z'$ and $\Gamma_2$ may go to zero with $z$. To avoid these indeterminate terms (5-20) will be written as

$$V_{12} \sim \frac{2e^{j\pi/4}}{k_1^2\Gamma_2 + k_2^2\Gamma_1}\Psi \tag{5-21}$$

where

$$\Psi = \frac{\Gamma_1\Gamma_2 e^{\Gamma_1 z' - \Gamma_2 z - j\lambda_s\rho}}{\sqrt{\frac{\rho}{\lambda_s}}\left(k_1^2\Gamma_2^2 z'/\Gamma_1 - k_2^2\Gamma_1^2 z/\Gamma_2\right)^{1/2}}. \tag{5-22}$$

The following formulas, obtained from equation (5-18), are then evaluated to avoid dividing by zero

$$\begin{aligned} \frac{z'}{\Gamma_1} &= \frac{z}{\Gamma_2} + j\frac{\rho}{\lambda_s} && \text{for} \quad \Gamma_1 \to 0 \\ \frac{z}{\Gamma_2} &= \frac{z'}{\Gamma_1} - j\frac{\rho}{\lambda_s} && \text{for} \quad \Gamma_2 \to 0 \\ \frac{\rho}{\lambda_s} &= j\left(\frac{z}{\Gamma_2} - \frac{z'}{\Gamma_1}\right) && \text{for} \quad \lambda_s \to 0. \end{aligned}$$

It is seen from (5-22) that the first order asymptotic approximation for $V_{12}$ is zero when either $\Gamma_1$ or $\Gamma_2$ is zero. Hence the result will go to zero at the grazing angle, with $z = z' = 0$. Higher order terms are needed to obtain a valid nonzero result in this case.

From the above result, the first order asymptotic approximations for the components of electric field are

$$E_\rho^V(\rho, z, z') \sim \frac{e^{j\pi/4}\omega\mu_0}{2\pi} \frac{\lambda_s \Gamma_2}{k_1^2\Gamma_2 + k_2^2\Gamma_1} \Psi \tag{5-23a}$$

$$E_z^V(\rho, z, z') \sim \frac{e^{-j\pi/4}\omega\mu_0}{2\pi} \frac{\lambda_s^2}{k_1^2\Gamma_2 + k_2^2\Gamma_1} \Psi \tag{5-23b}$$

$$E_\rho^H(\rho, z, z') \sim \frac{e^{-j\pi/4}\omega\mu_0}{2\pi} \left( \frac{-\lambda_s^2}{k_1^2\Gamma_2 + k_2^2\Gamma_1} + \frac{1}{\Gamma_1 + \Gamma_2} \right) \Psi \tag{5-23c}$$

$$E_\phi^H(\rho, z, z') \sim \frac{e^{-j\pi/4}\omega\mu_0}{2\pi} \left( \frac{j\lambda_s/\rho}{k_1^2\Gamma_2 + k_2^2\Gamma_1} - \frac{1}{\Gamma_1 + \Gamma_2} \right) \Psi \tag{5-23d}$$

$$E_z^H(\rho, z, z') \sim \frac{e^{j\pi/4}\omega\mu_0}{2\pi} \frac{\lambda_s \Gamma_1}{k_1^2\Gamma_2 + k_2^2\Gamma_1} \Psi. \tag{5-23e}$$

These equations are coded in subroutine GASY1.

### 5.2.4 Higher-Order and Uniform Approximations

Higher-order asymptotic approximations are found by retaining additional terms in the series (5-16) for $g(s)$. For integration from $-\infty$ to $\infty$ through a saddle point, the terms with odd powers of $s$ vanish. Hence the second-order approximation is obtained with the $s^2$ term. The explicit form in terms of $F$ and $G$ is given in [50], along with several higher order terms. From equations (6.2) and (5.20) in [50], the second-order approximation when $F'(\lambda_s) = 0$ and $F''(\lambda_s) \neq 0$ is

$$I \sim \left( \frac{2\pi}{F_2} \right)^{1/2} e^{-F_0} (Q_0 + Q_2) \tag{5-24}$$

where

$$Q_0 = G_0$$

$$Q_2 = \frac{1}{24F_2^3} \left[ G_0(5F_3^2 - 3F_2F_4) - 12G_1F_2F_3 + 12G_2F_2^2 \right].$$

Second-order approximations for the field components are given in Appendix J. These forms cannot be used for small $\rho$ due to the approximation of the Hankel function and other restrictions noted in Section 5.2.2.

Higher-order asymptotic approximations are also developed in Appendix J for the case $\rho = 0$, by integration on the SDP from the limit $\lambda = 0$. For coordinates ($\rho$, $z$, $z'$) with $0 < \rho < \sin\theta_A \sqrt{\rho^2 + (z - z')^2}$, where $\theta_A$ is somewhat greater than $\theta_c$, the first-order approximations are evaluated. Second-order terms are then interpolated from $\rho = 0$ and $\rho = \sin\theta_A \sqrt{\rho^2 + (z - z')^2}$ and added to the first-order result. This interpolation improves the accuracy when the limitation is the approximation of the Hankel function. It cannot

help when the saddle points merge or the convergence of the exponential is slow due to $\rho$ and $z$ being small relative to $|z'|$. In the latter cases only the first-order approximations are used in the code.

The steepest descent approximations converge slowly when $z$ and $|z'|$ are small relative to $\rho$ due to a pole in the integrand of $V_{12}$. When this occurs, the function $G(\lambda)$ cannot be considered slowly varying relative to the exponential, and the radius of convergence of the series (5-16) is limited to the distance between the saddle point and the pole. An asymptotic approximation taking correct account of the pole can be obtained by the modified saddle-point method, as described in [47] and other references.

In the modified saddle-point method, a singular term is subtracted from the integrand and evaluated separately. The integral (5-15) then becomes

$$I = e^{-F(\lambda_s)} \int_{-\infty}^{\infty} g(s) e^{-s^2}\, ds = e^{-F(\lambda_s)} \int_{-\infty}^{\infty} \left[ g(s) - \frac{a}{s-b} \right] e^{-s^2}\, ds + I_p \tag{5-25}$$

where

$$a = \lim_{s \to b} (s-b) g(s) = \lim_{\lambda \to \lambda_p} (\lambda - \lambda_p) G(\lambda)$$

and from (5-14)

$$b = \sqrt{F(\lambda_p) - F(\lambda_s)}.$$

The singularity is then isolated in the term

$$I_p = e^{-F(\lambda_s)} \int_{-\infty}^{\infty} \frac{a}{s-b} e^{-s^2}\, ds$$

which from equation 7.1.4 in [51] is evaluated as

$$I_p = \pm j\pi a e^{-F(\lambda_p)} \mathrm{erfc}(\mp jb) = \frac{\sqrt{\pi} a}{b} e^{-F(\lambda_s)} Q(\mp jb) \qquad \text{for } \mathrm{Im}(b) \gtrless 0$$

where erfc is the complementary error function

$$\mathrm{erfc}(z) = \frac{2}{\sqrt{\pi}} \int_z^{\infty} e^{-t^2}\, dt$$

and

$$Q(z) = -\sqrt{\pi} z e^{z^2} \mathrm{erfc}(z).$$

A uniform asymptotic expansion of $I$, including the contribution of the pole, can be obtained by adding $I_p$ to the steepest-descent approximation of the integral in (5-25) involving $g(s)$ with the pole removed. A more convenient procedure, used in evaluating diffraction integrals [52], is to use the steepest-descent evaluation with $g(s)$ containing the pole and add

$$\hat{I}_p = \frac{\sqrt{\pi} a}{b} e^{-F(\lambda_s)} [Q(\mp jb) - \hat{Q}(\mp jb)] \tag{5-26}$$

where $\hat{Q}(z)$ removes the asymptotic terms of $Q(z)$ of the order that are contained in the steepest-descent evaluation. The asymptotic expansion of $Q(z)$ is, from equation 7.1.23 in [51],

$$Q(z) \sim -1 - \sum_{m=1}^{\infty} (-1)^m \frac{1 \cdot 3 \ldots (2m-1)}{(2z^2)^m} \qquad |\arg z| < \frac{3\pi}{4}.$$

Thus for a first-order uniform approximation, $\hat{I}_p$ with $\hat{Q}(z) = -1$ is added to (5-17). For second-order, $\hat{I}_p$ with $\hat{Q}(z) = -1 + 1/(2z^2)$ is added to (5-24).

In the integral (5-19) for $V_{12}$ the pole at the zero of the denominator is located at

$$\lambda_p = \frac{k_1 k_2}{(k_1^2 + k_2^2)^{1/2}}$$

and

$$a = \lim_{\lambda \to \lambda_p} \left( \frac{2j}{\pi \rho} \right)^{1/2} \frac{(\lambda - \lambda_p)\lambda^{1/2}}{k_1^2 \gamma_2 + k_2^2 \gamma_1} = \left( \frac{2j}{\pi \rho} \right)^{1/2} \frac{j k_1^{3/2} k_2^{3/2}}{(k_2^4 - k_1^4)(k_1^2 + k_2^2)^{1/4}}.$$

For the first-order approximation, the pole contribution to $V_{12}$ is

$$V_{p12} = \frac{\sqrt{\pi} a}{b} e^{-F(\lambda_s)} [Q(jb) + 1]$$

where

$$b = \sqrt{F(\lambda_p) - F(\lambda_s)}.$$

$V_{p12}$ is then added to (5-21). The terms added to equations (5-23) to obtain a first-order uniform approximation for source and receiver approaching the interface are

$$E_{p\rho}^V = -\frac{j\omega\mu_0}{4\pi} \frac{\partial^2 V_{p12}}{\partial \rho \partial z} \approx -\frac{j\omega\mu_0}{4\pi} j\lambda_p (\lambda_p^2 - k_2^2)^{1/2} V_{p12} = -\frac{j\omega\mu_0}{4\pi} \frac{k_1 k_2^3}{k_1^2 + k_2^2} V_{p12} \quad \text{(5-27a)}$$

$$E_{pz}^V = -\frac{j\omega\mu_0}{4\pi} \left( \frac{\partial^2}{\partial z^2} + k_2^2 \right) V_{p12} \approx -\frac{j\omega\mu_0}{4\pi} \lambda_p^2 V_{p12} = -\frac{j\omega\mu_0}{4\pi} \frac{k_1^2 k_2^2}{k_1^2 + k_2^2} V_{p12} \quad \text{(5-27b)}$$

$$E_{p\rho}^H = -\frac{j\omega\mu_0}{4\pi} \frac{\partial^2 V_{p12}}{\partial \rho^2} \approx \frac{j\omega\mu_0}{4\pi} \lambda_p^2 V_{p12} = \frac{j\omega\mu_0}{4\pi} \frac{k_1^2 k_2^2}{k_1^2 + k_2^2} V_{p12} \quad \text{(5-27c)}$$

$$E_{p\phi}^H = \frac{j\omega\mu_0}{4\pi\rho} \frac{\partial V_{p12}}{\partial \rho} \approx \frac{-j\omega\mu_0}{4\pi\rho} j\lambda_p V_{p12} = \frac{\omega\mu_0}{4\pi\rho} \frac{k_1 k_2}{(k_1^2 + k_2^2)^{1/2}} V_{p12} \quad \text{(5-27d)}$$

$$E_{pz}^H = \frac{j\omega\mu_0}{4\pi} \frac{\partial^2 V_{p12}}{\partial \rho \partial z'} \approx \frac{-j\omega\mu_0}{4\pi} j\lambda_p (\lambda_p^2 - k_1^2)^{1/2} V_{p12} = \frac{j\omega\mu_0}{4\pi} \frac{k_1^3 k_2}{k_1^2 + k_2^2} V_{p12} \quad \text{(5-27e)}$$

The pole contribution added to the second-order approximation in Appendix J is

$$V_{p12} = \frac{\sqrt{\pi} a}{b} e^{-F(\lambda_s)} [Q(jb) + 1 + \frac{1}{2b^2}]$$

Since the second-order approximation of the Hankel function was used in the SDP evaluation, the terms added to equations (J-9) through (J-13) for a second-order uniform approximation are

$$E^V_{p\rho} = \frac{\omega\mu_0}{4\pi}\left(\lambda_p - \frac{3j}{8\rho}\right)(\lambda_p^2 - k_2^2)^{1/2} V_{p12} \tag{5-28a}$$

$$E^V_{pz} = \frac{-j\omega\mu_0}{4\pi}\left(\lambda_p^2 + \frac{j}{8\rho}\lambda_p\right) V_{p12} \tag{5-28b}$$

$$E^H_{p\rho} = \frac{j\omega\mu_0}{4\pi}\left(\lambda_p^2 - \frac{7j}{8\rho}\lambda_p\right) V_{p12} \tag{5-28c}$$

$$E^H_{p\phi} = \frac{\omega\mu_0}{4\pi\rho}\left(\lambda_p - \frac{3j}{8\rho}\right) V_{p12} \tag{5-28d}$$

$$E^H_{pz} = \frac{\omega\mu_0}{4\pi}\left(\lambda_p - \frac{3j}{8\rho}\right)(\lambda_p^2 - k_1^2)^{1/2} V_{p12}. \tag{5-28e}$$

The second-order uniform approximations are coded in subroutine GASY2.

### 5.2.5 Accuracy of the Approximations

Some tests of the accuracy of the asymptotic approximations are shown in figures Fig. 5-8 through Fig. 5-16. The relative errors were determined by comparison with the results of numerical evaluation of the Sommerfeld integrals. The result shown as a solid line is from the NEC subroutine GEASY which chooses an appropriate approximation for the given coordinates of source and receiver. The basic approximation is the second-order uniform result, including the surface wave. When $\theta = \tan^{-1}(\rho/|z-z'|)$ is less than $\theta_A = 11.3$ degrees the first-order approximation is evaluated and higher-order terms are interpolated between $\theta = 0$ and $\theta_A$. The error for the first-order asymptotic approximation is also shown on the plots. When the source is located at the interface ($z' = 0$) the relative errors for the Norton approximations [36], used in NEC–2, are shown as a dashed line. The Norton approximations are limited to source and receiver on or above the interface.

Errors for a ground with $\tilde{\epsilon}_1 = \epsilon_1 - j\sigma_1/\omega\epsilon_0 = 16 - j16$ are shown in Fig. 5-8 through Fig. 5-13. In most cases the errors from the NEC asymptotic approximations are substantially smaller than those from the Norton formulas or the first-order asymptotic results. The Norton formulas sometimes converge to a constant error, but this error level would decrease as $|\tilde{\epsilon}_1|^{-1}$.

The convergence is slower when $\theta$ and $\tilde{z} = z/|z-z'|$ are both small. When $\tilde{z}$ is less than 0.05, NEC uses the first-order approximations, since higher-order terms increase the error. The first-order result for $E_z^V$ vanishes as $\theta$ goes to zero, since it represents only the $R^{-1}$ term and the field has only higher-order components at $\theta = 0$. Hence this important field component is lost when source and evaluation points are both in the ground on a vertical line. The table-lookup algorithms are used to a depth of a free space wavelength for small $\theta$ to partially fill this gap. Interactions with the interface involving $E_z^V$ from greater depth in lossy ground can usually be neglected in antenna applications. For $\tilde{\epsilon}_1 = 16 - j16$ the attenuation is about $10^{-10}$ at $R/\lambda_0 = 2$.

The errors along the interface when $\tilde{\epsilon}_1 = 16 - j0$ are shown in Fig. 5-14. Both NEC and Norton approximations show poor convergence since they neglect the lateral wave in the ground. The $R^{-1}$ component of this wave will appear in the NEC approximation as the source is lowered into the ground. The real parts of the field components are plotted in Fig. 5-15. It is seen that the lateral wave in the ground is the dominant term in $E_\phi^H$, which accounts for the lack of convergence for this component. The errors for a dielectric ground decrease rapidly with height, as shown in Fig. 5-16.

The algorithm presently used in NEC to evaluate the field near ground, combining linear interpolation, least-squares approximation and asymptotic approximations, has been chosen to supply accurate field values for typical antenna applications, such as antennas on ground stakes or with buried or elevated screens. It can be seen that there are cases in which larger errors can occur. One such case is the interaction between two points at a significant depth in the ground, where the interaction via the interface is near the totally reflecting angle. The attenuation through a lossy ground should reduce the importance of this interaction. It should not be too difficult to add to or extend the algorithms to improve the accuracy. If necessary, a more extensive interpolation table, involving only two parameters, could be used for evaluating interactions between points that are both in the ground.

### 5.3 The Reflection Coefficient Approximation

The image equivalent of a source over a ground plane provides a simple and fast way to model the effect of ground on an antenna. If the ground is perfectly conducting, the structure and its image are exactly equivalent to the structure over the ground. Since the image only doubles the time to compute the field, it is always used with a perfectly conducting ground. NEC also includes an image approximation for a finitely conducting ground, in which the image fields are modified by the Fresnel plane-wave reflection coefficients. Although this model is far from exact for a finite ground, it has been shown to provide useful results for structures that are not too near to the ground [11, 32, 33]. When it can be used, the reflection coefficient approximation is two to four times faster than the Sommerfeld/Asymptotic method and avoids the need of computing the interpolation tables.

Implementation of the image and reflection coefficient methods in the code is relatively simple. For a perfectly conducting ground the Green's function in the kernel of the integral equation becomes the sum of the free-space Green's function for the source and the negative of the free-space Green's function of the image. The negative sign results from the reversal of the sign of charge on the image. For the electric field, with free-space Green's dyadic $\bar{\bar{\mathbf{G}}}(\mathbf{r}, \mathbf{r}')$ defined in (1), the Green's dyadic for a perfect ground is

$$\bar{\bar{\mathbf{G}}}_{\mathrm{pg}}(\mathbf{r}, \mathbf{r}') = \bar{\bar{\mathbf{G}}}(\mathbf{r}, \mathbf{r}') + \bar{\bar{\mathbf{G}}}_{\mathrm{I}}(\mathbf{r}, \mathbf{r}') \tag{5-29}$$

where

$$\bar{\bar{\mathbf{G}}}_{\mathrm{I}}(\mathbf{r}, \mathbf{r}') = -\bar{\bar{\mathbf{I}}}_{\mathrm{R}} \cdot \bar{\bar{\mathbf{G}}}(\mathbf{r}, \bar{\bar{\mathbf{I}}}_{\mathrm{R}} \cdot \mathbf{r}') \tag{5-30}$$

and $\bar{\bar{\mathbf{I}}}_{\mathrm{R}} = \hat{\mathbf{x}}\hat{\mathbf{x}} + \hat{\mathbf{y}}\hat{\mathbf{y}} - \hat{\mathbf{z}}\hat{\mathbf{z}}$ is a dyadic that produces a reflection in the $z = 0$ plane when used in a dot product. Similarly, for the magnetic field with free-space Green's dyadic

$$\bar{\bar{\mathbf{\Gamma}}}(\mathbf{r}, \mathbf{r}') = \bar{\bar{\mathbf{I}}} \times \nabla' g(\mathbf{r}, \mathbf{r}')$$

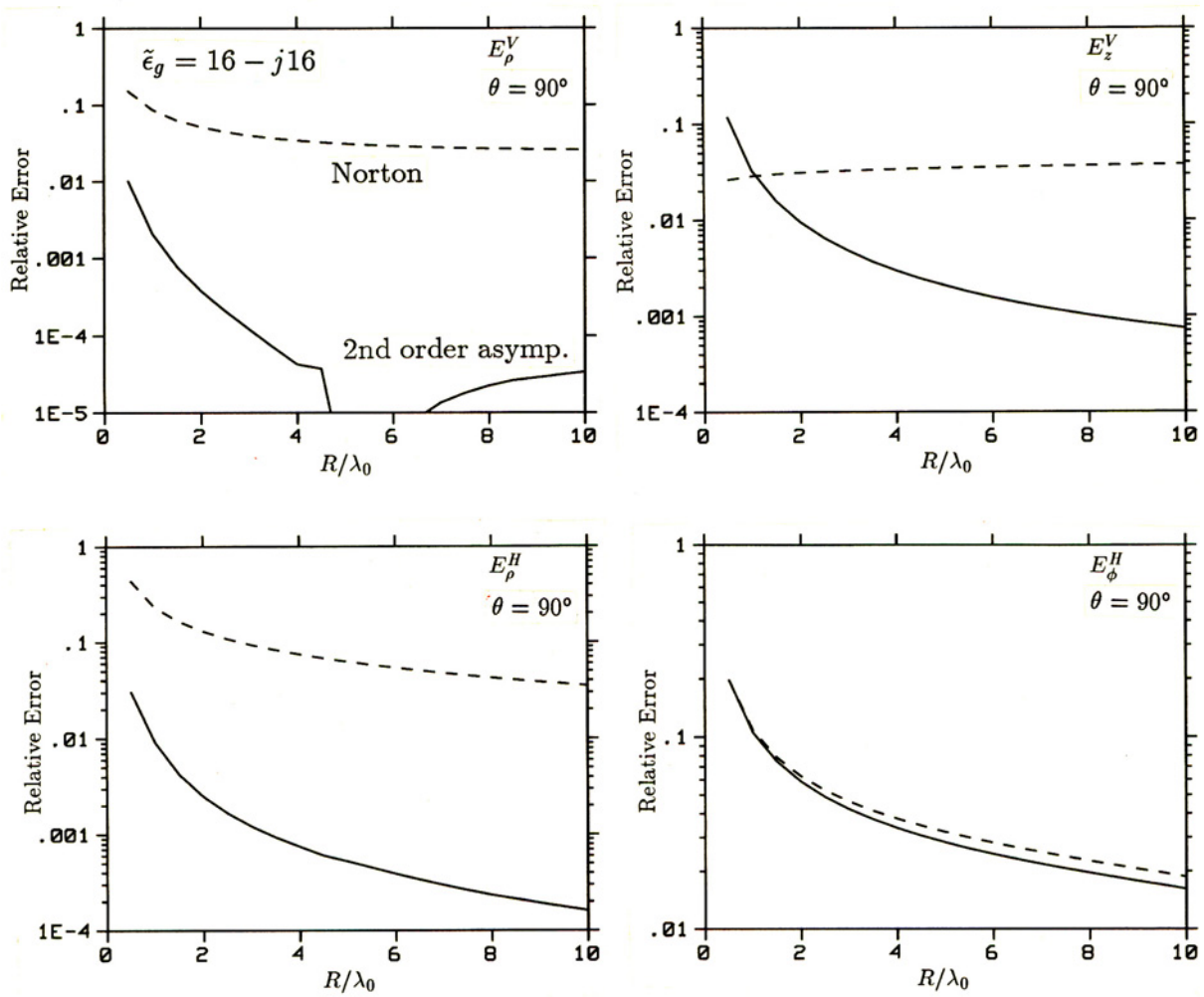


**Fig. 5-8** Relative errors in the second-order asymptotic approximation including surface wave and the Norton approximation for $z = z' = 0$. The complex permittivity of the ground is $16 - j16$. The error for $E_z^H$ is the same as for $E_\rho^V$.

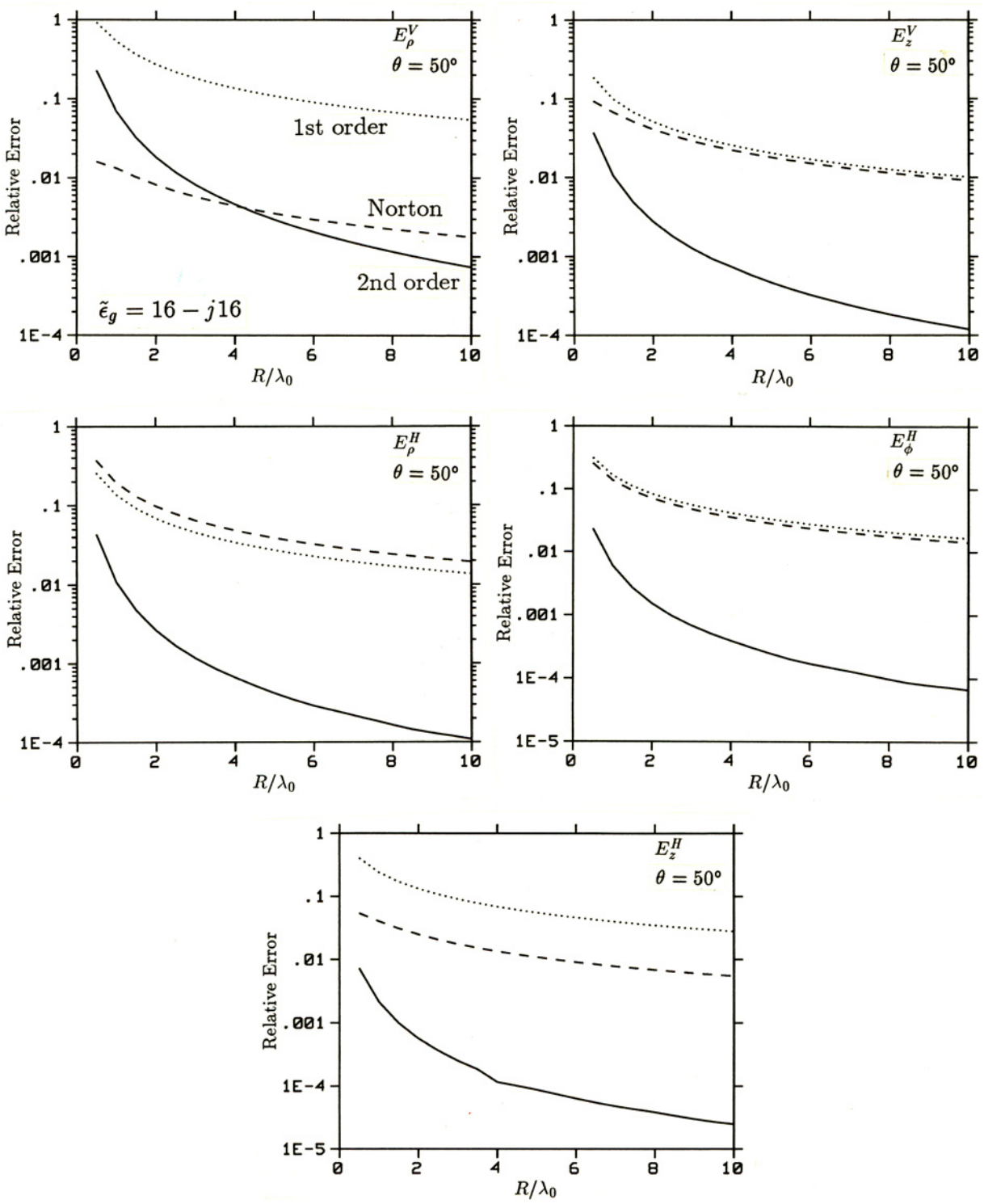


**Fig. 5-9** Relative errors in the first-order and the second-order plus surface wave asymptotic approximations and the Norton approximation for $\theta = \tan^{-1}[\rho/(z - z')] = 50°$ and $z' = 0$. The complex permittivity of the ground is $16 - j16$.

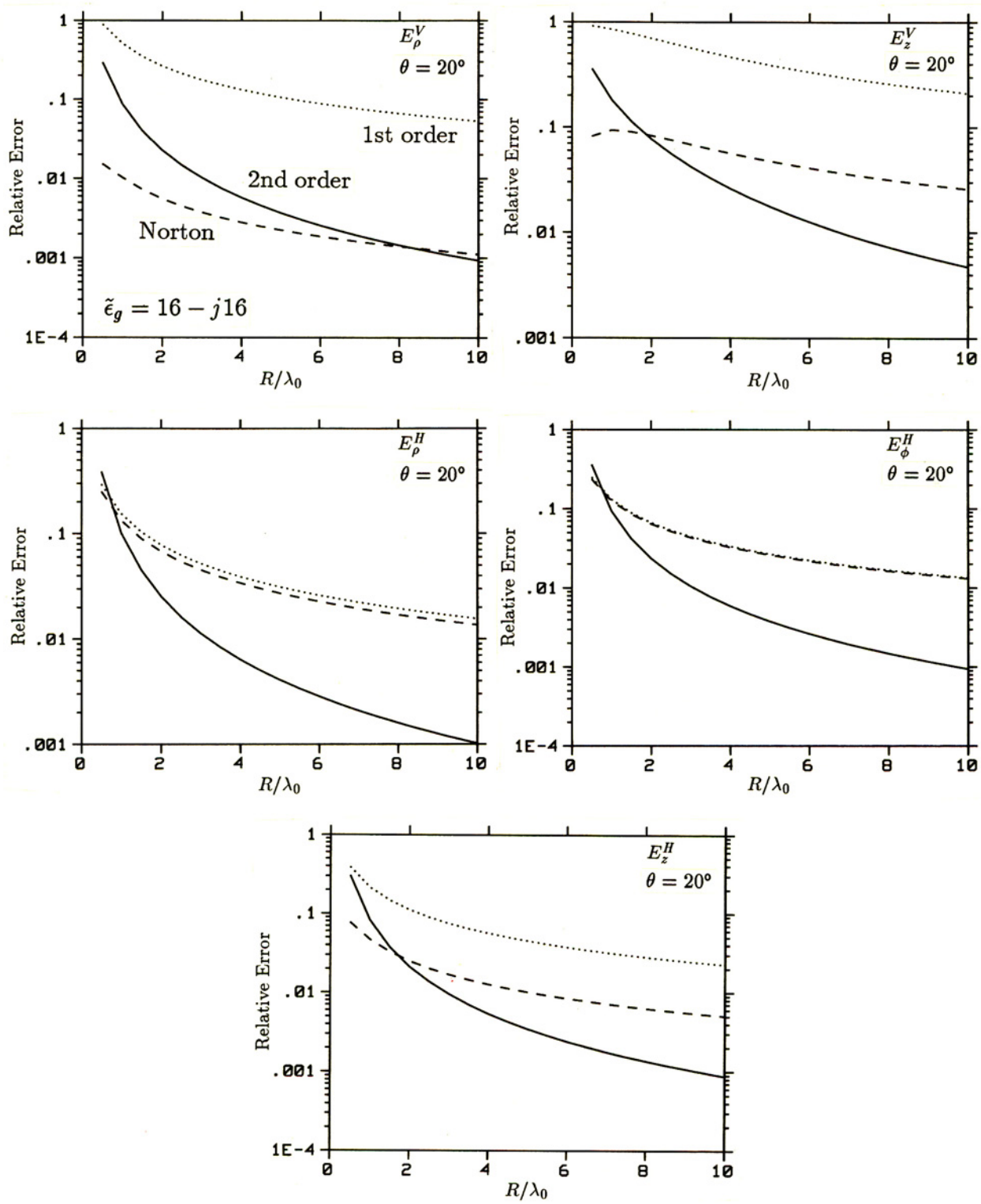


**Fig. 5-10** Relative errors in the first-order and the second-order plus surface wave asymptotic approximations and the Norton approximation for $\theta = \tan^{-1}[\rho/(z - z')] = 20°$ and $z' = 0$. The complex permittivity of the ground is $16 - j16$.

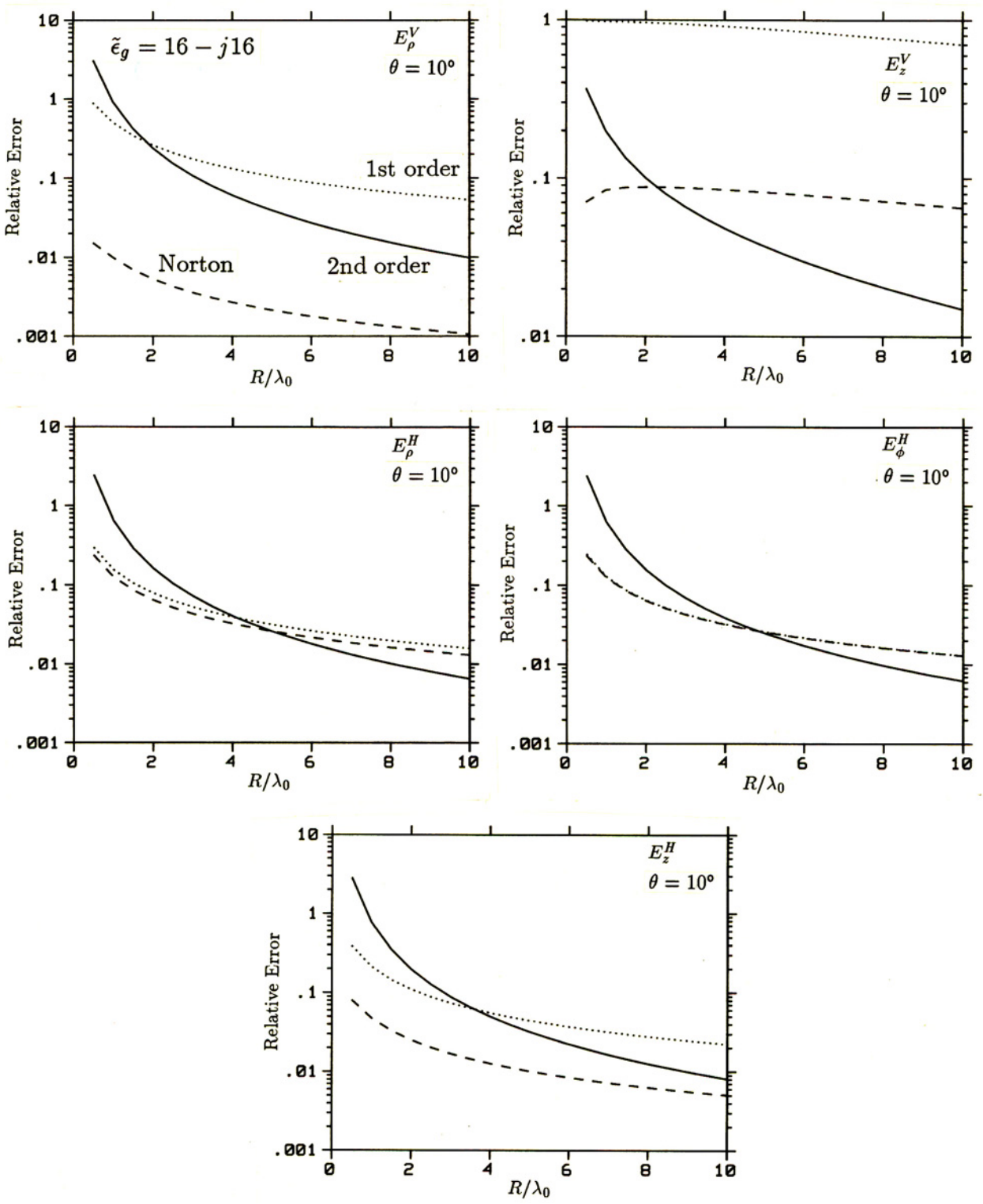


**Fig. 5-11** Relative errors in the first-order and the second-order plus surface wave asymptotic approximations and the Norton approximation for $\theta = \tan^{-1}[\rho/(z - z')] = 10°$ and $z' = 0$. The complex permittivity of the ground is $16 - j16$.

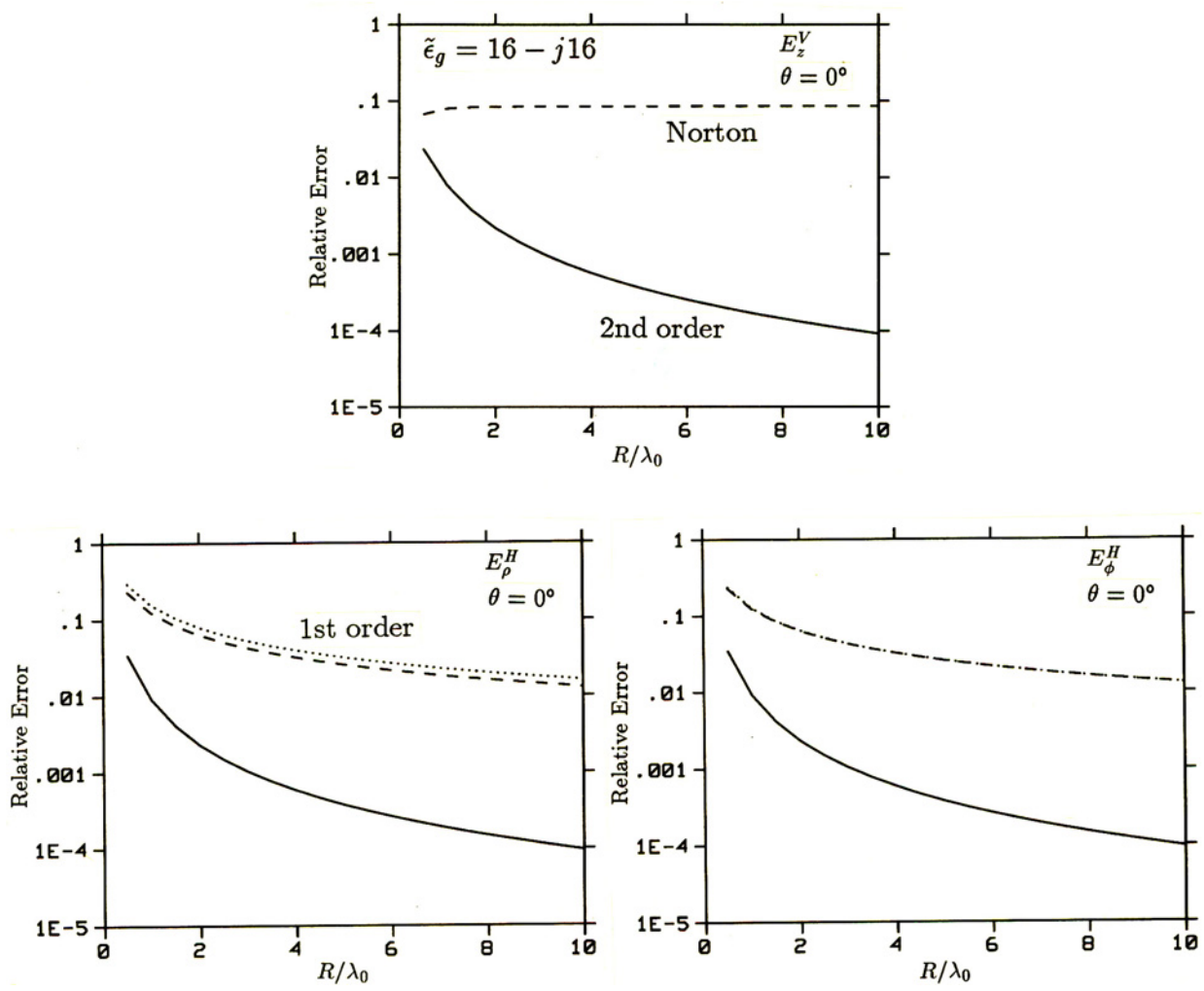


**Fig. 5-12** Relative errors in the first-order and the second-order asymptotic approximations and the Norton approximation for $\theta = \tan^{-1}[\rho/(z-z')] = 0°$ and $z' = 0$. The complex permittivity of the ground is $16 - j16$. The $E_\rho^V$ and $E_z^H$ components are zero.

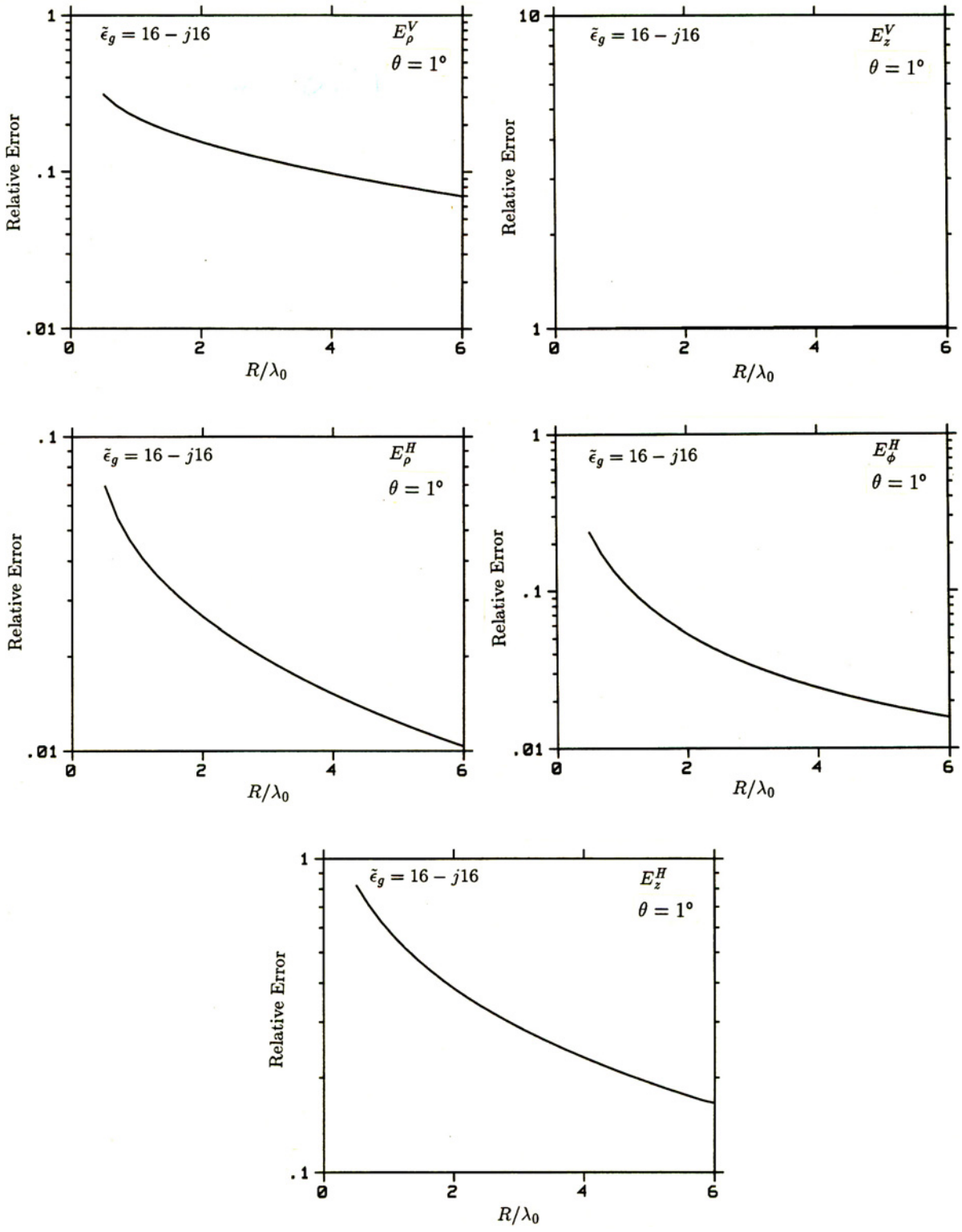


**Fig. 5-13** Relative errors in the first-order asymptotic approximations for $\theta = \tan^{-1}[\rho/(z - z')] = 1°$ and $\tilde{z} = z/(z - z') = 0.01$. The complex permittivity of the ground is $16 - j16$.

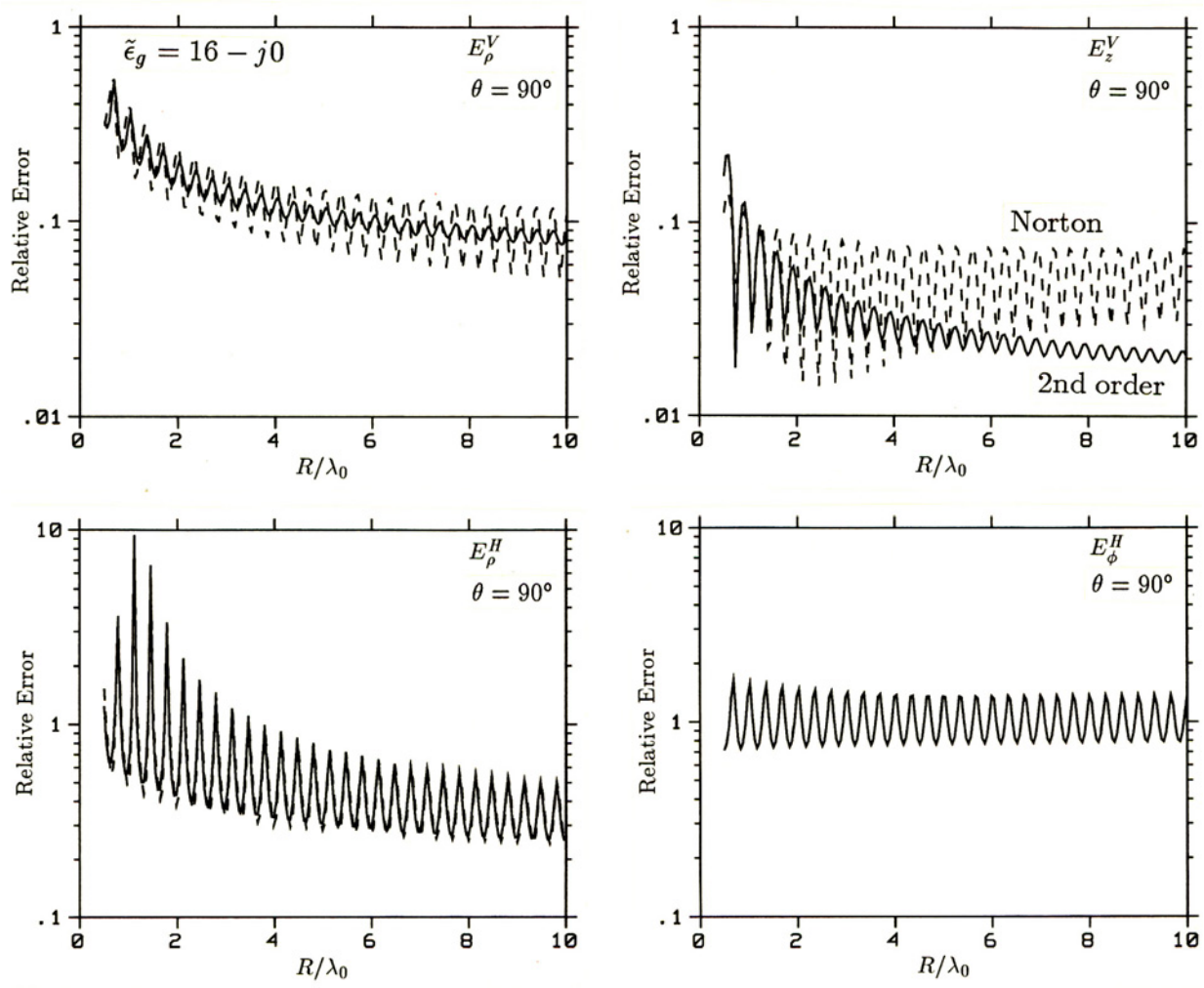


**Fig. 5-14** Relative errors in the second-order asymptotic approximation including surface wave and the Norton approximation for $z = z' = 0$. The complex permittivity of the ground is $16 - j0$. The large errors are due to the absence of a term representing a lateral wave in the ground in either approximation for grazing incidence.

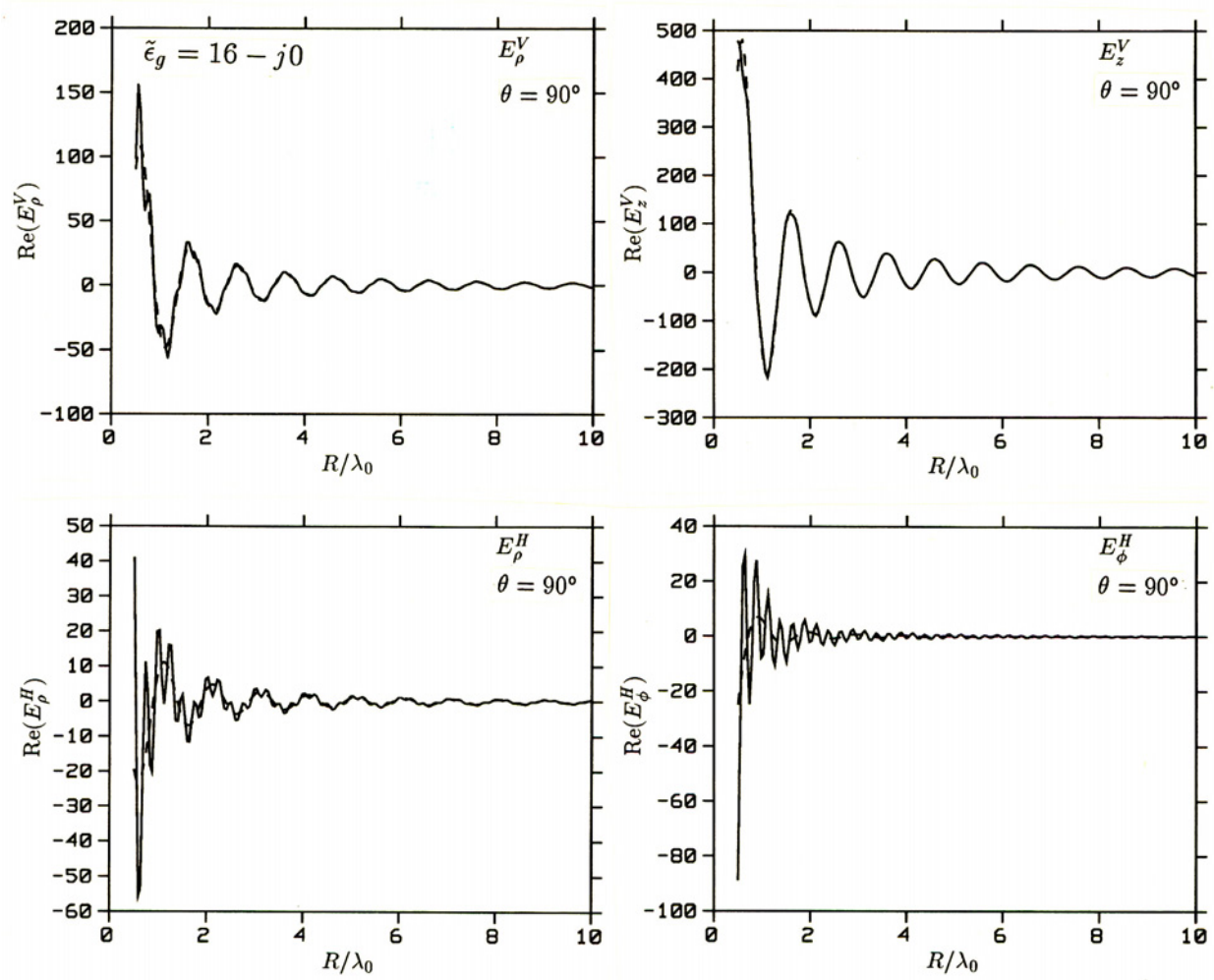


**Fig. 5-15** Real part of the field components computed by numerical evaluation of the Sommerfeld integrals (————) and the second-order asymptotic approximations (– – – –) for $z = z' = 0$. The complex permittivity of the ground is $16 - j0$.

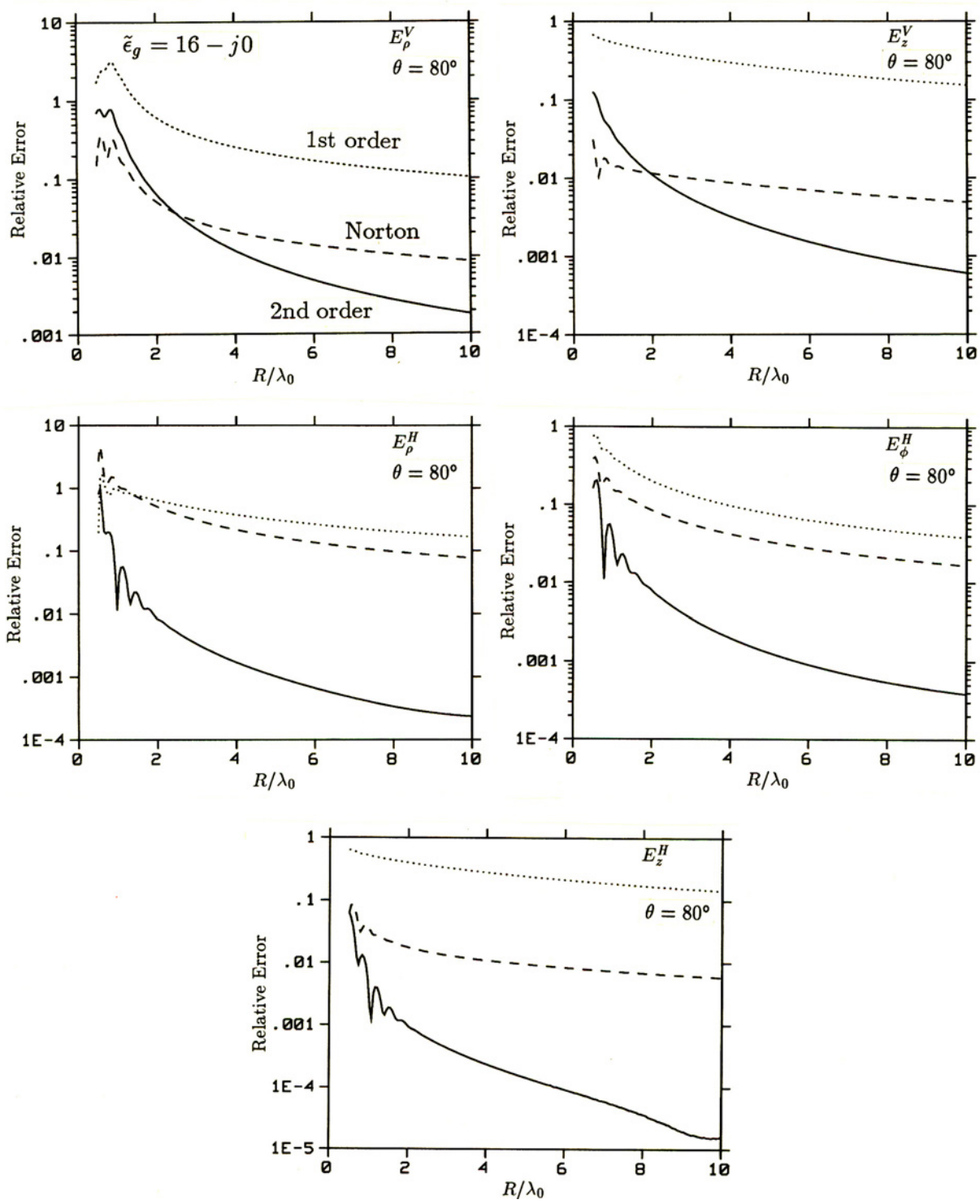


**Fig. 5-16** Relative errors in the first-order and the second-order plus surface wave asymptotic approximations and the Norton approximation for $\theta - \tan^{-1}[\rho/(z - z')] = 80°$ and $z' = 0$. The complex permittivity of the ground is $16 - j0$.

the Green's dyadic over perfect ground is

$$\bar{\bar{\mathbf{\Gamma}}}_{\mathrm{pg}}(\mathbf{r},\mathbf{r}') = \bar{\bar{\mathbf{\Gamma}}}(\mathbf{r},\mathbf{r}') + \bar{\bar{\mathbf{\Gamma}}}_{\mathrm{I}}(\mathbf{r},\mathbf{r}') \tag{5-31}$$

where

$$\bar{\bar{\mathbf{\Gamma}}}_{\mathrm{I}}(\mathbf{r},\mathbf{r}') = -\bar{\bar{\mathbf{I}}}_{\mathrm{R}} \cdot \bar{\bar{\mathbf{\Gamma}}}(\mathbf{r},\, \bar{\bar{\mathbf{I}}}_{\mathrm{R}} \cdot \mathbf{r}\,'). \tag{5-32}$$

In the reflection coefficient approximation for finitely conducting ground the image fields are multiplied by the Fresnel reflection coefficients. The coefficients are derived by considering an incident plane wave that produces a reflected wave and a wave refracted into the opposite medium. The field is resolved into TE and TM components relative to the plane of incidence formed by the incident ray and the normal to the interface. The TE component, with **E** normal to the plane of incidence, will be termed horizontal polarization, and the TM component, with **E** in the plane of incidence, will be vertical polarization. Matching the boundary conditions on the field components at the interface yields the reflection coefficients [30]

$$R_V = \frac{\cos\theta - Z_R\sqrt{1 - Z_R^2\sin^2\theta}}{\cos\theta + Z_R\sqrt{1 - Z_R^2\sin^2\theta}} \tag{5-33}$$

$$R_H = \frac{-\left(Z_R\cos\theta - \sqrt{1 - Z_R^2\sin^2\theta}\right)}{Z_R\cos\theta + \sqrt{1 - Z_R^2\sin^2\theta}} \tag{5-34}$$

where $\cos\theta = -\hat{\mathbf{k}}\cdot\hat{\mathbf{z}}$ and $Z_R = (\epsilon_1 - j\sigma_1/\omega\epsilon_0)^{-1/2}$. The signs have been chosen so that both coefficients go to 1 for perfectly conducting ground, and the reference directions for the field components are shown in Fig. 5-17.

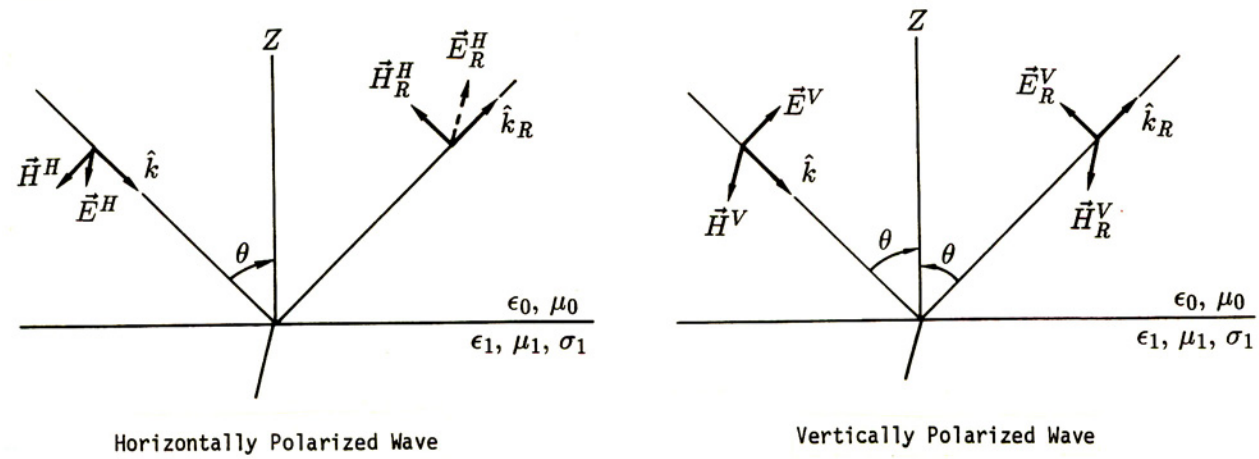


**Fig. 5-17** Reflection of a plane wave from an interface.

The reflection coefficients can also be written in terms of surface impedance and admittance for the TE and TM polarizations as

$$R_V = -\frac{Y_0^{\mathrm{TE}} - Y_s^{\mathrm{TE}}}{Y_0^{\mathrm{TE}} + Y_s^{\mathrm{TE}}}$$

$$R_H = \frac{Z_0^{\mathrm{TM}} - Z_s^{\mathrm{TM}}}{Z_0^{\mathrm{TM}} + Z_s^{\mathrm{TM}}}$$

where

$$Y_0^{\mathrm{TE}} = \eta_0^{-1}\cos\theta, \qquad Y_s^{\mathrm{TE}} = \eta_1^{-1}\cos\theta_t$$
$$Z_0^{\mathrm{TM}} = \eta_0\cos\theta, \qquad Z_s^{\mathrm{TM}} = \eta_1\cos\theta_t$$

with $\eta_0 = \sqrt{\mu_0/\epsilon_0}$, $\eta_1 = \sqrt{\mu_0/\epsilon_1}$ and $\cos\theta_t = [1-(k_0/k_1)^2\sin\theta]^{1/2}$.

The reflected fields due to incident fields $\mathbf{E}^{\mathrm{V}}$ and $\mathbf{E}^{\mathrm{H}}$, with vertical and horizontal polarization respectively, are

$$\mathbf{E}_{\mathrm{R}}^{\mathrm{V}} = -R_V\left(\bar{\bar{\mathbf{I}}}_{\mathrm{R}}\cdot\mathbf{E}^{\mathrm{V}}\right)$$
$$\mathbf{E}_{\mathrm{R}}^{\mathrm{H}} = -R_H\mathbf{E}^{\mathrm{H}}$$

and the reflected magnetic field components are

$$\mathbf{H}_{\mathrm{R}}^{\mathrm{V}} = R_V\mathbf{H}^{\mathrm{V}}$$
$$\mathbf{H}_{\mathrm{R}}^{\mathrm{H}} = R_H\left(\bar{\bar{\mathbf{I}}}_{\mathrm{R}}\cdot\mathbf{H}^{\mathrm{H}}\right).$$

An incident field with arbitrary polarization must be resolved into horizontal and vertical components to determine the reflected field. If $\hat{\mathbf{p}}$ is the unit vector normal to the plane of incidence, the reflected field due to an incident field $\mathbf{E}$ is

$$\begin{aligned}\mathbf{E}_{\mathrm{R}} =& R_H\left(\mathbf{E}_{\mathrm{I}}\cdot\hat{\mathbf{p}}\right)\hat{\mathbf{p}} + R_V\left[\mathbf{E}_{\mathrm{I}} - \left(\mathbf{E}_{\mathrm{I}}\cdot\hat{\mathbf{p}}\right)\hat{\mathbf{p}}\right]\\ =& R_V\mathbf{E}_{\mathrm{I}} + \left(R_H - R_V\right)\left(\mathbf{E}_{\mathrm{I}}\cdot\hat{\mathbf{p}}\right)\hat{\mathbf{p}}\end{aligned} \tag{5-35}$$

where $\mathbf{E}_{\mathrm{I}}$ is the field from the image of the source. Use of the image field in (5-35) accounts for the changes in sign and vector direction of the field that were shown explicitly for the vertically and horizontally polarized cases. For the magnetic field,

$$\mathbf{H}_{\mathrm{R}} = R_H\mathbf{H}_{\mathrm{I}} + \left(R_V - R_H\right)\left(\mathbf{H}_{\mathrm{I}}\cdot\hat{\mathbf{p}}\right)\hat{\mathbf{p}}$$

where $\mathbf{H}_{\mathrm{I}}$ is the magnetic field from the image of the source. Dyadic Green's functions for use in the integral equations can be constructed as

$$\bar{\bar{\mathbf{G}}}_g(\mathbf{r},\mathbf{r}') = \bar{\bar{\mathbf{G}}}(\mathbf{r},\mathbf{r}') + \bar{\bar{\mathbf{G}}}_{\mathrm{R}}(\mathbf{r},\mathbf{r}') \tag{5-36}$$
$$\bar{\bar{\mathbf{\Gamma}}}_g(\mathbf{r},\mathbf{r}') = \bar{\bar{\mathbf{\Gamma}}}(\mathbf{r},\mathbf{r}') + \bar{\bar{\mathbf{\Gamma}}}_{\mathrm{R}}(\mathbf{r},\mathbf{r}') \tag{5-37}$$

where

$$\bar{\bar{\mathbf{G}}}_{\mathrm{R}}(\mathbf{r},\mathbf{r}') = R_V\bar{\bar{\mathbf{G}}}_{\mathrm{I}}(\mathbf{r},\mathbf{r}') + \left(R_H - R_V\right)\hat{\mathbf{p}}\left[\hat{\mathbf{p}}\cdot\bar{\bar{\mathbf{G}}}_{\mathrm{I}}(\mathbf{r},\mathbf{r}')\right]$$

$$\bar{\bar{\Gamma}}_{\mathrm{R}}(\mathbf{r},\mathbf{r}') = R_H \bar{\bar{\Gamma}}_{\mathrm{I}}(\mathbf{r},\mathbf{r}') + (R_V - R_H)\,\hat{\mathbf{p}}\left[\hat{\mathbf{p}}\cdot\bar{\bar{\Gamma}}_{\mathrm{I}}(\mathbf{r},\mathbf{r}')\right]$$

with $\hat{\mathbf{p}} = \mathbf{p}/|\mathbf{p}\,|$, $\mathbf{p} = (\mathbf{r}-\mathbf{r}')\times\hat{\mathbf{z}}$ and $\bar{\bar{\mathbf{G}}}_{\mathrm{I}}$ and $\bar{\bar{\Gamma}}_{\mathrm{I}}$ are from (5-30) and (5-32).

The Fresnel reflection coefficients are exact when the wave reflecting from the ground is a plane wave, as that from a distant point source. The plane-wave reflection formulas also give the correct result for the field at a distant evaluation point when the source is near the interface, as can be seen by applying the reciprocity principle. More generally, the sum of the distances of the source and evaluation points from the interface should be large for the plane wave reflection solution to apply, although it becomes exact in any case in the limit of perfectly conducting ground. In practice, the reflection coefficient approximation has been found to give satisfactory results for antennas at least $0.1\lambda_0$ above the interface [11, 32, 33]. However, it is not suitable for modeling long wires over lossy ground. In fact, it may produce a solution in which the current grows exponentially away from the source [53].

The first-order asymptotic approximations obtained by steepest-descent evaluation of the Sommerfeld integrals include the same coefficients as (5-33) and (5-34). However, in the first-order asymptotic solution the coefficients multiply only the $R^{-1}$ components of the fields, while in the reflection coefficient approximation they multiply the total near field. While there is no clear justification for including the near-field terms in the reflection coefficient approximation, the result has been found to provide a useful asymptotic approximation for a field component such as $E_z^V$ with $\rho = 0$, in which the $R^{-1}$ term vanishes. The reflection coefficient approximation is only used in NEC for source and evaluation points above the ground. When source and evaluation points are in the earth the approximation was found to converge very slowly. An approximation for evaluating the field when source and evaluation points are on opposite sides of the interface can be obtained from the Fresnel transmission coefficients multiplied by a factor to account for the change in divergence of a ray tube on crossing the interface. The divergence factor is generally determined for conservation of power in a ray tube assuming a $R^{-1}$ field, so its application to the total near field may be questionable. The transmission coefficient approximation is not in the present version of NEC.

NEC also includes a reflection coefficient approximation for a radial-wire ground screen. This model is based on an approximation developed by Wait [54] for the surface impedance of a wire mesh on the surface of a finitely conducting ground. The use of the surface impedance in determining the reflection coefficients in a moment-method solution was demonstrated by Miller and Deadrick [55]. Using Wait's result, the surface impedance of the ground screen is approximated as

$$Z_g(\rho) = \frac{j\mu_0\omega\rho}{N}\ln\left(\frac{\rho}{NC_0}\right) \tag{5-38}$$

where $N$ is the number of radial wires in the screen and $C_0$ is the radius of the wires. Equation (5-38) is the surface impedance from Wait's result for a grid of parallel wires having the spacing that the radial wires have at a distance $\rho$ from the center of the screen. The impedance of the grid is combined in parallel with the impedance of the ground which

for high conductivity is approximately

$$\zeta_1 = \left[\frac{\mu_0}{\epsilon_0(\epsilon_1 - j\sigma/\omega\epsilon_0)}\right]^{1/2}.$$

The screen and ground together then have a surface impedance of

$$\zeta_e = \frac{\zeta_1 Z_g}{\zeta_1 + Z_g}.$$

If the intrinsic impedance of the upper medium is $\eta_0$ the reflection coefficients are

$$\begin{aligned} R_H =& \frac{\eta_0 - \zeta_e \cos\theta}{\eta_0 + \zeta_e \cos\theta} \\ R_V =& \frac{\eta_0 \cos\theta - \zeta_e}{\eta_0 \cos\theta + \zeta_e}. \end{aligned}$$

For this surface-impedance approximation for a ground screen to be valid the refractive index of the ground must be large compared to unity and the spacing of wires in the grid must be much less than the wavelength. Due to the assumption of specular reflection, only the properties of the ground directly under a vertical antenna will affect its current distribution. At the origin of the radial-wire screen the impedance is zero ($Z_g$ is not allowed to be negative) so the impedance and current distribution of a vertical antenna at the origin will be the same as over a perfectly conducting ground. The far fields will demonstrate the effect of the screen as the specular point moves away from the origin, although the effect of diffraction from the edge of the screen is absent. For antennas other than a vertical monopole, it should be remembered that the anisotropic nature of the screen has not been considered in this approximation. The extension of the approximation to account for anisotropy in a mesh screen was considered in [55].

# 6. Solution of the Matrix Equation

The matrix equation resulting from the Moment Method solution for wires and patches in NEC is solved by factoring the matrix into a product of upper and lower triangular matrices by Gauss elimination. The triangular matrices are saved and used to obtain the solutions for any number of excitations by a simple process of forward and backward substitution. Since the time to factor the matrix is proportional to the matrix order cubed, the solution time becomes critical for large problems.

When symmetry occurs in the structure, such that the complete structure can be formed by reflecting or rotating a subsection, the solution time and required computer memory can be reduced by decomposing the solution into a sum of eigenmodes. The solution is then obtained by solving a smaller matrix equation for each mode. The code also can implement a partitioned-matrix solution so that the matrix for a basic model can be saved in LU factored form, and the solution with additions to that model can be obtained with minimum computation. This partitioned-matrix solution, termed the Numerical Green's Function (NGF), can be used when moving an antenna around on a large model such as a ship, and also to take advantage of symmetry in part of a model when unsymmetric parts must be included. These matrix solution techniques are described in this section.

## 6.1 Solution of the Matrix Equation by L-U Factorization

The matrix equation in NEC is solved by factoring the matrix into a product of lower and upper triangular matrices. The matrix $\mathrm{A} = [a_{ij}]$ is factored so that $\mathrm{A} = \mathrm{LU} = [\ell_{ik}][u_{kj}]$ where L is a lower triangular matrix with ones on the diagonal and U is an upper triangular matrix. The matrix equation $[a_{ij}][I_j] = [E_i]$ then becomes

$$[\ell_{ik}][u_{kj}][I_j] = [E_i] \tag{6-1}$$

which is easily solved by first solving

$$[\ell_{ik}][f_k] = [E_i] \tag{6-2}$$

and then solving

$$[u_{kj}][I_j] = [f_k]. \tag{6-3}$$

The matrix is factored using a standard Gauss-elimination algorithm [56]. The elements of the L and U matrices are evaluated by sequentially solving equations resulting from the matrix product. The elements of the first columns of L and U are obtained by solving the equations

$$\begin{aligned} a_{11} &= u_{11} \\ a_{i1} &= \ell_{i1} u_{11}, \qquad i = 2, \ldots, n. \end{aligned}$$

The second columns are then obtained from

$$\begin{aligned} a_{12} &= u_{12} \\ a_{22} &= \ell_{21} u_{12} + u_{22} \\ a_{i2} &= \ell_{i1} u_{12} + \ell_{i2} u_{22}, \qquad i = 3, \ldots, n \end{aligned}$$

and the general form for column $r$ is

$$
\begin{aligned}
a_{1r} &= u_{1r} \\
a_{2r} &= \ell_{21}u_{1r} + u_{2r} \\
&\vdots \\
a_{rr} &= \ell_{r1}u_{1r} + \ell_{r2}u_{2r} + \cdots + \ell_{r,r-1}u_{r-1,r} + u_{rr} \\
a_{ir} &= \ell_{i1}u_{1r} + \ell_{i2}u_{2r} + \cdots + \ell_{i,r-1}u_{r-1,i} + \ell_{ir}u_{rr}, \quad i = r+1, \ldots, n.
\end{aligned}
$$

The coefficients of the L and U matrices can be written over the matrix A in memory and saved for use with multiple right-hand sides in (6-1). The solution is obtained by evaluating (6-2) as

$$f_i = \frac{1}{\ell_{ii}} \left( E_i - \sum_{j=1}^{i-1} \ell_{ij} f_j \right), \qquad i = 1, \ldots, n$$

and then evaluating (6-3) as

$$I_i = f_i - \sum_{j=i+1}^{n} u_{ij} I_j \,, \qquad i = n, n-1, \ldots, 1.$$

In the algorithm used in NEC, row interchanges are applied at each step of the Gauss elimination to obtain the pivot element of maximum magnitude. Using the maximum pivot element scaled by the equation size would be a better strategy. However, the equations in the moment-method solution will usually be of similar size, so this should not be too important. The EFIE for thin wires generally produces equations with diagonal elements several orders of magnitude larger than elements at least several rows off of the diagonal. Hence, the wire part of the matrix should be well conditioned, and use of optimum pivot elements may not be necessary. However, the propagation of roundoff errors in very large matrices, with orders of several thousand, has not been studied, so partial pivoting is retained in the code.

### 6.2 Solution for Symmetric Structures

Structures to be modeled often have symmetries or repetition patterns within their structure that can be exploited to reduce the computation time and storage requirements. Types of symmetry include rotational symmetry of degree $N_p$, where the structure repeats exactly on rotation about an axis by an angle $2\pi/N_p$, and reflection symmetry, where the complete structure can be formed by reflecting a sub-unit in one, two or three orthogonal planes. NEC can take advantage of overall rotational and reflection symmetry both in evaluating and solving the matrix equation. It can also take advantage of a situation where part of the structure is symmetric but unsymmetric parts are also present. A partitioned-matrix solution is used in the latter case as described in the next section.

A structure with rotational symmetry of order $N_p$ consists of $N_p$ identical sections with section number $i$ rotated from section 1 by an angle $2\pi(i-1)/N_p$. If the segments and patches

are numbered in the same order in each section the resulting matrix has the structure

$$\begin{pmatrix} \mathrm{A}_1 & \mathrm{A}_2 & \mathrm{A}_3 & \mathrm{A}_4 & \cdots & \mathrm{A}_{N_p} \\ \mathrm{A}_{N_p} & \mathrm{A}_1 & \mathrm{A}_2 & \mathrm{A}_3 & \cdots & \mathrm{A}_{N_p-1} \\ \mathrm{A}_{N_p-1} & \mathrm{A}_{N_p} & \mathrm{A}_1 & \mathrm{A}_2 & \cdots & \mathrm{A}_{N_p-2} \\ \vdots & & & & & \\ \mathrm{A}_2 & \mathrm{A}_3 & \mathrm{A}_4 & \mathrm{A}_5 & \cdots & \mathrm{A}_1 \end{pmatrix} \begin{pmatrix} \mathrm{I}_1 \\ \mathrm{I}_2 \\ \mathrm{I}_3 \\ \vdots \\ \mathrm{I}_{N_p} \end{pmatrix} = \begin{pmatrix} \mathrm{E}_1 \\ \mathrm{E}_2 \\ \mathrm{E}_3 \\ \vdots \\ \mathrm{E}_{N_p} \end{pmatrix} \tag{6-4}$$

where, if the order of the complete matrix is $N$, each $\mathrm{A}_i$ is a submatrix of order $N/N_p$. A matrix with this form, where each row of submatrices is the same as the previous row with a circular shift to the right, is termed block circulant. An immediate advantage of this structure is that only the entries in the first row of submatrices must be computed and stored. Hence the computation time to evaluate the matrix elements and the memory needed for storage are reduced by a factor of $N_p$.

The block-circulant structure offers a still larger advantage in inverting or factoring the matrix, due to the $N^3$ dependence of the computation time. The solution for an arbitrary excitation can be obtained by expanding the excitation in eigenmodes of the structure through a discrete Fourier transform, and solving for the response to each mode separately. The components of the excitation vector are transformed as

$$\mathrm{E}_i = \sum_{k=1}^{N_p} S_{ik}\mathcal{E}_k, \qquad i = 1, \ldots, N_p$$

$$\mathcal{E}_i = \frac{1}{N_p}\sum_{k=1}^{N_p} S^*_{ik}\mathrm{E}_k, \qquad i = 1, \ldots, N_p$$

where * indicates the conjugate of the complex number and

$$S_{ik} = \exp[j2\pi(i-1)(k-1)/N_p]$$

with $j = \sqrt{-1}$. With this transformation, the total excitation vector becomes

$$\mathrm{E} = \begin{pmatrix} \mathrm{E}_1 \\ \mathrm{E}_2 \\ \mathrm{E}_3 \\ \vdots \\ \mathrm{E}_{N_p} \end{pmatrix} = \sum_{k=1}^{N_p} \begin{pmatrix} S_{1k}\mathcal{E}_k \\ S_{2k}\mathcal{E}_k \\ S_{3k}\mathcal{E}_k \\ \vdots \\ S_{N_pk}\mathcal{E}_k \end{pmatrix}. \tag{6-5}$$

In each component vector of (6-5) the excitation on sector $i$ of the structure differs from the excitation on sector $i-1$ only by a uniform phase shift of $2\pi(k-1)/N_p$. If the structure has rotational symmetry, the response to each of these component vectors must repeat with the same phase shift around the structure. Hence the current response must have the form

$$\mathrm{I} = \begin{pmatrix} \mathrm{I}_1 \\ \mathrm{I}_2 \\ \mathrm{I}_3 \\ \vdots \\ \mathrm{I}_{N_p} \end{pmatrix} = \sum_{k=1}^{N_p} \begin{pmatrix} S_{1k}\mathcal{I}_k \\ S_{2k}\mathcal{I}_k \\ S_{3k}\mathcal{I}_k \\ \vdots \\ S_{N_pk}\mathcal{I}_k \end{pmatrix}. \tag{6-6}$$

where each vector in the expansion of I is the response to the component for the same $k$ in (6-5).

Substituting (6-5) and (6-6) into (6-4), it is seen that the solution can be obtained by transforming the submatrices as

$$\mathcal{A}_i = \sum_{k=1}^{N_p} S_{ik} \mathrm{A}_k, \qquad i = 1, \ldots, N_p$$

then solving for the current modes

$$\mathcal{I}_i = \mathcal{A}_i^{-1} \mathcal{E}_i, \qquad i = 1, \ldots, N_p$$

and finally summing the total current as

$$\mathrm{I}_i = \sum_{k=1}^{N_p} S_{ik} \mathcal{I}_k, \qquad i = 1, \ldots, N_p.$$

Thus the solution is obtained by factoring and solving $N_p$ matrix equations of order $N/N_p$. In the code, $\mathcal{I}$ is evaluated by factoring $\mathcal{A}$ into LU form and then solving.

The same procedure can be used for structures that have planes of symmetry. The Fourier transform is then replaced by decomposition into modes that are even and odd about the symmetry planes. All equations remain the same except that the transformation matrices $[S_{ik}]$ are, for one plane of symmetry,

$$\mathrm{S}_1 = \begin{pmatrix} 1 & 1 \\ 1 & -1 \end{pmatrix}$$

for two planes of symmetry,

$$\mathrm{S}_2 = \begin{pmatrix} 1 & 1 & 1 & 1 \\ 1 & -1 & 1 & -1 \\ 1 & 1 & -1 & -1 \\ 1 & -1 & -1 & 1 \end{pmatrix}$$

and for three planes of symmetry,

$$\mathrm{S}_3 = \begin{pmatrix} 1 & 1 & 1 & 1 & 1 & 1 & 1 & 1 \\ 1 & -1 & 1 & -1 & 1 & -1 & 1 & -1 \\ 1 & 1 & -1 & -1 & 1 & 1 & -1 & -1 \\ 1 & -1 & -1 & 1 & 1 & -1 & -1 & 1 \\ 1 & 1 & 1 & 1 & -1 & -1 & -1 & -1 \\ 1 & -1 & 1 & -1 & -1 & 1 & -1 & 1 \\ 1 & 1 & -1 & -1 & -1 & -1 & 1 & 1 \\ 1 & -1 & -1 & 1 & -1 & 1 & 1 & -1 \end{pmatrix}.$$

With either rotational or reflection symmetry, the solution is obtained by factoring $N_p$ matrices of order $N/N_p$ rather than one matrix of order $N$. For reflection symmetry

$N_p = 2^{N_r}$ where $N_r$ is the number of reflection planes. Since the time for factoring a matrix is approximately proportional to the order cubed, the relative computation time is reduced from $N^3$ to $N_p(N/N_p)^3$, or by a factor of $N_p^2$. The solution time for each right-hand side is reduced by a factor of $N_p$.

A further saving can be achieved if it is known that the excitation includes only a limit number of the possible modes. Such cases include an azimuthally uniform excitation ($k = 1$ mode) or a plane wave incident along the axis of rotation ($k = 2$ and $k = N_p$ modes.) The general NEC does not treat these special cases, but a code NEC-GS [57] has been developed to take maximum advantage of the symmetry and azimuthally uniform excitation of a vertical monopole on a radial-wire ground screen.

### 6.3 The Numerical Green's Function Solution

NEC includes an option to generate and factor an interaction matrix and save the result on a file. A later run, using the file, can add to the structure and solve the complete model by a partitioned-matrix algorithm without unnecessary repetition of calculations. This procedure is call the Numerical Green's Function (NGF), since it is the numerical equivalent of replacing the free-space Green's function in the integral equation with a Green's function for the model on the file. The NGF is particularly useful for a large structure, such as a ship, on which various antennas will be added or modified. It also permits taking advantage of partial symmetry, since a NGF file may be written for the symmetric part of a structure, taking advantage of the symmetry to reduce computation time. Unsymmetric parts can then be added in a later run.

For the NGF solution, the matrix is partitioned as

$$\begin{pmatrix} \mathrm{A} & \mathrm{B} \\ \mathrm{C} & \mathrm{D} \end{pmatrix} \begin{pmatrix} \mathrm{I}_1 \\ \mathrm{I}_2 \end{pmatrix} = \begin{pmatrix} \mathrm{E}_1 \\ \mathrm{E}_2 \end{pmatrix} \tag{6-6}$$

where A is the interaction matrix for the initial structure, D is the matrix for the added structure, and B and C represent mutual-interaction matrices.

In the first step of the NGF procedure the matrix A for the basic model is evaluated and factored into LU form. The factors $\mathrm{A}_\ell$ and $\mathrm{A}_u$ are then written on a file along with other necessary data, including the model geometry and frequency. When a solution is required with an addition to the basic model, matrices B, C and D in (6-6) are evaluated. Then the partitioned matrix is transformed so that

$$\begin{pmatrix} \mathrm{A} & \mathrm{B} \\ \mathrm{C} & \mathrm{D} \end{pmatrix} \rightarrow \begin{pmatrix} \mathrm{A}_\ell \mathrm{A}_u & \mathrm{A}^{-1}\mathrm{B} \\ \mathrm{C} & \mathrm{D}'_\ell \mathrm{D}'_u \end{pmatrix}$$

where $\mathrm{D}'_\ell$ and $\mathrm{D}'_u$ are LU factored matrices, such that

$$\mathrm{D}'_\ell \mathrm{D}'_u = \mathrm{D}' = \mathrm{D} - \mathrm{C}\mathrm{A}^{-1}\mathrm{B}.$$

Multiplication by $\mathrm{A}^{-1}$ is to be interpreted as solution for each column of the matrix on the right, using the LU factored form of A. For each excitation vector, the solution for current

is obtained as

$$\mathrm{I}_2 = \mathrm{D}'^{-1}(\mathrm{E}_2 - \mathrm{CA}^{-1}\mathrm{E}_1)$$
$$\mathrm{I}_1 = \mathrm{A}^{-1}\mathrm{E}_1 - (\mathrm{A}^{-1}\mathrm{B})\mathrm{I}_2.$$

A complete LU factored matrix could be obtained from the partitioned matrix, but then the advantage of symmetry in storing and operating with $\mathrm{A}_\ell \mathrm{A}_u$ would be lost.

Electrical connections between the new and old (NGF) structure require special treatment. If a new wire or patch connects to an old wire, the current basis function for the old wire segment is changed by the modified condition at the junction. Since the elements in matrix A cannot be changed, the old basis function is forced to have zero amplitude by adding a new equation having all zeros except for a one in the column of the old basis function. A new column is then added in matrices B and D for the modified basis function in the NGF structure. Hence, connection of a single new segment to a junction of $N_j$ segments in the NGF structure will result in $N_j + 1$ new unknowns in the new part of the partitioned matrix. When a new wire connects to a patch in the NGF structure the patch must be divided into four new patches to apply the surface-junction condition. Hence two equations are needed to set the two current components on the old patch to zero, and eight new unknowns are generated for the current components on the four new patches. Hence connection to a patch in the NGF model results in ten new unknowns, plus those for the new segments.

# 7. Extensions to the Model for Antennas and Scatterers

Previous sections have dealt with the problem of determining the current induced on a structure by an arbitrary excitation. We now consider some specific problems in modeling antennas and scatterers, including models for a voltage source on a wire, lumped and distributed loads, nonradiating networks and transmission lines. Methods of calculating some observable quantities are also covered, including input impedance, radiated field and antenna gain.

## 7.1 Voltage Source Models

Modeling voltage sources is probably the most critical step in the MoM analysis of wire antennas, since errors are directly reflected in the computed input admittance and hence in the gain and other related quantities. The basic requirements for the source model are that it accurately represent the desired source voltage and, as closely as possible, duplicate the physical characteristics of the actual antenna source, including the width of the excitation region on the wire. In addition the model should introduce a minimum of computational overhead. It is highly desirable that the MoM impedance matrix be independent of the location of the source so that solutions for several different excitations can be obtained with a single evaluation and inversion of the matrix.

NEC presently includes two models for voltage sources: the applied-field or gap model, and the bicone or charge-discontinuity model. These source models are described in this section and typical results are shown. A coaxial-line source model is included in this discussion, since this model is in some ways similar to the bicone source model and has been used successfully in codes similar to NEC. Each of these source models involves either a modification of the boundary condition to force a non-zero electric field on the wire or a modification of the current expansion to produce a discontinuity in charge density across the source, or a combination of these factors. Of the source models now offered in NEC, it will be seen that the applied-field source yields generally stable results but, particularly at low frequencies, may have a much wider distribution than the actual source. However, the source width is usually of secondary importance except for its effect on source-gap capacitance. The bicone source model produces a more localized excitation when used on thin wires, but may give inaccurate results for input impedance when used on thicker wires or on segments with large radius-to-length ratios. Hence the applied-field source model is recommended for general use.

### 7.1.1 The Applied-Field Source Model

The simplest and most reliable source model now available in NEC is the applied-field or gap source. For a source voltage $V_i$ on segment $i$ with segment length $\Delta_i$ the field at the match point at the center of segment $i$ is set to

$$E_i = V_i/\Delta_i. \tag{7-1}$$

The field at all match points without sources remains zero. It is recommended that the segments on either side of the source segment have lengths equal to that of the source

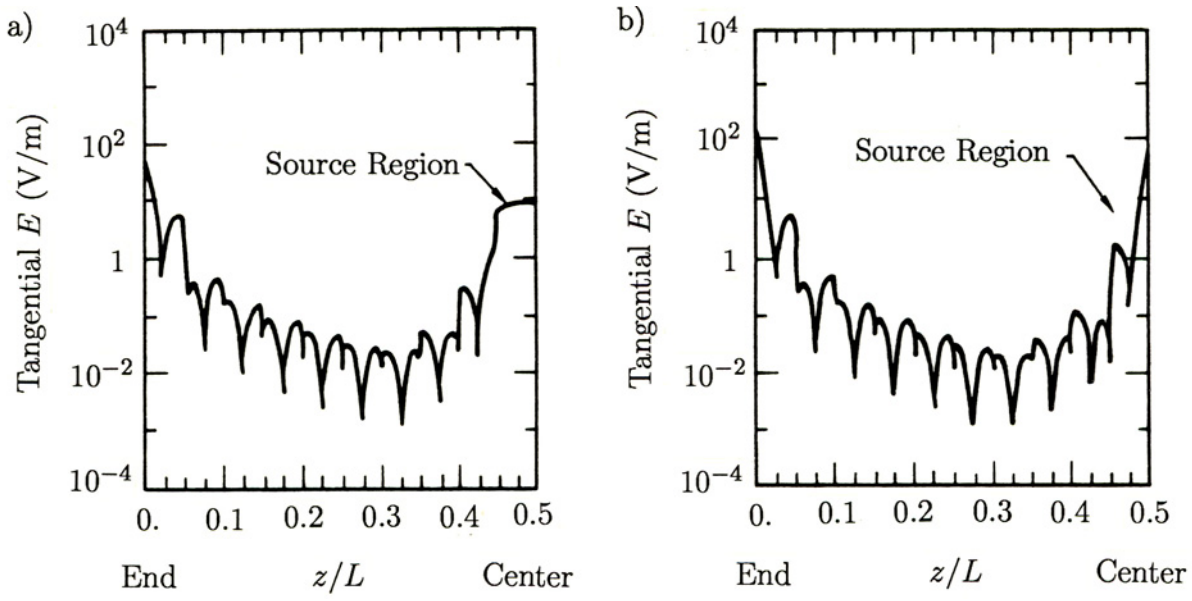


**Fig. 7-1** Near electric field along the wire on a linear dipole with $\Omega = 2\ln 2h/a = 15$ for: a) an applied-field voltage source and b) a bicone source. (From Adams et al. [58].)

segment. When this rule is followed, the electric field along the wire resulting from a solution using the applied-field source model will generally be found to have the prescribed value at the center of the source segment, remain approximately constant over the segment and drop to small values beyond the region of the segment ends. A typical near-field distribution is shown in Fig. 7-1a. The shape of this distribution will depend on the wire radius, since with the thin-wire approximation the field cannot change significantly over a distance much less than the wire radius. However, the line integral of field over the source region typically remains close to the source voltage over a wide range of wire radii.

When the source segment and adjacent segments have unequal lengths the voltage resulting from the applied-field model may differ from the prescribed value, resulting in inaccurate evaluation of the input impedance. Sometimes unequal segment lengths can be used without significant loss of accuracy. Good results have been obtained with a short source segment on the end of a transmission line connecting to much longer segments on the transmission line wires. However, in general caution is advised when equal-length segments cannot be used in the source region. The actual voltage resulting from the model can be obtained by integrating the near field, although the computation will require additional effort.

Ideally, the applied-field source model introduces a voltage $V_i$ between the ends of the source segment. Hence the antenna input admittance could be computed using the current at the segment ends, or in an unsymmetric case the average of the current at the two ends. In practice the segment is usually sufficiently short so that the current variation over its length is small and the current at the center can be used rather than at the ends. Hence the input admittance is computed as $I_i/V_i$ where $I_i$ is the current at the center of segment $i$. The use of the current value at the segment center may be a source of error when the current is changing rapidly as at the base of a $\lambda/2$ monopole. No modification of the current

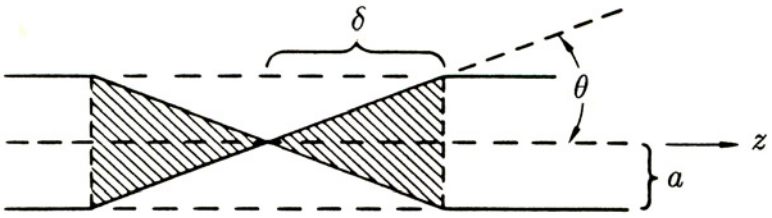


**Fig. 7-2** The biconical transmission line source on a wire.

expansion is needed with the applied-field source model, since the normal expansion allows the charge density to change sufficiently rapidly over the width of the source segment.

### 7.1.2 The Bicone Source Model

The bicone source was developed in an attempt to obtain a narrower distribution of the source field than is provided by the applied-field source. The bicone source model is similar to one used by Andreasen and Harris [59], and its adaptation to a code similar to NEC was reported by Adams et al. [58]. For this model the source region is viewed as a biconical transmission line, as shown in Fig. 7-2, with the apex of the cones at the junction between segments. The electric field due to the applied source voltage has been shrunk to a delta-function distribution in the bicone, so it is not seen at any of the match points on the wire. However, a discontinuity in the derivative of current is introduced at the source, as required by the transmission-line model, and this perturbation of the current produces a field that illuminates the entire structure.

The voltage between points at $\pm z$ on the bicone can be related to the derivative of current through the transmission-line equation as

$$V(z) = \frac{jZ_0}{k}\frac{dI(z)}{dz}$$

where $Z_0$ is the characteristic impedance of the bicone with half-angle $\theta$,

$$Z_0 = \frac{\eta}{\pi}\ln(\cot\theta/2) \approx 120\ln(2/\theta).$$

The actual biconical shape of the conductor is not modeled in NEC. Hence, since the choice of cone angle $\theta$ is uncertain for the cylindrical wire, Adams et al. [58] averaged $Z_0$ for $\delta$ in Fig. 7-2 varying from zero at the source to $\Delta/2$ at the match point, assuming the segments on either side of the source have lengths $\Delta$. The average impedance is then

$$Z_{\text{avg}} = \frac{2}{\Delta}\int_0^{\Delta/2} 120\ln\left(\frac{2\delta}{a}\right)\,d\delta = 120\left[\ln\left(\frac{\Delta}{a}\right) - 1\right].$$

Using this value for characteristic impedance and allowing for an unsymmetric current distribution about the source, the discontinuity in the derivative of current at the source for a voltage $V_0$ is

$$\left.\frac{dI(z)}{dz}\right|_{z=0+} - \left.\frac{dI(z)}{dz}\right|_{z=0-} = \frac{-jkV_0}{60[\ln(\Delta/a) - 1]}. \tag{7-2}$$

This discontinuity in the derivative of current is introduced into the NEC solution by modifying the current expansion on the wire. For a bicone source at the first end of segment $\ell$, the current expansion of equation (3-8) becomes

$$I(s) = \sum_{i=1}^{N} \alpha_i f_i(s) + \beta_\ell f_\ell^*(s) \tag{7-3}$$

where $f_\ell^*(s)$ is a new basis function centered on segment $\ell$, as defined in section 3.2, but computed as if the first end of segment $\ell$ were a free end and the segment radius were zero. Hence $f_\ell^*$ goes to zero with non-zero derivative at the source location. If the part of $f_\ell^*$ on segment $\ell$ is

$$f_\ell^*(s) = A_\ell^* + B_\ell^* \sin k(s - s_\ell) + C_\ell^* \cos k(s - s_\ell), \qquad |s - s_\ell| < \Delta_\ell/2$$

then

$$\left.\frac{d}{ds} f_\ell^*(s)\right|_{s=s_\ell - \Delta_\ell/2} = B_\ell^* \cos(k\Delta_\ell/2) + C_\ell^* \sin(k\Delta_\ell/2).$$

Since the sum of the normal basis functions has continuous value and derivative at $s = s_\ell - \Delta_\ell/2$, the current in (7-3) has a discontinuity in derivative of

$$\lim_{\epsilon \to 0} \left[ \left.\frac{d}{ds} I(s)\right|_{s=s_\ell - \Delta_\ell/2 + \epsilon} - \left.\frac{d}{ds} I(s)\right|_{s=s_\ell - \Delta_\ell/2 - \epsilon} \right] = \beta_\ell \left[ B_\ell^* \cos(k\Delta_\ell/2) + C_\ell^* \sin(k\Delta_\ell/2) \right].$$

Hence, from (7-2), a source voltage of $V_0$ requires a value of $\beta_\ell$ in (7-3) of

$$\beta_\ell = \frac{-jV_0}{60} \Big\{ \left[ \ln(\Delta_\ell/a_\ell) - 1 \right] \left[ B_\ell^* \cos(k\Delta_\ell/2) + C_\ell^* \sin(k\Delta_\ell/2) \right] \Big\}^{-1}. \tag{7-4}$$

While the introduction of a bicone source into a model changes the current expansion, it does not change the MoM impedance matrix. The amplitude of the $f_\ell^*$ function in (7-3) is a known value fixed by the source voltage, so the field due to this current function goes on the right-hand side of the matrix equation. The matrix equation then becomes

$$[G_{ij}][\alpha_j] = [E_i] + \beta_\ell [F_i]$$

where $F_i$ is the excitation for segment- or patch-equation number $i$ due to the field of $f_\ell^*$, and $E_i$ is the excitation field due to any other sources. Thus the matrix $G$ is independent of the bicone source location, as it is for other sources. The solution for the expansion coefficients needed in (7-3) is

$$[\alpha_i] = [G_{ij}]^{-1} \Big\{ [E_j] + \beta_\ell [F_j] \Big\}.$$

This implementation of the bicone source is easily extended to multiple sources. The addition of the basis function $f_\ell^*$ to the current expansion appears to introduce an asymmetry in the current. However, this is not the case, since the other basis functions have the same

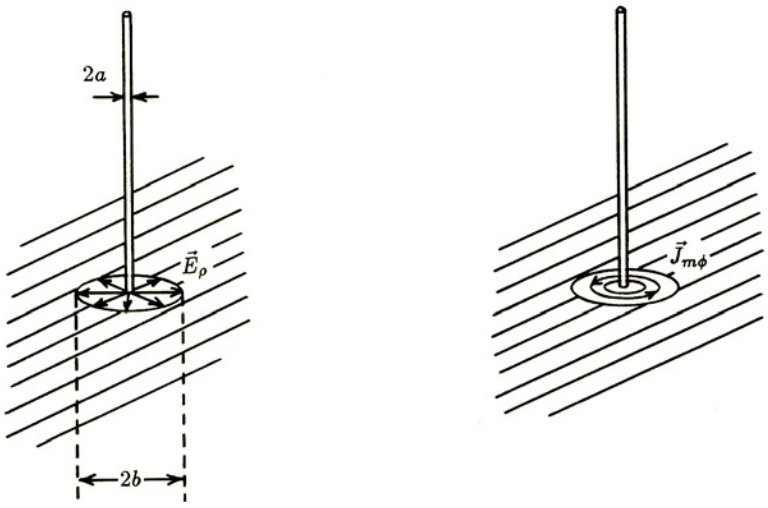


**Fig. 7-3** The coaxial-line source and equivalent magnetic current frill.

form as $f_\ell^*$ except for the discontinuous derivative, and their amplitudes can adjust to produce an exactly symmetric current if appropriate.

On a thin wire, the bicone source results in an effective applied field that is much more localized in the source region than that of the applied-field source, as can be seen in Fig. 7-1. The applied-field source results in a nearly rectangular field distribution over the source segment while the field of the bicone source approaches a delta function. The integrals of these two source-field distributions will yield approximately the same voltages. However, as the wire radius is increased both field distributions become more rounded. For larger wire radius the integral of the field produced by the bicone source will differ substantially from the required voltage due to approximations in deriving (7-2), so this source model should only be used with very thin wires.

### 7.1.3 A Coaxial-Line Source Model

A source model can also be developed to approximate the common practical case of excitation of a wire by a coaxial transmission line through a ground plane. This model is not implemented in the presently released versions of NEC, but results of tests are included here for comparison with the other source models. The coaxial source has been used in a number of wire antenna codes. Thiele [60] uses it with point matching and entire-domain basis functions. The treatment of Popović et al. [23] is more compatible with NEC since it uses point matching and a polynomial basis in which a discontinuity can be introduced into the derivative.

As illustrated in Fig. 7-3, the coaxial line with electric field

$$E_\rho(\rho) = \frac{V_0}{\rho \ln(b/a)} \qquad \text{for} \qquad a < \rho < b$$

in the opening is replaced by the equivalent case of a frill of magnetic current $J_{m\phi} = -E_\rho$ over the plane. It is assumed here that only the TEM mode is present in the coaxial line

opening, a condition that Popović et al. state is accurate for $kb < 0.1$. The magnetic current frill produces an excitation field over the structure. On the axis of the frill the $z$ component of this field is

$$E_z(z) = \frac{V_0}{2\ln(b/a)}\left(\frac{e^{-jkR_a}}{R_a} - \frac{e^{-jkR_b}}{R_b}\right)$$

where $R_a = (z^2 + a^2)^{1/2}$ and $R_b = (z^2 + b^2)^{1/2}$. Thiele [60] gives the field at an arbitrary location. This field illuminates the entire structure, and hence fills the excitation vector on the right of the matrix equation.

At the frill location the discontinuity in $\mathbf{E}_\rho$ requires a discontinuity in charge density and hence in the derivative of current on the wire of

$$\left.\frac{dI(z)}{dz}\right|_{z=0+} - \left.\frac{dI(z)}{dz}\right|_{z=0-} = \frac{-j2\pi kV_0}{\eta\ln(b/a)}.$$

This discontinuity in derivative of current is introduced into the current expansion as was done with the bicone source. Hence the coaxial-line source involves both a modification of the current expansion and a direct excitation due to the impressed field. As the wire radius is reduced the field due to the magnetic-current frill becomes increasingly concentrated in the source region. The difficulty in sampling this field is a limitation of the coaxial-line source for thin wires.

### 7.1.4 Comparison of Source Models

Input admittances obtained with the applied-field, bicone and coaxial-line source models were compared with the second order King-Middleton results [61] for a dipole with $kh = 1.6$ for half length $h$ and for three thicknesses, $\Omega = 8$, 11 and 20. The King-Middleton values are not necessarily "correct" but are a convenient and widely accepted standard. Second order King-Middleton is the result of two iterations of a solution of Hallén's integral equation with a delta-function source model.

Results from the applied-field source model are shown in Fig. 7-4. For $\Omega = 8$, G converges, although ten percent from King-Middleton. B continues to change due, at least in part, to the increasing susceptance as the source gap becomes narrower. It has been suggested [62] that the applied-field source model could be improved by subtracting a gap susceptance and then adding an empirically determined value for the actual antenna feed. King [63] applied a similar correction to the King-Middleton results using the measured susceptance at a single frequency. For $\Omega$ of 11 and 20 the NEC results show increasingly better convergence and agreement with King-Middleton.

The bicone source results, shown in Fig. 7-5, blow up for $\Omega = 8$ at 20 segments. A similar blow-up occurs for $\Omega = 11$ with 90 segments but is excluded from the plot. The results for $\Omega = 11$ appear useable to about 40 segments. At $\Omega = 20$ the results are acceptable but neither relative convergence nor agreement with King-Middleton is as good as with the applied-field source. These results demonstrate the failure of the bicone model with increasing wire radius or small $\Delta/a$.

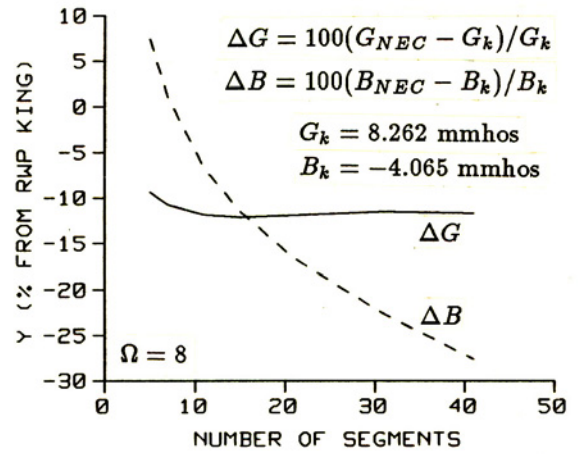


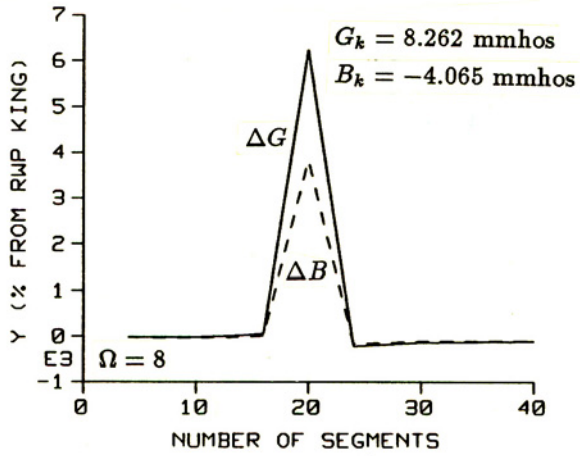


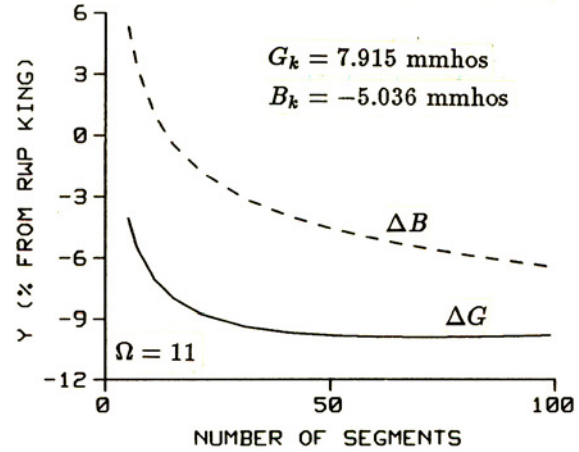


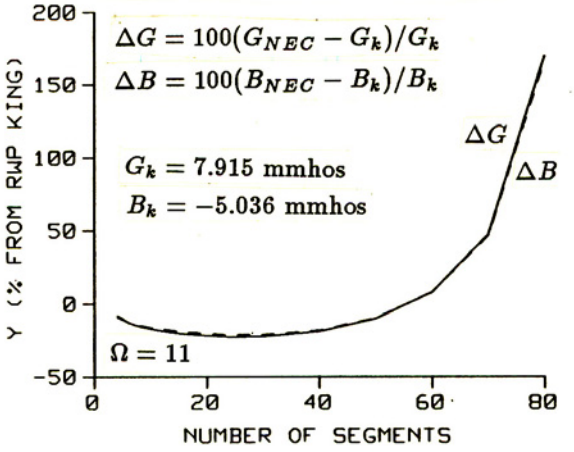


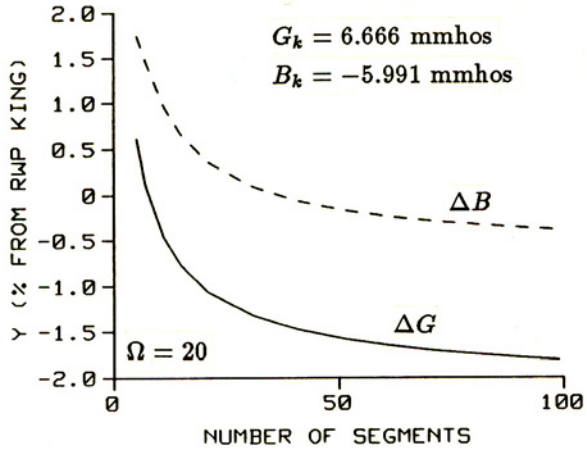


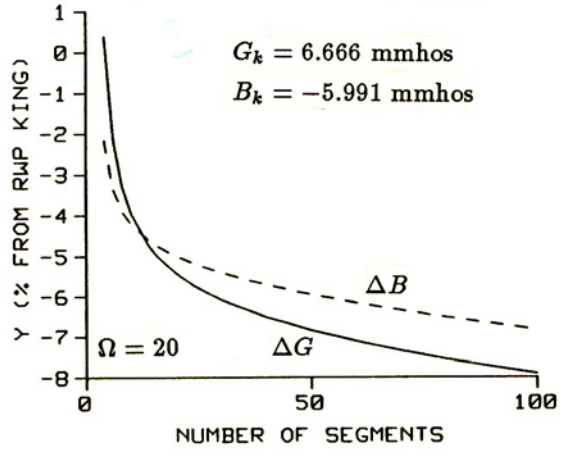


**Fig. 7-4** Convergence of input admittance from the applied-field source relative to King-Middleton result $G_k + jB_k$. Dipoles with $\Omega = 2\ln(2h/a)$ of 8, 11 and 20 are shown for length $kh = 1.6$.

**Fig. 7-5** Convergence of input admittance from the bicone source relative to King-Middleton result $G_k + jB_k$. Dipoles with $\Omega = 2\ln(2h/a)$ of 8, 11 and 20 are shown for length $kh = 1.6$.

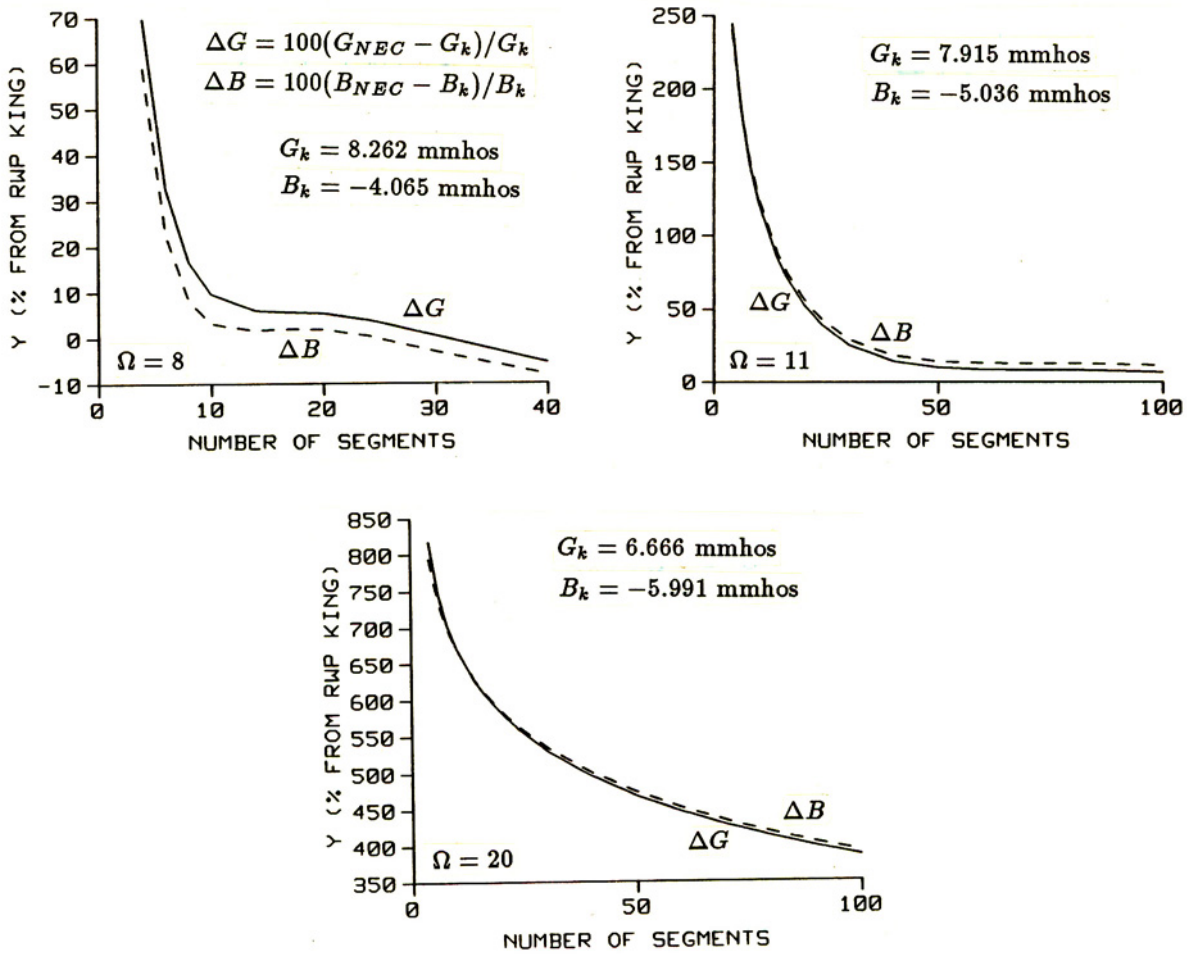


**Fig. 7-6** Convergence of input admittance from the coaxial-line source in NEC relative to King-Middleton result $G_k + jB_k$. Dipoles with $\Omega = 2\ln(2h/a)$ of 8, 11 and 20 are shown for length $kh = 1.6$.

Accuracy of the coaxial-line source model depends on a sufficient sampling of the field of the magnetic current frill. This field decreases by half in a distance on the order of the wire radius. As shown in Fig. 7-6, the convergence of the coaxial-line source is best for $\Omega = 8$. Convergence is slow for $\Omega = 11$ and very poor for $\Omega = 20$. Popović et al. [23] recommend a nonuniform sampling with about four match points within a distance of $3a$ to $10a$ on either side of the source. The NEC model also yielded better results with small segments in the source region, tapering to larger segments away from the source. However, this approach requires extra effort and makes the model source dependent. For very thin wires, such as the $\Omega = 20$ dipole, it seems nearly impractical to sample sufficiently finely to get good results from the coaxial source. However, the structure of the coaxial feed is important only when the radius of the wire and the outer conductor are of significant size relative to the wavelength. For thin wires the applied-field source could as well be used.

For reasons demonstrated by the above results, it is recommended that the applied-field voltage source model in NEC be used in most cases. For electrically thin wires the effect of the actual feed structure of an antenna on its input impedance will usually be negligible, and the results of the applied-field source can be used directly. In complicated cases, such

as the feed of an AM broadcast tower, the source region may not resemble any of the simple numerical models, and an empirical correction may be necessary.

### 7.2 Lumped or Distributed Loading

Thus far, it has been assumed that all structures to be modeled are perfect electric conductors. The EFIE is easily extended to imperfect conductors by modifying the boundary condition in equation (2-4) to

$$\hat{\mathbf{n}}(\mathbf{r}) \times \left[\mathbf{E}^s(\mathbf{r}) + \mathbf{E}^I(\mathbf{r})\right] = Z_s(\mathbf{r}) \left[\hat{\mathbf{n}}(\mathbf{r}) \times \mathbf{J}_s(\mathbf{r})\right]$$

where $Z_s(\mathbf{r})$ is the surface impedance at $\mathbf{r}$ on the conducting surface. For a wire the boundary condition is

$$\hat{\mathbf{s}} \cdot \left[\mathbf{E}^s(\mathbf{r}) + \mathbf{E}^I(\mathbf{r})\right] = Z_w(s) I(s)$$

with $\mathbf{r}$ and $\hat{\mathbf{s}}$ the position vector and tangent vector at $s$ on the wire and $Z_w(s)$ the impedance per unit length at $s$. The matrix equation can then be written

$$\sum_{j=1}^{N} G_{ij}\alpha_j = -E_i + \frac{Z_i}{\Delta_i} I_i, \qquad i = 1, \ldots, N$$

where $\alpha_j$ is the amplitude of basis function $j$, $E_i$ is the incident field on segment $i$, $I_i$ is the current at the center of the segment, $Z_i$ is the total impedance on the segment and $\Delta_i$ is the segment length.

The impedance term can be viewed as an applied-field model of a voltage source with the voltage proportional to the current. It is assumed that the current is essentially constant, with value $I_i$, over the length of the segment, which is reasonable for the electrically short segments used in the integral equation solution.

The impedance term can be combined with the matrix by expressing $I_i$ in terms of the $\alpha_j$ as

$$I_i = \sum_{j=1}^{N} \alpha_j A_j^i$$

where $A_j^i$ is the coefficient of the constant term in the current expansion of equation (3-3) for any basis function $j$ extending onto segment $i$. The matrix equation modified by loading is then

$$\sum_{j=1}^{N} G'_{ij}\alpha_j = -E_i, \qquad i = 1, \ldots, N$$

where

$$G'_{ij} = G_{ij} - A_j^i Z_i / \Delta_i.$$

For a lumped circuit element, $Z_i$ is computed from the circuit equations. For a distributed impedance, $Z_i$ represents the impedance of a length $\Delta_i$ of wire. In the case of a

round wire with finite conductivity $\sigma$ and permeability $\mu$ the impedance for a segment $i$ with length $\Delta_i$ and radius $a_i$ is

$$Z_i = \frac{j\Delta_i}{a_i}\sqrt{\frac{\omega\mu}{2\pi\sigma}}\left[\frac{\mathrm{Ber}(q)+j\mathrm{Bei}(q)}{\mathrm{Ber}'(q)+j\mathrm{Bei}'(q)}\right]$$

where $q=\sqrt{\omega\mu\sigma}a_i$ and Ber and Bei are Kelvin functions. This expression takes account of the limited penetration of the field into an imperfect conductor.

### 7.3 Nonradiating Networks and Transmission Lines

Antennas often include transmission lines, lumped-circuit networks or a combination of these connecting between different parts or elements. When the currents on transmission lines or at network ports are balanced, the fields produced by these elements, both for near field and radiation, can often be neglected. The effect of the network or transmission line is then simply to establish a relation between the voltage and current at each of the connection points. The solution for the antenna currents can be obtained by solving the equations describing the networks or transmission lines together with the moment-method equations for the radiating structure. This approach avoids the substantial increase in the number of unknowns that would result from modeling the transmission line wires or network leads with segments. For transmission lines with characteristic impedance on the order of 150 ohms or less the spacing of the wires relative to radius may be too small for a thin-wire model, so the ideal transmission line model becomes the only practical approach.

The procedure used in NEC is to compute a driving-point-interaction matrix from the complete moment-method matrix to characterize the electromagnetic interactions. The driving-point-interaction equations are then solved together with the network or transmission line equations to obtain the induced currents and voltages. In this way the larger moment-method matrix is not changed by addition or modification of networks or transmission lines. Another advantage of this approach is that the connection of networks does not alter the matrix structure resulting from symmetries in the model, so the efficient solution methods for symmetric structures can be used with asymmetric network connections. As a result, it may be advantageous in NEC to model a one-port load as a two-port network with appropriate parameters when the value of the load must be changed many times or when connection of the load would destroy structure symmetry.

The solution described below assumes an electromagnetic-interaction matrix equation of the form

$$[G_{ij}][I_j] = -[E_i] \tag{7-5}$$

where $E_i$ is the exciting electric field on wire segment $i$ and $I_j$ is the current at the center of segment $j$. In NEC the interaction equation has the form

$$[G'_{ij}][A_j] = -[E_i]$$

where $A_j$ is the amplitude of the $j$th basis function $f_j$ in the current expansion

$$I(s) = \sum_{j=1}^{N_s} A_j f_j(s).$$

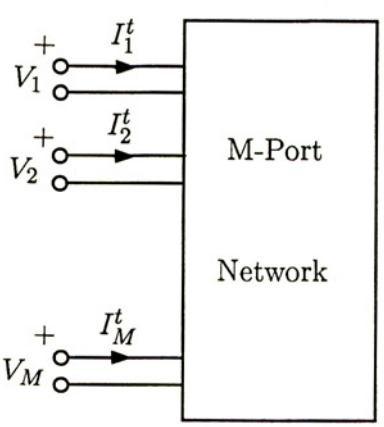


**Fig. 7-7** Voltage and current reference directions at network connection points.

The same solution procedure can be used, however, by computing $[I_j]$ from $[A_j]$ whenever $[I_j]$ is needed. This must be done when starting with the matrix $[G'_{ij}]$ and computing the elements of the inverse matrix $[G_{ij}]^{-1}$ representing the current on segment $i$ due to a unit field on segment $j$.

A model consisting of $N_s$ segments will be assumed with a general $M$-port network connected to segments 1 through $M$. The network is described by the admittance equation

$$\sum_{j=1}^{M} Y_{ij} V_j = I_i^t, \qquad i = 1, \ldots, M \tag{7-6}$$

where $V_i$ and $I_i^t$ are the voltage and current at port $i$, with reference directions as shown in Fig. 7-7. The connection of a network port to a segment is illustrated in Fig. 7-8. The segment is broken, and the port is connected so that

$$I_i^t = -I_i \tag{7-7}$$

where $I_i$ is the segment current. A voltage source of strength $V_j$ is shown connected across the network port at segment $j$ so that

$$I_j^t = I_j^g - I_j. \tag{7-8}$$

The port voltage, either with or without a voltage source, will be related to the field on the segment by the applied-field voltage source model of equation (6-1). This port voltage represents an additional unknown in the problem, unless its value is fixed by connection

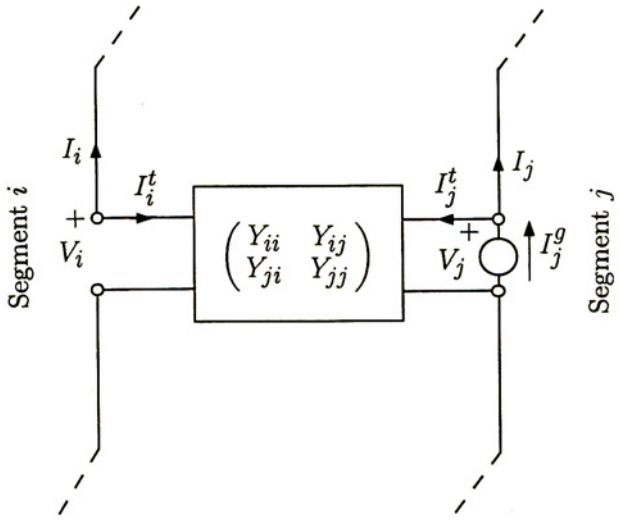


**Fig. 7-8** Network connections to segments with and without a voltage source.

of a voltage source. We will assume that segments 1 through $M_1$ are connected to network ports without voltage sources, and segments $M_1 + 1$ through $M$ are connected to network ports with voltage sources. The remaining segments have no network connections but may have voltage sources. In addition, all of the segments may be excited by an incident field represented by $E_i^I$ on segment $i$. The total field on segment $i$ is then

$$E_i = E_i^P + E_i^I, \qquad i = 1, \ldots, N_s$$

where $E_i^P = V_i/\Delta_i$, $V_i$ is the voltage due to either a network port or a voltage source and $\Delta_i$ is the segment length. An additional voltage drop can result from a finite impedance of the segment. This voltage is outboard of the network port. It is not shown explicitly here since, being proportional to the unknown current on the segment, it is included in the moment-method matrix.

Equation (7-5) may be solved for current as

$$I_i = -\sum_{j=1}^{N_s} G_{ij}^{-1} E_j, \qquad i = 1, \ldots, N_s \tag{7-9}$$

where $G_{ij}^{-1}$ is the $(i, j)$th element of the inverse of matrix $G$. The equations from (7-9) for segments that have network ports without voltage sources are then written, with known quantities on the right-hand side, as

$$\sum_{j=1}^{M_1} G_{ij}^{-1} E_j^P + I_i = B_i, \qquad i = 1, \ldots, M_1 \tag{7-10}$$

where

$$B_i = -\sum_{j=1}^{M_1} G_{ij}^{-1} E_j^I - \sum_{j=M_1+1}^{N_s} G_{ij}^{-1} E_j.$$

Similarly, the network equations (7-6) are written using (7-7) as

$$\sum_{j=1}^{M_1} Y'_{ij} E_j^P + I_i = C_i, \qquad i = 1, \ldots, M_1 \tag{7-11}$$

where

$$Y'_{ij} = \Delta_j Y_{ij}$$

$$C_i = -\sum_{j=M_1+1}^{M} Y_{ij} V_j.$$

The current is eliminated between (7-10) and (7-11) to yield

$$\sum_{j=1}^{M_1} \left( G_{ij}^{-1} - Y'_{ij} \right) E_j^P = B_i - C_i, \qquad i = 1, \ldots, M_1. \tag{7-12}$$

The solution procedure is then to solve (7-12) for $E_j^P$ for $j = 1, \ldots, M_1$. Then, with the complete excitation vector determined, (7-9) is evaluated to determine $I_i$ for $i = 1, \ldots, N_s$. Finally, the remaining network equations are used with (7-8) to compute the generator currents as

$$I_i^g = \sum_{j=1}^{M} Y_{ij} V_j + I_i, \qquad i = M_1 + 1, \ldots, M. \tag{7-13}$$

The currents $I_i^g$ determine the input admittances seen by the sources.

In NEC, the general $M$-port network considered here is restricted to multiple two-port networks, each connecting a pair of segments. A transmission line is treated as a special case of a two port network with admittance coefficients determined by the ideal transmission line equations. Including optional terminating admittances of $Y_{1T}$ and $Y_{2T}$ on ends one and two of the transmission line, respectively, the admittance coefficients for a line with characteristic admittance $Y_0$ and length $\ell$ are

$$\begin{aligned} Y_{11} &= -jY_0 \cot(k\ell) + Y_{1T} \\ Y_{22} &= -jY_0 \cot(k\ell) + Y_{2T} \\ Y_{12} &= Y_{21} = \pm jY_0 \csc(k\ell). \end{aligned}$$

The lower sign for $Y_{12}$ is used when the transmission line undergoes a twist relative to the reference directions at the connection points, as occurs between elements in a log-periodic dipole antenna, and the upper sign is used otherwise.

It should be remembered that the implicit transmission-line model neglects interactions between the transmission line and the antenna or its environment. This approximation is justified if the currents in the line are balanced, as in a log-periodic dipole antenna, and in general if the transmission line lies in an electric symmetry plane. However, the balance can be upset if the transmission line is connected to an unbalanced load or by unsymmetric interactions. For example, a vertically polarized log-periodic dipole antenna over ground could be unbalance by interaction with the ground, and the importance of this unbalance should be considered in deciding whether to use the ideal transmission-line model. If the unbalance is significant, the transmission line can be modeled explicitly with segments if the two-wire model with the correct characteristic impedance does not violate the thin-wire approximation. Another option would be to use the ideal transmission-line model to represent the balanced currents, and model a single wire with segments along the path of the line to carry the unbalanced component of current. However, this approach raises questions about how to connect the single wire.

### 7.4 Radiated Field, Directivity and Gain

The radiated field of an antenna or reradiated field of a scatterer is found with relative ease once the current induced on the structure has been evaluated through the moment-method solution. The integral to obtain the far-zone field of a straight wire segment or patch can be evaluated in closed form, and the field reflected from or transmitted across an interface with the ground can be evaluated exactly from the plane-wave reflection and transmission coefficients, without the need to evaluate Sommerfeld integrals. The far field

evaluation yields only the field components decreasing as $R^{-1}$, so the surface wave over ground is lost. To include the surface wave, the code offers an option to compute the field at large but finite distances using the asymptotic approximations for the field over ground given in section 5.

### 7.4.1 The Radiated Field in Free Space

For the far-zone evaluation it is assumed that the maximum dimension of the current distribution (actually the maximum distance from the origin) is small relative to the distance to the evaluation point $\mathbf{r}_0$ and also relative to the wavelength. When $|\mathbf{r}_0| \gg |\mathbf{r}'|$ the factor $|\mathbf{r}_0 - \mathbf{r}'|$ in the denominator of the Green's function in (2-1) can be replaced by $r_0 = |\mathbf{r}_0|$. The planar-phase front approximation is used in evaluating the phase, so that $k|\mathbf{r}_0 - \mathbf{r}'|$ in the argument of the exponential is approximated by $kr_0 + \mathbf{k} \cdot \mathbf{r}'$. The vector $\mathbf{k}$ is the wave vector at $\mathbf{r}'$ for the reciprocal problem, when a source is located at the evaluation point $\mathbf{r}_0$. When points $\mathbf{r}_0$ and $\mathbf{r}'$ are in the same medium, $\mathbf{k} = -k\hat{\mathbf{r}}_0$. When these points are on opposite sides of an interface between different media, $\mathbf{k}$ must be found by applying Snell's law at the interface with an incident wave from a source at $\mathbf{r}_0$.

The radiated field due to a structure including wires with current distribution $I_w(s)$ and surfaces with current $\mathbf{J}_s(s)$ is evaluated as

$$\mathbf{E}(\mathbf{r}_0) = \frac{-jk\eta}{4\pi} \frac{e^{-jkr_0}}{r_0} (\mathbf{F}_w + \mathbf{F}_s) \cdot \left( \overline{\overline{\mathbf{I}}} - \hat{\mathbf{r}}_0 \hat{\mathbf{r}}_0 \right) \tag{7-14}$$

where $\mathbf{F}_w$ is due to currents on wires

$$\mathbf{F}_w = \int_\ell \hat{\mathbf{s}} I_w(s) e^{-j(\mathbf{k} \cdot \mathbf{r})} \, ds \tag{7-15}$$

and $\mathbf{F}_s$ is due to currents on surfaces

$$\mathbf{F}_s = \int_S \mathbf{J}_s(\mathbf{r}) e^{-j(\mathbf{k} \cdot \mathbf{r})} \, dA. \tag{7-16}$$

The integrals are over the wire contour $\ell$ and the surface $S$, where $\mathbf{r}$ is the vector to the integration point on the surface or the point $s$ on the wire. The dot product in (7-14), where $\overline{\overline{\mathbf{I}}} = \hat{\mathbf{e}}_x \hat{\mathbf{e}}_x + \hat{\mathbf{e}}_y \hat{\mathbf{e}}_y + \hat{\mathbf{e}}_z \hat{\mathbf{e}}_z$, serves to remove the radial component from the vector integrals. This step is accomplished in the code by taking the dot products with the $\hat{\mathbf{e}}_\theta$ and $\hat{\mathbf{e}}_\phi$ unit vectors transverse to the direction of propagation.

The wire current is represented on each segment in the form

$$I_i(t) = A_i + B_i \sin(k_s t) + C_i[\cos(k_s t) - 1] \tag{7-17}$$

where $A_i$, $B_i$ and $C_i$ are obtained for each segment $i$ from the moment-method solution. The vector $\mathbf{r}$ to a point on segment $i$ is

$$\mathbf{r} = \mathbf{r}_i + t\hat{\mathbf{u}}_i$$

where $\mathbf{r}_i$ is the location of the segment center, $\hat{\mathbf{u}}_i$ is the unit vector in the direction of the segment, and $t$ varies from $-\Delta_i/2$ to $\Delta_i/2$ for segment length $\Delta_i$. Then for $N$ segments, the integral for $\mathbf{F}_w$ becomes

$$\mathbf{F}_w = \sum_{i=1}^{N} \hat{\mathbf{u}}_i Q_i e^{-j(\mathbf{k}\cdot\mathbf{r}_i)}$$

where

$$Q_i = \int_{-\Delta_i/2}^{\Delta_i/2} I_i(t) e^{-jt(\mathbf{k}\cdot\hat{\mathbf{u}}_i)}\, dt.$$

For the current function in (7-17), this integral can be evaluated as

$$\begin{aligned} Q_i = &\left\{ A_i \frac{2\sin(w_i\Delta_i/2)}{w_i} - jB_i \left[ \frac{\sin[(k_s - w_i)\Delta_i/2]}{k_s - w_i} - \frac{\sin[(k_s + w_i)\Delta_i/2]}{k_s + w_i} \right] \right. \\ &\left. + C_i \left[ \frac{\sin[(k_s - w_i)\Delta_i/2]}{k_s - w_i} + \frac{\sin[(k_s + w_i)\Delta_i/2]}{k_s + w_i} - \frac{2\sin(w_i\Delta_i/2)}{w_i} \right] \right\} \end{aligned}$$

where $w_i = \mathbf{k}\cdot\hat{\mathbf{u}}_i$. When $|k\Delta_i|$ is small $Q_i$ is evaluated by the series approximation

$$Q_i \approx \Delta_i A_i - \frac{(\Delta_i/2)^3}{3}\left(w_i^2 A_i + 2jk_s w_i B_i + k_s^2 C_i\right)$$

to avoid loss of precision.

The contribution from surface patches is

$$\mathbf{F}_s = \sum_{i=1}^{M} \mathbf{J}_i S_i e^{-j(\mathbf{k}\cdot\mathbf{r}_i)}$$

where $\mathbf{r}_i$ is the location of the center of patch $i$, $\mathbf{J}_i$ is the current associated with the patch center in the delta-function current expansion and $S_i$ is the area of the patch.

### 7.4.2 Effect of a Ground Plane

When a ground plane is present the total radiated field is evaluated as

$$\mathbf{E} = \mathbf{E}^{\mathrm{D}} + \mathbf{E}^{\mathrm{R}} + \mathbf{E}^{\mathrm{T}}$$

where $\mathbf{E}^{\mathrm{D}}$ and $\mathbf{E}^{\mathrm{R}}$ are the direct and reflected fields, respectively, from sources on the same side of the interface as the evaluation point and $\mathbf{E}^{\mathrm{T}}$ is the field due to sources on the opposite side of the interface from the evaluation point. $\mathbf{E}^{\mathrm{D}}$ is evaluated using (7-14), while $\mathbf{E}^{\mathrm{R}}$ is evaluated as

$$\mathbf{E}^{\mathrm{R}}(\mathbf{r}_0) = \frac{-jk\eta}{4\pi}\frac{e^{-jkr_0}}{r_0}(\mathbf{F}_w^{\mathrm{R}} + \mathbf{F}_s^{\mathrm{R}}) \cdot \left(\bar{\bar{\mathbf{I}}} - \hat{\mathbf{r}}_0\hat{\mathbf{r}}_0\right) \tag{7-18}$$

where

$$\mathbf{F}_w^{\mathrm{R}} = \int_\ell \hat{\mathbf{s}} \cdot \bar{\bar{\mathbf{I}}}_{\mathrm{R}} \cdot \bar{\bar{\mathbf{R}}} I_w(s) e^{-j[\mathbf{k}\cdot(\mathbf{r}\cdot\bar{\bar{\mathbf{I}}}_{\mathrm{R}})]}\, ds$$

and

$$\mathbf{F}_s^{\mathrm{R}} = \int_S \mathbf{J}_s(\mathbf{r}) \cdot \bar{\bar{\mathbf{I}}}_{\mathrm{R}} \cdot \bar{\bar{\mathbf{R}}} e^{-j[\mathbf{k}\cdot(\mathbf{r}\cdot\bar{\bar{\mathbf{I}}}_{\mathrm{R}})]}\, dA.$$

$\bar{\bar{\mathbf{R}}}$ is a dyadic reflection coefficient and $\bar{\bar{\mathbf{I}}}_{\mathrm{R}} = \hat{\mathbf{e}}_x\hat{\mathbf{e}}_x + \hat{\mathbf{e}}_y\hat{\mathbf{e}}_y - \hat{\mathbf{e}}_z\hat{\mathbf{e}}_z$. For perfectly conducting ground $\bar{\bar{\mathbf{R}}} = -\bar{\bar{\mathbf{I}}}$. For a finitely conducting ground, the reflection coefficients for TE and TM polarization are

$$R^{\mathrm{TE}} = \frac{Y_0^{\mathrm{TE}} - Y_s^{\mathrm{TE}}}{Y_0^{\mathrm{TE}} + Y_s^{\mathrm{TE}}} \qquad \text{and} \qquad R^{\mathrm{TM}} = -\frac{Z_0^{\mathrm{TM}} - Z_s^{\mathrm{TM}}}{Z_0^{\mathrm{TM}} + Z_s^{\mathrm{TM}}}$$

where $Y_0^{\mathrm{TE}} = \cos\theta_i/\eta_i$ and $Z_0^{\mathrm{TM}} = \eta_i \cos\theta_i$ with $\theta_i$ the angle between the incident ray and the normal to the interface and $\eta_i$ the intrinsic impedance of the medium in which the ray is propagating. $Y_s^{\mathrm{TE}}$ and $Z_s^{\mathrm{TM}}$ are the surface admittance and impedance of the ground for TE and TM polarization respectively, given in section 5.3. The reflected field is then evaluated from the field of the image of the source ((7-18) without $\bar{\bar{\mathbf{R}}}$) as

$$\mathbf{E}^{\mathrm{R}} = \left[\mathbf{E}^{\mathrm{I}} R^{\mathrm{TM}} + \hat{\mathbf{p}}(\mathbf{E}^{\mathrm{I}} \cdot \hat{\mathbf{p}})(R^{\mathrm{TE}} - R^{\mathrm{TM}})\right]$$

where $\hat{\mathbf{p}}$ is the unit vector normal to the plane of incidence.

The transmission coefficients for TE and TM polarizations are [30]

$$T^{\mathrm{TE}} = \frac{E_t^{\mathrm{TE}}}{E_i^{\mathrm{TE}}} = \frac{2k_{iz}}{k_{iz} + k_{tz}} \qquad \text{and} \qquad T^{\mathrm{TM}} = \frac{H_t^{\mathrm{TM}}}{H_i^{\mathrm{TM}}} = \frac{2k_t^2 k_{iz}}{k_t^2 k_{iz} + k_i^2 k_{tz}}$$

where $k_i$ and $k_t$ are the wave numbers of the incident and transmitted waves, respectively. The $z$ component of the incident wave vector $\mathbf{k}_i$ is $k_{iz} = -k_i \cos\theta_i$, and the $z$ component of the transmitted wave vector $\mathbf{k}_t$ is $k_{tz} = [k_t^2 - (k_i^2 - k_{iz}^2)]^{1/2}$.

The electric field components of the transmitted TM wave can be obtained from the relations $\mathbf{E}_i = \eta_i\, \hat{\mathbf{k}}_i \times \mathbf{H}_i$ and $\mathbf{E}_t = \eta_t\, \hat{\mathbf{k}}_t \times \mathbf{H}_t$. The results for $\rho$ and $z$ components of the electric field are

$$E_{tz}^{\mathrm{TM}} = \frac{k_i^2}{k_t^2} R^{\mathrm{TM}} E_{iz}^{\mathrm{TM}} \qquad \text{and} \qquad E_{t\rho}^{\mathrm{TM}} = \frac{k_i^2 k_{tz}}{k_t^2 k_{iz}} R^{\mathrm{TM}} E_{i\rho}^{\mathrm{TM}}.$$

The electric field transmitted across the interface from an incident wave with strength $\mathbf{E}$ and arbitrary polarization is then obtained with a dyadic transmission coefficient as

$$\mathbf{E}^{\mathrm{T}} = (T_{\rho\rho}\hat{\mathbf{e}}_\rho\hat{\mathbf{e}}_\rho + T_{zz}\hat{\mathbf{e}}_z\hat{\mathbf{e}}_z + T_{\phi\phi}\hat{\mathbf{e}}_\phi\hat{\mathbf{e}}_\phi) \cdot \mathbf{E}$$

where

$$T_{\rho\rho} = \frac{2k_i^2 k_{tz}}{k_i^2 k_{tz} + k_t^2 k_{iz}}, \quad T_{zz} = \frac{2k_i^2 k_{iz}}{k_i^2 k_{tz} + k_t^2 k_{iz}} \quad \text{and} \quad T_{\phi\phi} = \frac{2k_{iz}}{k_{iz} + k_{tz}}.$$

$\mathbf{E}$ is evaluated using (7-14), including only sources on the opposite side of the interface from the evaluation point and replacing $\mathbf{k}$ by $\mathbf{k}_t = (\mathbf{k}_i \cdot \hat{\mathbf{e}}_x)\hat{\mathbf{e}}_x + (\mathbf{k}_i \cdot \hat{\mathbf{e}}_y)\hat{\mathbf{e}}_y + k_{tz}\hat{\mathbf{e}}_z$.

### 7.4.3 Elliptic Polarization

In the code the $\hat{\mathbf{e}}_\theta$ and $\hat{\mathbf{e}}_\phi$ components of radiated electric field are computed in spherical coordinates. In general, these components will be out of phase, resulting in an elliptically polarized wave. The field components are described in time-varying form as

$$\begin{aligned} E_\phi &= E_{\phi 0} \exp[j(\omega t - kr)] \\ E_\theta &= E_{\theta 0} \exp[j(\omega t - kr + \xi)] \end{aligned}$$

so that the wave is linearly polarized when $\xi = 0$ or when either $E_{\theta 0} = 0$ or $E_{\phi 0} = 0$. Otherwise, it is elliptically polarized with major and minor axis magnitudes of

$$E_{\text{major}} = \left[E_{\theta 0}^2 - (E_{\theta 0}^2 - E_{\phi 0}^2)\sin^2\gamma + 2E_{\theta 0}E_{\phi 0}\sin\gamma\cos\gamma\cos\xi\right]^{1/2}$$

$$E_{\text{minor}} = \left[E_{\phi 0}^2 + (E_{\theta 0}^2 - E_{\phi 0}^2)\sin^2\gamma - 2E_{\theta 0}E_{\phi 0}\sin\gamma\cos\gamma\cos\xi\right]^{1/2}$$

where

$$\gamma = \tfrac{1}{2}\tan^{-1}\left(\frac{2E_{\theta 0}E_{\phi 0}\cos\xi}{E_{\theta 0}^2 - E_{\phi 0}^2}\right)$$

is the tilt angle of the major axis from the $\hat{\mathbf{e}}_\theta$ direction. The polarization ellipse is described by the ratio of minor axis to major axis, the tilt angle $\gamma$ and the sense of rotation, which is right-hand if $\xi < 0$ and left-hand if $\xi > 0$.

### 7.4.4 Gain and Directivity

The power gain of an antenna in the direction of the spherical coordinates ($\theta$, $\phi$) is defined as

$$G_p(\theta,\phi) = 4\pi\frac{P_\Omega(\theta,\phi)}{P_{\text{in}}}$$

where $P_\Omega(\theta, \phi)$ is the power radiated per unit solid angle in the direction $(\theta,\phi)$ and $P_{\text{in}}$ is the total power accepted by the antenna from the source. Since quantities in NEC are peak values rather than rms, the input power is evaluated from the voltage and current at the source as

$$P_{\text{in}} = \tfrac{1}{2}\text{Re}(VI^*)$$

and the radiated power density is

$$P_\Omega(\theta,\phi) = \tfrac{1}{2}R^2\text{Re}(\mathbf{E}\times\mathbf{H}^*) = \frac{R^2}{2\eta}|\mathbf{E}|^2$$

where $R$ is the evaluation distance. The power gain is then

$$G_p(\theta,\phi) = \frac{2\pi R^2}{\eta}\frac{|\mathbf{E}|^2}{P_{\text{in}}} = \frac{2\pi}{\eta}\frac{|\mathbf{E}'|^2}{P_{\text{in}}}$$

where $\mathbf{E}' = R\mathbf{E}$ for $R \to \infty$ is the quantity computed by subroutine FFLD in NEC.

The directivity, or directive gain, is

$$G_d(\theta,\phi) = 4\pi \frac{P_\Omega(\theta,\phi)}{P_{\rm rad}}$$

where $P_{\rm rad}$ is the total radiated power. $P_{\rm rad}$ is evaluated in NEC as $P_{\rm rad} = P_{\rm in} - P_{\rm loss}$ where $P_{\rm loss}$ is the power dissipated in ohmic loss in lumped and distributed loads on the wires and in non-radiating networks. $P_{\rm loss}$ does not include power dissipated in a lossy ground.

The power gain and directivity are also calculated for orthogonal field components ($\hat{\mathbf{u}}$, $\hat{\mathbf{v}}$) where $\hat{\mathbf{u}}$ and $\hat{\mathbf{v}}$ may be vertical and horizontal components $\hat{\mathbf{e}}_\theta$, $\hat{\mathbf{e}}_\phi$ or major-axis and minor-axis components. For the component gains $|\mathbf{E}|$ is replaced by $|\mathbf{E}\cdot\hat{\mathbf{u}}|$ or $|\mathbf{E}\cdot\hat{\mathbf{v}}|$ in evaluating $P_\Omega$. The total gain is the sum of these two components.

The code also will compute average power gain by integrating the far-field radiated power over a sector of space with solid angle $\Omega$

$$G_{\rm av} = \frac{1}{\Omega}\int_\Omega G_p(\theta,\phi)\,d\Omega = \frac{4\pi}{\Omega P_{\rm in}}\int_\Omega P_\Omega(\theta,\phi)\,d\Omega.$$

If the solid angle of integration $\Omega$ includes the entire sphere or a subsector of the sphere such that the the radiation pattern of the antenna in that subsector repeats exactly over the remainder of the sphere due to symmetry, then $P_{\rm in}G_{\rm av}$ will be the total radiated power obtained by integrating the far field. This evaluation represents a variational from for the radiated power, so is generally more accurate than $P_{\rm rad}$ evaluated from the voltage and current at the source and ohmic losses. Comparison of these two evaluations of radiated power can provide a useful check on the accuracy of the solution, and particularly on the voltage source model.

When a structure is excited by an incident plane wave the scattering cross section normalized to square wavelength is computed instead of gain. The cross section is

$$\frac{\sigma}{\lambda^2} = \frac{4\pi R^2}{\lambda^2}\frac{W_{\rm scat}}{W_{\rm inc}} = \frac{4\pi R^2}{\lambda^2}\frac{|\mathbf{E}_{\rm scat}|^2}{|\mathbf{E}_{\rm inc}|^2}$$

where $W_{\rm scat}$ is the scattered power per unit area at a distance $R$ in a given direction and $W_{\rm inc}$ is the power per unit area of the incident plane wave.

### 7.5 Maximum Coupling Calculation

Coupling between antennas is often a parameter of interest, especially when a receiving system must be protected from a nearby transmitter. Maximum power transfer between antennas occurs when the source impedance and receiver load impedance are conjugate-matched to their antennas. Determination of the conditions for simultaneously matching to the terminal impedances, and the resulting coupling, is complicated by the antenna interaction, since the input impedance of one antenna depends on the load connected to the other antenna. NEC includes an algorithm for determining the matched loads and maximum coupling by the Linville method [64], a technique used in rf amplifier design.

The first step is to determine the two-port admittance parameters for the coupled antennas by exciting each port with the other port short-circuited, and computing the self and mutual admittances from the MoM solution. In doing this it must be remembered that simple wire segments are shorted unless a voltage source or load is specified on the segment. However, segments with a network or transmission line connection represent open-circuited ports unless they are shorted with a zero voltage source or a shunt admittance on the transmission line. This shorting of network ports is taken care of in the NEC–4 code, but was not handled correctly in earlier versions of NEC.

The maximum coupling determined by the Linville method is

$$G_{\max} = \frac{1}{L}\left(1 - \sqrt{1 - L^2}\right)$$

where

$$L = \frac{|Y_{12}Y_{21}|}{2\mathrm{Re}(Y_{11})\mathrm{Re}(Y_{22}) - \mathrm{Re}(Y_{12}Y_{21})}.$$

The matched load admittance on antenna 2 for maximum coupling is

$$Y_L = \left(\frac{1-\rho}{1+\rho} + 1\right)\mathrm{Re}(Y_{22}) - Y_{22}$$

where

$$\rho = \frac{G_{\max}(Y_{12}Y_{21})^*}{|Y_{12}Y_{21}|}$$

and the corresponding input admittance of antenna 1 is

$$Y_{\mathrm{in}} = Y_{11} - \frac{Y_{21}Y_{12}}{Y_L + Y_{22}}.$$

The coupling for any other terminations is easily obtained from the coefficients $Y_{11}$, $Y_{22}$ and $Y_{12}$.

## REFERENCES


[1] J. Strauch and S. Thompson, *Interactive Graphics Utility for Army NEC Automation (IGUANA)*, Naval Ocean Systems Center, Rept. CR 308, 1985.

[2] R. J. Marhefka and J. W. Silvestro, *Near Zone – Basic Scattering Code User's Manual with Space Station Applications*, Technical Rept. 716199-13, The Ohio State University ElectroScience Laboratory, March 1989.

[3] R. R. McLeod, *Temporal Scattering And Response Software, Users' Manual, Version 2.1 (R)*, UCRL-MA-104861, Lawrence Livermore National Laboratory, CA, September 1990.

[4] A. J. Poggio and E. K. Miller, "Integral Equation Solutions of Three-Dimensional Scattering Problems," Chapter 4 in *Computer Techniques for Electromagnetics*, R. Mittra ed., Pergamon Press, New York, 1973.

[5] R. F. Harrington, *Field Computation by Moment Methods*, The Macmillan Co. New York, 1968.

[6] E. K. Miller et al., *Final Technical Report on the Log-Periodic Scattering Array Program*, MBAssociates Report No. MB-R-70/105, Contract No. F04701-68-C-0188, 1970.

[7] *RCS Computer Program BRACT, Log-Periodic Scattering Array Program – II*, MBAssociates Report No. MB-R-69/46, Contract No. F04801-68-C-0188, 1969.

[8] J. H. Richmond, "Digital Computer Solutions of the Rigorous Equations for Scattering Problems," *Proc. IEEE*, Vol. 53, p. 796, 1965.

[9] J. H. Richmond, "A Wire-Grid Model for Scattering by Conducting Bodies," *IEEE Trans. Antennas and Propagation*, Vol. AP-14, p. 782, 1966.

[10] Y. S. Yeh and K. K. Mei, "Theory of Conical Equiangular Spiral Antennas: Part I – Numerical Techniques," *IEEE Trans. Antennas and Propagation*, Vol. AP-15, p. 634, 1967.

[11] G. J. Burke, E. K. Miller and A. J. Poggio, *Dielectric Ground Interactions with a Log-Periodic Antenna*, Final Report, ECOM-0285-F, U.S. Army Electronics Command, Fort Monmouth, NJ, 1971 (Contract DAAB07-70-C-0285).

[12] *Antenna Modeling Program – Composite User's Manual*, MBAssociates Report No. MB-R-74/46, 1974.

[13] *Antenna Modeling Program – Engineering Manual*, MBAssociates Report No. MB-R-74/62, 1974.

[14] *Antenna Modeling Program – Systems Manual*, MBAssociates Report No. MB-R-74/62, 1974.

[15] *Antenna Modeling Program – Supplementary Computer Program Manual (AMP2)*, MB-Associates Report No. MB-R-75/4, 1975.

[17] G. J. Burke and A. J. Poggio, Numerical Electromagnetics Code (NEC) – Method of Moments, UCID-18834, Lawrence Livermore National Laboratory, CA, January 1981.

[18] G. J. Burke and E. K. Miller, "Modeling Antennas Near to and Penetrating a Lossy Interface," *IEEE Trans. Antennas and Propagation*, Vol. AP-32, No. 10, pp. 1040-1049, 1984.

[16] N. C. Albertsen, J. E. Hansen and N. E. Jensen, *Computation of Spacecraft Antenna Radiation Patterns*, The Technical University of Denmark, Lyngby, Denmark, June 1972.

[19] P. C. Waterman, "Matrix Formulation of Electromagnetic Scattering," *Proceedings of the IEEE*, Vol. 53, pp. 805-812, August 1965.

[20] J. Van Bladel, *Electromagnetic Fields*, McGraw-Hill, New York, 1964.

[21] A. R. Neureuther et al., "A Comparison of Numerical Methods for Thin-Wire Antennas," *Presented at the 1968 Fall URSI Meeting*, Dept. of Electrical Engineering and Computer Sciences, University of California, Berkeley, 1968.

[22] E. K. Miller, *An Evaluation of Computer Programs Using Integral Equations for the Electromagnetic Analysis of Thin Wire Structures*, UCRL-75566, Lawrence Livermore Laboratory, CA, March 1974.

[23] B. D. Popović, M. B. Dragović and A. R. Djordjević, *Analysis and Synthesis of Wire Antennas*, Research Studies Press, New York, 1982.

[24] E. P. Sayer, "Junction Discontinuities in Wire Antenna and Scattering Problems," *IEEE Trans. Antennas and Propagation*, Vol. AP-21, p. 216, 1973.

[25] J. L. Lin, W. L. Curtis and M. C. Vincent, "Radar Cross-Section of a Rectangular Conducting Plane by Wire Mesh Modelling," *IEEE Trans. Antennas and Propagation*, Vol. AP-22, p. 718, 1974.

[26] T. T. Wu and R. W. P. King, "The Tapered Antenna and its Application to the Junction Problem for Thin Wires," *IEEE Trans. Antennas and Propagation*, Vol. AP-24, pp. 42-45, 1976.

[27] S. A. Schelkunoff and H. T. Friis, *Antennas: Theory and Practice*, Wiley, New York, 1952.

[28] A. W. Glisson and D. R. Wilton, *Numerical Procedures for Handling Stepped-Radius Wire Junctions*, Department of Electrical Engineering, University of Mississippi, March 1979.

[29] Brillouin, *Radioélectricité*, April 1922.

[30] J. A. Stratton, *Electromagnetic Theory*, McGraw-Hill, New York, 1941.

[31] A. Sommerfeld, "Über die Ausbreitung der Wellen in der drahtlosen Telegraphie," *Ann. Physik*, Vol. 28, p. 665, 1909.

[32] E. K. Miller, A. J. Poggio, G. J. Burke and E. S. Selden, "Analysis of Wire Antennas in the Presence of a Conducting Half Space: Part I. The Vertical Antenna in Free Space," *Canadian J. Phys.*, Vol. 50, pp. 879-888, 1972.

[33] E. K. Miller, A. J. Poggio, G. J. Burke and E. S. Selden, "Analysis of Wire Antennas in the Presence of a Conducting Half Space: Part II. The Horizontal Antenna in Free Space," *Canadian J. Phys.*, Vol. 50, pp. 2614-2627, 1972.

[34] D. L. Lager and R. J. Lytle, *Fortran Subroutines for the Numerical Evaluation of Sommerfeld Integrals Unter Anderem*, UCRL-51821, Lawrence Livermore Laboratory, CA, May 21, 1975.

[35] J. N. Brittingham, E. K. Miller and J. T. Okada, *SOMINT: An Improved Model for Studying Conducting Objects Near Lossy Half-Spaces*, UCRL-52423, Lawrence Livermore Laboratory, CA, February 24, 1978.

[36] K. A. Norton, "The Propagation of Radio Waves Over the Surface of the Earth and in the Upper Atmosphere," *Proceedings of the Institute of Radio Engineers*, Vol. 25, No. 9, Sept. 1937.

[37] A. Baños, *Dipole Radiation in the Presence of a Conducting Half-Space*, Pergamon Press, New York, 1966.

[38] M. Siegel and R. W. P. King, "Electromagnetic Fields in a Dissipative Half-Space: A Numerical Approach," *J. Appl. Phys.*, 41(6), pp. 2415-2423, 1970.

[39] D. M. Bubenik, "A Practical Method for the Numerical Evaluation of Sommerfeld Integrals," *IEEE Trans. Antennas Propagat.*, vol. AP-25, no. 6, pp. 904-906, 1977.

[40] W. A. Johnson and D. G. Dudley, "Real Axis Integration of Sommerfeld Integrals: Source and Observation Points in Air", *Radio Science*, vol. 18, no. 2, pp. 175-186, March-April 1983.

[41] R. J. Lytle and D. L. Lager, *Numerical Evaluation of Sommerfeld Integrals*, UCRL-51688, Lawrence Livermore Laboratory, CA, October 23, 1974.

[42] P. Y. Parhami, Y. Rahmat-Samii and R. Mittra, "An Efficient Approach for Evaluating Sommerfeld Integrals Encountered in the Problem of a Current Element Radiating Over a Lossy Ground," *IEEE Trans. Antennas Propagat.*, vol. AP-28, no. 1, pp. 100-104, 1980.

[43] I. V. Lindell, E. Alanen and H. Von Bagh, "Exact Image Theory for the Calculation of Fields Transmitted Through a Planar Interface of Two Media," *IEEE Trans. Antennas Propagat.*, vol. AP-34, no. 2, pp. 129-137, Feb. 1986.

[44] W. L. Anderson, *Improved Digital Filters for Evaluating Fourier and Hankel Transform Integrals*, U. S. Geological Survey Report USGS-GD-75-012, Available from NTIS no. PB-242-800, 1975.

[45] E. K. Miller, "A Variable Interval Width Quadrature Technique Based on Romberg's Method," *Journal of Comp. Phys.*, vol. 5, no. 2, April 1970.

[46] J. J. Dongarra, C. B. Moler, J. R. Bunch and G. W. Stewart, *LINPAK User's Guide*, Siam Press, Philadelphia, 1979.

[47] L. B. Felsen and N. Marcuvitz, *Radiation and Scattering of Waves*, Prentice-Hall Inc., Englewood Cliffs, New Jersey, 1973.

[48] L. M. Brekhovskikh, *Waves in Layered Media*, Academic Press, New York, 1980.

[49] T. T. Wu and R. W. P. King, "Lateral Waves: A New Formula and Interference Patterns," *Radio Science*, Vol. 17, No. 3, pp. 521-531, May-June 1982.

[50] R. B. Dingle, *Asymptotic Expansions: Their Derivation and Interpretation*, Academic Press, London, 1973.

[51] M. Abramowitz and I. A. Stegun, *Handbook of Mathematical Functions with Formulas, Graphs and Mathematical Tables*, U. S. Dept. of Commerce, National Bureau of Standards, Applied Mathematics Series 55, December 1972.

[52] R. Ziolkowski, University of Arizona, Private Communication, 1983.

[53] E. K. Miller, R. J. Lytle, D. L. Lager and E. F. Laine, *On Increasing the Radiation Efficiency of Beverage-Type Antennas*, UCRL-52300, Lawrence Livermore National Laboratory, CA, July 6, 1977.

[54] J. R. Wait, "Characteristics of Antennas Over Lossy Earth," Chapter 23 in *Antenna Theory, Part 2*, R. E. Collin and F. J. Zucker, Eds., McGraw-Hill, New York, 1969.

[55] E. K. Miller and F. J. Deadrick, *Computer Evaluation of Loran-C Antennas*, UCRL-51464, Lawrence Livermore National Laboratory, CA 1973.

[56] A. Ralston, *A First Course in Numerical Analysis*, McGraw-Hill, New York, 1965.

[57] G. J. Burke, "Modeling Monopoles on Radial-Wire Ground Screens," *Applied Computational Electromagnetics Newsletter*, Vol. 1, No. 1, February 1986.

[58] R. W. Adams, A. J. Poggio and E. K. Miller, *Study of a New Antenna Source Model*, UCRL-51693, Lawrence Livermore National Laboratory, CA, October 28, 1974.

[59] M. G. Andreasen and F. G. Harris, *Analyses of Wire Antennas of Arbitrary Configuration by Precise Theoretical Numerical Techniques*, Tech. Rept. ECOM 0631-F, Granger Associates, Palo Alto, CA, Contract DAAB07-67-C-0631, 1968.

[60] G. A. Thiele, "Wire Antennas," Chapt. 2 in *Computer Techniques for Electromagnetics*, ed. by R. Mittra, International Series of Monographs in Electrical Engineering, Vol. 7, 1973.

[61] R. W. P. King, *Theory of Linear Antennas*, Harvard University Press, Cambridge, MA 1956.

[62] E. K. Miller, Los Alamos National Laboratory, Private Communication.

[63] R. W. P. King, E. A. Aronson and C. W. Harrison, Jr., "Determination of the Admittance and Effective Length of Cylindrical Antennas," *Radio Science*, Vol. 1, pp. 835-850, 1966.

[64] D. Rubin, *The Linville Method of High Frequency Transistor Amplifier Design*, Naval Weapons Center, Research Department, NWCCL TP 845, Corona Laboratories, Corona, California, March 1969.

[65] G. J. Burke, Enhancements and Limitations of the Code NEC for Modeling Electrically Small Antennas, UCID-20970, Lawrence Livermore National Laboratory, CA, January 1987.

[66] G. J. Burke, Treatment of Small Wire Loops in the Method of Moments Code NEC, UCID-21196, Lawrence Livermore National Laboratory, CA, October 1987.

# APPENDIX A

## Evaluation of the Scalar Potential for Triangular and Constant Charge Functions

The matrix elements in (3-42) represent the scalar potentials of triangular and semi-infinite charge distributions. Since the triangles overlap, their potentials are most efficiently evaluated by computing the potentials of positive and negative ramp functions on a segment and storing the contributions to the separate matrix elements. Considering a segment on the $z$ axis as in Fig. A-1, the matrix elements involve the integrals

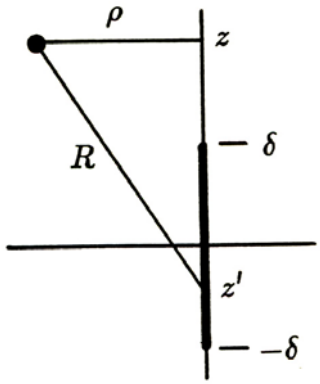


**Fig. A-1** Coordinates for evaluating the potenital due to a segment.

$$\Phi_p(\rho,z)=\frac{1}{4\pi\epsilon}\int_{-\delta}^{\delta}\frac{e^{-jkR}}{R}(\delta+z')\,dz'=\delta\Phi_0(\rho,z,-\delta,\delta)+\Phi_1(\rho,z,-\delta,\delta) \tag{A-1}$$

$$\Phi_m(\rho,z)=\frac{1}{4\pi\epsilon}\int_{-\delta}^{\delta}\frac{e^{-jkR}}{R}(\delta-z')\,dz'=\delta\Phi_0(\rho,z,-\delta,\delta)-\Phi_1(\rho,z,-\delta,\delta) \tag{A-2}$$

where

$$\Phi_0(\rho,z,z_1,z_2)=\frac{1}{4\pi\epsilon}\int_{z_1}^{z_2}\frac{e^{-jkR}}{R}\,dz'$$

$$\Phi_1(\rho,z,z_1,z_2)=\frac{1}{4\pi\epsilon}\int_{z_1}^{z_2}\frac{e^{-jkR}}{R}z'\,dz'$$

and $R=[\rho^2+(z'-z)^2]^{1/2}$. Since $R\,dR=(z'-z)\,dz'$, the integral $\Phi_1$ can be evaluated as

$$\begin{aligned}\Phi_1(\rho,z,z_1,z_2)&=\frac{1}{4\pi\epsilon}\int_{z_1}^{z_2}\frac{e^{-jkR}}{R}(z'-z)\,dz'+z\Phi_0(\rho,z,z_1,z_2)\\&=\frac{j}{4\pi k\epsilon}(e^{-jkR_2}-e^{-jkR_1})+z\Phi_0(\rho,z,z_1,z_2)\end{aligned}$$

where $R_1=[\rho^2+(z_1-z)^2]^{1/2}$ and $R_2=[\rho^2+(z_2-z)^2]^{1/2}$. Thus

$$\Phi_p(\rho,z)=(\delta+z)\Phi_0(\rho,z,z_1,z_2)+\frac{j}{4\pi k\epsilon}(e^{-jkR_2}-e^{-jkR_1}) \tag{A-3}$$

$$\Phi_m(\rho,z)=(\delta-z)\Phi_0(\rho,z,z_1,z_2)-\frac{j}{4\pi k\epsilon}(e^{-jkR_2}-e^{-jkR_1}). \tag{A-4}$$

with $z_1=-\delta$ and $z_2=\delta$.

The semi-infinite integral is evaluated as

$$\begin{aligned}\Phi_c(\rho,z) &= \frac{1}{4\pi\epsilon}\int_0^\infty \frac{e^{-jkR}}{R}\,dz' \\ &= \frac{1}{4\pi\epsilon}\int_0^z \frac{e^{-jkR}}{R}\,dz' + \frac{1}{4\pi\epsilon}\int_z^\infty \frac{e^{-jkR}}{R}\,dz' \\ &= \Phi_0(\rho,z,0,z) + \frac{1}{8\pi\epsilon}\int_{-\infty}^\infty \frac{e^{-jkR}}{R}\,dz' \\ &= \Phi_0(\rho,z,0,z) - \frac{j}{8\epsilon}H_0^{(2)}(k\rho). \end{aligned} \tag{A-5}$$

For electrically short segments, both the integral for $\Phi_0$ and the difference of exponentials in (A-3) and (A-4) are conveniently evaluated using the series approximation of the exponential

$$\begin{aligned} e^{aR} \approx & e^{aR_0}\left[1 + a(R-R_0) + \frac{a^2}{2}(R-R_0)^2 + \frac{a^3}{6}(R-R_0)^3 + \frac{a^4}{24}(R-R_0)^4\right] \\ \approx & e^{aR_0}(T_0 + T_1R + T_2R^2 + T_3R^3 + T_4R^4) \end{aligned}$$

where $a = -jk$, $R_0 = \{\rho^2 + [(z_1+z_2)/2 - z]^2\}^{1/2}$ and

$$\begin{aligned} T_0 =& 1 - aR_0 + \frac{a^2R_0^2}{2} - \frac{a^3R_0^3}{6} + \frac{a^4R_0^4}{24} \\ T_1 =& a - a^2R_0 + \frac{a^3R_0^2}{2} - \frac{a^4R_0^3}{6} \\ T_2 =& \frac{a^2}{2} - \frac{a^3R_0}{2} + \frac{a^4R_0^2}{4} \\ T_3 =& \frac{a^3}{6} - \frac{a^4R_0}{6} \\ T_4 =& \frac{a^4}{24}. \end{aligned}$$

Then

$$e^{aR_2} - e^{aR_1} \approx e^{aR_0}[T_1(R_2-R_1) + T_2(R_2^2-R_1^2) + T_3(R_2^3-R_1^3) + T_4(R_2^4-R_1^4)] \tag{A-6}$$

and

$$\Phi_0(\rho,z,z_1,z_2) \approx e^{aR_0}(T_0I_1 + T_1I_2 + T_2I_3 + T_3I_4 + T_4I_5) \tag{A-7}$$

where

$$I_n = \int_{z_1}^{z_2} R^{n-2}\,dz'.$$

The integrals $I_n$ are evaluated as

$$\begin{aligned} I_1 &= \log[(R_2+S_2)/(R_1+S_1)] && \text{for} \quad z < z_1 \\ &= \log[(R_1-S_1)(R_2+S_2)/\rho^2] && \text{for} \quad z_1 \le z < z_2 \\ &= \log[(R_1-S_1)/(R_2-S_2)] && \text{for} \quad z \ge z_2 \end{aligned} \tag{A-8}$$

$$I_2 = z_2 - z_1 \tag{A-9}$$

$$I_3 = \frac{\rho^2}{2} I_1 + \frac{1}{2}(S_2 R_2 - S_1 R_1) \tag{A-10}$$

$$I_4 = \rho^2 I_2 + \frac{1}{3}(S_2^3 - S_1^3) \tag{A-11}$$

$$I_5 = \frac{3}{4}\rho^2 I_3 + \frac{1}{4}(S_2 R_2^3 - S_1 R_1^3) \tag{A-12}$$

where $S_1 = z_1 - z$, $S_2 = z_2 - z$, $R_1 = (\rho^2 + S_1^2)^{1/2}$ and $R_2 = (\rho^2 + S_2^2)^{1/2}$. The option for $I_1$ is intended to avoid loss of accuracy due to cancellation.

The relative error in the five term approximation of the exponential is less than 0.01 for $|R - R_0| = 0.2\lambda$ and decreases as $|R - R_0|^5$. Since $|R - R_0| \le (z_2 - z_1)/2$ and $z_2 - z_1$ is the segment length in (A-3) and (A-4) or the distance of the evaluation point from the junction in (A-5), this approximation can be used for all matrix elements in the solution for charge at a junction.

## APPENDIX B

## Approximations for the Field of a Segment to Avoid Loss of Precision

The exact equations for the field of a straight filament of current on the $z$ axis were derived in section 4. The field components for currents $I_0 \sin ks$, $I_0 \cos ks$ and a constant current $I_0$; denoted $E^S$, $E^C$ and $E^K$, respectively; are

$$E_\rho^S = \frac{-j\eta I_0}{4\pi\rho}\left\{\left[(z-\delta)\frac{e^{-jkR_2}}{R_2} - (z+\delta)\frac{e^{-jkR_1}}{R_1}\right]\cos(k\delta) - j(e^{-jkR_2}+e^{-jkR_1})\sin(k\delta)\right\} \tag{B-1}$$

$$E_\rho^C = \frac{j\eta I_0}{4\pi\rho}\left\{\left[(z-\delta)\frac{e^{-jkR_2}}{R_2} + (z+\delta)\frac{e^{-jkR_1}}{R_1}\right]\sin(k\delta) + j(e^{-jkR_2}-e^{-jkR_1})\cos(k\delta)\right\} \tag{B-2}$$

$$E_z^S = \frac{j\eta I_0}{4\pi}\Big(\frac{e^{-jkR_2}}{R_2} - \frac{e^{-jkR_1}}{R_1}\Big)\cos(k\delta) \tag{B-3}$$

$$E_z^K = \frac{-j\eta I_0 k}{4\pi}\int_{-\delta}^{\delta}\frac{e^{-jkR}}{R}\,dz' \tag{B-4}$$

$$E_z^C - E_z^K = \frac{-j\eta I_0}{4\pi}\left[\Big(\frac{e^{-jkR_2}}{R_2} + \frac{e^{-jkR_1}}{R_1}\Big)\sin(k\delta) - k\int_{-\delta}^{\delta}\frac{e^{-jkR}}{R}\,dz'\right] \tag{B-5}$$

where the segment has length $\Delta = 2\delta$ extending from $z_1 = -\delta$ to $z_2 = \delta$ and $R_1 = [\rho^2 + (z+\delta)^2]^{1/2}$ and $R_2 = [\rho^2 + (z-\delta)^2]^{1/2}$. While these equations are exact, their evaluation can result in loss of precision due to cancellation in the limit of small $kR$ and when $R$ is much larger than $\Delta$. Equations (B-1) and (B-2) also fail for small $\rho$ when $|z| > \delta$. Approximations valid for these cases are given in the remainder of this appendix. Equation (B-5) was written for $E_z^C - E_z^K$ since this is the quantity needed in NEC, and the cancellation between $E_z^C$ and $E_z^K$ must be taken into account in the evaluation.

### B.1 Approximation for Small $\rho$ and $|z| > \delta$

When $|z| > \delta$ and $\rho \ll |z| - \delta$ the $\rho$ components of electric field are proportional to $\rho$. Since (B-1) and (B-2) contain $\rho^{-1}$ factors the terms must cancel as $\rho^2$, leading to a numerical disaster. A suitable approximation for this case is obtained by expanding $R$ in a power series in $\rho$. The result is

$$E_\rho^S \approx \frac{-j\eta I_0\rho}{4\pi}e^{-jk|z|}\left\{\frac{1}{2}\left[\frac{e^{-jk\delta}}{(|z|+\delta)^2} - \frac{e^{jk\delta}}{(|z|-\delta)^2}\right]\cos(k\delta) - \frac{jk\delta}{z^2-\delta^2}\right\} \tag{B-6}$$

$$E_\rho^C \approx \frac{-j\eta I_0 S_z\rho}{4\pi}e^{-jk|z|}\left\{\frac{1}{2}\left[\frac{e^{-jk\delta}}{(|z|+\delta)^2} + \frac{e^{jk\delta}}{(|z|-\delta)^2}\right]\sin(k\delta) - \frac{k\delta}{z^2-\delta^2}\right\} \tag{B-7}$$

where $S_z = z/|z|$. Terms of order $[\rho/(|z|-\delta)]^4$ were neglected in the expansion of $R$, and terms of order $k^2\rho^4/(|z|-\delta)^2$ were neglected in the expansion of the exponentials. Equations (B-1) and (B-2) are to be used for small $\rho$ when $|z| \le \delta$.

### B.2 Approximation for Small $|kR|$

When $|kR_1| \ll 1$ and $|kR_2| \ll 1$ cancellation occurs among the terms of (B-1) through (B-5). Cancellation is particularly severe for the real parts of the fields for real $k$. While the real parts become small their accurate evaluation is essential to computing the input resistance in the method of moments solution. For small $|kR|$ the exponentials can be expanded in power series in $kR$ with the results

$$E_\rho^S \approx \frac{-j\eta I_0}{4\pi\rho}\left\{ z\left[\frac{1}{R_2}-\frac{1}{R_1}-\frac{k^2}{2}(R_2-R_1)+\frac{k^4}{24}(R_2^3-R_1^3)\right]\cos(k\delta) \right.$$
$$-\delta\left[\frac{1}{R_2}+\frac{1}{R_1}-\frac{k^2}{2}(R_2+R_1)+\frac{k^4}{24}(R_2^3+R_1^3)\right]\cos(k\delta)$$
$$\left.-\left[k(R_2+R_1)-\frac{k^3}{6}(R_2^3+R_1^3)\right]\sin(k\delta)+\frac{2jk^3\rho^2\delta}{3}\right\} \qquad \text{(B-8)}$$

$$E_\rho^C \approx \frac{j\eta I_0}{4\pi\rho}\left\{ z\left[\frac{1}{R_2}+\frac{1}{R_1}-\frac{k^2}{2}(R_2+R_1)+\frac{k^4}{24}(R_2^3+R_1^3)\right]\sin(k\delta) \right.$$
$$-\delta\left[\frac{1}{R_2}-\frac{1}{R_1}-\frac{k^2}{2}(R_2-R_1)+\frac{k^4}{24}(R_2^3-R_1^3)\right]\sin(k\delta)$$
$$\left.+\left[k(R_2-R_1)-\frac{k^3}{6}(R_2^3-R_1^3)\right]\cos(k\delta)+\frac{2jk^6z\delta^3\rho^2}{45}\right\} \qquad \text{(B-9)}$$

$$E_z^S \approx \frac{j\eta I_0}{4\pi}\left[\frac{1}{R_2}-\frac{1}{R_1}-\frac{k^2}{2}(R_2-R_1)-\frac{2jk^3z\delta}{3}+\frac{k^4}{24}(R_2^3-R_1^3)\right]\cos(k\delta) \qquad \text{(B-10)}$$

$$E_z^K \approx \frac{-j\eta I_0 k}{4\pi}\left[I_1-2jk\delta-\frac{k^2}{2}I_3+\frac{jk^3}{6}I_4+\frac{k^4}{24}I_5\right] \qquad \text{(B-11)}$$

$$E_z^C - E_z^K \approx \frac{-j\eta I_0}{4\pi}\left\{\left[\frac{1}{R_2}+\frac{1}{R_1}-\frac{k^2}{2}(R_2+R_1)+\frac{jk^3}{6}(R_2^2+R_1^2)\right.\right.$$
$$\left.+\frac{k^4}{24}(R_2^3+R_1^3)\right]\sin(k\delta)+\frac{jk^4\delta^3}{3}$$
$$\left.-k\left[I_1-\frac{k^2}{2}I_3+\frac{jk^3}{6}I_4+\frac{k^4}{24}I_5\right]\right\}. \qquad \text{(B-12)}$$

The terms $I_1$ through $I_5$ are from the integration of $e^{-jkR}/R$ for small $kR$ and are defined in equations (C-3) through (C-7) of Appendix C. Terms of order $(kR)^5$ have been neglected except in the real part of $E_\rho^C$ where the $(kR)^6$ term was retained as the first nonzero contribution.

Equations (B-8) and (B-9) cannot be used when $\rho$ is very small and $|z| > \delta$. Equations (B-6) and (B-7), which were derived for this case, lose accuracy when $|kR|$ is small. Hence

(B-6) and (B-7) were approximated for small $|kR|$ by expanding the exponentials. The result for $|z| > \delta$, $\rho \ll |z| - \delta$ and $|kR| \ll 1$ is

$$E_\rho^S \approx \frac{j\eta I_0 \rho\delta}{4\pi}\left\{\frac{|z|[2+k^2(z^2-2\delta^2)]}{(z^2-\delta^2)^2} - \frac{2jk^3}{3}\right\} \tag{B-13}$$

$$E_\rho^C \approx \frac{-j\eta I_0 S_z k\rho\delta^3}{4\pi}\left\{\frac{6+k^2(z^2-2\delta^2)}{3(z^2-\delta^2)^2} - \frac{2jk^5|z|}{45}\right\} \tag{B-14}$$

Terms of order $(kR)^4$ have been neglected in the imaginary parts of the fields.

### B.3 Approximation for $R \gg \delta$

The last case needing approximation is $R \gg \delta$. $R_1$ and $R_2$ in (B-1) through (B-5) can then be expanded in powers of $\delta$ with the results

$$E_\rho^S \approx \frac{j\eta I_0}{4\pi}\,\frac{2\delta\rho}{R_0^3}(1+jkR_0)e^{-jkR_0} \tag{B-15}$$

$$E_\rho^C \approx \frac{-j\eta I_0}{4\pi}\,\frac{2k\delta^3\rho z}{R_0^5}\Big(1+jkR_0-\frac{k^2R_0^2}{3}\Big)e^{-jkR_0} \tag{B-16}$$

$$E_z^S \approx \frac{j\eta I_0}{4\pi}\,\frac{2\delta z}{R_0^3}\Big(1+jkR_0\Big)e^{-jkR_0} \tag{B-17}$$

$$E_z^K \approx \frac{-j\eta I_0}{4\pi}\,\frac{k\delta}{R_0}\left\{2+\frac{\delta^2}{3R_0^2}\left[\frac{2z^2-\rho^2}{R_0^2}(1+jkR_0)-k^2z^2\right]\right\}e^{-jkR_0} \tag{B-18}$$

$$E_z^C - E_z^K \approx \frac{-j\eta I_0}{4\pi}\,\frac{k\delta^3}{3R_0^3}\left[\frac{2(2z^2-\rho^2)}{R_0^2}(1+jkR_0)-k^2(2z^2+R_0^2)\right]e^{-jkR_0}. \tag{B-19}$$

where $R_0 = [\rho^2+z^2]^{1/2}$. Terms of order $(\delta/R_0)^4$ have been neglected in the expansion of $R$, and terms of order $(k\delta)^4$ were neglected in the expansion of the exponentials.

When $R \gg \delta$ and $|kR| \ll 1$ accuracy is lost in the real parts of the fields evaluated by equations (B-15) through (B-19). The problem can be seen when the exponentials are expanded in powers of $jkR_0$. When the products of this expansion with the terms in parentheses are evaluated the leading imaginary terms, contributing to the real parts of the field, cancel. The problem is worst for $E_\rho^C$ where $(kR)^5$ becomes the first imaginary term. Hence, once again, approximations for $R \gg \delta$ and $|kR| \ll 1$ are

$$E_\rho^S \approx \frac{j\eta I_0}{4\pi}\,\frac{2\rho\delta}{R_0^3}(1+\frac{k^2R_0^2}{2}-\frac{jk^3R_0^3}{3}-\frac{k^4R_0^4}{8}+\frac{jk^5R_0^5}{30}) \tag{B-20}$$

$$E_\rho^C \approx \frac{-j\eta I_0}{4\pi}\,\frac{2k\rho z\delta^3}{3R_0^5}(3+\frac{k^2R_0^2}{2}+\frac{k^4R_0^4}{8}-\frac{jk^5R_0^5}{15}) \tag{B-21}$$

$$E_z^S \approx \frac{j\eta I_0}{4\pi}\,\frac{2z\delta}{R_0^3}(1+\frac{k^2R_0^2}{2}-\frac{jk^3R_0^3}{3}-\frac{k^4R_0^4}{8}+\frac{jk^5R_0^5}{30}) \tag{B-22}$$

$$E_z^K \approx \frac{-j\eta I_0}{4\pi}\,\frac{k\delta}{3R_0^5}\Big[6R_0^4+(2z^2-\rho^2)\delta^2-6jkR_0^5-k^2R_0^2(3R_0^4+\frac{\rho^2\delta^2}{2}) + jk^3R_0^5(R_0^2+\delta^2)\Big] \tag{B-23}$$

$$E_z^C - E_z^K \approx \frac{-j\eta I_0}{4\pi}\,\frac{k\delta^3}{3R_0^5}\Big[2(2z^2-\rho^2)-k^2R_0^2(z^2+2\rho^2)+\frac{5jk^3R_0^5}{3} + \frac{k^4R_0^4}{4}(4z^2+3\rho^2)+\frac{jk^5R_0^5}{120}(13z^2-9\rho^2)\Big]. \tag{B-24}$$

Terms of order $(kR_0)^6$ have been neglected.

### B.4 Choice of the Method for Numerical Evaluation

For accurate evaluation of the fields, the appropriate equations must be chosen from those given above. The logic for making this choice was developed by running a program that determined the error in the single precision evaluation of the exact equations (B-1) through (B-5) and the error for a selected one of the sets of approximate equations. Equations (B-1) through (B-5) evaluated in double precision were used as a reference in computing the relative errors.

The logic developed for choosing the evaluation method is outlined in Fig. B-1. The values now being used in the tests are:

$$C_1 = 10.$$
$$C_2 = 0.01(2\pi)$$
$$C_3 = 0.01(2\pi)$$
$$C_4 = 0.01$$
$$C_5 = 0.04$$

These constants were chosen for single precision evaluation of the equations. If the code were to be converted to double precision the exact equations could be used over a wider range of parameters. Hence constant $C_1$ could be increased and $C_2$ through $C_5$ reduced to delay the use of the approximations until their accuracy is comparable with double precision results. Determination of the optimum values is complicated by the lack of an accuracy reference unless (B-1) through (B-5) are evaluated in quadruple precision. A reasonable first guess might be to increase $C_1$ and decrease $C_2$ through $C_5$ by two orders of magnitude for double precision.

| | SUBROUTINE |
|---|---|
| If ($R_0 > C_1\delta$) then | EKSCMN |
| If ($\|kR_0\| > C_2$) then | |
| Use Eq. B15 through B19 | EKSCLR |
| Else | |
| Use Eq. B20 through B24 | |
| End if | |
| Else if ($\|kR_0\| > C_3$) then | EKSCMN |
| Use Eq. B3 through B5 | |
| If ($\rho > C_4 \min(R_1, R_2)$) then | EKSCEX |
| Use Eq. B1 and B2 | |
| Else | |
| Use Eq. B6 and B7 | ESMLRH |
| End if | |
| Else | |
| Use Eq. B10 through B12 | |
| If ($\rho > C_5 \min(R_1, R_2)$) then | |
| Use Eq. B8 and B9 | EKSMR |
| Else | |
| Use Eq. B13 and B14 | |
| End if | |
| End if | |

**Fig. B-1** Logic for choosing the field equations for given coordinates. The names of the subroutines containing the code in NEC–4 are shown at the right.

# APPENDIX C

## Evaluation of $\int e^{aR}/R\, dz'$

The z component of electric field due to a constant current element on the z axis involves the integral

$$I = \int_{-\delta}^{\delta} \frac{e^{aR}}{R}\, dz' \tag{C-1}$$

where $a = -jk$, $\delta = \Delta/2$ for segment length $\Delta$ and

$$R = [\rho^2 + (z - z')^2]^{1/2}.$$

This integral cannot be evaluated in closed form. In NEC–2 and NEC–3 it was evaluated numerically using adaptive Romberg quadrature and subtracting an analytically integrable $1/R$ function to smooth the integrand when the evaluation point was on the source segment. A more efficient method has been found to be the use of a series expansion.

The integral is written as

$$I = e^{aR_0} \int_{-\delta}^{\delta} \frac{e^{a(R-R_0)}}{R}\, dz'$$

where

$$R_0 = [\rho^2 + z^2]^{1/2}.$$

Then $|R - R_0| \leq \delta$ and for typical segment lengths, with $k\delta$ less than about 0.4, the exponential is approximated to good accuracy by the series

$$e^{a(R-R_0)} \approx 1 + a(R - R_0) + \frac{a^2}{2}(R - R_0)^2 + \frac{a^3}{6}(R - R_0)^3 + \frac{a^4}{24}(R - R_0)^4.$$

After expanding the products and separating terms in $R$ and $R_0$ the approximation of the integral is obtained as

$$\begin{aligned} I \approx e^{aR_0}\Big[&(1 - aR_0 + \frac{a^2R_0^2}{2} - \frac{a^3R_0^3}{6} + \frac{a^4R_0^4}{24})I_1 \\ &+(a - a^2R_0 + \frac{a^3R_0^2}{2} - \frac{a^4R_0^3}{6})I_2 \\ &+(\frac{a^2}{2} - \frac{a^3R_0}{2} + \frac{a^4R_0^2}{4})I_3 \\ &+(\frac{a^3}{6} - \frac{a^4R_0}{6})I_4 \\ &+\frac{a^4}{24}I_5\Big]. \end{aligned} \tag{C-2}$$

The integrals

$$I_n = \int_{-\delta}^{\delta} R^{n-2}\, dz'$$

are evaluated as

$$\begin{aligned} I_1 &= \log[(R_2 + S_2)/(R_1 + S_1)] \qquad \text{for} \qquad S_1 > 0 \\ &= \log[(R_1 - S_1)/(R_2 - S_2)] \qquad \text{for} \qquad S_1 \le 0 \end{aligned} \tag{C-3}$$

$$I_2 = 2\delta \tag{C-4}$$

$$I_3 = \frac{\rho^2}{2} I_1 + \frac{1}{2}(S_2 R_2 - S_1 R_1) \tag{C-5}$$

$$I_4 = \rho^2 I_2 + \frac{1}{3}(S_2^3 - S_1^3) \tag{C-6}$$

$$I_5 = \frac{3}{4}\rho^2 I_3 + \frac{1}{4}(S_2 R_2^3 - S_1 R_1^3) \tag{C-7}$$

where $S_1 = -\delta - z$, $S_2 = \delta - z$, $R_1 = (\rho^2 + S_1^2)^{1/2}$ and $R_2 = (\rho^2 + S_2^2)^{1/2}$. The option for $I_1$ is intended to avoid loss of accuracy due to cancellation. When $S_1 \le 0 < S_2$ and $\rho$ is small compared to $R_2$ the second form is used with $R_2 - S_2$ evaluated as

$$R_2 - S_2 \approx \frac{\rho^2}{2S_2}(1 - \frac{\rho^2}{4S_2^2}).$$

At the maximum normal segment length of $0.12\lambda$ equation (C-2) yields a result with a relative error of about $10^{-5}$ due to truncation of the series. This error is similar to that with the Romberg integration and decreases as $(k\delta)^5$. However, for R much larger than $\delta$ precision is lost due to cancellation of terms in (C-2). Hence for $R_0 > 10\delta$ the integral in (C-1) is evaluated numerically by three point Gaussian quadrature with very good accuracy. The three point integration is about twenty percent slower than the series due to the need to evaluate three complex exponentials. Either method is faster that the Romberg integration by a factor of two to twenty or more, depending on $\rho$, $z$ and $\delta$. The overall time for filling the interaction matrix in NEC is typically reduced by twenty to forty percent over that with Romberg integration. The Romberg integration routine remains in the code, however, for use in evaluating the fields due to a ground plane.

# APPENDIX D

## Comparison of Approximations for the Thin-Wire Kernel

The problem of evaluating the kernel of the electric field integral equation for a thin wire has been studied by a number of investigators. Several approximations to the kernel are derived in [1] and in references cited in that report. Most often attention has been directed to evaluation of the exact kernel on a straight wire and the singularity that results when the integration point coincides with the evaluation point on the wire surface. When the extended boundary condition is enforced with the evaluation points on the wire axis, as is now done in NEC, the singularity is no longer a problem. Questions remain, however, about the appropriate approximations for the field of the tubular current distribution and the resulting accuracy of the field.

In the thin-wire approximation the current on a wire is assumed to be axially directed and uniformly distributed around the wire surface. The evaluation of the field of this current then involves a surface integral around the wire circumference and along the length of the wire segment. The integral along the wire was evaluated in section 4, and the integration over $\phi$ was reduced to evaluating the four integrals

$$G_1 = \frac{1}{2\pi}\int_0^{2\pi} \frac{e^{-jkR}}{R}\, d\phi \tag{D-1}$$

$$G_2 = \frac{1}{2\pi}\int_0^{2\pi} \frac{\cos\alpha}{\rho'}\frac{e^{-jkR}}{R}\, d\phi \tag{D-2}$$

$$G_3 = \frac{1}{2\pi}\int_0^{2\pi} \frac{\cos\alpha}{\rho'} e^{-jkR}\, d\phi \tag{D-3}$$

$$G_4 = \frac{1}{2\pi}\int_0^{2\pi}\int_{z_1}^{z_2} \frac{e^{-jkR}}{R}\, dz'\, d\phi \tag{D-4}$$

where

$$R = (\rho^2 + a^2 + z^2 - 2a\rho\cos\phi)^{1/2}$$

$$\rho' = (\rho^2 + a^2 - 2\rho a\cos\phi)^{1/2}$$

$$\cos\alpha = \frac{\rho - a\cos\phi}{\rho'}.$$

Approximations for these integrals are developed below, with alternate forms representing a current filament on the wire axis or on the wire surface at a position ninety degrees from the direction of observation.

### D.1 Approximation as a Current Filament on the Wire Axis

An approximation in which the leading term represents a current filament on the wire axis for evaluation points outside of the wire can be obtained by expanding the integrands in Maclaurin series in the wire radius $a$. The result is equivalent to the extended thin-wire

approximation derived in [1] and used in NEC–3. The result is derived here for the specific integrals of interest in (D-1) through (D-4). First, the exponential terms are expanded in Maclaurin series in $a$ when $\rho > a$ or series in $\rho$ when $a > \rho$. For $\rho > a$ the approximations are

$$\begin{aligned}\frac{e^{-jkR}}{R} \approx & \frac{e^{-jkR_0}}{R_0} + \rho a \cos\phi(1+jkR_0)\frac{e^{-jkR_0}}{R_0^3} \\ & + \frac{a^2}{2}\left[\rho^2\cos^2\phi(3+3jkR_0-k^2R_0^2) - (1+jkR_0)R_0^2\right]\frac{e^{-jkR_0}}{R_0^5} \\ e^{-jkR} \approx & e^{-jkR_0} + jka(\rho\cos\phi - \frac{a}{2})\frac{e^{-jkR_0}}{R_0} + \frac{jk\rho^2a^2}{2}\cos^2\phi(1+jkR_0)\frac{e^{-jkR_0}}{R_0^3}\end{aligned}$$

where $R_0 = (\rho^2+z^2)^{1/2}$. When $\rho < a$ the expansions are

$$\begin{aligned}\frac{e^{-jkR}}{R} \approx & \frac{e^{-jkR_a}}{R_a} + \rho a \cos\phi(1+jkR_a)\frac{e^{-jkR_a}}{R_a^3} \\ & + \frac{\rho^2}{2}\left[a^2\cos^2\phi(3+3jkR_a-k^2R_a^2) - (1+jkR_a)R_a^2\right]\frac{e^{-jkR_a}}{R_a^5} \\ e^{-jkR} \approx & e^{-jkR_a} + jk\rho(a\cos\phi - \frac{\rho}{2})\frac{e^{-jkR_a}}{R_a} + \frac{jka^2\rho^2}{2}\cos^2\phi(1+jkR_a)\frac{e^{-jkR_a}}{R_a^3}\end{aligned}$$

where $R_a = (a^2+z^2)^{1/2}$. The integrals over $\phi$ can then be evaluated using, for $G_2$ and $G_3$, the following integrals derived from Eq. (3.613-2) in [2].

$$\begin{aligned}\frac{1}{2\pi}\int_0^{2\pi}\frac{\rho - a\cos\phi}{\rho^2+a^2-2a\rho\cos\phi}\,d\phi &= \frac{1}{\rho} \qquad \text{for} \quad \rho > a \\ &= 0 \qquad \text{for} \quad \rho < a\end{aligned} \tag{D-5}$$

$$\begin{aligned}\frac{1}{2\pi}\int_0^{2\pi}\frac{(\rho - a\cos\phi)\cos\phi}{\rho^2+a^2-2a\rho\cos\phi}\,d\phi &= \frac{a}{2\rho^2} \qquad \text{for} \quad \rho > a \\ &= \frac{-1}{2a} \qquad \text{for} \quad \rho < a\end{aligned} \tag{D-6}$$

$$\begin{aligned}\frac{1}{2\pi}\int_0^{2\pi}\frac{(\rho - a\cos\phi)\cos^2\phi}{\rho^2+a^2-2a\rho\cos\phi}\,d\phi &= \frac{1}{4\rho}(2+\frac{a^2}{\rho^2}) \qquad \text{for} \quad \rho > a \\ &= \frac{-\rho}{4a^2} \qquad \text{for} \quad \rho < a.\end{aligned} \tag{D-7}$$

Then, when $\rho > a$, the approximations for $G_1$, $G_2$ and $G_3$ are

$$G_1 \approx G_1^A = \frac{e^{-jkR_0}}{R_0} + \frac{a^2}{4}\left[\rho^2(3+3jkR_0-k^2R_0^2) - 2(1+jkR_0)R_0^2\right]\frac{e^{-jkR_0}}{R_0^5} \tag{D-8}$$

$$G_2 \approx G_2^A = \frac{e^{-jkR_0}}{\rho R_0} + \frac{a^2\rho}{8}(\frac{a^2}{\rho^2}+2)(3+3jkR_0-k^2R_0^2)\frac{e^{-jkR_0}}{R_0^5} \tag{D-9}$$

$$G_3 \approx G_3^A = \frac{e^{-jkR_0}}{\rho} + \frac{jka^2\rho}{8}(\frac{a^2}{\rho^2}+2)(1+jkR_0)\frac{e^{-jkR_0}}{R_0^3}. \tag{D-10}$$

When $\rho < a$ the approximations are

$$G_1 \approx G_1^A = \frac{e^{-jkR_a}}{R_a} + \frac{\rho^2}{4}\left[a^2(3+3jkR_a-k^2R_a^2) - 2(1+jkR_a)R_a^2\right]\frac{e^{-jkR_a}}{R_a^5} \quad \text{(D-11)}$$

$$G_2 \approx G_2^A = \frac{-\rho}{2}(1+jkR_a)\frac{e^{-jkR_a}}{R_a^3} - \frac{\rho^3}{8}(3+3jkR_a-k^2R_a^2)\frac{e^{-jkR_a}}{R_a^5} \quad \text{(D-12)}$$

$$G_3 \approx G_3^A = \frac{-jk\rho}{2}\frac{e^{-jkR_a}}{R_a} - \frac{jk\rho^3}{8}(1+jkR_a)\frac{e^{-jkR_a}}{R_a^3}. \quad \text{(D-13)}$$

The results for $G_2$ and $G_3$ differ from those in [3] due to the use of the exact integrals in (D-5) through (D-7). In [3] series approximations of $\rho'$ were used to evaluate these integrals. Hence the approximations here should be more accurate than in [3].

An approximation for $G_4$ can be obtained, as done in [1], by noting that (D-8) is equivalent to

$$G_1 \approx \left[1 - \frac{(ka)^2}{4} - \frac{a^2}{4}\frac{\partial^2}{\partial z'^2}\right]\frac{e^{-jkR_0}}{R_0}.$$

Then

$$G_4 \approx G_4^A = \left(1 - \frac{(ka)^2}{4}\right)\int_{z_1}^{z_2}\frac{e^{-jkR_0}}{R_0}\,dz' - \frac{a^2}{4}\frac{\partial}{\partial z'}\frac{e^{-jkR_0}}{R_0}. \quad \text{(D-14)}$$

The leading terms in (D-8) through (D-10) and (D-14)

$$G_1^a = \frac{e^{-jkR_0}}{R_0}$$
$$G_2^a = \frac{e^{-jkR_0}}{\rho R_0}$$
$$G_3^a = \frac{e^{-jkR_0}}{\rho}$$
$$G_4^a = \int_{z_1}^{z_2}\frac{e^{-jkR_0}}{R_0}\,dz'$$

represent the approximations to these integrals obtained by setting the wire radius to zero for $\rho > a$. Hence, the resulting approximation to the field is that of a current filament on the wire axis. From the higher order terms, the approximate relative errors in $G_1^a$, $G_2^a$ and $G_3^a$ for small $kR_0$ are

$$E_1^a = \left|\frac{3a^2\rho^2}{4R_0^4} - \frac{a^2}{2R_0^2}\right|$$
$$E_2^a = \frac{3a^2\rho^2}{4R_0^4}$$
$$E_3^a = \frac{ka^2\rho^2}{4R_0^3}.$$

### D.2 Approximation as a Current Filament on the Wire Surface

An approximation in which the leading term represents a filament of current on the surface of the cylinder can be obtained by writing

$$R = (\rho^2 + a^2 + z^2 - 2b\cos\phi)^{1/2}$$

where $b = a\rho$ and expanding in powers of $b$. This approximation can be used for $\rho > a$ or $\rho < a$ as long as $a\rho \ll R_t^2$ where

$$R_t = (\rho^2 + a^2 + z^2)^{1/2}.$$

The approximations for the exponential terms are

$$\frac{e^{-jkR}}{R} \approx \frac{e^{-jkR_t}}{R_t} + a\rho\cos\phi(1+jkR_t)\frac{e^{-jkR_t}}{R_t^3} + \frac{a^2\rho^2}{2}\cos^2\phi(3+3jkR_t-k^2R_t^2)\frac{e^{-jkR_t}}{R_t^5}$$

$$e^{-jkR} \approx e^{-jkR_t} + jka\rho\cos\phi\frac{e^{-jkR_t}}{R_t} + \frac{jka\rho^2}{2}\cos^2\phi(1+jkR_t)\frac{e^{-jkR_t}}{R_t^3}.$$

Then, integrating over $\phi$ the approximation for $G_1$ is

$$G_1 \approx G_1^B = \frac{e^{-jkR_t}}{R_t} + \frac{a^2\rho^2}{4}(3+3jkR_t-k^2R_t^2)\frac{e^{-jkR_t}}{R_t^5}. \tag{D-15}$$

For $\rho > a$

$$G_2 \approx G_2^B = \frac{e^{-jkR_t}}{\rho R_t} + \frac{a^2}{2\rho}(1+jkR_t)\frac{e^{-jkR_t}}{R_t^3} + \frac{a^2\rho}{8}(2+\frac{a^2}{\rho^2})(3+3jkR_t-k^2R_t^2)\frac{e^{-jkR_t}}{R_t^5} \tag{D-16}$$

$$G_3 \approx G_3^B = \frac{e^{-jkR_t}}{\rho} + \frac{jka^2}{2\rho}\frac{e^{-jkR_t}}{R_t} + \frac{jka^2\rho}{8}(2+\frac{a^2}{\rho^2})(1+jkR_t)\frac{e^{-jkR_t}}{R_t^3} \tag{D-17}$$

while for $\rho < a$

$$G_2 \approx G_2^B = \frac{-\rho}{2}(1+jkR_t)\frac{e^{-jkR_t}}{R_t^3} - \frac{\rho^3}{8}(3+3jkR_t-k^2R_t^2)\frac{e^{-jkR_t}}{R_t^5} \tag{D-18}$$

$$G_3 \approx G_3^B = \frac{-jk\rho}{2}\frac{e^{-jkR_t}}{R_t} - \frac{jk\rho^3}{8}(1+jkR_t)\frac{e^{-jkR_t}}{R_t^3}. \tag{D-19}$$

The leading terms in (D-15) through (D-17) for $\rho > a$

$$G_1^b = \frac{e^{-jkR_t}}{R_t}$$

$$G_2^b = \frac{e^{-jkR_t}}{\rho R_t}$$

$$G_3^b = \frac{e^{-jkR_t}}{\rho}$$

resemble the terms for a current filament on the wire surface since $R_t$ is the distance to a point on the surface at ninety degrees from the direction of observation. However, $\rho$ in these terms is the distance to the wire axis. Use of the radial distance to the wire surface, as for an actual current filament on the wire surface, results in significantly larger errors than the above terms. The relative errors in these approximations for small $kR_t$ are

$$\begin{aligned} E_1^b =& \frac{3a^2\rho^2}{4R_t^4} \\ E_2^b =& \frac{3a^2\rho^2}{4R_t^4} + \frac{a^2}{2R_t^2} \\ E_3^b =& \frac{ka^2\rho^2}{4R_t^3} + \frac{ka^2}{2R_t}. \end{aligned}$$

### D.3 Comparison of Results

Approximations have been derived for the integrals $G_1$, $G_2$, $G_3$ and $G_4$ which, for evaluation points outside of the wire ($\rho > a$) represent filaments of current located on the wire axis ($G_1^a$, $G_2^a$, $G_3^a$, $G_4^a$) or on the wire surface ($G_1^b$, $G_2^b$, $G_3^b$). The integral $G_4$ can also be approximated with a filament on the surface as

$$G_4^b = \int_{z_1}^{z_2} \frac{e^{-jkR_t}}{R_t}\, dz'.$$

For $\rho < a$ there are no simple current-filament approximations for $G_2$ or $G_3$ in the expressions for the radial electric field. On the wire axis $G_2$ and $G_3$ are zero and the approximations $G_1^a$, $G_1^b$, $G_4^a$ and $G_4^b$ for the axial electric field become exact.

For evaluation points outside of the wire surface the relative errors of the current-filament approximations were derived above. The properties of these error terms are summarized below. Conditions at $\rho = 0$ are noted as an indication of the trend for small $\rho$, although these approximations are not used for $\rho < a$.

$E_1^a$ has a maximum at $\rho = 0$ of $E_1^a = a^2/(2z^2)$ and a second maximum at $\rho = \sqrt{5}z$ of $E_1^a = a^2/(48z^2)$. $E_1^b$ is zero at $\rho = 0$ and maximum at $\rho^2 = a^2 + z^2$ where $E_1^b = 3z^2/[16(a^2 + z^2)]$.

$E_2^a$ is zero at $\rho = 0$ and maximum at $\rho = z$ where $E_2^a = 3a^2/(16z^2)$. $E_2^b$ has a minimum at $\rho = 0$ of $E_2^b = a^2/[2(a^2+z^2)]$ and a maximum at $\rho^2 = (a^2+z^2)/5$ of $E_2^b = 25a^2/[48(a^2+z^2)]$.

$E_3^a$ is zero at $\rho = 0$ and has a maximum at $\rho = \sqrt{2}z$ of $E_3^a = ka^2/\sqrt{108}z$. $E_3^b$ has a maximum at $\rho = 0$ of $E_3^b = ka^2/(2\sqrt{a^2 + z^2})$.

The actual errors in these approximations, including $G_4$, are shown in Fig. D-1 through Fig. D-4 for a wire radius of $a = 0.001\lambda$. In Fig. D-2 and D-3 additional approximations are

included which are

$$G_2^s = \frac{e^{-jkR_t}}{\rho_t R_t}$$

$$G_3^s = \frac{e^{-jkR_t}}{\rho_t}$$

where $\rho_t = (\rho^2 + a^2)^{1/2}$. These expressions represent the result of actually putting a current filament on the wire surface, as opposed to $G_2^b$ and $G_3^b$ in which $\rho$ is the distance to the wire axis. In all cases the relative errors were determined from a reference value computed by numerically integrating over $\phi$. It should be noted that, in evaluating the fields, the terms $G_1$, $G_2$ and $G_3$ are evaluated at the segment ends. Hence $z = 0$ in these integrals occurs when the evaluation point is aligned with the segment end. $G_4$, however, represents an integral over a segment which in Fig. D-4 extends from $z_1 = -0.005\lambda$ to $z_2 = 0.005\lambda$. Hence for $G_4$, $z = 0$ corresponds to an evaluation point aligned with the segment center.

For evaluating the field outside of the wire surface the current filament on the wire axis ($G^a$) is seen to yield smaller errors than the filament on the surface ($G^b$) over much of the parameter range shown. The exceptions occur for $G_1$ and $G_4$ when $\rho$ is less than about $z/2$. For the radial field terms, $G_2$ and $G_3$, the axial approximation $G^a$ yields smaller errors than the $G^b$ approximation. The $G^s$ approximations result in about 30 percent error on the wire surface. The $G^A$ approximations, which are used in NEC-3 as the "extended thin-wire kernel", are seen to yield substantially smaller errors than any of the first order approximations at the expense of additional complexity. For large $\rho$ all terms eventually converge to the correct result, although in the plots shown here the convergence appears slow due to the limited range of $\rho$.

## References


[1] A. J. Poggio and R. W. Adams, *Approximations for Terms Related to the Kernel in Thin-Wire Integral Equations*, Lawrence Livermore National Lab. Rept. UCRL-51985, December 1975.

[2] I. S. Gradshteyn and I. M. Ryzhik, *Table of Integrals, Series and Products*, Academic Press, New York, 1965.

[3] G. J. Burke and A. J. Poggio, *Numerical Electromagnetics Code (NEC) – Method of Moments*, Lawrence Livermore National Laboratory, Rept. UCID–18834, Jan. 1981.

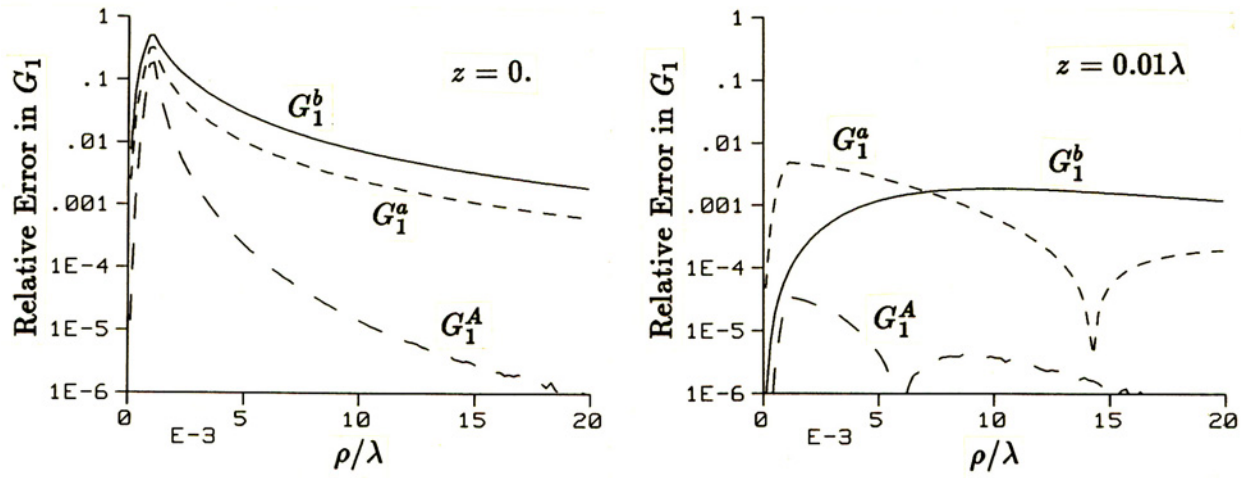


**Fig. D-1** Relative error in approximations for $G_1$ for $a = 0.001\lambda$.

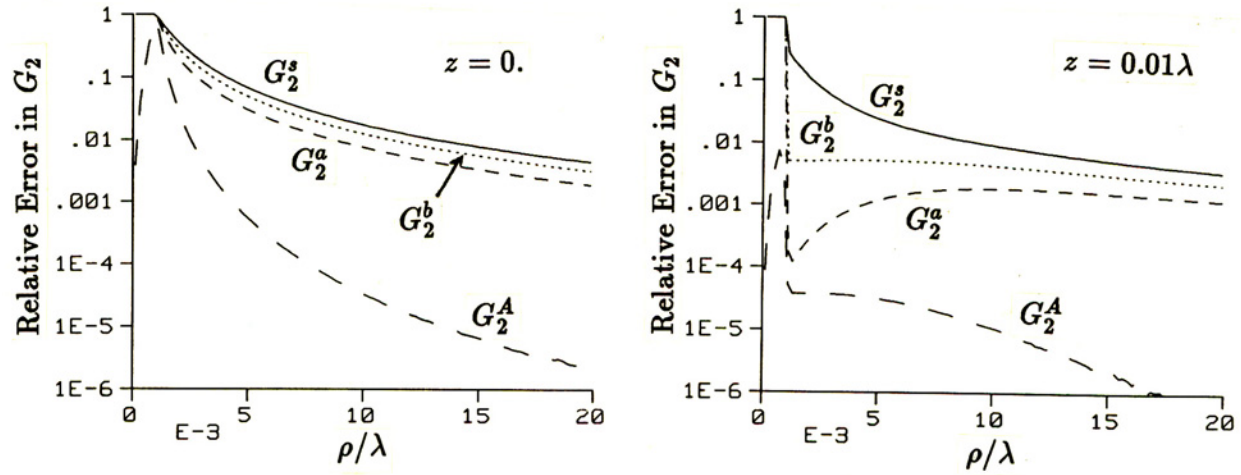


**Fig. D-2** Relative error in approximations for $G_2$ for $a = 0.001\lambda$

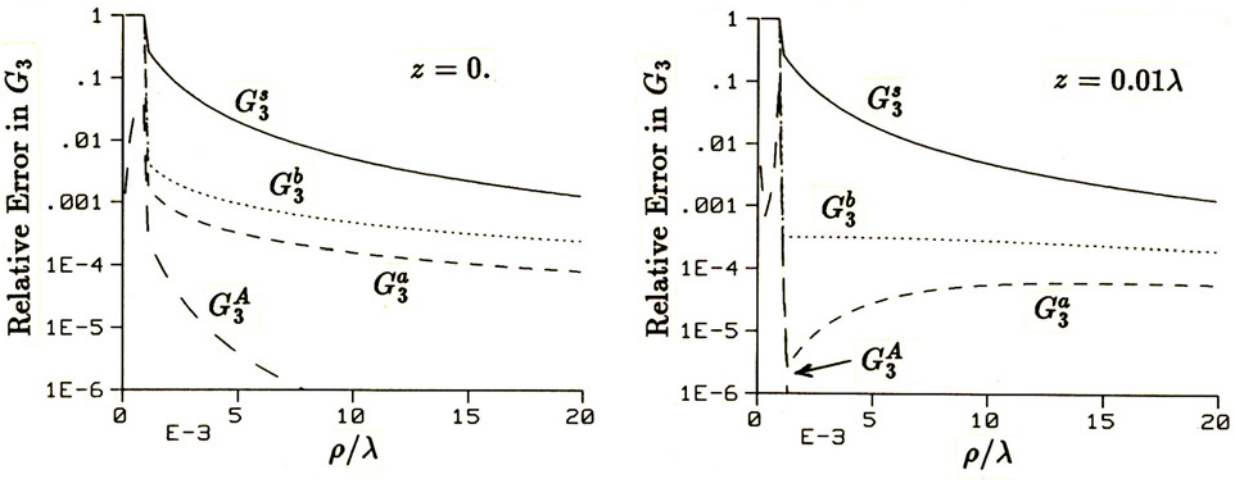


**Fig. D-3** Relative error in approximations for $G_3$ for $a = 0.001\lambda$.

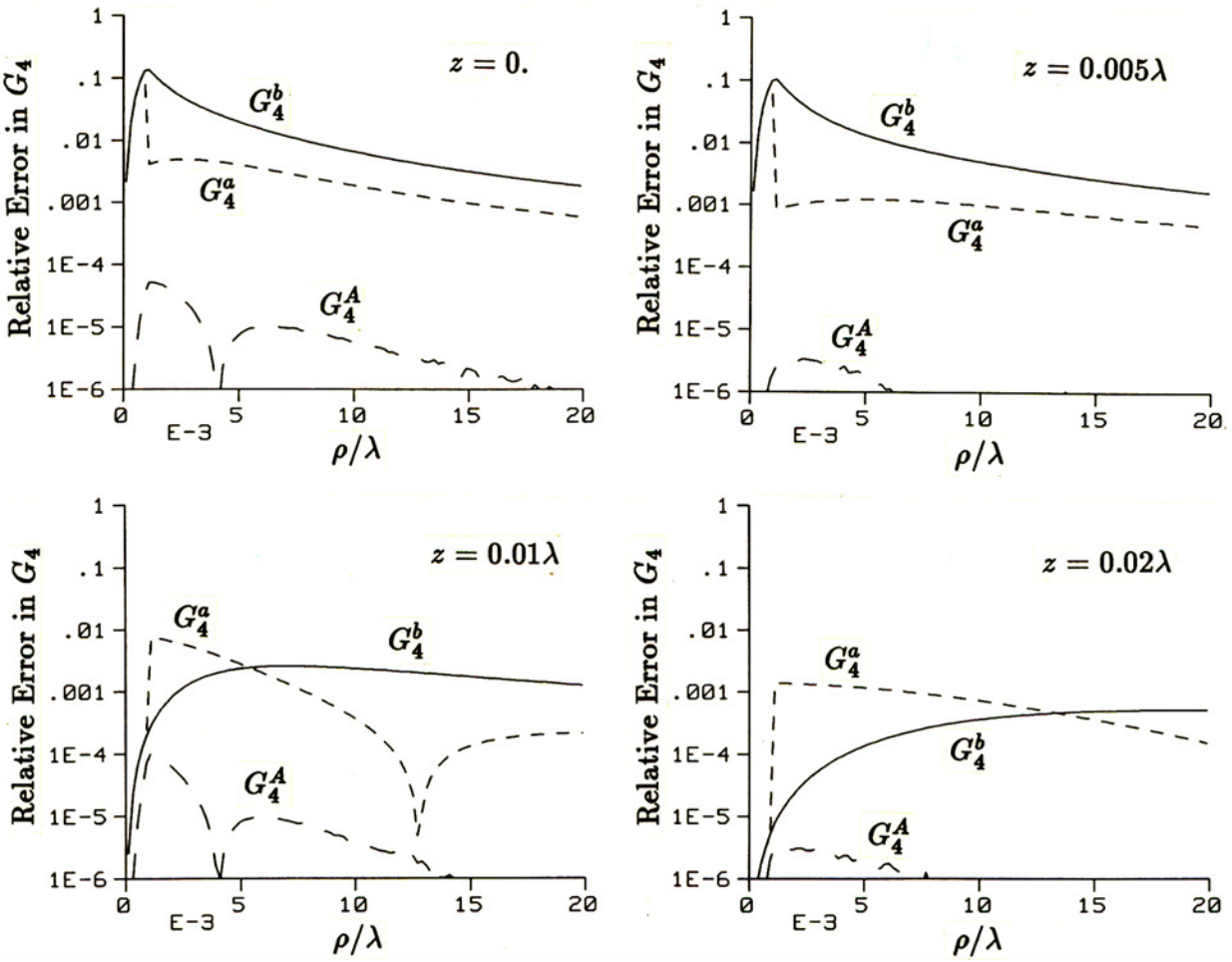


**Fig. D-4** Relative error in approximations for $G_4$ for $z_1 = -0.005\lambda$, $z_2 = 0.005\lambda$ and $a = 0.001\lambda$.

## APPENDIX E

### Evaluation of the Field due to a Constant Charge on a Wire End Cap

The wire end cap is represented as a flat disk as shown in Fig. E-1. Since the current on the cap has no azimuthal variation in the thin-wire approximation, the vector potential is zero on the axis of the disk and greatly reduced by cancellation at points off of the axis. Assuming a constant surface charge density $\rho_e$ on the end cap, the scalar potential is

$$\Phi(\rho, z) = \frac{\rho_e}{4\pi\epsilon} \int_0^a d\rho' \int_0^{2\pi} \rho' \, d\phi \frac{e^{-jkR}}{R}$$

where

$$R = (\rho^2 + \rho'^2 + z^2 - 2\rho\rho' \cos\phi)^{1/2}$$

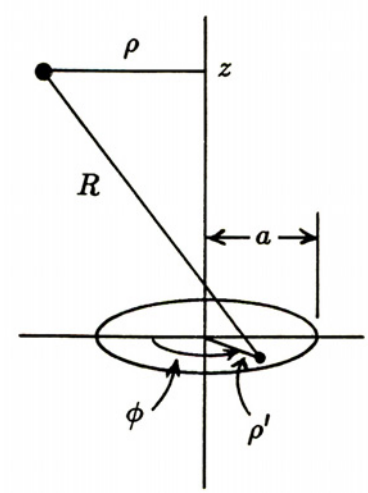


**Fig. E-1** Coordinates for evaluation of the field due to a charged end cap.

For $R_0 = (\rho^2 + z^2)^{1/2} \gg a$ an approximation for $\Phi(\rho, z)$ can be obtained by approximating the integrand by a Maclaurin series in $\rho'$ as

$$\frac{e^{-jkR}}{R} \approx \frac{e^{-jkR_0}}{R_0} + \rho\rho' \cos\phi(1 + jkR_0)\frac{e^{-jkR_0}}{R_0^3} + \frac{\rho'^2}{2}\left[\rho^2 \cos^2\phi(3 + 3jkR_0 - k^2R_0^2) - (1 + jkR_0)R_0^2\right]\frac{e^{-jkR_0}}{R_0^5}.$$

Then

$$\Phi(\rho, z) \approx \frac{\rho_e}{2\epsilon}\left\{\frac{a^2}{2} + \frac{a^4}{16R_0^4}\left[(3 + 3jkR_0 - k^2R_0^2)\rho^2 - 2jkR_0^3 - 2R_0^2\right]\right\}\frac{e^{-jkR_0}}{R_0}$$

The field components are then

$$E_z(\rho, z) = -\frac{\partial\Phi}{\partial z} \approx \frac{\rho_e z a^2}{4\epsilon}\frac{e^{-jkR_0}}{R_0^3}\left\{(1 + jkR_0) - \frac{a^2}{4R_0^2}[3(1 + jkR_0) - k^2R_0^2] - \frac{a^2\rho^2}{8R_0^4}[jk^3R_0^3 + 6k^2R_0^2 - 15(1 + jkR_0)]\right\} \quad \text{(E-1)}$$

and

$$E_\rho(\rho,z) = -\frac{\partial\Phi}{\partial\rho} \approx \frac{\rho_e \rho a^2}{4\epsilon}\frac{e^{-jkR_0}}{R_0^3}\left\{(1+jkR_0) - \frac{a^2}{2R_0^2}[3(1+jkR_0) - k^2R_0^2] \right.$$
$$\left. -\frac{a^2\rho^2}{8R_0^4}[jk^3R_0^3 + 6k^2R_0^2 - 15(1+jkR_0)]\right\} \qquad \text{(E-2)}$$

On the axis of the disk the field has only a $z$ component that can be evaluated in closed form. When $\rho = 0$

$$R = (\rho'^2 + z^2)^{1/2}$$

and the integral for $\Phi$ becomes

$$\Phi(0,z) = \frac{\rho_e}{2\epsilon}\int_0^a \frac{e^{-jkR}}{R}\rho'\,d\rho' = \frac{\rho_e}{2\epsilon}\int_{R_0}^{R_a} e^{-jkR}\,dR$$
$$= \frac{j}{2\epsilon k}(e^{-jkR_a} - e^{-jk|z|})$$

where $R_a = (a^2+z^2)^{1/2}$. Then

$$E_z(0,z) = -\frac{\rho_e z}{2\epsilon|z|}e^{-jk|z|}\left(\frac{|z|}{R_a}e^{-jk(R_a-|z|)} - 1\right) \qquad \text{(E-3)}$$

Equation (E-1) should be used on the axis when $|z| \gg a$ since accuracy is lost due to cancellation in evaluating (E-3).

# APPENDIX F

## Sommerfeld Integrals for the Field Near Ground

The exact solution for the field of a point source near an interface was first published by A. Sommerfeld [1], and involves integrals over wave number, commonly called Sommerfeld integrals. Only the solution for the source below the interface and evaluation point above the interface is used in NEC, with the field for other configurations obtained by applying reciprocity and adding the direct and image terms when appropriate. The full set of electric field equations from Baños [2] is given below for reference, however.

The geometry of the half-space problem is shown in Fig. 5-1, and the wave numbers in the lower medium $k_1$ and upper medium $k_2$ are

$$k_1^2 = \omega^2 \mu_0 \epsilon_0 (\epsilon_1 - j\sigma_1/\omega\epsilon_0)$$

$$k_2^2 = \omega^2 \mu_0 \epsilon_0 (\epsilon_2 - j\sigma_2/\omega\epsilon_0).$$

The notation for electric field will use a subscript to indicate the field component in cylindrical coordinates ($\rho$, $\phi$, $z$) and a superscript to indicate the source orientation, $V$ for a vertical source and $H$ for a horizontal source. In addition, subscripts will be used to indicate the medium in which the source and evaluation points are located. The horizontal dipole source is oriented along the $x$ axis.

For the source below the interface in medium 1 and evaluation point above the interface in medium 2 ($z' < 0$, $z \geq 0$) the field components are

$$\begin{aligned}
E^V_{\rho 12} &= \frac{-j\omega\mu_0}{4\pi} \frac{\partial^2 V_{12}}{\partial\rho\partial z} \\
E^V_{z12} &= \frac{-j\omega\mu_0}{4\pi} \left( \frac{\partial^2}{\partial z^2} + k_2^2 \right) V_{12} \\
E^H_{\rho 12} &= \frac{-j\omega\mu_0}{4\pi} \cos\phi \left( \frac{\partial^2 V_{12}}{\partial\rho^2} + U_{12} \right) \\
E^H_{\phi 12} &= \frac{j\omega\mu_0}{4\pi} \sin\phi \left( \frac{1}{\rho} \frac{\partial V_{12}}{\partial\rho} + U_{12} \right) \\
E^H_{z12} &= \frac{j\omega\mu_0}{4\pi} \cos\phi \frac{\partial^2 V_{12}}{\partial\rho\partial z'}
\end{aligned}$$

where $V_{12}$ and $U_{12}$ are the Sommerfeld integrals

$$\begin{aligned}
V_{12} &= 2\int_0^\infty \frac{e^{\gamma_1 z' - \gamma_2 z}}{k_1^2\gamma_2 + k_2^2\gamma_1} J_0(\lambda\rho)\lambda\, d\lambda \\
U_{12} &= 2\int_0^\infty \frac{e^{\gamma_1 z' - \gamma_2 z}}{\gamma_1 + \gamma_2} J_0(\lambda\rho)\lambda\, d\lambda
\end{aligned}$$

with $\gamma_1 = (\lambda^2 - k_1^2)^{1/2}$ and $\gamma_2 = (\lambda^2 - k_2^2)^{1/2}$. For the source above the interface in medium 1 and evaluation point below the interface in medium 2 ($z' \geq 0$, $z < 0$) the field is

$$
\begin{aligned}
E^V_{\rho 21} &= \frac{-j\omega\mu_0}{4\pi} \frac{\partial^2 V_{21}}{\partial\rho\partial z} \\
E^V_{z21} &= \frac{-j\omega\mu_0}{4\pi} \left( \frac{\partial^2}{\partial z^2} + k_1^2 \right) V_{21} \\
E^H_{\rho 21} &= \frac{-j\omega\mu_0}{4\pi} \cos\phi \left( \frac{\partial^2 V_{21}}{\partial\rho^2} + U_{21} \right) \\
E^H_{\phi 21} &= \frac{j\omega\mu_0}{4\pi} \sin\phi \left( \frac{1}{\rho} \frac{\partial V_{21}}{\partial\rho} + U_{21} \right) \\
E^H_{z21} &= \frac{j\omega\mu_0}{4\pi} \cos\phi \frac{\partial^2 V_{21}}{\partial\rho\partial z'}
\end{aligned}
$$

where

$$
\begin{aligned}
V_{21} &= 2\int_0^\infty \frac{e^{\gamma_1 z - \gamma_2 z'}}{k_1^2\gamma_2 + k_2^2\gamma_1} J_0(\lambda\rho)\lambda\, d\lambda \\
U_{21} &= 2\int_0^\infty \frac{e^{\gamma_1 z - \gamma_2 z'}}{\gamma_1 + \gamma_2} J_0(\lambda\rho)\lambda\, d\lambda.
\end{aligned}
$$

For source and evaluation points above the interface ($z' \geq 0$, $z \geq 0$)

$$
\begin{aligned}
E^V_{\rho 22} &= \frac{-j\omega\mu_0}{4\pi k_2^2} \left[ \frac{\partial^2}{\partial\rho\partial z} (G_{22} - G_{21} + k_1^2 V_{22}) \right] \\
E^V_{z22} &= \frac{-j\omega\mu_0}{4\pi k_2^2} \left[ \left( \frac{\partial^2}{\partial z^2} + k_2^2 \right) (G_{22} - G_{21} + k_1^2 V_{22}) \right] \\
E^H_{\rho 22} &= \frac{-j\omega\mu_0}{4\pi k_2^2} \cos\phi \left[ \frac{\partial^2}{\partial\rho^2} (G_{22} - G_{21} + k_2^2 V_{22}) + k_2^2 (G_{22} - G_{21} + U_{22}) \right] \\
E^H_{\phi 22} &= \frac{j\omega\mu_0}{4\pi k_2^2} \sin\phi \left[ \frac{1}{\rho} \frac{\partial}{\partial\rho} (G_{22} - G_{21} + k_2^2 V_{22}) + k_2^2 (G_{22} - G_{21} + U_{22}) \right] \\
E^H_{z22} &= \frac{-j\omega\mu_0}{4\pi k_2^2} \cos\phi \left[ \frac{\partial^2}{\partial\rho\partial z} (G_{22} + G_{21} - k_1^2 V_{22}) \right]
\end{aligned}
$$

where

$$
\begin{aligned}
V_{22} &= 2\int_0^\infty \frac{e^{-\gamma_2(z+z')}}{k_1^2\gamma_2 + k_2^2\gamma_1} J_0(\lambda\rho)\lambda\, d\lambda \\
U_{22} &= 2\int_0^\infty \frac{e^{-\gamma_2(z+z')}}{\gamma_1 + \gamma_2} J_0(\lambda\rho)\lambda\, d\lambda \\
G_{22} &= e^{-jk_2 R_D}/R_D, \qquad R_D = \left[\rho^2 + (z - z')^2\right]^{1/2} \\
G_{21} &= e^{-jk_2 R_I}/R_I, \qquad R_I = \left[\rho^2 + (z + z')^2\right]^{1/2}.
\end{aligned}
$$

For source and evaluation points below the interface ($z' < 0$, $z < 0$)

$$E^V_{\rho 11} = \frac{-j\omega\mu_0}{4\pi k_1^2}\left[\frac{\partial^2}{\partial\rho\partial z}(G_{11} - G_{12} + k_2^2 V_{11})\right]$$
$$E^V_{z11} = \frac{-j\omega\mu_0}{4\pi k_1^2}\left[\left(\frac{\partial^2}{\partial z^2} + k_1^2\right)(G_{11} - G_{12} + k_2^2 V_{11})\right]$$
$$E^H_{\rho 11} = \frac{-j\omega\mu_0}{4\pi k_1^2}\cos\phi\left[\frac{\partial^2}{\partial\rho^2}(G_{11} - G_{12} + k_1^2 V_{11}) + k_1^2(G_{11} - G_{12} + U_{11})\right]$$
$$E^H_{\phi 11} = \frac{j\omega\mu_0}{4\pi k_1^2}\sin\phi\left[\frac{1}{\rho}\frac{\partial}{\partial\rho}(G_{11} - G_{12} + k_1^2 V_{11}) + k_1^2(G_{11} - G_{12} + U_{11})\right]$$
$$E^H_{z11} = \frac{-j\omega\mu_0}{4\pi k_1^2}\cos\phi\left[\frac{\partial^2}{\partial\rho\partial z}(G_{11} + G_{12} - k_2^2 V_{11})\right]$$

where

$$V_{11} = 2\int_0^\infty \frac{e^{\gamma_1(z+z')}}{k_1^2\gamma_2 + k_2^2\gamma_1} J_0(\lambda\rho)\lambda\, d\lambda$$
$$U_{11} = 2\int_0^\infty \frac{e^{\gamma_1(z+z')}}{\gamma_1 + \gamma_2} J_0(\lambda\rho)\lambda\, d\lambda$$
$$G_{11} = e^{-jk_1R_D}/R_D, \qquad R_D = \left[\rho^2 + (z-z')^2\right]^{1/2}$$
$$G_{12} = e^{-jk_1R_I}/R_I, \qquad R_I = \left[\rho^2 + (z+z')^2\right]^{1/2}.$$

## References


[1] A. Sommerfeld, "Über die Ausbreitung der Wellen in der drahtlosen Telegraphie," *Ann. Physik*, Vol. 28, p. 665, 1909.

[2] A. Baños, *Dipole Radiation in the Presence of a Conducting Half-Space*, Pergamon Press, New York, 1966.

# APPENDIX G

## Conversion Formulas for Source and Observer Locations

The Sommerfeld-integral and asymptotic field evaluations in NEC are coded for the case of a source below the interface and evaluation point above the interface. Fields for other cases are obtained from this buried-source elevated-observer evaluation by appropriate conversions, including addition of direct and image fields. The source is located at a height $z'$ and the evaluation point at height $z$, with radial separation $\rho$. The conversions are derived by applying reciprocity, boundary conditions at the interface and the fact that the direct field depends on $(z - z')$ while the image field depends on $(z + z')$.

The direct and image fields are evaluated for a source in a finite medium with wave number $k_n$, where $n$ is 1 or 2. The cylindrical components of the electric field, for a source with current moment $I\ell = 1$, are

$$E^V_{\rho n}(\rho, z', z) = \frac{-j\omega\mu_0}{4\pi k_n^2}\left[\frac{\rho(z-z')}{R^2}(3 + 3jk_nR - k_n^2R^2)\right]\frac{e^{-jk_nR}}{R^3} \tag{G-1}$$

$$E^V_{zn}(\rho, z', z) = \frac{-j\omega\mu_0}{4\pi k_n^2}\left[\frac{(z-z')^2}{R^2}(3 + 3jk_nR - k_n^2R^2) - 1 - jk_nR + k_n^2R^2\right]\frac{e^{-jk_nR}}{R^3} \tag{G-2}$$

$$E^H_{\rho n}(\rho, z', z) = \frac{-j\omega\mu_0}{4\pi k_n^2}\left[\frac{\rho^2}{R^2}(3 + 3jk_nR - k_n^2R^2) - 1 - jk_nR + k_n^2R^2\right]\frac{e^{-jk_nR}}{R^3} \tag{G-3}$$

$$E^H_{\phi n}(\rho, z', z) = \frac{-j\omega\mu_0}{4\pi k_n^2}\left[1 + jk_nR - k_n^2R^2\right]\frac{e^{-jk_nR}}{R^3} \tag{G-4}$$

$$E^H_{zn}(\rho, z', z) = \frac{-j\omega\mu_0}{4\pi k_n^2}\left[\frac{\rho(z-z')}{R^2}(3 + 3jk_nR - k_n^2R^2)\right]\frac{e^{-jk_nR}}{R^3} \tag{G-5}$$

where $R = [\rho^2 + (z - z')^2]^{1/2}$. For a horizontal source along the x axis, the factor $\cos\phi$ would be included in $E^H_\rho$ and $E^H_z$, and $\sin\phi$ in $E^H_\phi$ for the complete field.

The fields for various locations of source and observer will be written as a function of $(\rho, z', z)$ where the second argument is the source height and the third is the observer's height. For clarity, however, $a$ and $b$, which are always positive numbers, will be substituted for the source and observer's heights. For source above the interface and observer below:

$$E^V_{\rho 21}(\rho, a, -b) = -E^H_{z12}(\rho, -b, a) \tag{G-6}$$

$$E^V_{z21}(\rho, a, -b) = E^V_{z12}(\rho, -b, a) \tag{G-7}$$

$$E^H_{\rho 21}(\rho, a, -b) = E^H_{\rho 12}(\rho, -b, a) \tag{G-8}$$

$$E^H_{\phi 21}(\rho, a, -b) = E^H_{\phi 12}(\rho, -b, a) \tag{G-9}$$

$$E^H_{z21}(\rho, a, -b) = -E^V_{\rho 12}(\rho, -b, a). \tag{G-10}$$

For source and observer below the interface:

$$E^V_{\rho 11}(\rho,-a,-b) = E^V_{\rho 12}(\rho,-a-b,0_+) + E^V_{\rho 1}(\rho,-a,-b) - E^V_{\rho 1}(\rho,-a,b) \tag{G-11}$$

$$E^V_{z 11}(\rho,-a,-b) = \frac{1}{\tilde{\epsilon}_1} E^V_{z 12}(\rho,-a-b,0_+) + E^V_{z 1}(\rho,-a,-b) - E^V_{z 1}(\rho,-a,b) \tag{G-12}$$

$$E^H_{\rho 11}(\rho,-a,-b) = E^H_{\rho 12}(\rho,-a-b,0_+) + E^H_{\rho 1}(\rho,-a,-b) - E^H_{\rho 1}(\rho,-a,b) \tag{G-13}$$

$$E^H_{\phi 11}(\rho,-a,-b) = E^H_{\phi 12}(\rho,-a-b,0_+) + E^H_{\phi 1}(\rho,-a,-b) - E^H_{\phi 1}(\rho,-a,b) \tag{G-14}$$

$$\begin{aligned} E^H_{z 11}(\rho,-a,-b) &= \frac{1}{\tilde{\epsilon}_1} E^H_{z 12}(\rho,-a-b,0_+) + E^H_{z 1}(\rho,-a,-b) - E^H_{z 1}(\rho,-a,b) \\ &= -E^V_{\rho 12}(\rho,-a-b,0_+) + E^H_{z 1}(\rho,-a,-b) + E^V_{\rho 1}(\rho,-a,b) \end{aligned} \tag{G-15}$$

For source and observer above the interface:

$$E^V_{\rho 22}(\rho,a,b) = -E^H_{z 12}(\rho,0_-,a+b) + E^V_{\rho 2}(\rho,a,b) - E^V_{\rho 2}(\rho,a,-b) \tag{G-16}$$

$$E^V_{z 22}(\rho,a,b) = \tilde{\epsilon}_1 E^V_{z 12}(\rho,0_-,a+b) + E^V_{z 2}(\rho,a,b) - E^V_{z 2}(\rho,a,-b) \tag{G-17}$$

$$E^H_{\rho 22}(\rho,a,b) = E^H_{\rho 12}(\rho,0_-,a+b) + E^H_{\rho 2}(\rho,a,b) - E^H_{\rho 2}(\rho,a,-b) \tag{G-18}$$

$$E^H_{\phi 22}(\rho,a,b) = E^H_{\phi 12}(\rho,0_-,a+b) + E^H_{\phi 2}(\rho,a,b) - E^H_{\phi 2}(\rho,a,-b) \tag{G-19}$$

$$\begin{aligned} E^H_{z 22}(\rho,a,b) &= -\tilde{\epsilon}_1 E^V_{\rho 12}(\rho,0_-,a+b) + E^H_{z 2}(\rho,a,b) - E^H_{z 2}(\rho,a,-b) \\ &= E^H_{z 12}(\rho,0_-,a+b) + E^H_{z 2}(\rho,a,b) - E^V_{\rho 2}(\rho,-a,b). \end{aligned} \tag{G-20}$$

# APPENDIX H

## Singularity Subtraction in the Sommerfeld Integrals for the Field Due to Ground

To facilitate numerical evaluation of the Sommerfeld integrals near the field singularity, the singular part is removed in an analytically integrable form. This is done by subtracting the term $V_0$ from $V_{12}$ where

$$V_0 = \frac{2}{k_1^2 + k_2^2} \int_0^\infty \frac{e^{-\gamma_2(z-z')}}{\gamma_2} J_0(\lambda\rho)\lambda \, d\lambda = \frac{2}{k_1^2 + k_2^2} \frac{e^{-jk_2R}}{R}$$

and

$$R = [\rho^2 + (z - z')^2]^{1/2}.$$

The remainder, which must be evaluated by numerical integration, is then

$$V'_{12} = V_{12} - V_0 = 2 \int_0^\infty \left[ \frac{e^{\gamma_1 z' - \gamma_2 z}}{k_1^2\gamma_2 + k_2^2\gamma_1} - \frac{e^{-\gamma_2(z-z')}}{\gamma_2(k_1^2 + k_2^2)} \right] J_0(\lambda\rho)\lambda \, d\lambda$$

where $\gamma_1 = (\lambda^2 - k_1^2)^{1/2}$ and $\gamma_2 = (\lambda^2 - k_2^2)^{1/2}$. When $R$ is small the subtraction must be done in the integrand with careful treatment of cancelling terms, while for larger $R$, $V_0$ can be subtracted from the numerical result for $V_{12}$ to retain the simpler integrand.

Substituting $V'_{12}$ into the equations (5-2) for electric field yields the remainder terms

$$E'^V_{\rho 12} = E^V_{\rho 12} - S^V_{\rho 12} = \frac{-j\omega\mu_0}{4\pi} \frac{\partial^2 V'_{12}}{\partial\rho\partial z} \tag{H-1a}$$

$$E'^V_{z12} = E^V_{z12} - S^V_{z12} = \frac{-j\omega\mu_0}{4\pi} \left( \frac{\partial^2}{\partial z^2} + k_2^2 \right) V'_{12} \tag{H-1b}$$

$$E'^H_{\rho 12} = E^H_{\rho 12} - S^H_{\rho 12} = \frac{-j\omega\mu_0}{4\pi} \left( \frac{\partial^2 V'_{12}}{\partial\rho^2} + U_{12} \right) \tag{H-1c}$$

$$E'^H_{\phi 12} = E^H_{\phi 12} - S^H_{\phi 12} = \frac{j\omega\mu_0}{4\pi} \left( \frac{1}{\rho} \frac{\partial V'_{12}}{\partial\rho} + U_{12} \right) \tag{H-1d}$$

$$E'^H_{z12} = E^H_{z12} - S^H_{z12} = \frac{j\omega\mu_0}{4\pi} \frac{\partial^2 V'_{12}}{\partial\rho\partial z'} \tag{H-1e}$$

where

$$S^V_{\rho 12} = \frac{-j\omega\mu_0}{4\pi} \frac{2}{k_1^2 + k_2^2} \left[ \rho(z - z') \left( \frac{3}{R^2} + j\frac{3k_2}{R} - k_2^2 \right) \right] \frac{e^{-jk_2R}}{R^3} \tag{H-2a}$$

$$S^V_{z12} = \frac{-j\omega\mu_0}{4\pi} \frac{2}{k_1^2 + k_2^2} \left[ (z - z')^2 \left( \frac{3}{R^2} + j\frac{3k_2}{R} - k_2^2 \right) - 1 - jk_2R + k_2^2R^2 \right] \frac{e^{-jk_2R}}{R^3} \tag{H-2b}$$

$$S^H_{\rho 12} = \frac{-j\omega\mu_0}{4\pi} \frac{2}{k_1^2 + k_2^2} \left[ \rho^2 \left( \frac{3}{R^2} + j\frac{3k_2}{R} - k_2^2 \right) - 1 - jk_2R \right] \frac{e^{-jk_2R}}{R^3} \tag{H-2c}$$

$$S^H_{\phi 12} = \frac{-j\omega\mu_0}{4\pi}\frac{2}{k_1^2+k_2^2}(1+jk_2R)\frac{e^{-jk_2R}}{R^3} \tag{H-2d}$$

$$S^H_{z12} = \frac{-j\omega\mu_0}{4\pi}\frac{2}{k_1^2+k_2^2}\left[\rho(z-z')\left(\frac{3}{R^2}+j\frac{3k_2}{R}-k_2^2\right)\right]\frac{e^{-jk_2R}}{R^3}. \tag{H-2e}$$

After subtracting $V_0$, $V'_{12}$ is finite at $R=0$, while the field components in equations (H-1) have $1/R$ singularities. The $1/R$ singularities will be subtracted from these field terms in a later step to leave a finite remainder at $R=0$, but first the evaluation of the integrand for $V'_{12}$ is considered.

Careful treatment of canceling terms in the integrand of $V'_{12}$ is needed when $|\lambda|$ is large to avoid loss of precision. This is especially important with the adaptive quadrature used in NEC. The cancellation can be isolated in simple terms by writing

$$V'_{12} = 2\int_0^\infty \left[\frac{\gamma_2 k_1^2 T_1 + k_2^2 T_2}{\gamma_2(k_1^2+k_2^2)(k_1^2\gamma_2+k_2^2\gamma_1)}\right] e^{-\gamma_2(z-z')} J_0(\lambda\rho)\lambda\, d\lambda. \tag{H-3}$$

The derivative of $V'_{12}$ with respect to $z$ brings out a factor of $-\gamma_2$. However, the derivative with respect to $z'$ changes the canceling terms, so that

$$\frac{\partial}{\partial z'}V'_{12} = 2\int_0^\infty \left[\frac{\gamma_1 k_2^2 T_1 + k_1^2 T_3}{(k_1^2+k_2^2)(k_1^2\gamma_2+k_2^2\gamma_1)}\right] e^{-\gamma_2(z-z')} J_0(\lambda\rho)\lambda\, d\lambda \tag{H-4}$$

where

$$\begin{aligned} T_1 &= e^{z'(\gamma_1-\gamma_2)} - 1 \\ T_2 &= \gamma_2 e^{z'(\gamma_1-\gamma_2)} - \gamma_1 \\ T_3 &= \gamma_1 e^{z'(\gamma_1-\gamma_2)} - \gamma_2. \end{aligned}$$

For large $|\lambda|$ the differences can be evaluated with a series expansion in $\lambda^{-1}$. Assuming $\mathrm{Im}(\lambda) < 0$ and vertical branch cuts,

$$\gamma_1 \approx S_1\left(\lambda - \tfrac{1}{2}k_1^2\lambda^{-1} - \tfrac{1}{8}k_1^4\lambda^{-3} - \tfrac{1}{16}k_1^6\lambda^{-5}\right)$$

$$S_1 = \mathrm{Sign}[\mathrm{Re}(\lambda - k_1)], \qquad |\lambda| \gg |k_1|$$

and

$$\gamma_2 \approx S_2\left(\lambda - \tfrac{1}{2}k_2^2\lambda^{-1} - \tfrac{1}{8}k_2^4\lambda^{-3} - \tfrac{1}{16}k_2^6\lambda^{-5}\right)$$

$$S_2 = \mathrm{Sign}[\mathrm{Re}(\lambda - k_2)], \qquad |\lambda| \gg |k_2|.$$

The series for the exponential with large $|\lambda|$ is

$$e^{z'(\gamma_1-\gamma_2)} \approx 1 + a_1 S\lambda^{-1} + a_2\lambda^{-2} + a_3 S\lambda^{-3} + a_4\lambda^{-4} + a_5 S\lambda^{-5}$$

where

$$a_1 = \frac{z'(k_2^2 - k_1^2)}{2}$$
$$a_2 = \frac{z'^2(k_2^2 - k_1^2)^2}{8}$$
$$a_3 = \frac{z'}{8}\left[k_2^4 - k_1^4 + \frac{z'^2(k_2^2 - k_1^2)^3}{6}\right]$$
$$a_4 = \frac{z'^2}{16}\left[(k_2^2 - k_1^2)(k_2^4 - k_1^4) + \frac{z'^2(k_2^2 - k_1^2)^4}{24}\right]$$
$$a_5 = \frac{z'}{16}\left[k_2^6 - k_1^6 + \frac{z'^2(k_2^2 - k_1^2)^2(k_2^4 - k_1^4)}{4} + \frac{z'^4(k_2^2 - k_1^2)^5}{240}\right]$$

and

$$S = \begin{cases} 1 & \text{if } \mathrm{Re}(\lambda) > \mathrm{Re}(k_1) \\ -1 & \text{if } \mathrm{Re}(\lambda) < \mathrm{Re}(k_2). \end{cases}$$

It is assumed here that $\mathrm{Re}(k_2) < \mathrm{Re}(k_1)$. When $\mathrm{Re}(k_2) < \mathrm{Re}(\lambda) < \mathrm{Re}(k_1)$ the terms in $V'_{12}$ do not cancel. This is not a problem, since the integration contour used for numerical evaluation goes between the branch cuts to large $|\lambda|$ only when $R$ is large, in which case singularity subtraction is not done. Using the series expansions for large $|\lambda|$ the difference terms are

$$T_1 \approx a_1 S\lambda^{-1} + a_2\lambda^{-2} + a_3 S\lambda^{-3} + a_4\lambda^{-4} + a_5 S\lambda^{-5}$$
$$T_2 \approx S(a_1 + b_1\lambda^{-1} + b_2\lambda^{-2} + b_3\lambda^{-3} + b_4\lambda^{-4} + b_5\lambda^{-5})$$
$$T_3 \approx S(a_1 + c_1\lambda^{-1} + c_2\lambda^{-2} + c_3\lambda^{-3} + c_4\lambda^{-4} + c_5\lambda^{-5})$$

where

$$b_1 = \tfrac{1}{2}(k_1^2 - k_2^2) + a_2$$
$$b_2 = a_3 - \tfrac{1}{2}a_1 k_2^2$$
$$b_3 = \tfrac{1}{8}(k_1^4 - k_2^4) - \tfrac{1}{2}a_2 k_2^2 + a_4$$
$$b_4 = a_5 - \tfrac{1}{2}k_2^2(\tfrac{1}{4}a_1 k_2^2 + a_3)$$
$$b_5 = \tfrac{1}{16}(k_1^6 - k_2^6) - \tfrac{1}{2}k_2^2(\tfrac{1}{4}a_2 k_2^2 + a_4)$$

and

$$c_1 = \tfrac{1}{2}(k_2^2 - k_1^2) + a_2$$
$$c_2 = a_3 - \tfrac{1}{2}a_1 k_1^2$$
$$c_3 = \tfrac{1}{8}(k_2^4 - k_1^4) - \tfrac{1}{2}a_2 k_1^2 + a_4$$
$$c_4 = a_5 - \tfrac{1}{2}k_1^2(\tfrac{1}{4}a_1 k_1^2 + a_3)$$
$$c_5 = \tfrac{1}{16}(k_2^6 - k_1^6) - \tfrac{1}{2}k_1^2(\tfrac{1}{4}a_2 k_1^2 + a_4).$$

The equations (H-1) retain $R^{-1}$ singularities from the derivatives of $V'_{12}$ and from $U_{12}$. These singularities can be evaluated and subtracted, although this was not done within the integrand. To get the singular terms, the difference factors are approximated by their leading

terms for large $\lambda$ and small $z'$, with $\mathrm{Re}(\lambda) > \mathrm{Re}(k_1)$, as

$$\begin{aligned} T_1 &\approx \tfrac{1}{2} z'(k_2^2 - k_1^2)\lambda^{-1} \\ T_2 &\approx \tfrac{1}{2} z'(k_2^2 - k_1^2) + \tfrac{1}{2}(k_1^2 - k_2^2)\lambda^{-1} \\ T_3 &\approx \tfrac{1}{2} z'(k_2^2 - k_1^2) + \tfrac{1}{2}(k_2^2 - k_1^2)\lambda^{-1} \end{aligned}$$

The $\lambda^{-1}$ terms must be included in $T_2$ and $T_3$ when they are not multiplied by $z'$. The integrals (H-3) and (H-4) for $|k_1 R| \ll 1$ then become

$$V'_{12} \approx 2\int_0^\infty \left[\frac{z'(k_2^2 - k_1^2)}{2(k_2^2 + k_1^2)}\lambda^{-1} - \frac{k_2^2(k_2^2 - k_1^2)}{2(k_2^2 + k_1^2)^2}\lambda^{-2}\right] e^{-\gamma_2(z-z')} J_0(\lambda\rho)\, d\lambda.$$

$$\frac{\partial}{\partial z'} V'_{12} \approx 2\int_0^\infty \left[\frac{z'(k_2^2 - k_1^2)}{2(k_2^2 + k_1^2)}\lambda^{-1} + \frac{k_1^2(k_2^2 - k_1^2)}{2(k_2^2 + k_1^2)^2}\lambda^{-2}\right] e^{-\gamma_2(z-z')} J_0(\lambda\rho)\, d\lambda$$

The $R^{-1}$ components of the $E'$ terms in (H-1) can then be evaluated using the integrals from [1]

$$\begin{aligned} \int_0^\infty e^{-\lambda(z-z')} J_0(\lambda\rho)\, d\lambda &= \frac{1}{R} \\ \int_0^\infty e^{-\lambda(z-z')} J_0(\lambda\rho)\lambda\, d\lambda &= \frac{\sin\theta}{R^2} \\ \int_0^\infty e^{-\lambda(z-z')} J'_0(\lambda\rho)\, d\lambda &= \frac{\sin\theta - 1}{R\cos\theta} \\ \int_0^\infty e^{-\lambda(z-z')} J'_0(\lambda\rho)\lambda\, d\lambda &= \frac{-\cos\theta}{R^2} \end{aligned}$$

where $R = [\rho^2 + (z - z')^2]^{1/2}$ and $\sin\theta = (z - z')/R$. The results, for $k_2 R \ll 1$ are

$$\begin{aligned} E'^V_{\rho 12} \approx S'^V_{\rho 12} &= \frac{-j\omega\mu_0}{4\pi}\left[C_2\frac{1-\sin\theta}{\cos\theta} - C_1\frac{z'\cos\theta}{R}\right]\frac{e^{-jk_2R}}{R} \\ E'^V_{z12} \approx S'^V_{z12} &= \frac{-j\omega\mu_0}{4\pi}\left[C_2 - C_1\frac{z'\sin\theta}{R}\right]\frac{e^{-jk_2R}}{R} \\ E'^H_{\rho 12} \approx S'^H_{\rho 12} &= \frac{-j\omega\mu_0}{4\pi}\left[C_2\left(\frac{1-\sin\theta}{\cos^2\theta} - 1\right) + C_1\frac{z'}{R}\left(\frac{\sin\theta(1+\cos^2\theta) - 1}{\cos^2\theta}\right) + 1\right]\frac{e^{-jk_2R}}{R} \\ E'^H_{\phi 12} \approx S'^H_{\phi 12} &= \frac{j\omega\mu_0}{4\pi}\left[-C_2\frac{1-\sin\theta}{\cos^2\theta} + C_1\frac{z'(1-\sin\theta)}{R\cos^2\theta} + 1\right]\frac{e^{-jk_2R}}{R} \\ E'^H_{z12} \approx S'^H_{z12} &= \frac{j\omega\mu_0}{4\pi}\left[\frac{k_1^2 C_2}{k_2^2}\frac{(1-\sin\theta)}{\cos\theta} + C_1\frac{z'\cos\theta}{R}\right]\frac{e^{-jk_2R}}{R} \end{aligned}$$

where

$$C_1 = \frac{k_1^2 - k_2^2}{k_1^2 + k_2^2}, \qquad C_2 = k_2^2\frac{k_1^2 - k_2^2}{(k_1^2 + k_2^2)^2}.$$

Terms of $1/R$ have been added to $S'^H_{\rho 12}$ and $S'^H_{\phi 12}$ to cancel the singularity of $U12$. Although the factor $e^{-jk_2R}$ does not result from the integrals, it is included since it is contained in other field components. Subtracting these terms from the $E'$ terms leaves the remainder

$$\begin{aligned}
E''^V_{\rho 12} &= E^V_{\rho 12} - S^V_{\rho 12} - S'^V_{\rho 12} \\
E''^V_{z12} &= E^V_{z12} - S^V_{z12} - S'^V_{z12} \\
E''^H_{\rho 12} &= E^H_{\rho 12} - S^H_{\rho 12} - S'^H_{\rho 12} \\
E''^H_{\phi 12} &= E^H_{\phi 12} - S^H_{\phi 12} - S'^H_{\phi 12} \\
E''^H_{z12} &= E^H_{z12} - S^H_{z12} - S'^H_{z12}
\end{aligned}$$

The $E''$ quantities are finite at $R = 0$, so the origin can be included in an interpolation table.

## References


[1] I. S. Gradshteyn and I. M. Ryzhik, *Tables of Integrals, Series and Products*, Academic Press, New York, 1980.

# APPENDIX I

## Numerical Solution for Saddle Points in the Sommerfeld Integrals

For asymptotic evaluation, the Sommerfeld integrals are written in the form

$$U = \int_{-\infty}^{\infty} G(\lambda) e^{-F(\lambda)}\, d\lambda$$

where $G$ is a slowly varying function of $\lambda$, relative to the exponential. With the coordinates as shown in Fig. I-1, the function $F(\lambda)$ is

$$F(\lambda) = (\lambda^2 - k_2^2)^{1/2} z - (\lambda^2 - k_1^2)^{1/2} z' + j\lambda\rho$$

and is the same for all components of the field. The saddle points $\lambda_s$, needed in the steepest descent evaluation, are solutions of the equation

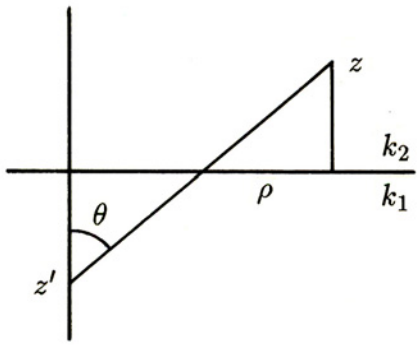


**Fig. I-1** Coordinates for evaluating the saddle point.

$$F'(\lambda_s) = \lambda_s(\lambda_s^2 - k_2^2)^{-1/2} z - \lambda_s(\lambda_s^2 - k_1^2)^{-1/2} z' + j\rho = 0. \tag{I-1}$$

When $z = 0$ or $z' = 0$, (I-1) can easily be solved for $\lambda_s$. For general values of $\rho$, $z$ and $z'$ the value of $\lambda_s$ can be found by solving a quartic equation in $\lambda_s^2$, but a numerical solution is usually more practical. The numerical procedure is complicated by the existence of multiple solutions that can mislead the solution algorithm. An additional problem with (I-1) is that in the limits as $z$ or $z'$ approach zero the saddle points should approach $k_2$ or $k_1$, respectively, with the steepest-descent paths becoming branch-cut integrals. However terms in (I-1) become indeterminate in these limits. Hence (I-1) was multiplied by the denominator terms to yield

$$f(\lambda_s) = \lambda_s(\lambda_s^2 - k_1^2)^{1/2} z - \lambda_s(\lambda_s^2 - k_2^2)^{1/2} z' + j(\lambda_s^2 - k_1^2)^{1/2}(\lambda_s^2 - k_2^2)^{1/2}\rho = 0 \tag{I-2}$$

This equation is then solved by Newton's method. Using the derivative

$$f'(\lambda) = \frac{2\lambda^2 - k_1^2}{(\lambda^2 - k_1^2)^{1/2}} z - \frac{2\lambda^2 - k_2^2}{(\lambda^2 - k_2^2)^{1/2}} z' + \frac{j\rho\lambda(2\lambda^2 - k_1^2 - k_2^2)}{(\lambda^2 - k_1^2)^{1/2}(\lambda^2 - k_2^2)^{1/2}}$$

the iteration equation is

$$\lambda_{i+1} = \lambda_i - f(\lambda_i)/f'(\lambda_i) = \lambda_i - D(\lambda_i) \tag{I-3}$$

where

$$D(\lambda) = \frac{\lambda(\lambda^2 - k_1^2)(\lambda^2 - k_2^2)^{1/2} z - \lambda(\lambda^2 - k_2^2)(\lambda^2 - k_1^2)^{1/2} z' + j\rho(\lambda^2 - k_1^2)(\lambda^2 - k_2^2)}{(2\lambda^2 - k_1^2)(\lambda^2 - k_2^2)^{1/2} z - (2\lambda^2 - k_2^2)(\lambda^2 - k_1^2)^{1/2} z' + j\rho\lambda(2\lambda^2 - k_1^2 - k_2^2)}. \tag{I-4}$$

Since (I-2) can be scaled by a constant, the solution depends on only two distance parameters. The normalized parameters

$$\tilde{z} = z/(z - z')$$
$$\tilde{\rho} = \rho \Big/ \sqrt{\rho^2 + (z - z')^2} = \sin\theta$$

will be used, since they can independently range from 0 to 1.

Solutions for $\lambda_s$ for a typical case are shown in Fig. 5-6. On the principal Riemann sheet there is a saddle point between $\lambda = 0$ and $k_2$, and a second SDP through a saddle point between $k_2$ and $k_1$ may be needed. When $z' = 0$, a saddle point lies on the line between 0 and $k_2$ at $\lambda_s = k_2 \sin\theta$, with a possible branch-cut integral from $k_1$. When $z = 0$, a saddle point is at $\lambda_s = k_1 \sin\theta$, and the branch cut integral from $k_2$ may contribute. When $z$ is small, but not zero, the saddle point near the line from 0 to $k_1$ passes onto the lower sheet at the branch cut from $k_2$, and a saddle point near $k_2$ moves onto the principal sheet and approaches the branch point as $\tilde{\rho}$ increases. This detail near $k_2$ is not shown on the plot.

Since the asymptotic approximations used here do not uniformly include the two branch points and a pole that occur in the Sommerfeld integrals, there is some arbitrariness in the choice of saddle points. Equation (I-2) is solved only for the saddle point between 0 and $k_2$ in NEC, since this solution represents the wave traveling mostly through air. The saddle point between $k_2$ and $k_1$ represents a wave traveling mainly through the ground (the lateral wave for $z$, $z' \geq 0$). When this wave is considered important, the approximation $\lambda_s \approx k_1 \sin\theta$ is used.

To obtain a reliable solution for $\lambda_s$ between 0 and $k_2$, a table is first generated for the given ground parameters. For a particular value of $\tilde{z}$, the solution is started at $\tilde{\rho} = 0$ where $\lambda_s = 0$. The parameter $\tilde{\rho}$ is then incremented and the iteration in (I-3) is started with the previous $\lambda_s$ to find the new solution. This process is continued until $\tilde{\rho} = 1$, and then repeated for a new $\tilde{z}$. A plot from a typical table of $\lambda_s$ versus $\tilde{\rho}$ and $\tilde{z}$ is shown in Fig. I-2. For particular values of $\rho$, $z$ and $z'$, an estimate of $\lambda_s$ is obtained by interpolating in the table for $\tilde{\rho}$ and $\tilde{z}$. Iteration of (I-3) is then used to improve the accuracy. If the iteration results in Re($\lambda_s$) > Re ($k_2$) then $\lambda_s$ is set to $k_2$.

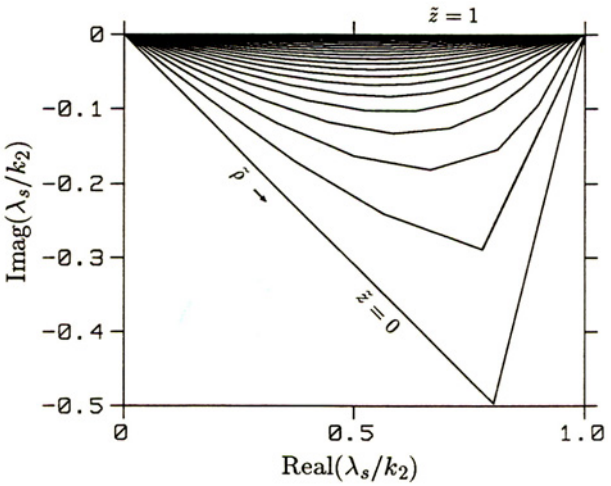


**Fig. I-2** Loci of saddle points between $\lambda = 0$ and $k_2$, from the table generated for starting the iterative solution. The complex relative permittivity of the ground was $10 - j20$.

# APPENDIX J

## Second Order Asymptotic Approximations for the Field Due to Ground

In the first section of this Appendix, second-order asymptotic approximations, from the saddle-point method, are developed for the field transmitted across the air-earth interface. Corrections to these terms to obtain a uniform approximation valid for source and receiver approaching the interface are included in Section 5.2.4. These approximations for general source and receiver coordinates fail as the radial separation $\rho$ becomes small. A uniform asymptotic expansion including $\rho = 0$ is not attempted here. First-order approximations are used for small $\rho$, and higher-order terms are obtained by interpolation when possible. This interpolation of higher-order terms is described in the second section of this Appendix.

### J.1 Second-Order Approximation for the Saddle Point Contribution

For an integral of the form

$$I = \int_{-\infty}^{\infty} G(\lambda) e^{-F(\lambda)}\, d\lambda$$

a second-order asymptotic approximation with a saddle point $\lambda_s$, where $F'(\lambda_s) = 0$ and $F''(\lambda_s) \neq 0$, is from equations (6.2) and (5.20) in [1]

$$I \sim \left(\frac{2\pi}{F_2}\right)^{1/2} e^{-F_0}(Q_0 + Q_2) \tag{J-1}$$

where

$$Q_0 = G_0$$
$$Q_2 = \frac{1}{24F_2^3}\left[G_0(5F_3^2 - 3F_2F_4) - 12G_1F_2F_3 + 12G_2F_2^2\right]$$

and the notation

$$F_n = \frac{d^n}{d\lambda^n}F(\lambda)\bigg|_{\lambda=\lambda_s} \qquad \text{and} \qquad G_n = \frac{d^n}{d\lambda^n}G(\lambda)\bigg|_{\lambda=\lambda_s}$$

has been used. The square root in (J-1) is chosen so that the argument of $F^{-1/2}$ is equal to the argument of $d\lambda$ on the steepest descent path. The term $Q_0$ represents the first-order approximation, and $Q_2$ is the next higher order term. A term $Q_1$ is included for an integral from a limit, but is not present for an integral through a saddle point.

In the integrals for the field components due to ground, $F$ is the same for each component while the function $G$ varies. Hence (J-1) will be written in the form

$$I \sim \sqrt{2\pi}e^{-F_0}\left[\left(\frac{1}{F_2^{1/2}} + \frac{5F_3^2 - 3F_2F_4}{24F_2^{7/2}}\right)G_0 - \frac{1}{2}\frac{F_3}{F_2^{5/2}}G_1 + \frac{1}{2}\frac{1}{F_2^{3/2}}G_2\right]. \tag{J-2}$$

In the Sommerfeld integrals for a buried source at $z'$ ($z' < 0$), field evaluation point at height $z$ ($z \geq 0$) and radial separation $\rho$, as in Fig. 5-1, $F$ and its derivatives are

$$\begin{aligned}
F_0 &= \Gamma_2 z - \Gamma_1 z' + j\lambda_s \rho \\
F_1 &= \Gamma_1^{-1}\Gamma_2^{-1}(\lambda_s \Gamma_1 z - \lambda_s \Gamma_2 z' + j\Gamma_1\Gamma_2\rho) \\
F_2 &= \Gamma_1^{-3}\Gamma_2^{-3}(-k_2^2\Gamma_1^3 z + k_1^2\Gamma_2^3 z') \\
F_3 &= 3\lambda_s\Gamma_1^{-5}\Gamma_2^{-5}(k_2^2\Gamma_1^5 z - k_1^2\Gamma_2^5 z') \\
F_4 &= 3\Gamma_1^{-7}\Gamma_2^{-7}\left[-k_2^2(4\lambda_s^2 + k_2^2)\Gamma_1^7 z + k_1^2(4\lambda_s^2 + k_1^2)\Gamma_2^7 z'\right]
\end{aligned}$$

where $\Gamma_1 = (\lambda_s^2 - k_1^2)^{1/2}$ and $\Gamma_2 = (\lambda_s^2 - k_2^2)^{1/2}$ and $\lambda_s$ is the solution of the equation

$$F'(\lambda_s) = \lambda_s(\lambda_s^2 - k_2^2)^{-1/2} z - \lambda_s(\lambda_s^2 - k_1^2)^{-1/2} z' + j\rho = 0. \tag{J-3}$$

The terms involving $F$ in (J-2) are then

$$\begin{aligned}
\frac{1}{F_2^{1/2}} &= \frac{\Gamma_1^{3/2}\Gamma_2^{3/2}}{(-k_2^2\Gamma_1^3 z + k_1^2\Gamma_2^3 z')^{1/2}} \\
\frac{F_3^2}{F_2^{7/2}} &= \frac{9\lambda_s^2\Gamma_1^{1/2}\Gamma_2^{1/2}(k_2^2\Gamma_1^5 z - k_1^2\Gamma_2^5 z')^2}{(-k_2^2\Gamma_1^3 z + k_1^2\Gamma_2^3 z')^{7/2}} \\
\frac{F_4}{F_2^{5/2}} &= \frac{3\Gamma_1^{1/2}\Gamma_2^{1/2}\left[-k_2^2(4\lambda_s^2 + k_2^2)\Gamma_1^7 z + k_1^2(4\lambda_s^2 + k_1^2)\Gamma_2^7 z'\right]}{(-k_2^2\Gamma_1^3 z + k_1^2\Gamma_2^3 z')^{5/2}} \\
\frac{F_3}{F_2^{5/2}} &= \frac{3\lambda_s\Gamma_1^{5/2}\Gamma_2^{5/2}(k_2^2\Gamma_1^5 z - k_1^2\Gamma_2^5 z')}{(-k_2^2\Gamma_1^3 z + k_1^2\Gamma_2^3 z')^{5/2}} \\
\frac{1}{F_2^{3/2}} &= \frac{\Gamma_1^{9/2}\Gamma_2^{9/2}}{(-k_2^2\Gamma_1^3 z + k_1^2\Gamma_2^3 z')^{3/2}}
\end{aligned}$$

Care is needed in evaluating these expressions to avoid division by zero. Although (J-3) may have multiple solutions representing two ray paths crossing the interface, the second-order approximation here will be used only for the saddle point between 0 and $k_2$ and is not valid for small $\rho$. Hence we need only be concerned with indeterminate forms resulting when $z$ goes to zero and simultaneously $\Gamma_2$ goes to zero. To avoid division by zero, the ratio $\Gamma_2/z$ will be evaluated as

$$\Lambda_2 = \frac{\Gamma_2}{z} = \frac{\lambda_s}{\lambda_s z'/\Gamma_1 - j\rho}$$

obtained from (J-3). Then the terms involving $F$ become

$$\frac{1}{F_2^{1/2}} = \frac{\Gamma_1^{3/2}\Lambda_2^{3/2} z}{(-k_2^2\Gamma_1^3 + k_1^2\Lambda_2^3 z^2 z')^{1/2}} \tag{J-4a}$$

$$\frac{F_3^2}{F_2^{7/2}} = \frac{9\lambda_s^2\Gamma_1^{1/2}\Lambda_2^{1/2}(k_2^2\Gamma_1^5 - k_1^2 z^4 z'\Lambda_2^5)^2}{z(-k_2^2\Gamma_1^3 + k_1^2 z^2 z'\Lambda_2^3)^{7/2}} \tag{J-4b}$$

$$\frac{F_4}{F_2^{5/2}} = \frac{3\Gamma_1^{1/2}\Lambda_2^{1/2}\left[-k_2^2(4\lambda_s^2+k_2^2)\Gamma_1^7 + k_1^2(4\lambda_s^2+k_1^2)\Lambda_2^7 z^6 z'\right]}{z(-k_2^2\Gamma_1^3 + k_1^2\Lambda_2^3 z^2 z')^{5/2}} \tag{J-4c}$$

$$\frac{F_3}{F_2^{5/2}} = \frac{3\lambda_s\Gamma_1^{5/2}\Lambda_2^{5/2} z(k_2^2\Gamma_1^5 - k_1^2\Lambda_2^5 z^4 z')}{(-k_2^2\Gamma_1^3 + k_1^2\Lambda_2^3 z^2 z')^{5/2}} \tag{J-4d}$$

$$\frac{1}{F_2^{3/2}} = \frac{\Gamma_1^{9/2}\Lambda_2^{9/2} z^3}{(-k_2^2\Gamma_1^3 + k_1^2\Lambda_2^3 z^2 z')^{3/2}} \tag{J-4e}$$

Equations (J-4b) and (J-4c) are still singular as $z$ goes to zero, but the singular terms cancel when combined in (J-2) to yield

$$\begin{aligned}\frac{5F_3^2 - 3F_2F_4}{F_2^{7/2}} =& \frac{9\Gamma_1^{5/2}\Lambda_2^{5/2} z}{(-k_2^2\Gamma_1^3 + k_1^2\Lambda_2^3 z^2 z')^{7/2}}\Big\{k_2^4\Gamma_1^8 + k_1^4\Lambda_2^8 z^6 z'^2 \\ & - k_1^2 k_2^2\Gamma_1\Lambda_2 z'[10\lambda_s^2\Gamma_1^2\Lambda_2^2 z^2 - \Lambda_2^4 z^4(4\lambda_s^2+k_1^2) - \Gamma_1^4(4\lambda_s^2+k_2^2)]\Big\}\end{aligned} \tag{J-5}$$

Equation (J-2) can then be written in a form that can be evaluated when $z$ and $\Gamma_2$ go to zero, which is

$$I \sim \sqrt{2\pi}e^{-F_0}(f_0 g_0 + f_1 g_1 + f_2 g_2) \tag{J-6}$$

where $g_0 = G_0$, $g_1 = zG_1$, $g_2 = z^3 G_2$ and

$$f_0 = \frac{1}{F_2^{1/2}} + \frac{5F_3^2 - 3F_2F_4}{24F_2^{7/2}} \tag{J-7a}$$

$$f_1 = -\frac{1}{2}\frac{F_3}{zF_2^{5/2}} = -\frac{3\lambda_s\Gamma_1^{5/2}\Lambda_2^{5/2}(k_2^2\Gamma_1^5 - k_1^2\Lambda_2^5 z^4 z')}{2(-k_2^2\Gamma_1^3 + k_1^2\Lambda_2^3 z^2 z')^{5/2}} \tag{J-7b}$$

$$f_2 = \frac{1}{2}\frac{1}{z^3 F_2^{3/2}} = \frac{\Gamma_1^{9/2}\Lambda_2^{9/2}}{(-k_2^2\Gamma_1^3 + k_1^2\Lambda_2^3 z^2 z')^{3/2}}. \tag{J-7c}$$

Equations (J-4a) and (J-5) are used in evaluating $f_0$.

In approximating the integrals for field components, the two-term asymptotic expansion for the Hankel function will be used

$$H_0^{(2)}(z) \sim \sqrt{\frac{2}{\pi z}}\left(1 + \frac{j}{8z}\right)e^{-jz+j\pi/4}$$

$$H_0'^{(2)}(z) \sim \sqrt{\frac{2}{\pi z}}\left(1 - j\frac{3}{8z}\right)e^{-jz-j\pi/4}$$

$$H_0''^{(2)}(z) \sim -\sqrt{\frac{2}{\pi z}}\left(1 - j\frac{7}{8z}\right)e^{-jz+j\pi/4}.$$

The asymptotic approximations for the field components are then obtained by substituting the appropriate expressions for the function $G$ and its derivatives into (J-6). For $U_{12}$ the

approximation is

$$\begin{aligned} U_{12} &= \int_{-\infty}^{\infty} \frac{\lambda H_0^{(2)}(\lambda\rho)}{\gamma_1+\gamma_2} e^{\gamma_1 z' - \gamma_2 z}\, d\lambda \\ &\approx e^{j\pi/4}\sqrt{\frac{2}{\pi\rho}} \int_{-\infty}^{\infty} \frac{\lambda^{1/2} + \frac{j}{8\rho}\lambda^{-1/2}}{\gamma_1+\gamma_2} e^{-(\gamma_2 z - \gamma_1 z' + j\lambda\rho)}\, d\lambda \\ &\sim e^{j\pi/4}\frac{2}{\sqrt{\rho}}\Big(f_0 g_0 + f_1 g_1 + f_2 g_2\Big) e^{-(\Gamma_2 z - \Gamma_1 z' + j\lambda_s\rho)} \end{aligned} \tag{J-8}$$

so that

$$G(\lambda) = \left(\lambda^{1/2} + \frac{j}{8\rho}\lambda^{-1/2}\right) D_U(\lambda) \qquad \text{and} \qquad D_U(\lambda) = \frac{1}{\gamma_1+\gamma_2}$$

with $\gamma_1 = (\lambda^2 - k_1^2)^{1/2}$ and $\gamma_2 = (\lambda^2 - k_2^2)^{1/2}$. The coefficients in (J-8) are then

$$\begin{aligned} g_0 = \quad G_0 &= \left(\lambda_s^{1/2} + \frac{j}{8\rho}\lambda_s^{-1/2}\right) d_U \\ g_1 = \; zG_1 &= \frac{z}{2}\left(\lambda_s^{-1/2} - \frac{j}{8\rho}\lambda_s^{-3/2}\right) d_U + \left(\lambda_s^{1/2} + \frac{j}{8\rho}\lambda_s^{-1/2}\right) d_U' \\ g_2 = z^3 G_2 &= -\frac{z^3}{4}\left(\lambda_s^{-3/2} - \frac{3j}{8\rho}\lambda_s^{-5/2}\right) d_U + z^2\left(\lambda_s^{-1/2} - \frac{j}{8\rho}\lambda_s^{-3/2}\right) d_U' \\ &\quad + \left(\lambda_s^{1/2} + \frac{j}{8\rho}\lambda_s^{-1/2}\right) d_U'' \end{aligned}$$

where

$$\begin{aligned} d_U = \quad D_U(\lambda_s) &= \frac{1}{\Gamma_1 + z\Lambda_2} \\ d_U' = \; zD_U'(\lambda_s) &= \frac{-\lambda_s}{\Gamma_1\Lambda_2(\Gamma_1 + z\Lambda_2)} \\ d_U'' = z^3 D_U''(\lambda_s) &= \frac{k_1^2\Gamma_1^{-3}z^3 + k_2^2\Lambda_2^{-3}}{(\Gamma_1 + z\Lambda_2)^2} + \frac{2z\lambda_s^2}{\Gamma_1^2\Lambda_2^2(\Gamma_1 + z\Lambda_2)}\,. \end{aligned}$$

The approximations for the field components involve the derivatives of $V_{12}$ and where necessary the term $U_{12}$. The derivatives of the denominator of $V_{12}$, $D_V(\lambda)$ will be represented as

$$\begin{aligned} d_V = \quad D_V(\lambda_s) &= \frac{1}{k_1^2 z\Lambda_2 + k_2^2\Gamma_1} \\ d_V' = \; zD_V'(\lambda_s) &= \frac{-\lambda_s(k_1^2\Lambda_2^{-1} + k_2^2 z\Gamma_1^{-1})}{(k_1^2 z\Lambda_2 + k_2^2\Gamma_1)^2} \\ d_V'' = z^3 D_V''(\lambda_s) &= \frac{k_1^2 k_2^2(z^3\Gamma_1^{-3} + \Lambda_2^{-3})}{(k_1^2 z\Lambda_2 + k_2^2\Gamma_1)^2} + \frac{2\lambda_s^2 z(k_1^2\Lambda_2^{-1} + k_2^2 z\Gamma_1^{-1})^2}{(k_1^2 z\Lambda_2 + k_2^2\Gamma_1)^3}. \end{aligned}$$

For field component $E_\rho^V$

$$\begin{aligned}
E_\rho^V &= \frac{-j\omega\mu_0}{4\pi}\frac{\partial^2 V_{12}}{\partial\rho\partial z} \\
&= \frac{j\omega\mu_0}{4\pi}\int_{-\infty}^{\infty}\frac{\lambda^2\gamma_2 H_0^{\prime(2)}(\lambda\rho)}{k_1^2\gamma_2+k_2^2\gamma_1}e^{\gamma_1 z'-\gamma_2 z}\,d\lambda \\
&\approx \frac{\omega\mu_0}{4\pi}e^{j\pi/4}\sqrt{\frac{2}{\pi\rho}}\int_{-\infty}^{\infty}\frac{\gamma_2(\lambda^{3/2}-j\frac{3}{8\rho}\lambda^{1/2})}{k_1^2\gamma_2+k_2^2\gamma_1}e^{-(\gamma_2 z-\gamma_1 z'+j\lambda\rho)}\,d\lambda \\
&\sim \frac{\omega\mu_0}{4\pi}e^{j\pi/4}\frac{2}{\sqrt{\rho}}\Big(f_0g_0+f_1g_1+f_2g_2\Big)e^{-(\Gamma_2 z-\Gamma_1 z'+j\lambda_s\rho)}
\end{aligned} \tag{J-9}$$

where

$$\begin{aligned}
g_0 = \quad G_0 =& z\Lambda_2\left(\lambda_s^{3/2}-\frac{3j}{8\rho}\lambda_s^{1/2}\right)d_V \\
g_1 = \; zG_1 =& \Lambda_2^{-1}\left(\lambda_s^{5/2}-\frac{3j}{8\rho}\lambda_s^{3/2}\right)d_V+\frac{3z^2}{2}\Lambda_2\left(\lambda_s^{1/2}-\frac{j}{8\rho}\lambda_s^{-1/2}\right)d_V \\
&+ z\Lambda_2\left(\lambda_s^{3/2}-\frac{3j}{8\rho}\lambda_s^{1/2}\right)d_V' \\
g_2 = z^3G_2 =& -\Lambda_2^{-3}\left(\lambda_s^{7/2}-\frac{3j}{8\rho}\lambda_s^{5/2}\right)d_V \\
&+\Lambda_2^{-1}\left[z^2\left(4\lambda_s^{3/2}-\frac{3j}{4\rho}\lambda_s^{1/2}\right)d_V+z\left(2\lambda_s^{5/2}-\frac{3j}{4\rho}\lambda_s^{3/2}\right)d_V'\right] \\
&+z\Lambda_2\left[\frac{3z^3}{4}\left(\lambda_s^{-1/2}+\frac{j}{8\rho}\lambda_s^{-3/2}\right)d_V+3z^2\left(\lambda_s^{1/2}-\frac{j}{8\rho}\lambda_s^{-1/2}\right)d_V'\right. \\
&\left.+\left(\lambda_s^{3/2}-\frac{3j}{8\rho}\lambda_s^{1/2}\right)d_V''\right].
\end{aligned}$$

For field component $E_z^V$

$$\begin{aligned}
E_z^V &= \frac{-j\omega\mu_0}{4\pi}\left(\frac{\partial^2}{\partial z^2}+k_2^2\right)V_{12} \\
&= \frac{-j\omega\mu_0}{4\pi}\int_{-\infty}^{\infty}\frac{\lambda^3 H_0^{(2)}(\lambda\rho)}{k_1^2\gamma_2+k_2^2\gamma_1}e^{\gamma_1 z'-\gamma_2 z}\,d\lambda \\
&\approx \frac{\omega\mu_0}{4\pi}e^{-j\pi/4}\sqrt{\frac{2}{\pi\rho}}\int_{-\infty}^{\infty}\frac{\lambda^{5/2}+\frac{j}{8\rho}\lambda^{3/2}}{k_1^2\gamma_2+k_2^2\gamma_1}e^{-(\gamma_2 z-\gamma_1 z'+j\lambda\rho)}\,d\lambda \\
&\sim \frac{\omega\mu_0}{4\pi}e^{-j\pi/4}\frac{2}{\sqrt{\rho}}\Big(f_0g_0+f_1g_1+f_2g_2\Big)e^{-(\Gamma_2 z-\Gamma_1 z'+j\lambda_s\rho)}
\end{aligned} \tag{J-10}$$

where

$$
\begin{aligned}
g_0 = \quad G_0 =& \left(\lambda_s^{5/2} + \frac{j}{8\rho}\lambda_s^{3/2}\right) d_V \\
g_1 = \; zG_1 =& z\left(\frac{5}{2}\lambda_s^{3/2} + \frac{3j}{16\rho}\lambda_s^{1/2}\right) d_V + \left(\lambda_s^{5/2} + \frac{j}{8\rho}\lambda_s^{3/2}\right) d_V' \\
g_2 = z^3 G_2 =& \frac{3z^3}{4}\left(5\lambda_s^{1/2} + \frac{j}{8\rho}\lambda_s^{-1/2}\right) d_V + z^2\left(5\lambda_s^{3/2} + \frac{3j}{8\rho}\lambda_s^{1/2}\right) d_V' \\
&+ \left(\lambda_s^{5/2} + \frac{j}{8\rho}\lambda_s^{3/2}\right) d_V''.
\end{aligned}
$$

For field component $E_\rho^H$

$$
\begin{aligned}
E_\rho^H &= \frac{-j\omega\mu_0}{4\pi}\left(\frac{\partial^2 V_{12}}{\partial\rho^2} + U_{12}\right) \\
&= \frac{-j\omega\mu_0}{4\pi}\left[\int_{-\infty}^{\infty} \frac{\lambda^3 H_0''^{(2)}(\lambda\rho)}{k_1^2\gamma_2 + k_2^2\gamma_1} e^{\gamma_1 z' - \gamma_2 z}\, d\lambda + U_{12}\right] \\
&\approx \frac{j\omega\mu_0}{4\pi}\left[e^{j\pi/4}\sqrt{\frac{2}{\pi\rho}}\int_{-\infty}^{\infty} \frac{\lambda^{5/2} - \frac{7j}{8\rho}\lambda^{3/2}}{k_1^2\gamma_2 + k_2^2\gamma_1} e^{-(\gamma_2 z - \gamma_1 z' + j\lambda\rho)}\, d\lambda - U_{12}\right] \\
&\sim \frac{j\omega\mu_0}{4\pi}\left[e^{j\pi/4}\frac{2}{\sqrt{\rho}}\Big(f_0 g_0 + f_1 g_1 + f_2 g_2\Big) e^{-(\Gamma_2 z - \Gamma_1 z' + j\lambda_s\rho)} - U_{12}\right] \qquad \text{(J-11)}
\end{aligned}
$$

where

$$
\begin{aligned}
g_0 = \quad G_0 =& \left(\lambda_s^{5/2} - \frac{7j}{8\rho}\lambda_s^{3/2}\right) d_V \\
g_1 = \; zG_1 =& z\left(\frac{5}{2}\lambda_s^{3/2} - \frac{21j}{16\rho}\lambda_s^{1/2}\right) d_V + \left(\lambda_s^{5/2} - \frac{7j}{8\rho}\lambda_s^{3/2}\right) d_V' \\
g_2 = z^3 G_2 =& \frac{3z^3}{4}\left(5\lambda_s^{1/2} - \frac{7j}{8\rho}\lambda_s^{-1/2}\right) d_V + z^2\left(5\lambda_s^{3/2} - \frac{21j}{8\rho}\lambda_s^{1/2}\right) d_V' \\
&+ \left(\lambda_s^{5/2} - \frac{7j}{8\rho}\lambda_s^{3/2}\right) d_V''.
\end{aligned}
$$

For field component $E_\phi^H$

$$
\begin{aligned}
E_\phi^H &= \frac{j\omega\mu_0}{4\pi}\left(\frac{1}{\rho}\frac{\partial V_{12}}{\partial\rho} + U_{12}\right) \\
&= \frac{j\omega\mu_0}{4\pi}\left[\frac{1}{\rho}\int_{-\infty}^{\infty} \frac{\lambda^2 H_0'^{(2)}(\lambda\rho)}{k_1^2\gamma_2 + k_2^2\gamma_1} e^{\gamma_1 z' - \gamma_2 z}\, d\lambda + U_{12}\right] \\
&\approx \frac{j\omega\mu_0}{4\pi}\left[\frac{e^{-j\pi/4}}{\rho}\sqrt{\frac{2}{\pi\rho}}\int_{-\infty}^{\infty} \frac{\lambda^{3/2} - \frac{3j}{8\rho}\lambda^{1/2}}{k_1^2\gamma_2 + k_2^2\gamma_1} e^{-(\gamma_2 z - \gamma_1 z' + j\lambda\rho)}\, d\lambda + U_{12}\right]
\end{aligned}
$$

$$\sim \frac{j\omega\mu_0}{4\pi}\left[\frac{e^{-j\pi/4}}{\rho}\frac{2}{\sqrt{\rho}}\Big(f_0g_0+f_1g_1+f_2g_2\Big)e^{-(\Gamma_2 z-\Gamma_1 z'+j\lambda_s\rho)}+U_{12}\right] \tag{J-12}$$

where

$$\begin{aligned}
g_0 = \quad G_0 =& \left(\lambda_s^{3/2}-\frac{3j}{8\rho}\lambda_s^{1/2}\right)d_V\\
g_1 = \; zG_1 =& \frac{3z}{2}\left(\lambda_s^{1/2}-\frac{j}{8\rho}\lambda_s^{-1/2}\right)d_V+\left(\lambda_s^{3/2}-\frac{3j}{8\rho}\lambda_s^{1/2}\right)d_V'\\
g_2 = z^3G_2 =& \frac{3z^3}{4}\left(\lambda_s^{-1/2}+\frac{j}{8\rho}\lambda_s^{-3/2}\right)d_V+3z^2\left(\lambda_s^{1/2}-\frac{j}{8\rho}\lambda_s^{-1/2}\right)d_V'\\
&+\left(\lambda_s^{3/2}-\frac{3j}{8\rho}\lambda_s^{1/2}\right)d_V''.
\end{aligned}$$

For field component $E_z^H$

$$\begin{aligned}
E_z^H &= \frac{j\omega\mu_0}{4\pi}\frac{\partial^2 V_{12}}{\partial\rho\partial z'}\\
&= \frac{j\omega\mu_0}{4\pi}\int_{-\infty}^{\infty}\frac{\lambda^2\gamma_1 H_0'^{(2)}(\lambda\rho)}{k_1^2\gamma_2+k_2^2\gamma_1}e^{\gamma_1 z'-\gamma_2 z}\,d\lambda\\
&\approx \frac{\omega\mu_0}{4\pi}e^{j\pi/4}\sqrt{\frac{2}{\pi\rho}}\int_{-\infty}^{\infty}\frac{\gamma_1(\lambda^{3/2}-j\frac{3}{8\rho}\lambda^{1/2})}{k_1^2\gamma_2+k_2^2\gamma_1}e^{-(\gamma_2 z-\gamma_1 z'+j\lambda\rho)}\,d\lambda\\
&\sim \frac{\omega\mu_0}{4\pi}e^{j\pi/4}\frac{2}{\sqrt{\rho}}\Big(f_0g_0+f_1g_1+f_2g_2\Big)e^{-(\Gamma_2 z-\Gamma_1 z'+j\lambda_s\rho)}
\end{aligned} \tag{J-13}$$

where

$$\begin{aligned}
g_0 = \quad G_0 =& \Gamma_1\left(\lambda_s^{3/2}-\frac{3j}{8\rho}\lambda_s^{1/2}\right)d_V\\
g_1 = \; zG_1 =& \frac{z}{\Gamma_1}\left(\lambda_s^{5/2}-\frac{3j}{8\rho}\lambda_s^{3/2}\right)d_V+\frac{3z}{2}\Gamma_1\left(\lambda_s^{1/2}-\frac{j}{8\rho}\lambda_s^{-1/2}\right)d_V\\
&+\Gamma_1\left(\lambda_s^{3/2}-\frac{3j}{8\rho}\lambda_s^{1/2}\right)d_V'\\
g_2 = z^3G_2 =& -\frac{z^3}{\Gamma_1^3}\left(\lambda_s^{7/2}-\frac{3j}{8\rho}\lambda_s^{5/2}\right)d_V\\
&+\frac{z^2}{\Gamma_1}\left[z\left(4\lambda_s^{3/2}-\frac{3j}{4\rho}\lambda_s^{1/2}\right)d_V+\left(2\lambda_s^{5/2}-\frac{3j}{4\rho}\lambda_s^{3/2}\right)d_V'\right]\\
&+\Gamma_1\left[\frac{3z^3}{4}\left(\lambda_s^{-1/2}+\frac{j}{8\rho}\lambda_s^{-3/2}\right)d_V+3z^2\left(\lambda_s^{1/2}-\frac{j}{8\rho}\lambda_s^{-1/2}\right)d_V'\right.\\
&\left.+\left(\lambda_s^{3/2}-\frac{3j}{8\rho}\lambda_s^{1/2}\right)d_V''\right].
\end{aligned}$$

## J.2 Approximations for Near Vertical Incidence

The approximations developed in the previous section fail when $\rho$ becomes small relative to $|z - z'|$. One reason for this limitation is the use of the large argument forms for Hankel functions with an argument involving $\rho$. More fundamentally, when the propagation path is mainly in the lower medium, two rays (two saddle points) may merge when $\theta = \sin^{-1}\left(\rho/\sqrt{\rho^2 + (z - z')^2}\right)$ is near the totally reflecting angle $\theta_c = \sin^{-1}(k_2/k_1)$. This case is discussed in [2], and it is shown that the transmission or reflection coefficients can no longer be treated as slowly varying relative to the exponential. A correct asymptotic evaluation in this case shows that the reflected ray in the lower medium develops a lateral shift as it merges with the lateral wave, and a caustic occurs in the field near $\theta_c$.

A higher-order uniform asymptotic approximation for small $\rho$ has not been attempted here. Rather, the first-order asymptotic forms are used, since these remain valid for small $\rho$. The first-order approximations can also be derived through geometrical optics, without restrictions on $\rho$. However, they converge much more slowly to the correct result, with increasing separation of source and receiver, when $\theta$ is near $\theta_c$ and $z$ is much less than $|z - z'|$. When the accuracy is limited by the approximation of the Hankel function for small $\rho$, higher-order terms are obtained here by interpolation between $\rho = 0$ and a limiting value greater than $\tan\theta_c|z - z'|$ and added to the first-order result. A higher-order approximation for the field at $\rho = 0$ is developed below for use in this interpolation.

Expressions for $\rho = 0$ can be obtained by letting $\rho$ go to zero in the Bessel function form of the Sommerfeld integrals. For the terms involving $V_{12}$ the results are

$$\begin{aligned}
\frac{\partial^2}{\partial\rho\partial z}V_{12}(0,z,z') &= -2\lim_{\rho\to 0}\int_0^\infty \frac{\gamma_2\lambda^2 e^{\gamma_1 z' - \gamma_2 z}}{k_1^2\gamma_2 + k_2^2\gamma_1}J_0'(\lambda\rho)\,d\lambda = 0 \\
\left(\frac{\partial^2}{\partial z^2} + k_2^2\right)V_{12}(0,z,z') &= 2\lim_{\rho\to 0}\int_0^\infty \frac{\lambda^3 e^{\gamma_1 z' - \gamma_2 z}}{k_1^2\gamma_2 + k_2^2\gamma_1}J_0(\lambda\rho)\,d\lambda = 2I_V \\
\frac{\partial^2}{\partial\rho^2}V_{12}(0,z,z') &= 2\lim_{\rho\to 0}\int_0^\infty \frac{\lambda^3 e^{\gamma_1 z' - \gamma_2 z}}{k_1^2\gamma_2 + k_2^2\gamma_1}J_0''(\lambda\rho)\,d\lambda = -I_V \\
\frac{1}{\rho}\frac{\partial}{\partial\rho}V_{12}(0,z,z') &= \lim_{\rho\to 0}\frac{2}{\rho}\int_0^\infty \frac{\lambda^2 e^{\gamma_1 z' - \gamma_2 z}}{k_1^2\gamma_2 + k_2^2\gamma_1}J_0'(\lambda\rho)\,d\lambda = -I_V \\
\frac{\partial^2}{\partial\rho\partial z'}V_{12}(0,z,z') &= 2\lim_{\rho\to 0}\int_0^\infty \frac{\gamma_1\lambda^2 e^{\gamma_1 z' - \gamma_2 z}}{k_1^2\gamma_2 + k_2^2\gamma_1}J_0'(\lambda\rho)\,d\lambda = 0
\end{aligned}$$

where

$$I_V = \int_0^\infty \frac{\lambda^3}{k_1^2\gamma_2 + k_2^2\gamma_1}e^{-(\gamma_2 z - \gamma_1 z')}\,d\lambda. \tag{J-14}$$

An asymptotic expansion for the integral $I_V$ can be obtained by applying Eq. (5.21) from [1], for an integral from a limit at which $F$ has a quadratic dependence on the integrand.

Including the first three terms, this result is

$$\int_0 e^{-F} u^\sigma G\, du \sim \tfrac{1}{2}(\tfrac{1}{2}\sigma - \tfrac{1}{2})!\,(2/F_2)^{(\sigma+1)/2} e^{-F_0}[Q_0^{(\sigma)} + Q_1^{(\sigma)} + Q_2^{(\sigma)}] \qquad \text{(J-15)}$$

where

$$\begin{aligned}
Q_0^{(\sigma)} =& G_0 \\
Q_1^{(\sigma)} =& -\frac{(\frac{1}{2}\sigma)!}{3\sqrt{2}(\frac{1}{2}\sigma - \frac{1}{2})!\,F_2^{3/2}}[(\sigma+2)G_0F_3 - 6G_1F_2] \\
Q_2^{(\sigma)} =& \frac{\sigma+1}{72F_2^3}\Big\{(\sigma+3)G_0[(\sigma+5)F_3^2 - 3F_2F_4] - 12(\sigma+3)G_1F_2F_3 + 36G_2F_2^2\Big\}
\end{aligned}$$

and with

$$F_n = \frac{d^n}{d\lambda^n}F(\lambda)\bigg|_{\lambda=0} \qquad \text{and} \qquad G_n = \frac{d^n}{d\lambda^n}G(\lambda)\bigg|_{\lambda=0}.$$

For $I_V$ from (J-14),

$$\begin{aligned}
F_0 =& jk_2z - jk_1z' \\
F_1 =& 0 \\
F_2 =& -jk_2^{-1}z + jk_1^{-1}z' \\
F_3 =& 0 \\
F_4 =& -3jk_2^{-3}z + 3jk_1^{-3}z'
\end{aligned}$$

and

$$\begin{aligned}
G_{V0} =& \frac{1}{k_1^2\gamma_2 + k_2^2\gamma_1}\bigg|_{\lambda=0} = \frac{-j}{k_1k_2(k_1+k_2)} \\
G_{V1} =& \frac{-\lambda(k_1^2\gamma_2^{-1} + k_2^2\gamma_1^{-1})}{(k_1^2\gamma_2 + k_2^2\gamma_1)^2}\bigg|_{\lambda=0} = 0 \\
G_{V2} =& \left[\frac{k_1^2k_2^2(\gamma_1^{-3} + \gamma_2^{-3})}{(k_1^2\gamma_2 + k_2^2\gamma_1)^2} + \frac{2\lambda^2(k_1^2\gamma_2^{-1} + k_2^2\gamma_1^{-1})}{(k_1^2\gamma_2 + k_2^2\gamma_1)^3}\right]_{\lambda=0} = \frac{-j(k_1^{-3} + k_2^{-3})}{(k_1+k_2)^2}.
\end{aligned}$$

Then (J-15) with $\sigma = 3$ yields

$$I_V \sim \hat{I}_V = \frac{2}{F_2^2}e^{-F_0}\left[G_{V0} + \frac{1}{F_2^2}(2G_{V2}F_2 - G_{V0}F_4)\right]. \qquad \text{(J-16)}$$

Similarly, $U_{12}$ with $\rho = 0$ is

$$U_{12}(0, z, z') = 2\int_0^\infty \frac{\lambda}{\gamma_1 + \gamma_2}e^{-(\gamma_2 z - \gamma_1 z')}\, d\lambda$$

so that

$$\begin{aligned}
G_{U0} =& \frac{2}{\gamma_1 + \gamma_2}\bigg|_{\lambda=0} = \frac{-2j}{k_1 + k_2} \\
G_{U1} =& \frac{-2\lambda(\gamma_1^{-1} + \gamma_2^{-1})}{(\gamma_1 + \gamma_2)^2}\bigg|_{\lambda=0} = 0 \\
G_{U2} =& 2\left[\frac{k_1^2\gamma_1^{-3} + k_2^2\gamma_2^{-3}}{(\gamma_1 + \gamma_2)^2} + \frac{2\lambda^2(\gamma_1^{-1} + \gamma_2^{-1})^2}{(\gamma_1 + \gamma_2)^3}\right]_{\lambda=0} = \frac{-2j(k_1^{-1} + k_2^{-1})}{(k_1 + k_2)^2}.
\end{aligned}$$

Eq. (J-21) with $\sigma = 1$ then yields

$$U_{12} \sim \hat{U}_{12} = \frac{1}{F_2} e^{-F_0} \left[ G_{U0} + \frac{1}{F_2^2} (G_{U2} F_2 - \tfrac{1}{3} G_{U0} F_4) \right] \tag{J-17}$$

The approximations for the field components for $\rho = 0$ are then

$$E_\rho^V(0, z, z') = 0 \tag{J-18a}$$

$$E_z^V(0, z, z') \sim \frac{-j\omega\mu_0}{4\pi} 2\hat{I}_V \tag{J-18b}$$

$$E_\rho^H(0, z, z') \sim \frac{-j\omega\mu_0}{4\pi} (-\hat{I}_V + \hat{U}_{12}) \tag{J-18c}$$

$$E_\phi^H(0, z, z') \sim \frac{j\omega\mu_0}{4\pi} (-\hat{I}_V + \hat{U}_{12}) \tag{J-18d}$$

$$E_z^H(0, z, z') = 0 \tag{J-18e}$$

with $\hat{I}_V$ and $\hat{U}_{12}$ given by (J-16) and (J-17).

The differences between the field approximations in (J-18) and the first-order approximations for general $\rho$, from (5-23), are needed for the interpolated correction of the first-order asymptotic terms. For the general asymptotic approximation, the saddle point $\lambda_s$ for small $\rho$ is from (J-3)

$$\frac{\lambda_s}{\rho} = -j \left( \frac{z}{\Gamma_2} - \frac{z'}{\Gamma_1} \right)^{-1} \approx \left( \frac{z}{k_2} - \frac{z'}{k_1} \right)^{-1}.$$

The first-order approximations for the components of the field for small $\rho$ are then

$$\frac{\partial^2}{\partial\rho\partial z} V_{12}(\rho, z, z') \sim \frac{-2\rho}{k_1(k_1 + k_2)} \frac{e^{-j(k_2 z - k_1 z')}}{(z/k_2 - z'/k_1)^2}$$

$$\left( \frac{\partial^2}{\partial z^2} + k_2^2 \right) V_{12}(\rho, z, z') \sim \frac{2\rho^2}{k_1 k_2 (k_1 + k_2)} \frac{e^{-j(k_2 z - k_1 z')}}{(z/k_2 - z'/k_1)^3}$$

$$\frac{\partial^2}{\partial\rho^2} V_{12}(\rho, z, z') \sim \frac{-2\rho^2}{k_1 k_2 (k_1 + k_2)} \frac{e^{-j(k_2 z - k_1 z')}}{(z/k_2 - z'/k_1)^3}$$

$$\frac{1}{\rho} \frac{\partial}{\partial\rho} V_{12}(\rho, z, z') \sim \frac{-2j}{k_1 k_2 (k_1 + k_2)} \frac{e^{-j(k_2 z - k_1 z')}}{(z/k_2 - z'/k_1)^2}$$

$$\frac{\partial^2}{\partial\rho\partial z'} V_{12}(\rho, z, z') \sim \frac{2\rho}{k_2(k_1 + k_2)} \frac{e^{-j(k_2 z - k_1 z')}}{(z/k_2 - z'/k_1)^2}$$

$$U_{12}(\rho, z, z') \sim \frac{2}{k_1 + k_2} \frac{e^{-j(k_2 z - k_1 z')}}{(z/k_2 - z'/k_1)}.$$

Hence for $\rho = 0$ the only nonzero terms are $\frac{1}{\rho}\frac{\partial}{\partial\rho} V_{12}$ and $U_{12}$. Subtracting these from (J-18), the higher-order terms for $\rho = 0$ are

$$E_\rho'^V(0, z, z') = 0 \tag{J-19a}$$

$$E_z'^V(0,z,z') \sim \frac{-j\omega\mu_0}{4\pi} 2\hat{I}_V \tag{J-19b}$$

$$E_\rho'^H(0,z,z') \sim \frac{-j\omega\mu_0}{4\pi}(-\hat{I}_V + \hat{U}'_{12}) \tag{J-19c}$$

$$E_\phi'^H(0,z,z') \sim \frac{j\omega\mu_0}{4\pi}\left(-\hat{I}_V + \hat{U}'_{12} + \frac{2j}{k_1k_2(k_1+k_2)}\frac{e^{-j(k_2z-k_1z')}}{(z/k_2 - z'/k_1)^2}\right) \tag{J-19d}$$

$$E_z'^H(0,z,z') = 0 \tag{J-19e}$$

where

$$\hat{U}'_{12} = \hat{U}_{12} - \frac{2}{k_1+k_2}\frac{e^{-j(k_2z-k_1z')}}{(z/k_2 - z'/k_1)}.$$

For $\rho$ less than a limit $\rho_x = |z-z'|\tan\theta_A$, where $\tan\theta_A$ is currently set at 0.2, the first-order asymptotic expressions (5-23) are evaluated for the coordinates ($\rho$, $z$, $z'$). Higher-order terms are then evaluated for $\rho = 0$, using (J-19), and for $\rho = \rho_x$ by subtracting the first-order approximations of (5-23) from the second-order approximations (J-9) through (J-13). These higher-order terms are interpolated to ($\rho$, $z$, $z'$) and added to the first-order result. The exponential factor is omitted from the higher-order terms used in the interpolation, and the correct exponential for coordinates ($\rho$, $z$, $z'$) is included in the final result. Since $E_\rho^V$ and $E_z^H$ are odd functions of $\rho$ the second-order terms are interpolated using the formula The field components $E_z^V$, $E_\rho^H$ and $E_\phi^H$ are even functions of $\rho$, so their higher-order terms are interpolated as

$$\hat{f}(\rho) = \frac{1}{\rho_x^2}\Big[\rho^2 f(\rho_x) - (\rho+\rho_x)(\rho-\rho_x)f(0)\Big].$$

When the propagation path is largely in the lower medium ($z/|z-z'| \ll 1$) the two rays, from the saddle point between 0 and $k_2$ and the saddle point between $k_2$ and $k_1$, merge when $\theta = \tan^{-1}(\rho/|z-z'|)$ is near the totally reflecting, or critical angle $\theta_c = \sin^{-1}(k_2/k_1)$. In this region,the asymptotic approximations based on isolated saddle points converge much more slowly than normal as the separation of source and receiver are increased. The second-order terms tend to blow up in this region until the distance becomes very large, so only the first-order approximation is used.

## References


[1] R. B. Dingle, *Asymptotic Expansions: Their Derivation and Interpretation*, Academic Press, London, 1973.

[2] L. M. Brekhovskikh, *Waves in Layered Media*, Academic Press, New York, 1980.